# Estimating the Location of Faults and Damaged Parts in Cable during Offline and Online Condition

# **Doctoral Thesis**

by

ARITRA DAS 2020EEZ0014



# DEPARTMENT OF ELECTRICAL ENGINEERING INDIAN INSTITUTE OF TECHNOLOGY ROPAR

**April 2025** 

# Estimating the Location of Faults and Damaged Parts in Cable during Offline and Online Condition

# **A Thesis Submitted**

In Partial Fulfilment of the Requirements

for the Degree of

# **DOCTOR OF PHILOSOPHY**

by

ARITRA DAS 2020EEZ0014



# DEPARTMENT OF ELECTRICAL ENGINEERING

# INDIAN INSTITUTE OF TECHNOLOGY ROPAR

**April 2025** 

ADITDA DAC, Estimativa de La vicina d'Escale and Danner d'Danie in Calla danie Office
ARITRA DAS: Estimating the Location of Faults and Damaged Parts in Cable during Offline and Online Condition
Copyright © 2024, Indian Institute of Technology Ropar All Rights Reserved
iii

# DEDICATED TO FAMILY

I wish to dedicate all my knowledge owned through my degree to my parents. I am dedicating my thesis to them. Grateful to my parents for believing in me and for their prolonged support. I would like to appreciate my family for being a driving force in my PhD Journey and expecting the same to be continued in all my future endeavours.

**Declaration of Originality** 

I hereby declare that the work which is being presented in the thesis entitled Estimating the

Location of Faults and Damaged Parts in Cable during Offline and Online Condition

has been solely authored by me. It presents the result of my own independent research conducted during the time period from September 2020 to August 2024 under the

conducted during the time period from September 2020 to Magast 2021 under the

supervision of Prof. C.C. Reddy, IIT Ropar. To the best of my knowledge, it is an original

work, both in terms of research content and narrative, and has not been submitted or accepted

elsewhere, in part or in full, for the award of any degree, diploma, fellowship, associateship,

or similar title of any university or institution. Further, due credit has been attributed to the

relevant state-of-the-art and collaborations with appropriate citations and acknowledgments,

in line with established ethical norms and practices. I also declare that any idea stated in my

thesis has not been misrepresented. All the principles of academic honesty and integrity have

been followed. I fully understand that if the thesis is found to be unoriginal, fabricated, or

plagiarized, the Institute reserves the right to withdraw the thesis from its archive and revoke

the associated Degree conferred. Additionally, the Institute also reserves the right to appraise

all concerned sections of society of the matter for their information and necessary action (if

any). If accepted, I hereby consent for my thesis to be available online in the Institute's Open

Access repository, inter-library loan, and the title & abstract to be made available to outside

organizations.

Signature

Name: ARITRA DAS

Entry Number: 2020 EEZ 0014

Program: PhD. Department: EED

Indian Institute of Technology Ropar

Rupnagar, Punjab 140001

Date:

v

# **Acknowledgments**

I wish to thank my supervisor Prof. C.C. Reddy for the continuous support and encouragement throughout my journey as a PhD candidate. I am inspired by his knowledge and problem solving skills. I wish to continue in his path to share my knowledge with others.

I am also immensely thankful to the IIT Ropar for giving me the opportunity to pursue my professional degree. I extend my gratitude to the Chairman Dr. Subramanya Murala for his valuable guidance and support. I am deeply appreciative to the doctoral committee members Dr. Ravi Mohan Prasad, Dr. Prabhat K. Agnihotri and Dr. Ravi Teja for their constructive direction and timely support.

I am grateful to the IEEE DEIS Educational Committee for granting me the 2022 IEEE DEIS Graduate Student Fellowship. for offering me the fellowship for the project and publishing article "Location of Damaged Insulation for an Underground Power Cable Under High-Frequency Model"

Thanks to Nisha and respectful seniors Dr. Birender Singh, Dr. Ajith John Thomas, Dr. Sathyamoorthy, Dr. Iyappan. C, and Dr. Priyesh Pandey for sharing their knowledge, and valuable technical discussions. To my present collegues - Ritesh, Purna, Pranav, Harshith, Parimal, Anas, Priti, Akshay, Manika, Adarsh, Manoj, Mayank, Subham and Amit I am grateful for your continuous support.

Finally, I extend my heartfelt thanks to Mr. Dilbag Singh and Mr. Jaspreet Singh for their continuous assistance throughout my research journey in laboratory experiments.

# Certificate

This is to certify that the thesis entitled Estimating the Location of Faults and Damaged Parts in Cable during Offline and Online Condition, submitted by ARITRA DAS (2020EEZ0014) for the award of the degree of Doctor of Philosophy of Indian Institute of Technology Ropar, is a record of bona fide research work carried out under my (our) guidance and supervision. To the best of my knowledge and belief, the work presented in this thesis is original and has not been submitted, either in part or full, for the award of any other degree, diploma, fellowship, associateship or similar title of any university or institution.

In my (our) opinion, the thesis has reached the standard fulfilling the requirements of the regulations relating to the Degree.

Signature of the Supervisor

Prof. C.C. Reddy
Electrical Engineering Department
Indian Institute of Technology Ropar
Rupnagar, Punjab 140001

Date:

# Lay Summary

Estimating the location of faults and damaged parts in high-voltage cables is a critical process with profound implications for safety, operational efficiency, and economic viability. High-voltage cables are fundamental components of power transmission systems, and any faults within these cables can have significant consequences.

Operational efficiency is the major reason for estimating the location of faults and damaged parts in high-voltage cables. When a fault occurs, it can cause substantial service interruptions, affecting a large number of consumers and critical infrastructure. Quick and precise fault localization allows for faster repairs, minimizing downtime and ensuring that the power supply is restored swiftly. This is particularly important in industries and services that rely on continuous power supply. Moreover, early detection of faults prevents minor issues from escalating into major failures that require extensive repairs or complete cable replacements, which are far more expensive.

Additionally, accurate fault localization supports proactive maintenance strategies. By continuously monitoring high-voltage cables and detecting faults early, maintenance teams can perform timely interventions, ensuring that the cables remain in optimal condition. This proactive approach not only extends the lifespan of the cable infrastructure but also reduces the frequency and severity of failures, contributing to long-term operational stability.

The thesis proposes systems and methods to locate faults and damaged parts in cables with high accuracy for both online and offline conditions.

# **Abstract**

Condition monitoring in high voltage (HV) cables is essential to ensure reliability, prevent failures, and enhance safety. It helps in the early detection of faults, reduces downtime, and extends the cable's lifespan. By monitoring, maintenance can be planned proactively, avoiding costly emergency repairs and ensuring continuous, efficient power supply. In this thesis, analytical methods are proposed for the location of a short circuit fault and damaged insulation and conductor screen parts in a power cable using impedance spectroscopy (IS) obtained from sweep frequency response analysis (SFRA). The driving point impedance function (DPIF) construction of a power cable is introduced as an initial step toward using the SFRA technique for power cable condition monitoring. It is proposed that SFRA data be used to generate the DPIF. Furthermore, the DPIF of the cable is generated analytically using the knowledge of the cable's frequency-dependent characteristics, material qualities, and dimensions, while the impedance spectroscopy is estimated using conventional transmission line theory. For the first time in the instance of a cable, a relationship is established between the sum of frequencies of zeroes and the electrical properties of the cable. The relationship between zeroes and the electrical parameters of the cable and the propagation constant is established using the state space model and transmission line theory, respectively. This thesis achieves the location of defects of different sizes in the semiconducting layer by using the frequency location of zeros and their cumulative sum and product to locate defects, and by using the proposed analytical formulae to locate a short-circuit fault using the location of poles and zeros of the impedance function before and after the fault.

Further, a novel method is proposed to estimate sheath-to-ground (SG) faults at any arbitrary locations in a cross-bonded (CB) and non-cross-bonded cable (NCB) by only measuring the earthing current from both grounding boxes during online conditions. In CB cable system, the range of grounding current in SG fault condition is estimated for a cable having SG fault at different minor sections using the analytical method which is based on the proposed circuit model of the CB cable. The measured grounding current is compared with the analytical fault current range, and if the measured current is in the proposed analytical range, the SG fault is confirmed and the location of the same is estimated by the proposed analytical formulae. In NCB cable system, the healthy condition grounding current is estimated for different types of bonding using the analytical method which is based on the proposed circuit model of the cable. The measured grounding current is compared with the

analytically obtained healthy condition current, and if the measured current is not the same as the former, an SG fault is confirmed in the cable. The location of the SG fault at any arbitrary location is estimated using the proposed analytical formulae. The grounding current in HVDC cable will be negligible, therefore to estimate the location of SG fault, the proposed method is further enhanced by integrating online TDR measurements with the Decision Tree Regression (DTR) approach, utilizing an inductive coupler for signal acquisition. In HVDC systems. The online TDR captures reflection signals indicative of sheath-to-ground faults caused by impedance mismatches along the cable length. The DTR model is trained using features extracted from these TDR signals. The proposed integration of online TDR and DTR for HVDC cables enhances fault localization accuracy, offering a reliable, real-time method to identify SG faults at arbitrary locations under online conditions, even in the presence of operational noise and system variations.

Along with this a comparative study of different end bonding methods in a non-uniform length minor section in a CB HV power cable is also performed in this thesis. In a practical case scenario, sometimes the old cable route has to be replaced with a new route of a different cable length. Due to an imbalance in the cable length, a huge circulating current flows in the sheath. Therefore different end-bonding methods were presented along a new end-bonding method is proposed in this thesis to mitigate the circulating current and voltage. Sheath currents and voltage are analytically obtained at different cable parts using the proposed sheath circuit model to validate the proposed model. Steady-state experiments were conducted in the laboratory as well as simulations for both steady-state and transient conditions were performed on MATLAB Simulink to verify the proposed method and analytical formulae.

**Keywords**: Power cable, Driving Point Impedance Function, ladder network of cable, Frequency response, Short-circuit faults, conductor screen defect, insulation screen defect, sheath to ground fault, Cross Bonded cable, Non-Cross Bonded Cable System, Sheath to ground fault, Circuit model of cross bonded and non cross bonded cable system, HVDC cable, online TDR, Special bonding technique.

# **List of Publications and Awards**

### **Patents**

- 1. **A. Das,** and C. C. Reddy "System and Method of Locating a Fault in Power Cable", Indian Patent, Application No: 202111030999, Patent no: 543793. (Granted).
- 2. **A. Das,** and C. C. Reddy "Method Of Locating Inception Of Water Treeing In A Power Cable", Indian Patent, Application No: 202311020840, Date of Filing: 24/03/2023. (Published).
- 3. **A. Das,** and C. C. Reddy "System And Method of Locating a Sheath to Ground Fault in Electric Cables", **US patent**, Application No: 18647131, D Recordation Date: 30/04/2024. (Published).
- 4. **A. Das,** and C. C. Reddy "Method For Mitigating Circulating Currents And Voltages Of Different Minor Sections Of Cross-Bonded Cables", Application No: 202411056182, Date of Filing: 23/07/2024. (Published).
- 5. **A. Das,** and C. C. Reddy "System and Methods to Estimate Sheath to Ground Faults Using Online Contactless Time Domain Reflectometry in an HVDC cable system", Application No: 202511004843, Date of Filing: 21/01/2025. (Published)..

### Journals

- 1. **A. Das** and C. C. Reddy, "A Novel Technique for Estimating the Location of Defect or Inception of Water Treeing in the Semiconducting Screen of a Cable," in *IEEE Transactions on Industrial Electronics*, doi: 10.1109/TIE.2023.3340216. (Impact factor: **8.4**).
- 2. **A. Das** and C. C. Reddy, "An Analytical Approach to Locate Short Circuit Fault in a Cable Using Sweep Frequency Response Analysis," in *IEEE Transactions on Industrial Electronics*, vol. 70, no. 5, pp. 5235-5244, May 2023, doi: 10.1109/TIE.2022.3189080. (Impact factor: **8.4**).
- 3. **A. Das** and C. C. Reddy, "A novel method for condition monitoring in cable in the frequency domain," in Power Engineer Journal, vol. 25, pp. 16-20, September 2023, Print ISSN:2229-4465, Online ISSN: 0976-2396.
- 4. **A. Das** and C. C. Reddy, "Locating Sheath-to-Ground Fault Using Earthing Currents in a Cross-Bonded Power Cable During Online Condition," in IEEE Transactions on Instrumentation and Measurement, (Under Review).
- 5. **A. Das** and C. C. Reddy, "On the Estimation of a Sheath-to-Ground Fault on a Non-Cross-Bonded Power Cable in Online Condition," in IEEE Transactions on Power Delivery. (Under Review).
- 6. **A. Das** and C. C. Reddy, "Comparative Study of Different End Bonding Methods in a Non-Uniform Minor Section Length of a Cross-Bonded Cable in IEEE Transactions on Industrial Application. (Under Review).
- 7. **A. Das** and C. C. Reddy, "On The Estimation of Sheath-to-Ground Fault in HVDC cable During Online Condition," in IEEE Transactions on Industrial Informatics, (Under Review).

## Conferences

- 1. **A. Das** and C. C. Reddy, "Burn Down phenomenon of covered conductors," 2021 Proceedings of National Conference High Voltage Engineering and Technology (HVET), UHVRL, CPRI, Hyderabad, India, March 2021, pp. 35-37
- 2. Devendra Parmar, Kuldeep Meena, Parimal Sharma, A. Das, C.C.Reddy, "Surface Temperature Monitoring of Cables Using IoT," 2022 11'th International Conference on Cables, CABLETECH, CPRI, Bengaluru, India, February 2022, pp. 37-40.
- 3. Kuldeep Meena, Devendra Parmar, A. Das, C. C.Reddy, "Estimation of Cable maximum operating temperature using different machine learning algorithms," 2022 11'th International Conference on Cables, CABLETECH, CPRI, Bengaluru, India, February 2022, pp. 131-134.
- 4. **A. Das** and C.C. Reddy, "Construction of Physically Realizable Driving Point Impedance Function From Impedance Spectroscopy of the Cable Using Sweep Frequency Response Analysis", P-P2-20June 2023 Lyon, France.
- 5. **A. Das** and C. C. Reddy, "Sheath Voltage and Sheath Current Phenomenon for Different Types of Bonding for HV Power Cable Under Steady State," 2022 IEEE 6th International Conference on Condition Assessment Techniques in Electrical Systems (CATCON), Durgapur, India, 2022, pp. 202-206, doi: 10.1109/CATCON56237.2022.10077653.
- 6. A. P. Pandey, **A. Das** and C. C. Reddy, "Transient Over Voltages in Cross-Bonded Power Cables due to Lightning Impulse," 2022 IEEE 10th Power India International Conference (PIICON), New Delhi, India, 2022, pp. 1-4, doi: 10.1109/PIICON56320.2022.10045121.
- 7. **A. Das** and C. C. Reddy, "Investigations on Sheath Voltage and Current During Short-Circuited Condition On a Cross-Bonded Cable," 2022 IEEE 10th Power India International Conference (PIICON), New Delhi, India, 2022, pp. 1-5, doi: 10.1109/PIICON56320.2022.10045244.
- 8. S. Dhayalan, A. Das, P. Johri and C. C. Reddy, "Estimation of Electric Field and Temperature in HVDC Cables Under Different Environmental Conditions," 2021 IEEE 16th International Conference on Industrial and Information Systems (ICIIS), Kandy, Sri Lanka, 2021, pp. 262-264, doi: 10.1109/ICIIS53135.2021.9660725.
- 9. **A. Das** and C. C. Reddy, "Location of Damaged Insulation for an Underground Power Cable Under High-Frequency Model," 2024 IEEE 7th International Conference on Condition Assessment Techniques in Electrical Systems (CATCON), Kolkata, India, 2024, pp. 133-137, doi: 10.1109/CATCON60527.2024.10831763
- 10. **A. Das**, S. M. Anas and C. C. Reddy, "Investigation of Sheath Current at Different Joints for Different Types of Bonding During Busbar Fault," 2024 IEEE 7th International Conference on Condition Assessment Techniques in Electrical Systems (CATCON), Kolkata, India, 2024, pp. 138-141, doi: 10.1109/CATCON60527.2024.10831062.
- 11. **A. Das** and C. C. Reddy, "Recent Advances in Condition Monitoring in Cable using Impedance Spectroscopy," 2024 12th International Conference on Cables, CABLETECH, CPRI, Bengaluru, India, 13th June 2024.
- 12. **A. Das** and C. C. Reddy, "New Advances in Power Cable Condition Monitoring" GRIDCON, New Delhi, India, 9<sup>th</sup> -11<sup>th</sup> Mrach 2025.(Accepted)
- 13. A. Kumar, A. Das and C. C. Reddy, "Partial Discharge Simulation in High Voltage Cables" IEEE 18th International Conference on Industrial and Information Systems

(ICIIS), IIT Madras, India, 21st -23rd December 2024. (Accepted)

# **Book Chapters**

- 1. Kumar, M., **Das, A.**, Reddy, C.C. (2024). Estimation of the Impedance of a Distributed Model of a Transmission Line Under a Frequency Sweep. In: Sharma, A. (eds) High Voltage–Energy Storage Capacitors and Their Applications. HV-ESCA 2023. Lecture Notes in Electrical Engineering, vol 1143. Springer, Singapore.
- 2. Saini, M., **Das, A.,** Reddy, C.C. (2024). Behavioral Study of the Impulse Waveform Superimposed with Sinusoidal Power Frequency in Transmission Line. In: Sharma, A. (eds) High Voltage–Energy Storage Capacitors and Their Applications. HV-ESCA 2023. Lecture Notes in Electrical Engineering, vol 1143. Springer, Singapore.

### **Awards**

- 1. Prime Minister Research Fellow (PMRF) 2021.
- 2. **IEEE** Dielectric Insulation and System (**DEIS**) graduate fellowship award 2023
- 3. 3rd prize in the "Young Researcher Award" in Jicable'23, Lyon, France, organized by the International Council on Large Electric Systems (CIGRE).
- 4. GRID-INDIA Power System Award (GIPSA) 2024-25 in the Ph.D./Doctoral category.

# **Table of Contents**

Declaration of	of Originalityv
Acknowledg	mentsvi
Certificate	vii
Lay Summar	yviii
Abstract	ix
List of Public	cations and Awardsxi
List of Figur	esxix
List of Table	s
Notations an	d Abbreviationsxxvi
Chapter 1	1
1.1 Ove	erview of Underground Power Cables1
1.2 Def	Fects, Damage and Short-circuit Faults in a Cable
1.2.1	Defects and Short-Circuited faults in Power Cable
1.2.1.1	Mechanical Damage
1.2.1.2	Electrical and Thermal Damage
1.2.1.3	Sheath to ground faults in cable5
1.2.1.4	Partial Discharge and water treeing6
1.2.1.5	Short-circuit faults or Catastrophic Faults in power cable
1.3 Ove	erview of Estimating the location of defects and catastrophic faults Techniques8
1.3.1	Time Domain Reflectometry (TDR)8
1.3.2	Frequency Domain Reflectometry (FDR)9
1.3.3	Partial Discharge Detection9
1.3.4	Electrical Resistance Measurement
1.4 Mo	tivation for Condition Monitoring in Cable in Offline and Online Mode11
1.4.1 and Sho	Motivation to Use Impedance Spectroscopy to Estimate the Location of Defects rt-Circuit Faults in Cable in Offline Mode
1.4.2 Any Arl	Motivation to Use Grounding Current to Estimate Sheath to Ground Faults at pitrary Location during Online Conditions for HVAC Cables
1.4.3 Cables	Motivation to Use Online TDR to Detect Sheath to Ground Fault In HVDC 13
1.4.4	Motivation to Use Special Sheath Bonding Technique
1.5 Org	ganization of thesis
Chapter 2	17

2.1 Topic 1: Introduction of Sweep Frequency Response Analysis in Cable and Estimating the Location of Short-circuit Fault Using Impedance Spectroscopy
2.1.1 Introduction of Sweep Frequency Response Analysis in Cable
2.1.2 Estimating the Location of Short-circuit Fault in Cable
2.2 Topic 2: Estimating the Location of Semiconducting Screen Defect Using Impedance Spectroscopy
2.3 Topic 3: Estimating the Location of Sheath-to-ground fault in a cross-bonded HVAC cable
2.4 Topic 4: Estimating the Location of Sheath-to-ground fault in a non-cross-bonded HVAC cable
2.5 Topic 5: Estimating the Location of Sheath-to-ground fault in a HVDC cable22
2.6 Topic 6: New End Bonding Technique in an Existing Non Uniform Length Cross Bonded HVAC Cable
2.7 Methodology Proposed
2.7.1 Methodology to Estimate the Location of short-circuit faults in a cable26
2.7.2 Methodology to Estimate the Location of Semiconducting Screen Defect in a cable 26
2.7.3 Methodology to Estimate the Location of Sheath-to-Ground Fault in a CB and NCB HVAC Cable
2.7.4 Methodology to Estimate the Location of Sheath-to-Ground Fault in a HVDC Cable 27
2.7.5 Methodology to Mitigate Excessive Sheath Current and Voltage due to Non-Uniform Minor Section Length in a CB power Cable
Chapter 3
3.1 Estimated DPIF for the cable using Electrical Parameters
3.1.1 Deriving Impedance Spectroscopy Using the Traditional Transmission Line (TL) Model 30
3.1.2 Estimating the DPIF of the Cable by Solving the Ladder Network of the Cable31
3.2 Estimated Short Circuit Fault Location Using Impedance Spectroscopy32
3.3 Experiments and Simulations to Estimate the Locations of Short Circuit Faults in a Cable 34
3.4 Results and Discussion of the Estimating the Location of Short-circuit Fault in a Cable 38
3.4.1 Impedance Spectroscopy of a Healthy Cable of 25m long
3.4.2 Estimating the Location of Short-Circuit Fault in a Laboratory Cable of 25m long 40
3.4.3 Estimating the Location of Short-Circuit Fault in an On-Field Case Study42

3.4.4 Es	stimating the Location of Short-Circuit Fault in a Simulation Study44
Chapter 4	47
	ationship Between Zeroes of the Impedance Graph and Electrical Parameters of
4.1.1	Obtaining the Relationship through Classical Transmission Line Model47
4.1.2	Obtaining the Relationship through State Space Model
	tionship between Zeroes of the Impedance Graph and Electrical Parameters of
1	eriments and Simulations Performed to Estimate the Location of cting Screen Defect in a Cable
	alts and Discussion of the Experiments and Simulations Performed to Estimate on of Semiconducting Screen Defect in a Cable
4.4.1 H	ealthy Cable Impedance Analysis (25m Test Cable)56
4.4.2 H	ealthy Cable Impedance Analysis (25m Test Cable)57
4.4.3 M	fulti-point Defects in an Experimental Cable
4.4.4 Si	mulation Results for Defects in a 1000m Cable60
4.4.5 M	Tulti-point Defects in Simulated Conductor Screens
Chapter 5	64
	lytical Formulae For Grounding Current in a CB Power Cable During Healthy
5.1.1	Inductive current in the metallic sheath
5.1.2	Capacitive current in the metallic sheath67
5.2 Ana	lytical formulae for the location of the SG fault69
5.2.2	Sheath fault at first minor section
5.2.2	Sheath fault at second minor section
5.2.3	Sheath fault at third minor section
5.3 Sim	ulations and Experiments on CB Cable76
5.4 Resu	ults and Discussions79
5.4.1.	Experimental results for SG fault location for the first experimental case study 79
5.4.2.	Experimental results for SG fault location for the first experimental case study 83
Chapter 6	84
	lytical Formulae for Circulating Current in An NCB Power Cable - Healthy

6.1.1	Single-point bonding (bonding at the end or beginning)84
6.1.2	Single-point bonding (bonding in the middle)85
6.1.3	Two-point bonding86
6.2 Ana	alytical formulae for the location of the SG fault for different types of bonding 87
6.2.1 or begin	Estimating the location of SG fault at Single-point bonding (bonding at the end ning)
6.2.2 middle)	Estimating the location of SG fault at Single-point bonding (bonding at the 89
6.2.3	Inductive current in the metallic sheath91
6.3 Exp fault. 92	periments and Simulation in a NCB power cable to Estimate the Location of SG
6.3.1	Experiments on Single-point bonding (bonding at the beginning)93
6.3.2	Experiments on Single-point bonding (bonding at the middle)93
6.3.3	Experiments on Two-point bonding94
6.4 Exp	periments and Simulations on a NCB cable to estimate the location of SG fault.94
6.4.1	Healthy condition grounding current for different types of bonding94
6.4.2	Experimental results for SG fault location for different types of bonding95
6.4.2.1	Experiments on Single-point bonding (bonding at the beginning)95
6.4.2.2	Experiments on Single-point bonding (bonding at the middle)96
6.4.2.3	Experiments on Two-point bonding98
Chapter 7	99
	cuit Model And Feature Extraction from Cable Dimension To Perform Online Sheath
7.1.1	Circuit Model to Perform Online TDR in the Sheath99
7.1.2 Dimensi	Transmission Line Model of the Sheath to Extract Key Parameters from Cable ons
7.2 She	ath Fault Location Using Fast Fourier Transform and DTR102
7.2.1	FFT on the Captured Signal on the DSO: Problem and Solution102
7.2.1.1	Challenges of Applying FFT to the Entire Signal102
7.2.1.2 Differen	Proposed Method to Apply FFT to Obtain Distinctive features for Faults at Lengths
7.2.2	DTR Method to Estimate the Location of SG Fault
7.3 Exp 107	periments and Simulation to Estimate the Location of SG fault in a HVDC cable
7.4 Exp	periments to estimate the location of SG fault in a HVDC cable109

7.4.1	Estimating the location of SG fault in type 1 cable system	109
7.4.2	Estimating the location of SG fault in type 2 cable system	111
Chapter 8		115
8.1 Sh	eath Circuit model of different types of end bonding of sheath	115
8.1.1	The second set of Straight joints are individually solidly grounded	116
8.1.2	Second Straight joints are individually grounded with SVL	117
8.1.3 Propose	Last Straight through joints are connected and grounded together with	
8.2 An 119	nalytical Model of Total Current in the Joints for Different Types of End B	Bonding
8.2.1	Current in the loop 1, 2, and 3 due to inductive effect	119
8.2.2	Current in the joints due to capacitive effect	119
8.3 An	nalytical Model of Voltage in the Joints for Different Types of End Bonding	g121
8.3.1	Voltage in the joints due to inductive effect	121
8.3.2	Voltage in the joints due to inductive effect	122
	periments and Simulation to Estimate the Sheath Current and Volta End Bonding Methods.	_
	periments to estimate to Estimate the Sheath Current and Voltage for D ling Methods	
8.5.1	Practical Case Study	125
8.5.2	Simulation Case Study	128
Chapter 9		134
References		130

# **List of Figures**

Figure 1.1 (a) The core length of DC-XLPE cables installed and under construction in the year 2018 (b) Future growth predicted length of cable [1]
Figure 1.2 Excessive Bending as a part of Mechanical Damage in Power Cable [2]3
Figure 1.3 Electro thermal Damage in Cable [3]4
Figure 1.4 Water tree in XLPE Insulated Cable [4]6
Figure 2.1 Schematic diagram of a single point bonding at the beginning22
Figure 2.2 Schematic diagram of a single point bonding at the middle
Figure 2.3 Schematic diagram of a two point bonding system
Figure 2.4 Schematic diagram of a major section in a CB cable with a new minor cable route for a third minor section
Figure 3.1 Configuration of a single-core cable with the outer sheath connected to the ground.
Figure 3.2 Ladder network representation of a healthy cable at power frequencies divided into <i>n</i> sections
Figure 3.3 FEM analysis of a 25m long cable showing (a) resistance and (b) inductive reactance.
Figure 3.4 Ladder network representation of a healthy cable at high frequencies divided into <i>n</i> sections
Figure 3.5 Proposed ladder network model for the cable at high frequencies with a fault33
Figure 3.6 Simulation results showing: (a) Current from the function generator without a current-limiting resistor, and (b) Current from the function generator with the inclusion of the current-limiting resistor <i>RC</i>
Figure 3.7 Illustration of the connection setup for a three-core cable with a DSO, function generator, and current-limiting resistor
Figure 3.8 Experimental setup for measuring DPIF: (a) (1) Remaining phases short-circuited using a wire, (2) Current-limiting resistor of 20 $\Omega$ , (b) Short-circuit fault introduced using a nail
Figure 3.9 Experimental configuration for determining the location of the short-circuited fault
Figure 3.10 (a) Top view of a practical setup with a 146.7m cable connected at both ends, (b) 360-degree panoramic view of the setup, (c) Section of the cable with a short circuit37
Figure 3.11 Estimating driving point impedance function analytically with practical and simulation results.
Figure 3.12 Impedance spectroscopy of healthy cable along with six different cases of fault with fault resistance of $1 \text{m} \Omega$

Figure 3.13 Various fault resistance scenarios in a 25-meter experimental cable located at (a 5 meters, (b) 10 meters, (c) 15 meters, (d) 20 meters, (e) 22.5 meters, and (f) 25 meters4	
Figure 3.14 Impedance measurement graph: Case I represents the impedance graph measured from open-end I, while Case II corresponds to the impedance graph measured from open-end II	ıd
Figure 3.15 Various fault scenarios in a simulated cable with a fault resistance of 1 m $\Omega$ 4	14
Figure 3.16 Various fault resistance scenarios in a 1000m-long simulated cable at the following locations: (a) 50m, (b) 250m, (c) 500m, (d) 750m, (e) 950m, and (f) 1000m4	
Figure 4.1 (a) Comprehensive parametric representation of a cross sectional single-core cab with a grounded outer sheath., (b) Simplified parametric model of a cross sectional single core cable with a grounded outer sheath	e-
Figure 4.2 Parametric representation of a single-core cable with defects in (a) the conductor screen and (b) the insulation screen	
Figure 4.3 Experimental setup for locating insulation screen defects5	54
Figure 4.4 (a) Polyethylene-coated nails of varying diameters, (b) Process of creating defection the insulation screen	
Figure 4.5 Cable model for simulation with three factory joints and defects located at : Conductor screen: 50 m, 250 m, and 500 m. ii) Insulation screen: 750 m, 950 m, and 1000 m	n.
Figure 4.6 FEM-based model of a straight-through joint showing defects in (a) the insulation screen and (b) the conductor, each with defect diameter <i>d</i>	on
Figure 4.7 Driving point impedance plot of the 25-meter length healthy test cable5	57
Figure 4.8 Impedance plots for the healthy cable and various defect cases with a diameter of the figure 4.8 Impedance plots for the healthy cable and various defect cases with a diameter of the figure 4.8 Impedance plots for the healthy cable and various defect cases with a diameter of the figure 4.8 Impedance plots for the healthy cable and various defect cases with a diameter of the figure 4.8 Impedance plots for the healthy cable and various defect cases with a diameter of the figure 4.8 Impedance plots for the healthy cable and various defect cases with a diameter of the figure 4.8 Impedance plots for the healthy cable and various defect cases with a diameter of the figure 4.8 Impedance plots for the healthy cable and various defect cases with a diameter of the figure 4.8 Impedance plots for the healthy cable and various defect cases with a diameter of the figure 4.8 Impedance plots for the healthy cable and various defect cases with a diameter of the figure 4.8 Impedance plots for the figure 4.8 Impedance plots	
Figure 4.9 Impedance plots for defects of varying diameters in a 25-meter cable at: (a) 5 m (b) 10 m, (c) 15 m, (d) 20 m, (e) 22.5 m, (f) 25 m	
Figure 4.10 Impedance plots for two insulation defects near the source (3 m and 5 m) and or defect at 25 m	
Figure 4.11 Impedance plots for the simulated cable with defects (diameter: 2 mm)6	50
Figure 4.12 Accuracy with varying numbers of zeroes for defect location estimation6	51
Figure 4.13 Impedance plots for different screen defect diameters at: (a) 50 m, (b) 250 m, (c) 500 m, (d) 750 m, (e) 950 m, (f) 1000 m	
Figure 4.14 Impedance plots for two conductor defects (3 m and 5 m) and one defect at 100 m.	
Figure 5.1 Schematic diagram of a trefoil laying cable configuration6	55
Figure 5.2 Schematic diagram of a major section in a CB cable6	55
Figure 5.3 Circuit model of a major section CB cable6	55
Figure 5.4 Schematic diagram of loop 1 ( <b>R1-Y2-B3</b> ) in a major section	56

Figure 5.5 Equivalent circuit for inductive current in loop 1
Figure 5.6 Equivalent circuit for capacitive current in loop 1
Figure 5.7 Schematic diagram of three simultaneous major sections
Figure 5.8 (a) Schematic diagram for SG fault in loop 1 (b) Grounding currents for fault at different locations.
Figure 5.9 Equivalent circuit for an SG fault (a) inductive current (b) capacitive current in first minor section
Figure 5.10 Equivalent circuit for an SG fault (a) inductive current (b) capacitive current in second minor section
Figure 5.11 Equivalent circuit for an SG fault (a) inductive current (b) capacitive current in third minor section
Figure 5.12 Flowchart to estimate the location of SG fault at any arbitrary location in a CB cable system during online condition
Figure 5.13 Experimental setup to estimate the location of the SG fault77
Figure 5.14 (a) Experimental setup to measure the grounding current to estimate the location of the SG fault on a filed case (b) SG fault in the cable (c) Single line diagram of the on field case study
Figure 5.15 Measured faults current from DSO at <b>RG1</b> and <b>RG2</b> for different practical case studies (a) Case I, (b) Case II, (c) Case III, (d) Case IV (e) Case V (f) Case VI (g) Case VII (h) legend for case I-V (i) legend for case VI-VII
Figure 5.16 Measured rms faults current at <b>RG1</b> and <b>RG2</b> for different practical case studies (a) Case I, (b) Case II, (c) Case III, (d) Case IV (e) Case V (f) Case VI (g) Case VII
Figure 6.1 Circuit model (a) inductive, (b) capacitive for a healthy single point bonding at the beginning
Figure 6.2 Circuit model (a) inductive, (b) capacitive for a healthy single point bonding at the middle
Figure 6.3 Schematic diagram of three simultaneous sections
Figure 6.4 Circuit model (a) inductive, (b) capacitive for a single point bonding at the beginning having an SG fault.
Figure 6.5 Grounding resistance currents for fault at different locations for a single point bonding at the beginning
Figure 6.6 Circuit model (a) inductive, (b) capacitive for a single point bonding at the middle having an SG fault90
Figure 6.7 (a) Grounding resistance currents (b) Phase difference between sheath and conductor current for fault at different locations for a single point bonding at the middle90
Figure 6.8 Grounding resistance currents for fault at different locations for a single point bonding at the beginning

Figure 6.9 Flowchart to estimate the location of SG fault at any arbitrary location in a NCB cable system during online condition
Figure 6.10 Experimental setup to estimate the location of the SG fault93
Figure 6.11 Measured faults current at <b>RG1</b> for single-point bonding at the beginning of practical case studies (a) Case I, (b) Case II
Figure 6.12 Measured (a) current (b) phase at <b>RG1</b> for Case I of single point bonding at the middle96
Figure 6.13 Measured (a) current (b) phase at <b>RG1</b> for Case II of single point bonding at the middle
Figure 6.14 Measured (a) current (b) phase at <b>RG1</b> for Case III of single point bonding at the middle
Figure 6.15 Measured faults current at <b>RG1</b> and <b>RG2</b> for different practical case studies (a) Case I, (b) Case II, (c) Case III, (d) Case IV (e) Case V of two-point bonded cable98
Figure 7.1 Proposed schematic model to perform online TDR in the metallic sheath to estimate SG fault location
Figure 7.2 Double-circuit transmission line model to represent the sheath of a cable 100
Figure 7.3 (a) Simulation results of TDR response for faults at different locations in its complete time spectrum of a 220 Kv long cable, (b) FFT of the complete time spectrum of simulated TDR response having fault at different locations
Figure 7.4 (a) Simulation results of TDR response for faults at different locations in its modified time spectrum of a 25000m long cable, (b) FFT of the modified time spectrum of simulated TDR response having fault at different locations
Figure 7.5 Complete flowchart of the proposed methodology to estimate the location of SG fault
Figure 7.6 Illustration of a basic regression decision tree
Figure 7.7 Experimental setup to perform online TDR on type 1 HVDC cable. FG stands for Function Generator
Figure 7.8 Experimental results of TDR response for faults at different locations in its complete time spectrum of a Type 1 cable
Figure 7.9 FFT of the modified time spectrum of practical cable of Type 1 having fault at (a) 5m, (b) 10m, (c) 15m, (d) 20m, (e) 22.5m (f) 25m110
Figure 7.10 The magnitude of <b>fpeak</b> and <b>V'Z, f</b> of faults at different locations for Type 1 cable, obtained from the FFT graph and Algorithm 1
Figure 7.11 Experimental results of TDR response for faults at different locations in its complete time spectrum of a Type 2 cable
Figure 7.12 FFT of the modified time spectrum of practical cable of Type 1 having fault at (a) 7m, (b) 12.5m, (c) 18m, (d) 28m, (e) 35m (f) 38.5m112

Figure 7.13 The magnitude of <b>fpeak</b> and <b>V'Z, f</b> of faults at different locations for Type 2 cable, obtained from FFT graph and Algorithm 1
Figure 8.1 Schematic diagram of a non-uniform length minor sections in a CB cable with solid grounding at the end
Figure 8.2 Equivalent circuit for inductive effect in a non-uniform length minor section CB cable with solid grounding at the end.
Figure 8.3 Equivalent circuit for capacitive effect in a non-uniform length minor section CB cable with solid grounding at the end.
Figure 8.4 Schematic diagram of a non-uniform length minor sections CB cable grounded with SVL at the end
Figure 8.5 Schematic diagram of a non-uniform length minor sections CB cable with three straight-through joints terminals connected together at the end with SVL
Figure 8.6 Equivalent circuit for inductive effect in a non-uniform length minor section with three straight-through joints connected together at the end with SVL
Figure 8.7 Equivalent circuit for capacitive effect in a non-uniform length minor section cable with three straight-through joints connected together at the end with SVL
Figure 8.8 Experimental setup to measure current and voltage at different joints for the proposed end bonding method.
Figure 8.9 Measured (a) current and (b) voltage across the different joints of a 3m long third minor section for solid grounding
Figure 8.10 Measured (a) current and (b) voltage across different joints of a 7m long third minor section for solid grounding
Figure 8.11 Measured (a) current and (b) voltage across different joints of a 3m long third minor section for sheath grounded with SVL.
Figure 8.12 Measured (a) current and (b) voltage across different joints of a 7m long third minor section for sheath grounded with SVL
Figure 8.13 Measured (a) current and (b) voltage across different joints of a 3m long third minor section for the proposed method.
Figure 8.14 Measured (a) current and (b) voltage across the different joints of a 7m long third minor section for the proposed method.
Figure 8.15 Measured (a) ST joints and (b) CB joints current for the proposed method case II and original case study
Figure 8.16 Measured (a) ST joints and (b) CB joints voltage for the proposed method case II and original case study
Figure 8.17 Simulated (a) current and (b) voltage across different joints of a 150m long third minor section for solid grounding
Figure 8.18 Simulated (a) current and (b) voltage across different joints of an 800m long third minor section for solid grounding

Figure 8.19 Simulated (a) current and (b) voltage across different joints of a 150m long third minor section for sheath grounded with SVL
Figure 8.20 Simulated (a) current and (b) voltage across different joints of an 800m long third minor section for sheath grounded with SVL.
Figure 8.21 Simulated (a) current and (b) voltage across different joints of a 150m long third minor section for the proposed method.
Figure 8.22 Simulated (a) current and (b) voltage across different joints of an 800m long third minor section for the proposed method.
Figure 8.23 Simulated (a) ST joints and (b) CB joints current for the proposed method case and original case study
Figure 8.24 Simulated (a) ST joints and (b) CB joints voltage for the proposed method case and original case study
Figure 8.25 (a) Simulated peak current (b) Simulated peak voltage during transient conditions across all joints in the first phase (~ represents 2m from the particular joints)

# **List of Tables**

Table 3.1 Position of Zeroes (w.r.t Fig. 3.11)
Table 3.2 Position of Poles (w.r.t Fig. 3.11)40
Table 3.3 Accuracy to estimate the location of fault a/c to proposed formula in a experimental cable
Table 3.4 Accuracy to estimate the location of fault a/c to proposed formula in an on-field cable
Table 3.5 Accuracy to estimate the location of fault a/c to proposed formula in an simulated cable
Table 4.1 Comparison of the sum and product of zeroes for the healthy cable57
Table 4.2 Accuracy to detect defect in a practical cable
Table 4.3 Accuracy to detect defect in a simulated cable
Table 5.1 Analytically Obtained Range of Fault Current
Table 5.2 Accuracy of the Location of an SG Fault
Table 5.3 Range of Fault Current for On-field Case
Table 5.4 Accuracy for an On-field Cable
Table 6.1 Healthy Condition grounding current
Table 6.2 Accuracy of the SG fault location for a single-point bonded practical cable (bonding at the beginning)96
Table 6.3 Accuracy of the SG fault location for a single-point bonded practical cable (bonding at the middle)
Table 7.1 Algorithm 1: Extracting key parameters from time domain data104
Table 7.2 Different Types of Cable Considered in Simulation
Table 7.3 Two Types of Cable Considered for practical test
Table 7.4 Accuracy of the Proposed Method For Cable Type 1
Table 7.5 Accuracy of the Proposed Method For Cable Type 2
Table 8.1 Comparison of practical maximum current and voltage
Table 8.2 Comparison of simulated maximum current and voltage

# **Notations and Abbreviations**

**FRA** Frequency Response Analysis

**DPIF** Driving Point Impedance Spectroscopy

IS Impedance Spectroscopy

**TFDR** Time-Frequency Domain Reflectometry

SSTDR Spread Spectrum Time Domain Reflectometry

**SFWR** Stepped Frequency Waveform Analysis

SVL Sheath Voltage Limiter

KVL Kirchhoff's Voltage Law

KCL Kirchhoff's Voltage Law

**DSO** Digital Storage Oscilloscope

TL Transmission Line

LCX Leaky Coaxial Cable

LDPE Low-Density Polyethylene

**XLPE** Cross Linked Density Polyethylene

**HVAC** High Voltage Alternating Current

**HVDC** High Voltage Direct Current

**TDR** Time Domain Reflectometry

**FDR** Frequency Domain Reflectometry

**CB** Cross Bonding

NCB Non-cross Bonding

SG Sheath-to-Ground

**DTR** Decision Tree Regression

**FFT** Fast Fourier Transform

**SFRA** Sweep Frequency Response Analysis

This chapter outlines the overview of power cables in section 1.1 and the different types of defects, damage, and catastrophic/short-circuited faults that can appear in a power cable in section 1.2. Along with these different existing techniques to estimate the location of these damaged short-circuited faults are also mentioned in section 1.3 followed by setting the motivation of the thesis in section 1.4. Finally, section 1.5 includes an outline of the remaining chapters of the thesis

# 1.1 Overview of Underground Power Cables

Multitudinous factors including increase in urbanization, right of way issues, hike in energy infrastructure expenditure, and demand for renewable energy power transmission systems (viz., off-shore and on-shore wind farms, solar panels, hydel power plants, etc.) resulted in a rapid increase of high voltage underground (UG) cable installations. This is evident from the current and projected core length trends of UG cables all over the world [1] shown in Figure 1.1.

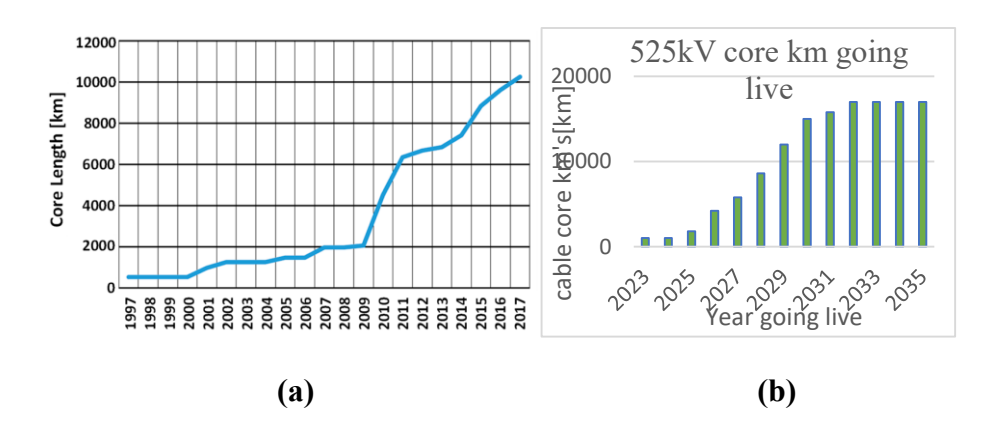


Figure 1.1 (a) The core length of DC-XLPE cables installed and under construction in the year 2018 (b) Future growth predicted length of cable [1].

Different insulating materials are used to make the UG cables including PVC, polyethylene, kraft paper, silicone rubber, etc. Oil-impregnated paper (OIP) and cross-linked polyethylene (XLPE) are typically used in high-voltage cable applications. Although OIP cables are more reliable than extruded polymeric cables (In cities like Mumbai, there are still several OIP cables in the distribution network operating since the 1970s, whereas recently laid polymeric

cables often experience premature failures), they were phased out by the latter because manufacturing OIP cables is extremely time consuming and expensive, unlike polymeric cables which can be extruded faster and conveniently manufactured to the designed length. In addition, polymeric cables have higher load current carrying (thermal) capacity, better mechanical properties, and are light in weight.

XLPE is the most commonly used material among extruded polymers since higher polymers require higher extrusion temperatures. Therefore, XLPE cables are the subject of in-depth research, chiefly focused on increasing their service life and power-carrying capacity.

Rapid economic growth demands faster installation of energy infrastructure to meet the ever-rising power demands, which in turn leads to the tremendous growth of the UG power cables network, especially considering the right-of-way advantages that the UG cables have over overhead transmission lines. However, on the flip side, this also demands stringent reliability and performance criteria, in order to justify the huge expenditure involved. Hence, the enhancement of insulation strength of power cables is focused more on improving their reliability, extending service life, and ensuring safe operation under higher electrical stresses. Numerous prequalification tests such as tan delta, space charge, volume resistivity, and breakdown tests are part of the insulation design. Moreover, the insulation assessment criteria vary significantly based on its HVAC or HVDC applications.

The UG cables are operated either under HVAC or HVDC voltage stresses. Under HVAC, the degradation of insulation is quantified in terms of dielectric loss factor. In HVDC, the insulation degradation is related with the presence of space charge and with the changes in volume resistivity of insulation. Continuous degradation of the insulation leads to a catastrophic fault, which eventually shuts down the entire power system.

Therefore, condition monitoring of both HVAC and HVDC cables is crucial for maintaining the reliability and safety of power systems. It enables early detection of potential issues like insulation degradation, partial discharges, and thermal hotspots. By identifying these problems early, utilities can schedule maintenance proactively, preventing costly failures and minimizing downtime. This proactive approach not only extends the lifespan of the cables but also ensures a stable and continuous power supply, reducing the risk of outages and enhancing overall system efficiency and safety.

# 1.2 Defects, Damage and Short-circuit Faults in a Cable

Defects, damage, and short-circuit faults in a cable can lead to power outages, reduced efficiency, and increased maintenance costs. These issues compromise system reliability and safety, cause equipment damage, and necessitate costly emergency repairs, disrupting continuous power supply and overall operational stability. There are different types of damage in cable which ultimately leads to catastrophic short-circuited faults. The different damage and defects in a cable is discussed in details in the section below.

## 1.2.1 Defects and Short-Circuited faults in Power Cable.

# 1.2.1.1 Mechanical Damage



Figure 1.2 Excessive Bending as a part of Mechanical Damage in Power Cable [2]

The insulation of high voltage cables is susceptible to degradation due to mechanical damage, which can occur during installation, operation, and maintenance activities. This type of damage can significantly compromise the cable's performance and longevity, leading to potential failures and safety hazards.

Mechanical damage often begins during the installation process. Excessive bending or flexing of the cable beyond its design limits can cause cracks or breaks in the insulation. Similarly, pulling the cable with too much force can stretch and weaken the insulation, particularly at bends and terminations. These initial damages may seem minor but can become critical over time as they provide entry points for moisture and contaminants, accelerating the insulation's degradation.

During the cable's operational life, continuous vibration from nearby machinery or vehicular traffic can lead to abrasion and wear on the insulation. This constant movement causes friction, gradually thinning the insulation and creating weak spots. Additionally, external pressure from heavy equipment or soil compaction can deform the cable, causing compressive stress that damages the insulation material. Deformation alters the physical structure, leading to areas where electrical stress is concentrated, further degrading the insulation.

Environmental factors also play a significant role in mechanical damage. Contact with sharp objects, such as rocks or tools, can puncture or cut the insulation, creating immediate pathways for moisture ingress. In some environments, rodents may chew on the cable insulation, causing localized damage that compromises the cable's integrity. These small punctures and cuts can lead to significant degradation over time, as moisture and contaminants infiltrate the insulation.

The consequences of mechanical damage to cable insulation are severe. Cracks and abrasions can initiate partial discharges, which further erode the insulation. Punctures and deformations provide direct pathways for environmental contaminants, accelerating the breakdown of the insulation material. As the insulation degrades, its ability to withstand electrical and thermal stresses diminishes, increasing the risk of partial discharges, dielectric losses, and ultimately, insulation failure. Regular inspections, proper handling during installation, and preventive maintenance are essential to minimize mechanical damage and extend the lifespan of high voltage cables, ensuring a reliable power supply.

# 1.2.1.2 Electrical and Thermal Damage

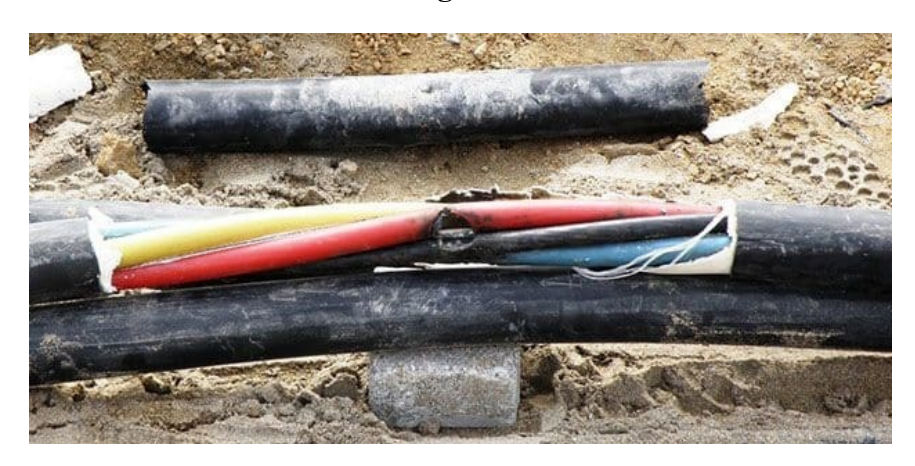


Figure 1.3 Electro thermal Damage in Cable [3]

The insulation of a high voltage cable degrades over time due to both electrical and thermal stress, which can compromise the cable's performance and longevity.

Electrical stress occurs when high voltages create intense electric fields within the cable's insulation. Over time, these fields can cause partial discharges—localized electrical discharges that don't completely bridge the insulation but can erode it gradually. These discharges can create tiny voids and channels, leading to insulation breakdown. Continuous exposure to high electrical stress can also lead to phenomena like water treeing, where moisture ingress and electric fields combine to form tree-like structures within the insulation, reducing its dielectric strength.

Thermal stress is caused by the heat generated from the current flowing through the cable and the external environment. Repeated heating and cooling cycles cause the insulation material to expand and contract, leading to thermal aging. This aging can make the insulation brittle and prone to cracking. Elevated temperatures accelerate the chemical reactions that degrade the polymer chains in the insulation material, further weakening it. In severe cases, thermal runaway can occur, where increased temperature leads to higher electrical resistance and more heat generation, ultimately resulting in insulation failure.

Together, electrical and thermal stresses create a synergistic effect that progressively deteriorates the cable insulation, leading to potential faults and failures that necessitate proactive monitoring and maintenance.

## 1.2.1.3 Sheath to ground faults in cable

The insulation of a power cable can degrade significantly due to sheath-to-ground faults, which occur when the cable's outer sheath becomes electrically connected to the ground. This type of fault can have serious implications for the integrity and performance of the cable.

Sheath-to-ground faults typically result from physical damage to the cable's outer sheath. This damage can be caused by mechanical impacts, such as digging activities or heavy equipment operating near the cable. Once the sheath is compromised, moisture and contaminants can enter the cable structure, leading to corrosion and further degradation of the materials. This direct connection to the ground allows fault currents to flow, which can heat the surrounding soil and further damage the cable.

The presence of a sheath-to-ground fault creates a path for electrical leakage currents, which can significantly affect the insulation system. These leakage currents cause localized heating and can accelerate the aging process of the insulation material. Over time, the insulation becomes brittle and loses its dielectric properties, making it more susceptible to

electrical stress and partial discharges. This degradation can lead to the formation of conductive paths through the insulation, eventually causing a complete electrical breakdown.

Additionally, sheath-to-ground faults can lead to the development of electrochemical trees within the insulation. These trees form as a result of electrochemical reactions between the insulation material and the contaminants introduced through the compromised sheath. Electrochemical trees further reduce the dielectric strength of the insulation, creating additional weak points that are prone to failure under electrical stress.

In conclusion, sheath-to-ground faults cause a series of detrimental effects on power cable insulation. The initial physical damage allows moisture and contaminants to enter, while the resulting leakage currents and electrochemical reactions accelerate the degradation process. Regular inspection and maintenance of cable sheaths, along with protective measures during installation and operation, are crucial to preventing sheath-to-ground faults and ensuring the long-term reliability of power cables.

# 1.2.1.4 Partial Discharge and water treeing

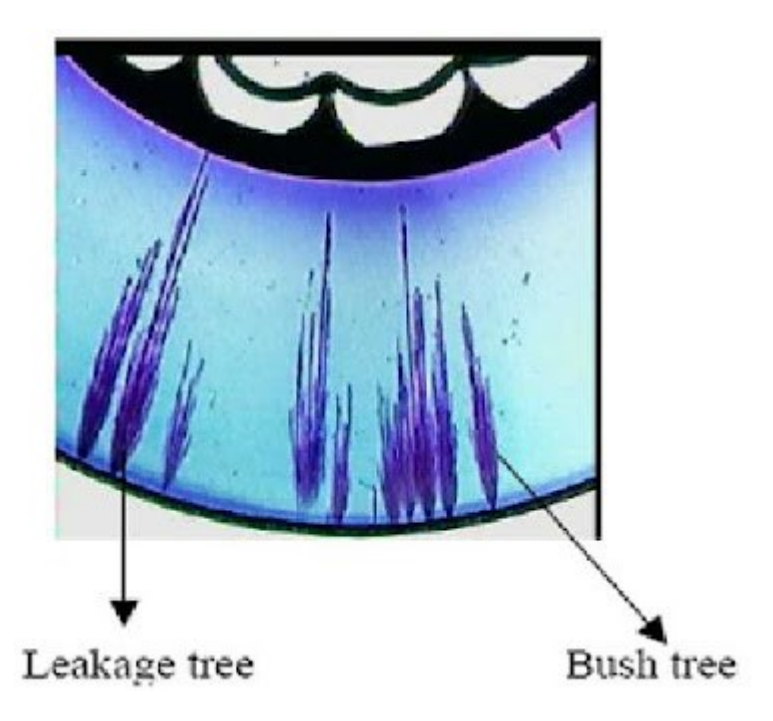


Figure 1.4 Water tree in XLPE Insulated Cable [4]

The insulation of high voltage cables can degrade significantly due to partial discharge and water treeing, two phenomena that are often interrelated and contribute to the breakdown of the cable's dielectric properties.

Partial discharge is a localized electrical discharge that occurs within the insulation of high voltage cables. It happens when the electric field strength exceeds the dielectric strength of a small region within the insulation, but not enough to cause a complete breakdown. These discharges create small voids or cavities within the insulation material. Over time, repeated partial discharges erode the insulation, forming carbonized tracks and pits. This process progressively weakens the insulation, reducing its effectiveness and increasing the likelihood of catastrophic failure.

Water treeing is another critical factor in the degradation of cable insulation. It occurs when moisture infiltrates the insulation material, usually through microscopic defects or imperfections. Under the influence of an electric field, water molecules become polarized and migrate along the field lines, creating tree-like structures called water trees. These structures can span significant portions of the insulation, creating pathways for further moisture ingress and electrical discharges. Water treeing reduces the dielectric strength of the insulation, making it more susceptible to partial discharges and other forms of electrical stress.

The combined effect of partial discharge and water treeing accelerates the degradation process. Water trees create weak points within the insulation, which are prone to partial discharges. Each discharge event further erodes the insulation, expanding the existing water trees and forming new ones. This cyclical process of degradation can eventually lead to complete insulation breakdown, resulting in cable failure.

# 1.2.1.5 Short-circuit faults or Catastrophic Faults in power cable

A short circuit fault in a power cable occurs when the conductive parts of the cable come into direct contact, bypassing the insulation. This can be caused by insulation failure, mechanical damage, or contamination. When the insulation breaks down, usually due to aging, thermal stress, or electrical stress, it can no longer effectively separate the conductive parts.

Mechanical damage, such as cuts or abrasions, can also lead to a short circuit by directly exposing the conductors. Contamination from moisture, dust, or chemicals can create conductive paths across the insulation, facilitating a short circuit.

Once a short circuit occurs, a large amount of current flows through the path of least resistance, generating significant heat. This heat can cause further damage to the cable,

melting the conductors and insulation. The excessive current can also trigger protective devices, leading to power outages and potential damage to connected equipment. Regular maintenance and prompt repair of any detected damage are essential to prevent short circuit faults.

In this thesis, the location of the inception point of water treeing, sheath to ground faults in HVAC and HVDC cables, and location of catastrophic/ short circuit faults are only considered.

# 1.3 Overview of Estimating the location of defects and catastrophic faults Techniques

Estimating the location of defects and catastrophic faults in power cables is crucial for maintaining the reliability and efficiency of electrical power systems. These techniques help in identifying issues before they lead to significant failures, reducing downtime and maintenance costs. This section provides an overview of various methods used for locating defects and faults in power cables industrially, highlighting their principles, advantages and disadvantages.

# 1.3.1 Time Domain Reflectometry (TDR)

Time-domain reflectometry (TDR) works by sending a low-voltage pulse along the power cable and measuring the time it takes for the reflection to return. When the pulse encounters a defect or fault, a portion of it is reflected back to the source. The time delay between sending and receiving the pulse is proportional to the distance to the fault, allowing for precise location estimation.

TDR offers several advantages in locating defects and catastrophic faults in power cables. It is a non-destructive testing method, meaning it does not cause further damage to the cable during the diagnostic process. The technique provides high accuracy in determining the location of faults, making it an effective tool for maintenance and repair. TDR is applicable to various types of cables, including underground and overhead cables, and can detect a wide range of fault types such as open circuits, short circuits, and impedance mismatches.

Despite its advantages, TDR has some limitations. The technique can be less effective in complex cable networks with numerous branches and joints, where multiple reflections can complicate the analysis. Additionally, TDR may struggle with detecting very small or subtle defects, as the reflected signals from these minor faults can be weak and difficult to

distinguish from noise. The initial cost of TDR equipment can also be relatively high, which might be a consideration for some organizations. Furthermore, skilled personnel are required to interpret the results accurately, adding to the operational costs.

# 1.3.2 Frequency Domain Reflectometry (FDR)

Frequency-Domain Reflectometry (FDR) estimates the location of defects and catastrophic faults in power cables by analyzing their frequency response. Unlike TDR, which uses a single pulse, FDR sends a range of frequencies through the cable. The reflected signals are measured, and changes in phase and magnitude are analyzed to identify and locate faults. The differences between the healthy cable and faulty cable signals' frequencies indicate the presence and position of anomalies within the cable.

FDR offers several advantages for fault detection in power cables. It has higher sensitivity to small defects, making it capable of identifying minor issues that might be missed by other methods. FDR performs well in noisy environments, as the frequency analysis can filter out background noise more effectively. Additionally, FDR can provide more detailed information about the nature of the fault, such as its type and severity. This method is also suitable for complex cable networks, where it can detect and differentiate between multiple faults.

Despite its benefits, FDR has some drawbacks. The technique can be complex and requires sophisticated equipment and software, which can be costly. Interpreting FDR results often requires specialized training and expertise, adding to operational costs. Additionally, the higher sensitivity of FDR may result in false positives, where minor or harmless anomalies are flagged as significant issues, potentially leading to unnecessary inspections or repairs.

## 1.3.3 Partial Discharge Detection

Partial Discharge Detection identifies defects in power cables by detecting small electrical discharges that occur within the insulation material. These discharges are indicative of insulation deterioration and defects. Sensors detect the electromagnetic emissions from partial discharges, and the timing and magnitude of these emissions are analyzed to estimate the location of the fault. Advanced algorithms and signal processing techniques help pinpoint the exact location and severity of the defects.

Partial Discharge Detection offers several advantages in locating defects in power cables. It can detect incipient faults that may not be visible through other diagnostic methods,

providing early warning signs of potential failures. This method provides valuable information about the insulation condition, helping in preventive maintenance and extending the lifespan of the cables. Partial Discharge detection is highly sensitive and can identify even minor insulation defects, which helps in addressing issues before they escalate into catastrophic failures. Moreover, it is a non-invasive technique, allowing for continuous monitoring without disrupting the cable's operation.

Despite its advantages, Partial Discharge Detection has some limitations. The initial setup cost for Partial Discharge detection equipment can be high, and the system requires regular calibration and maintenance. Interpreting the results can be complex and requires specialized training and expertise. False positives can occur due to external noise or interference, leading to unnecessary inspections or repairs. Additionally, while Partial Discharge detection can identify the presence of a defect, it may not always provide detailed information about the exact location of the defect, also it cannot identify the location of water treeing in cable.

## 1.3.4 Electrical Resistance Measurement

Electrical resistance measurement locates defects and catastrophic faults in power cables by analyzing changes in the cable's resistance. A known current is passed through the cable, and the resulting voltage drop is measured. Using Ohm's law (V = IR), the resistance is calculated. Variations in resistance indicate potential defects or faults, as a healthy cable has a uniform resistance along its length.

This technique offers several advantages. It is simple and cost-effective, requiring basic equipment and straightforward calculations. Electrical resistance measurement is useful for detecting resistive faults such as corrosion, mechanical damage, or poor connections, which may not be evident through other diagnostic methods. It can be applied to various types of cables and is particularly effective for identifying localized issues in metallic conductors. Additionally, it can be used in conjunction with other methods to provide a comprehensive analysis of the cable's condition.

Despite its benefits, electrical resistance measurement has limitations. It may not detect very small or incipient defects, as slight changes in resistance can be difficult to identify. This method is less effective for complex cable networks with multiple branches and joints, where resistance variations can be more challenging to interpret. Environmental factors such as temperature can also affect resistance measurements, potentially leading to inaccurate results. Additionally, the technique does not provide detailed information about the exact

nature or cause of the defect, often requiring further investigation to confirm the fault and determine its severity.

In this thesis, a novel method based on impedance spectroscopy and sweep frequency response analysis is used to estimate the location of inception point of water treeing and short circuited faults in cable in offline condition. Where as the location of sheath to ground faults is estimated in HVAC cables in online condition by only measuring the grounding current at the earthing box, where as in HVDC cable a non contact online TDR method is proposed to estimate the location of sheath to ground faults.

#### 1.4 Motivation for Condition Monitoring in Cable in Offline and Online Mode.

### 1.4.1 Motivation to Use Impedance Spectroscopy to Estimate the Location of Defects and Short-Circuit Faults in Cable in Offline Mode.

Impedance spectroscopy has garnered significant attention as a powerful technique for estimating the location of defects and short-circuit faults in cables. This method's core appeal lies in its ability to provide detailed insights into the electrical properties of cable materials and the intricate interactions within them. Unlike traditional methods such as reflectometry and partial discharge measurement, impedance spectroscopy offers several distinct advantages that make it particularly effective for fault detection and localization in cable systems.

One of the primary motivations to use impedance spectroscopy is its high sensitivity to a wide range of defects. Impedance spectroscopy measures the frequency response of a cable system to an applied alternating current (AC) signal. By analyzing the impedance spectrum, it is possible to detect subtle changes in the cable's properties, which may indicate the presence of defects such as insulation degradation, moisture ingress, or mechanical damage. This method provides a more comprehensive picture of the cable's condition compared to reflectometry, which primarily relies on the reflection of high-frequency pulses to identify discontinuities or faults. Reflectometry can sometimes miss minor defects or provide ambiguous results, especially in complex cable systems with multiple branches or varying impedance characteristics.

Another significant advantage of impedance spectroscopy is its ability to pinpoint the exact location of faults with high accuracy. The technique involves sweeping a range of frequencies and analyzing the impedance at each point, which allows for a detailed characterization of the cable's impedance profile. This detailed frequency response data can

be used to create a precise model of the cable, enabling the identification of specific fault locations. In contrast, partial discharge measurement, which detects electrical discharges occurring within insulation defects, often provides less precise localization. Partial discharge signals can propagate along the cable and be influenced by various factors, making it challenging to accurately determine the fault's location.

Impedance spectroscopy also excels in non-destructive testing, which is crucial for maintaining the integrity of cable systems. Traditional methods like partial discharge measurement often involve high voltages that can potentially exacerbate existing defects or introduce new ones. Reflectometry, while generally non-destructive, can sometimes induce stress in the cable due to the high-frequency pulses used. In contrast, impedance spectroscopy operates at lower energy levels, minimizing the risk of causing additional damage during testing. This makes it an ideal choice for routine monitoring and preventive maintenance.

## 1.4.2 Motivation to Use Grounding Current to Estimate Sheath to Ground Faults at Any Arbitrary Location during Online Conditions for HVAC Cables

The use of grounding current to estimate sheath-to-ground faults at any arbitrary location in HVAC cross-bonded and non-cross-bonded cables during online conditions presents a highly effective and innovative approach to cable fault management. This method's primary motivation lies in its ability to provide real-time, accurate fault detection without interrupting the cable's operation. In a world where the reliability of power transmission systems is paramount, the advantages of using grounding current for fault estimation are particularly compelling.

Grounding current analysis offers a significant advantage by allowing continuous monitoring of the cable system under live conditions. Traditional fault detection methods often require the cable to be de-energized, leading to operational downtimes and potential service interruptions. This is particularly problematic in critical infrastructure where maintaining constant power supply is essential. By utilizing grounding current, faults can be detected and localized without the need to shut down the system, thus ensuring uninterrupted service. This capability is especially crucial for cross-bonded and non-cross-bonded cables in HVAC systems, which are integral to modern power grids.

One of the key motivations for using grounding current is its high sensitivity to sheath-toground faults. The sheath, or outer conductive layer of a cable, plays a crucial role in maintaining electrical integrity and shielding the internal conductors from external influences. Any faults in the sheath, such as breaches or insulation failures, can lead to significant operational issues. Grounding current methods involve measuring the current that flows through the cable's grounding system. Changes in the grounding current can indicate the presence of faults, as they alter the normal current distribution within the cable system. This high sensitivity allows for the detection of even minor sheath-to-ground faults, which might otherwise go unnoticed until they escalate into more severe problems.

### 1.4.3 Motivation to Use Online TDR to Detect Sheath to Ground Fault In HVDC Cables

The motivation to use online Time Domain Reflectometry (TDR) to detect sheath-to-ground faults in HVDC cables centers on its ability to provide precise and immediate fault detection while maintaining uninterrupted operation. HVDC cables are critical for long-distance power transmission, and their reliability is paramount. In HVDC cable, the sheath current at the grounding box is negligible due to the absence of inductive effect, therefore online and contactless TDR becomes the only method to detect a sheath-to-ground fault. Online TDR offers a significant advantage by allowing real-time monitoring of the cable system without the need for shutdowns, which is crucial for maintaining a consistent power supply.

TDR works by sending a signal down the cable and analyzing the reflected waves to identify discontinuities or faults. In the case of sheath-to-ground faults, TDR can accurately locate the fault by detecting variations in the reflected signal, enabling precise fault localization. This precision is vital for effective maintenance and rapid response to potential issues, minimizing downtime and repair costs.

#### 1.4.4 Motivation to Use Special Sheath Bonding Technique

In practical case scenario, sometimes the old cable route has to be replaced with a new cable route. The new route signifies the minor section of an HVAC cross-bonded cable. Sometimes the new minor section length can either exceed or plummets from the remaining minor section length. Whenever the minor section length differs from one another, a huge circulating current and voltage will appear across different joints and terminals of the cross-bonded cables.

The above mentioned problem motivates to introduce a special end bonding technique in an existing cross bonded cable of different minor section length to mitigate huge circulating current and voltage in different joints and terminals of the cable.

### 1.5 Organization of thesis

In the initial chapter, the focus lies on establishing the background briefly yet thoroughly. Several topics pertaining to the thesis including, the overview of high voltage cables and the cause of different defects, damage and short circuit faults in the cable. The principle, advantages and disadvantages of the existing techniques and models used to estimate the location of damage and short circuit faults, followed by setting the motivation of the thesis. The chapter ends with the organization of thesis.

The second chapter involves a detailed literature survey of existing technique to estimate the location of short circuited fault, semiconducting screen defect, and sheath to ground fault location for both HVAC and HVDC cables. Along with this, a wide literature survey is performed on different end bonding technique in a cross bonded power cable. The need for investigation is also defined in the literature survey for the above mentioned topics. Along with this the methodologies to achieve high accuracy while estimating the location of above mentioned defects and faults is also discussed briefly.

The third chapter introduces the novel application of Sweep Frequency Response Analysis (SFRA) for diagnosing the condition of power cables, marking its first implementation in this domain. The study employs advanced analytical methods to derive a physically accurate driving point impedance function from the measured impedance characteristics of the cable. By constructing this reliable function, the research establishes an analytical formula capable of representing the cable's impedance behavior in its pristine, or "virgin," condition. This formula serves as a baseline, enabling the precise estimation of impedance variations that can pinpoint the location of short-circuit faults along the cable. As an offline diagnostic method, the proposed technique ensures a controlled and systematic approach to fault detection without requiring active system operation. The following sections provide a detailed explanation of the methodology, emphasizing its potential to enhance fault localization accuracy and contribute to more effective cable condition assessment practices.

The fourth chapter explores the application of impedance spectroscopy to locate single-point defects in the semiconducting screens of high-voltage power cables. In such cables,

semiconducting screens play a critical role, serving as both conductor and insulation screens to ensure uniform electrical field distribution and minimize stress within the insulation. Even minor defects in these screens can significantly accelerate the development of water trees, a degradation phenomenon that compromises the cable's insulation and overall performance. To address this issue, the study employs rigorous analytical methods to precisely determine the location of these defects. The chapter provides a comprehensive discussion of the methodologies utilized, offering a detailed account of the theoretical framework and its practical application to enhance cable condition assessment and defect localization accuracy.

The fifth chapter delves into the methodology for estimating the location of sheath-to-ground (SG) faults in cross-bonded (CB) HVAC power cables during online operation, regardless of the fault's position along the cable's length. A detailed explanation of the process is provided, supported by both an experimental study and a real-world field case study to validate the proposed approach. The fault localization is achieved through the application of analytical formulas derived from a circuit model specifically developed for the cable. This model captures the electrical behavior of the system under fault conditions, enabling accurate and reliable identification of the fault location. The chapter provides an in-depth discussion of the formulation, experimental validation, and practical implications of this methodology, demonstrating its potential for effective fault diagnosis in CB HVAC power cablesThe sixth chapter lists tangible conclusions drawn from the thesis that are of utmost significance to cable manufacturers and utilities, apart from a brief summary of the future scope of this work.

The sixth chapter provides a comprehensive explanation of the method for locating sheath-to-ground (SG) faults in non-cross-bonded (NCB) HVAC power cables under online operating conditions, regardless of where the fault occurs along the cable. In line with IEEE Standard 575, various types of NCB cable configurations are analyzed to ensure the methodology's applicability across different systems. The fault location is determined using analytical formulas derived from a carefully designed circuit model that represents the electrical characteristics of the cable and its faulted condition. This approach offers a systematic and accurate means of diagnosing SG faults in real-time scenarios. The chapter discusses the theoretical framework, derivation of the formulas, and practical considerations in detail, providing valuable insights into the effective management and fault localization of NCB HVAC power cables.

The seventh chapter details an innovative approach for locating sheath-to-ground (SG) faults in HVAC power cables at arbitrary positions during online operation. The proposed method integrates online Time-Domain Reflectometry (TDR) with advanced Machine Learning techniques, specifically Decision Tree Regression (DTR), and employs Fast Fourier Transform (FFT) analysis to enhance fault detection accuracy. By leveraging the complementary strengths of these tools, the method enables precise estimation of SG fault locations under dynamic operating conditions. The chapter provides a thorough explanation of the proposed model, including its theoretical foundation, implementation steps, and the synergy between TDR, DTR, and FFT in fault localization. This approach represents a significant advancement in online cable monitoring, offering a robust and efficient solution for ensuring the reliability of HVAC power cables.

The eighth chapter, explores a comparative analysis of different end-bonding configurations for cross-bonded (CB) cable systems with varying minor section lengths. The study evaluates the performance of existing configurations in terms of their ability to manage circulating currents and voltages in cable joints, which are critical factors in preventing premature insulation breakdown and ensuring long-term reliability. Additionally, the chapter introduces an innovative end-bonding configuration specifically designed for systems with non-uniform minor section lengths. The proposed solution aims to minimize circulating currents and joint voltages effectively, enhancing the overall stability and durability of the cable system. A detailed discussion of the proposed configuration, its design rationale, and potential advantages is presented, offering valuable insights into improving CB cable performance under challenging conditions.

### Chapter 2

### **Literature Survey**

The thesis covered six different topics related to estimating the location of short circuit faults, insulation screen defects, sheath-to-ground faults in HVAC and HVDC cables, and introducing a new end bonding method to an existing cross-bonded cable. In this chapter existing literature and problem statement of the above-mentioned topics are discussed in detail along with the methodology used to achieve the solution of the mentioned problem.

# 2.1 Topic 1: Introduction of Sweep Frequency Response Analysis in Cable and Estimating the Location of Short-circuit Fault Using Impedance Spectroscopy

#### 2.1.1 Introduction of Sweep Frequency Response Analysis in Cable

A popular test for power apparatus diagnostics and condition monitoring is the sweep frequency response analysis (SFRA) test [5]–[7]. The corresponding amplitude and phase angle of current and voltage are determined in the SFRA test by sweeping a sinusoidal voltage signal over a band of frequencies at any two terminals of the testing apparatus (one of the two terminals can be the ground or main core). This test is very competent of condition monitoring in various power apparatuses; yet, there is not much research conducted in cable about the application of SFRA.

With various modifications to the circuit compared to transformers, the thesis explores the viability of executing SFRA in a single-core power cable by predicting DPIF from the measured SFRA data. After that, a ladder network was synthesized using the data. To create a rational function, this data must be expressed as a polynomial in the form of "s". It is necessary for this rational function to meet certain requirements in order to synthesize the suggested ladder network. The requirements are as follows [8]: the created rational function must be real and positive; the measured data must correspond to DPIFs, or admittance and impedance functions. Experiments can be used to verify the first of these. Experiments are conducted with great care and planning for this reason. Every function has been validated by writing it as a Hurwitz polynomial in order to assess physical reliability [9].

#### 2.1.2 Estimating the Location of Short-circuit Fault in Cable

Finding the location of a power line problem is crucial for reducing the time and expense involved in fixing and replacing power cables [10]. There are two main approaches that are now in use to find faults in cables: the first uses Impedance Spectroscopy (IS) to locate faults in cables by sending a signal and analyzing its characteristics [11]. Reflectometry is the most well-known approach among the first methodologies for pinpointing the site of a power cable defect. The many forms of reflectometry were classified according to the various signal types (used in a certain domain) found in the cable. For instance, a pulse signal is conveyed over the wire in time domain reflectometry (TDR) [12], whereas a stepped sinusoidal waveform is employed in frequency domain reflectometry (FDR) [13]. A reference chirp signal with the desired bandwidth is delivered down the cable in Time-Frequency Domain Reflectometry (TFDR), which can be employed in both the time and frequency domains [14]. In addition to reflectometry, techniques such as sweep frequencies are used to identify LCX faults. In these methods, the fault's distance is estimated based on changes in the frequency of the excitation and reflected signals over time [15], whereas in other publications, the fault is identified solely based on its voltage gain [16].

Every approach mentioned above has its own drawbacks. For example, the signal-to-noise ratios for TDR and FDR are higher than average, and the accuracy varies due to the sensitivity of the electronics. On the other hand, choosing the central frequency for TFDR is a laborious task since it is dependent on attenuation, which changes depending on how far the fault is from the source. These drawbacks can be solved by applying the IS technique with SFRA. IS uses the cable's impedance to monitor its status in order to do a condition evaluation. Several optimization techniques, such as genetic algorithms, were combined with IS to extract electrical parameters, which were then processed to find flaws [17]–[18]. Using an iterative procedure, the genetic algorithm creates a fitness function by comparing the simulation graph in a given bandwidth with the measured impedance graph. This process is repeated until the function converges to the threshold value. In some other literature, the IS is combined with signal processing techniques to extract magnitude and cable impedance angle to detect faults [19]. In other words, the IS is combined with FFT and uses the propagation velocity of the signal to locate faults [19]–[20].

While there has been prior exploration of the IS through SFRA, it was limited to feature extraction and subsequent comparison for fault location. The work of this thesis describes an

analytical technique that does not require feature extraction. It is based on comparing the locations of poles and zeros.

## 2.2 Topic 2: Estimating the Location of Semiconducting Screen Defect Using Impedance Spectroscopy

In high voltage polymeric power cables, semiconducting layers protect the insulation and conductor while simultaneously smoothing out surface defects of the insulation and conductor and ensuring homogeneity of the electric field. For both the conductor and the insulating screen, the semiconducting layer typically has a thickness of a few millimeters (around 1.5 mm) [21]. Because the semiconducting screen serves as a barrier between conducting material and insulation, it is crucial to keep its design consistent.

The water treeing phenomena in a cable can be caused by any flaw or sharp protrusion in the semiconducting screen (usually from the conducting material), which may ultimately lead to premature failure [22]. The defect diameter is often in the range of a few millimeters (1mm ~ 10mm), while the tip of this sharp protrusion in the semiconducting screen is typically in the order of a few micrometers [23]. It has been claimed that water treeing is exclusively launched by this kind of sharp protrusion [24], as opposed to electrical treeing, which can originate from a void.

The industry employed techniques such as reflectometry to identify only catastrophic damage, such as short circuit faults [25], or parts that had previously sustained damage from electrothermal heating [26], partial discharge [27], and water treeing [28]. Of all these flaws, water treeing is the only one that does not result in partial discharge and is not picked up in partial discharge measurements [29]. There is also a dearth of research regarding potential flaws that could occur prior to a water tree's emergence. When these flaws are small, they don't interfere with the cable's ability to conduct power. However, with time, these flaws become a source of entry for moisture intrusion, which ultimately causes early collapse [22]. The position of soft faults, such as imperfections in the semiconducting screen, cannot be accurately determined by the reflectometry approach [30]. Consequently, it is critical to locate these flaws utilizing a novel method in order to extend the cable's lifespan.

### 2.3 Topic 3: Estimating the Location of Sheath-to-ground fault in a cross-bonded HVAC cable

Metallic sheath protects the cable's insulation from water ingress, provides mechanical strength, and acts as a return path for the capacitive and inductive current during healthy operating and short-circuited fault conditions. For an HVAC cable, the metallic sheath of a

particular phase has to be grounded in at least one point [31], consequently acting as a shield that electrically isolates the particular phase from the remaining phases. Since the metallic sheath is grounded at least at one point, a continuous circulating current flows in the sheath, which impacts the cable's ampacity [32]. Therefore to reduce the losses in the metallic sheath due to circulating current, cross-bonding (CB) of the metallic sheath was introduced [33].

In a CB cable system, the whole cable network is divided into major sections (the number of major sections depends on the total length of the cable network). Both ends of a major section are solidly grounded through grounding resistance (in the grounding box). Each major section will have three minor sections. The metallic sheath of one phase is CB with the other phase in the link box through a sheath voltage limiter (SVL). A minute SG fault will cause a huge flow of circulating current in the sheath, which results in the premature breakdown of the insulation of the cable [34]. Therefore condition monitoring of the cable sheath is of utmost importance for extending the lifespan of the cable

The condition of the metallic sheath deteriorated mainly due to its poor handling or maintenance, adverse climate conditions, and substandard workmanship [35]. According to the published statistics of the last twenty years for a CB HV cable, most ground faults occur at link boxes, joints, and terminals [36]. However, premature breakdown due to SG faults in the third minor section is reported by a local utility sector for a 220 kV cable network of the Mumbai su-urban region of Maharashtra, India. Therefore to maintain the continuous power flow, estimation of the location of the sheath to a ground fault before the breakdown of cable at any arbitrary location is of paramount importance.

Online condition monitoring of electrical apparatus is always preferred over offline techniques (to prevent the shutdown of the system) [37]-[38]. Since in power cable, the metallic sheath of the CB cable is grounded at the grounding boxes, methods like reflectometry [39]- [40], and impedance spectroscopy [41] –[42]. becomes improbable (since reflectometry and impedance spectroscopy are used to localize defects in cable insulation and hard faults only not on the return grounding path). The study of sheath current and its voltage at different locations (grounding box and link box) is the only method for condition monitoring of the sheath [43]. Estimation of the sheath current under normal operating conditions using numerical methods was presented in [44]. The study of sheath current was utilized to detect the inception of the short-circuited fault [45] and insulation monitoring in a CB cable [46]-[47]. The feasibility of identifying SG fault only at the ends of the cross-bonded section was first reported in [43]. Attempts were made to identify and localize the

presence of a sheath fault at the link box only by measuring the sheath current from the preinstalled sensor at the link box was also reported in [48], [31].

Although the identification of the presence of sheath fault is accomplished from the measured sheath current at the link boxes, however, the pinpoint location at any arbitrary position is still unachievable. Along with this, installation of the current sensor into the link during operational conditions can prove to be hazardous for the maintenance workers, due to the presence of sudden switching impulses. In this thesis, an analytical method based on the measurement of the sheath current only at the grounding box to identify and pinpoint the location of the SG fault for a cross-bonded high-voltage cable is presented.

### 2.4 Topic 4: Estimating the Location of Sheath-to-ground fault in a non-cross-bonded HVAC cable

For short to medium-length (< 550m) cables, Cross Bonded (CB) and Non-Cross Bonded (NCB) methods are typically employed. However, the NCB systems enjoy certain advantages over CB systems, namely, constant voltage stress between the conductor and the grounding shield [49] and the lesser complexity involved in laying, due to which NCB systems are preferred over CB systems for short to medium-length cables.

According to IEEE standard 575 [32], there are three types of bonding for NCB HVAC power cables. The very basic type of bonding is the single point bonding at the beginning or the end, where one end of the cable sheath is grounded with a grounding resistance while the other end is connected with a sheath voltage limiter (SVL) as shown in Fig. 2.1. The second type of bonding is the single-point bonding at the middle of the cable, where both ends of the cable sheath are connected with SVLs while the grounding is provided at the middle of the cable using a grounding resistance as shown in Fig. 2.2. The third type of bonding is two-point bonding, where both ends of the cable are grounded with a grounding resistance. There are no SVLs used in this type of bonding as shown in Fig. 2.3. The value of grounding resistances for each type of bonding is considered  $0.2\Omega$  [43].

Detecting the presence of SG fault only in the joints of a cross-bonded cable is widely explored [46], [48]. For an NCB cable attempts were made to obtain the voltage and current waveform during a steady state condition [49], however, the estimation of the location of an SG fault for an NCB short to medium-length power apparently has not been explored until now. In this thesis, a novel method to estimate the location of an SG fault in any arbitrary location by only using the magnitude of the sheath current measured from the grounding

resistance and the phase difference between the sheath current and conductor current is presented.

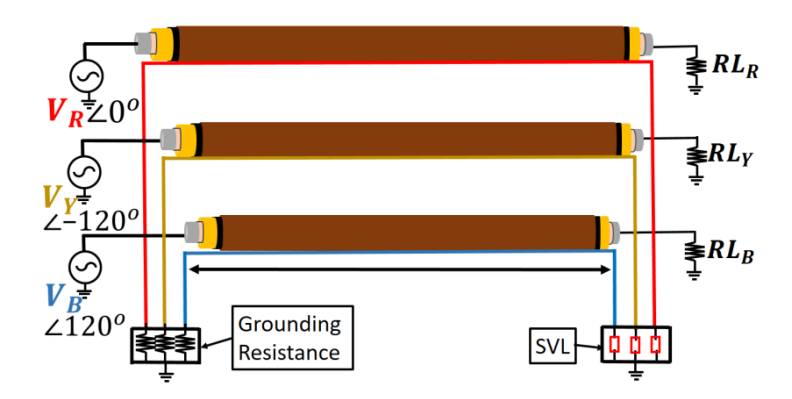


Figure 2.1 Schematic diagram of a single point bonding at the beginning.

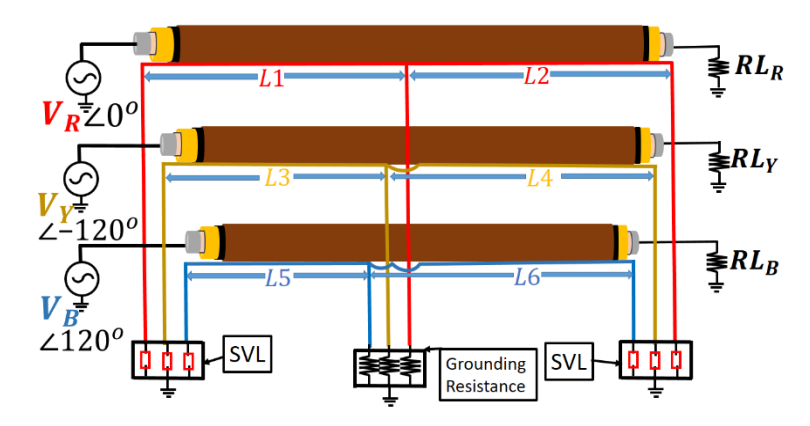


Figure 2.2 Schematic diagram of a single point bonding at the middle

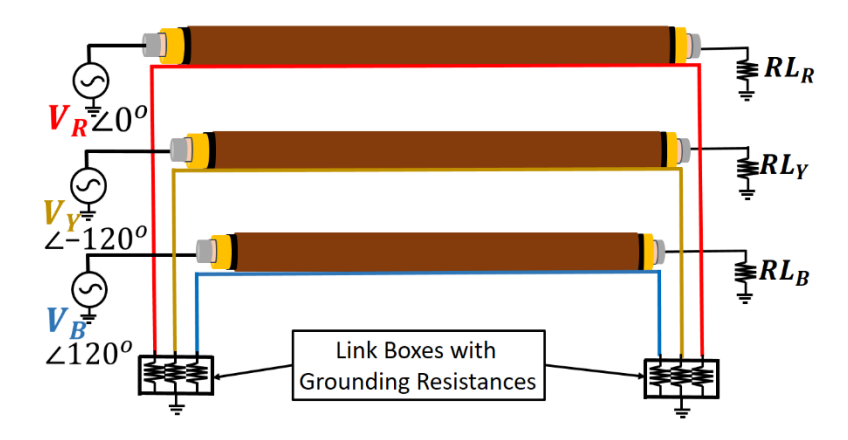


Figure 2.3 Schematic diagram of a two point bonding system.

#### 2.5 Topic 5: Estimating the Location of Sheath-to-ground fault in a HVDC cable

HVDC cables form the backbone of the HVDC systems. In HVDC cables, the metallic sheath is an indispensable part that protects the inner insulation from environmental factors

such as moisture, and mechanical damage and also provides electrical insulation, preventing leakage currents [36]. Maintaining the integrity of the sheath is essential for ensuring the overall performance of the HVDC cable, as a well-maintained sheath helps extend the cable's lifespan by mitigating issues like moisture ingress and mechanical wear.

SG faults in a cable arise when the cable's outer jacket is punctured, causing the metallic sheath to come into direct contact with the environment. When the sheath is compromised, moisture can penetrate the insulation layer, leading to the formation of water trees [24]. Over time, these water trees causing partial discharges and eventually leading to catastrophic cable breakdown [22]. In addition, moisture ingress exacerbates the aging process of the cable, reducing its overall life expectancy [50]. Therefore early detection and localization of SG faults in HVDC cables are crucial for mitigating the risks of premature breakdown and enhancing overall system reliability.

Attempts were made to detect the presence of the SG faults at cable joints in cross-bonded HVAC systems by measuring the sheath current at the link box during online conditions [48], [51]. The sheath current in a cable is primarily caused by inductive coupling from the conductor current and capacitive effects from the source voltage [51]. The sheath current in the cable is also used to locate faults and condition monitoring of insulation in HVAC cable [52]. However, the inductive effect in an HVDC cable is negligible, and since the current is solely due to capacitive effects, the sheath current remains in the microampere range, both under normal conditions and during an SG fault. Due to the presence of noise in the low sheath current measurements, existing methods used for HVAC cables cannot be directly applied to HVDC cables for condition monitoring of the sheath.

Online and non-intrusive reflectometry techniques have become powerful tools for detecting and locating faults and damaged insulation in cables as part of condition monitoring. Among online reflectometry applied on the conductor, the most adopted methods include Time Domain Reflectometry (TDR) [53], Time-Frequency Domain Reflectometry (TFDR) [54], Spread Spectrum Time Domain Reflectometry (SSTDR) [55], and stepped-frequency waveform reflectometry (SFWR) [56]. According to the existing literature, TFDR, SSTDR, and SFWR are preferred over TDR due to limitations in TDR, such as the skin effect in cable conductors and accuracy in detecting multiple insulation faults, as most of the signal energy reflects at the first impedance mismatch. However, when estimating the location of SG faults in online conditions, these concerns are not relevant. Since the sheath has a significantly smaller thickness compared to the conductor, the skin effect becomes

negligible. Since the sheath is a metallic conducting medium, the fault resistance range will be in milli-ohm, making TDR an effective technique for SG fault localization.

Recent reflectometry studies have also demonstrated the advantages of using a Gaussian chirp signal over traditional impulse signals for fault detection [53]-[54]. The Gaussian chirp has less signal distortion and can distinguish closely spaced reflected signals compared to simple impulse waveform. However, selecting the optimal central frequency for system training presents a challenge, as it depends on the level of attenuation, which varies with the distance of the fault from the source. This variability introduces complexity in ensuring accurate and efficient fault localization, highlighting the need for careful tuning of signal parameters in practical applications, and the problem of overlapping and signal distortion can be improved by using a simple signal processing technique. Therefore impulse waveform offers more straightforward implementation and reliable performance for the specific application studied.

The accuracy of TDR can be significantly enhanced by integrating signal processing techniques and machine learning algorithms with it. Leveraging artificial intelligence, machine learning has been widely applied for fault detection and localization [57]-[59], enabling the identification and isolation of faulty cables before tripping occurs. While deep learning can also be utilized for fault localization in cables, it demands significantly higher computational resources [60]. However, limited research addresses the estimation of SG faults in HVDC cables. To bridge this gap, this thesis proposes a novel approach that involves using an inductive coupler to perform online TDR on the sheath of HVDC cables for the first time. Signal processing is applied to the reflected waveforms, and key feature extraction is used to inform a DTR model for accurately estimating the location of SG faults.

### 2.6 Topic 6: New End Bonding Technique in an Existing Non Uniform Length Cross Bonded HVAC Cable

Single-core shielded HVAC power cables are prevalent in both the transmission as well as in distribution sectors. The metallic sheath of the single-core cable electrically shields the particular phase of the cable, prevents water ingress in insulation, and also gives mechanical support to the cable. Because of capacitive and inductive phenomena, the metallic sheath has voltage relative to the ground and conducts a circulating current [61]. This circulating current causes ohmic loss [62] and restrains the ampacity of the cable [63]. According to IEEE Standard 575 [32], to reduce the circulating current and voltage (induced voltage should not

exceed 50V during operating conditions [64]) in this metallic sheath, CB of the cable sheath was introduced.

In a CB system, the whole cable network is split into major sections. The end of the major section is solidly grounded with a grounding resistance. The metallic sheath of one phase is CB with the other phase in the link box through a sheath voltage limiter (SVL), therefore each major section will have three minor sections. To maintain minimal current and voltage in the sheath, the length of each minor section of the cable should not exceed the other by 10% [32]. However, one practical case scenario was reported by a utility sector in Maharashtra, India, where a particular cable route required to be changed. To do that, an existing length of the third minor section has to be replaced with a new length as shown in Fig. 2.4. According to standard [32], whenever a particular section exceeds or plummets from the remaining two sections huge amount of circulating current and voltage will appear across the joints and terminals sheath. According to the published statistics of the last twenty years for a CB HV cable, most sheath-to-ground faults occur at joints, and terminals [36], therefore to extend the lifespan of the cable, sheath joints should have a minimal voltage and current profile.

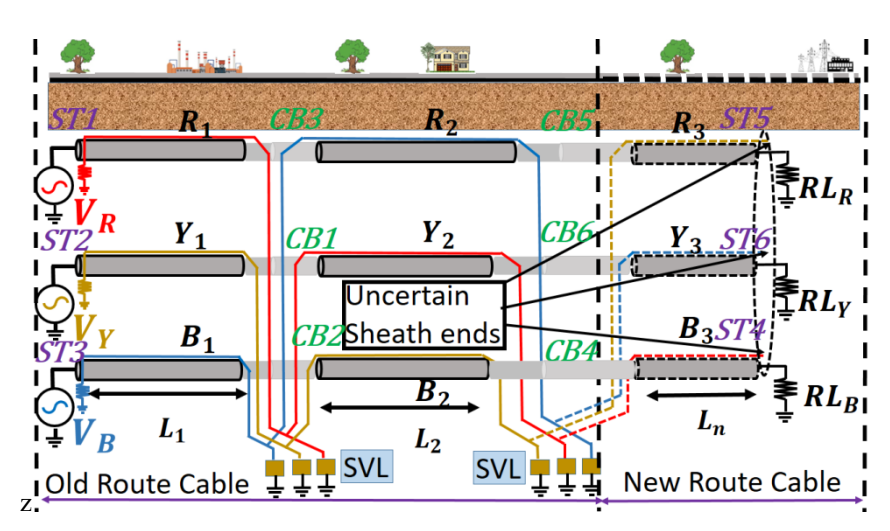


Figure 2.4 Schematic diagram of a major section in a CB cable with a new minor cable route for a third minor section.

According to the existing literature [65], special types of bonding like solid bonding [32], single point bonding [66], reactance and resistance bonding [67]-[68], and mixed bonding [69] were used to replace the CB method (due to laying complexity of CB system) and to maintain a low profile of current and voltage throughout the cable sheath. When solid end bonding or grounding system [32] is applied to a non-uniform length CB cable, the voltage across different joints and terminals will be minimal however the current will be high (the

inductive effect will be dominant), similarly for a single point end bonding [7], sheath current will be minimal while sheath voltage across terminal will be high during steady state condition (presence of high SVL impedance treated as open). These two types of bonding can only be applied to the existing CB cable if there is a change in length after the first minor section or in the second minor section since the length of the major section will be less when compared with the change in the third minor section [65]. However, the existing method of end bondings [32], [66]-[69] will fail when the third minor section length is changed (huge circulating current and voltage due to imbalance in length in three minor sections).

#### 2.7 Methodology Proposed

#### 2.7.1 Methodology to Estimate the Location of short-circuit faults in a cable

According to the literature review, the impedance graphs of working and malfunctioning transformers are compared using SFRA and the signature of a transfer function. Because it only requires the operation of one port, the DPIF transfer function has an advantage over the others. Furthermore, cables will always operate at a single port. Therefore, DPIF was selected. When a cable was in good health, the DPIF signature is required in order to apply the SFRA technique to it. Though it is feasible to obtain such signatures experimentally prior to placement for newly laid cables, the experimental data may not be available for already laid cables. The method's successful implementation depends on the ability to anticipate DPIF (healthy) for cables that have already been installed. In order to generate a signature for already-installed cables without the need for actual experiments on a healthy cable, this thesis uses classical TL theory to obtain the impedance spectroscopy of the cable. Additionally, the DPIF of a cable is proposed, which can be formulated from the dimensions and parametric values of the cable. Any system's impedance function can be estimated from the impedance vs. frequency graph to get its pole-zero form. Lastly, a formula for estimating the fault's location is proposed.

### 2.7.2 Methodology to Estimate the Location of Semiconducting Screen Defect in a cable

To estimate the location of semiconducting screen defect, it is observed that any minor flaw in the cable structure generates a change in the total impedance of the cable, and this is only noticeable in the high-frequency impedance spectrum (as seen in the case of a transformer [70]), which is seen to estimate the location defects at semiconducting screens. A damaged cable will have a different impedance spectrum than a cable in good condition. Thus, in order

to find the minute flaw in the semiconducting screen for either insulation or conductor in a lengthy power cable, a unique technique based on impedance spectroscopy is given in this study. Because the impedance graph of a short-circuited fault alters (zeroes become poles when compared with a healthy one), the position of the fault can be determined using just one zero. However, the relationship between all the poles or zeroes with electrical factors should be well defined in order to locate minute flaws in a lengthy wire. Mathematical software is needed to determine the roots of the higher-order polynomials using the proposed function [71]. A specific solution is obtained instead of a generalized form. In order to obtain a generalized relationship between the zeroes with propagation constant and electrical properties of the cable, transmission line theory and the state space model are employed in this study.

### 2.7.3 Methodology to Estimate the Location of Sheath-to-Ground Fault in a CB and NCB HVAC Cable

To estimate the location of sheath-to-ground faults in a CB and NCB HVAC cable it is observed that, the sheath current mainly consists of inductive, capacitive, and leakage current. The value of leakage current would be in the range of < 10<sup>-11</sup>A (depending on the operating voltage and except during conductor-to-ground fault) [72], and the cumulative sum of inductive and capacitive currents is in amperes [43]. Therefore the value effect of leakage current is negligible in the measurement of sheath current. According to existing literature, the flow of capacitive current is difficult to calculate for a cross-bonded cable network [73]. To estimate the pinpoint location of the SG fault, the exact value of inductive and capacitive current is extremely vital. In this thesis, a circuit theory model is used for the first time to estimate the effect of both the capacitive and inductive effect in sheath current both under normal operating conditions and SG fault. Finally, formulae are proposed by which the location of the sheath fault can be estimated from the measurement of the ground current for both balance and unbalancing conditions.

### 2.7.4 Methodology to Estimate the Location of Sheath-to-Ground Fault in a HVDC Cable

The invention introduces an innovative approach for condition monitoring of HVDC cables by performing online TDR (Time-Domain Reflectometry) using an inductive coupler, integrated with Decision Tree Regression (DTR) for accurate fault estimation. The TDR method involves sending a test impulse through the cable, and the inductive coupler allows

this process to be conducted non-intrusively, without interrupting the normal operation of the cable system. The reflected signals from the cable are captured and analyzed for identifying anomalies indicative of sheath faults.

The integration of the inductive coupler with the TDR system is the key novel aspect, enabling real-time, continuous monitoring of the cable sheath. The reflected signal data is then processed using Decision Tree Regression (DTR), which is trained on a dataset of historical TDR signals and their corresponding fault locations. By leveraging DTR, the model can handle complex, non-linear signal patterns and noise, providing precise fault localization even in challenging scenarios, such as shorter transmission lines with overlapping reflections.

This invention's primary novelty lies in its ability to perform online TDR using an inductive coupler, combined with advanced machine learning techniques for fault estimation. The inductive coupler facilitates uninterrupted condition monitoring, while the Decision Tree Regression model enhances the analysis, allowing for accurate, real-time identification of sheath faults. This integrated solution significantly improves the reliability and efficiency of fault detection in HVDC cable systems, paving the way for proactive maintenance and reduced downtime.

## 2.7.5 Methodology to Mitigate Excessive Sheath Current and Voltage due to Non-Uniform Minor Section Length in a CB power Cable

To mitigate excessive current and voltage due to non-uniform minor section length in an existing CB cable system, a special end bonding method is proposed in this thesis, by merging the single point and solid end bonding (without any change in the bonding of the existing two sections) to mitigate both high currents and voltage in different joints and terminals caused due to non-uniform minor section lengths. Along with the proposed model, both solid-end bonding and single-point end bonding methods are discussed in detail in this thesis with their analytical model and comparisons are presented on sheath circulating currents and voltages on different joints for these three types of bonding and also compared with the original case.

### Chapter 3

# Introduction of Sweep Frequency Response Analysis in Cable and Estimating the Location of Short-circuit Fault

This chapter presents the use of sweep frequency response analysis (SFRA) for the first time in cable. The analytical methods were utilized for the construction of a physically reliable driving point impedance function from the obtained impedance graph of the cable, then an analytical formula was proposed to estimate the impedance graph of the cable during its virgin condition, and this formula was further used to estimate the location of short-circuit faults in the cable. The proposed technique is an offline method. The details of the proposed methodology is discussed below:

#### 3.1 Estimated DPIF for the cable using Electrical Parameters

Several approaches exist for determining and forecasting the impedance function in simple LC ladder networks [74]. However, when dealing with cables featuring frequency-dependent parameters, the ladder network becomes significantly more complex, rendering traditional methods ineffective. This section introduces two methodologies: one for estimating the cable's impedance spectroscopy and another for evaluating its DPIF.

According to transmission line theory, the ladder network of a single-core power cable, as depicted in Fig. 3.1, is characterized by four fundamental frequency-dependent parameters (per unit length): R (series resistance), L (series inductance), G (shunt conductance), and C (shunt capacitance), as described in [75].

$$R = \frac{1}{\pi \sigma \left[ r_1^2 - \left( r_1 - \frac{1}{\sqrt{\pi \mu \sigma f}} \right)^2 \right]} \Omega/m \tag{3.1}$$

$$L = \frac{\mu_0}{2\pi} \ln\left(\frac{r_2^2}{r_1^2}\right) \text{H/m}$$
 (3.2)

$$C = \frac{\frac{\mu_0}{2\pi} \ln\left(\frac{r_2^2}{r_1^2}\right)}{\left(\frac{1}{\mu\epsilon}\right) \left(\left(\frac{\mu_0}{2\pi} \ln\left(\frac{r_2^2}{r_1^2}\right)\right)^2 - \left(\frac{\mu_0}{2\pi} \ln\left(\frac{r_2}{r_1}\right)\right)^2\right)} F/m$$
(3.3)

$$G = 2\pi f \times \tan \delta \times C \text{ S/m}$$
(3.4)

In this context,  $\mu_0$  represents the permeability of free space,  $\mu_r$  denotes the relative permeability of the conductor material,  $\sigma$  is the conductivity of the conductor material,  $\varepsilon_0$  stands for the permittivity of free space,  $\varepsilon_r$  is the relative permittivity of the insulating material, and  $\tan \delta$  refers to the dissipation factor. Additionally,  $r_1$  and  $r_2$  correspond to the radii of the conductor and the insulation.

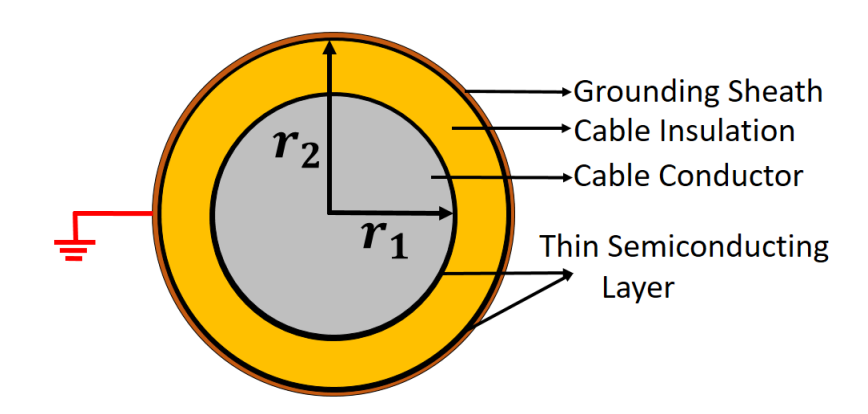


Figure 3.1 Configuration of a single-core cable with the outer sheath connected to the ground.

## 3.1.1 Deriving Impedance Spectroscopy Using the Traditional Transmission Line (TL) Model

Based on the classical transmission line (TL) model and as illustrated in Fig. 3.2, the impedance plot of an open-circuited cable is provided as [76]:

$$z_{open} = \frac{\Gamma}{\tanh(\gamma.l)} \tag{3.5}$$

Using (3.1)-(3.4),

$$\Gamma$$
 (Characteristics impedance) =  $\sqrt{\frac{(R+j\omega L)}{(G+j\omega C)}}$  (3.6)

 $\gamma$ (Propagation constant)= $\sqrt{(R+j\omega L)(G+j\omega C)}$  (3.7)

 $l=Total\ length\ of\ the\ cable$  (3.8)

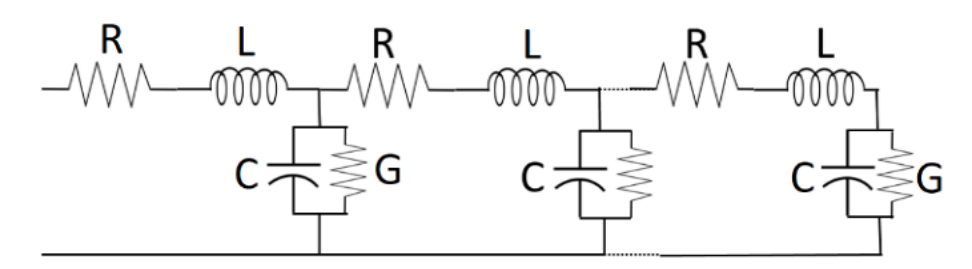


Figure 3.2 Ladder network representation of a healthy cable at power frequencies divided into *n* sections.

However, the classical TL approach does not provide insights into the DPIF of the cable. To address this limitation, this chapter introduces a circuit theory-based model, offering a novel perspective for estimating the cable's impedance spectroscopy.

#### 3.1.2 Estimating the DPIF of the Cable by Solving the Ladder Network of the Cable

In the frequency range under consideration, the series resistance is significantly smaller compared to the series inductive reactance ( $j\omega L$ ) and can therefore be disregarded, as illustrated in Fig. 3.3. While neglecting RRR alters the magnitude of the cable's input impedance, it has minimal effect on the resonance frequency. Additionally, although the dissipation factor ( $\tan \delta$ ) depends on frequency, its variation is relatively minor within the frequency range of interest [75].

As shown in Fig. 3.4, the inductance and capacitance in the ladder network of a healthy cable naturally give rise to resonant frequencies.

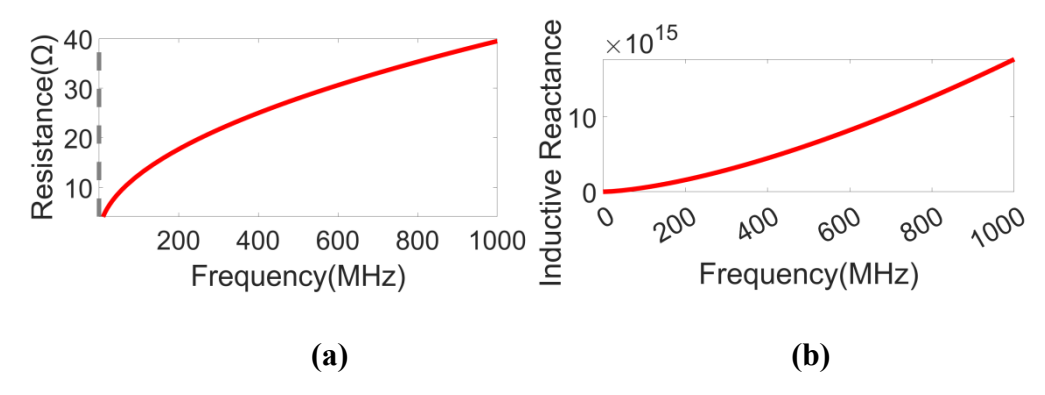


Figure 3.3 FEM analysis of a 25m long cable showing (a) resistance and (b) inductive reactance.

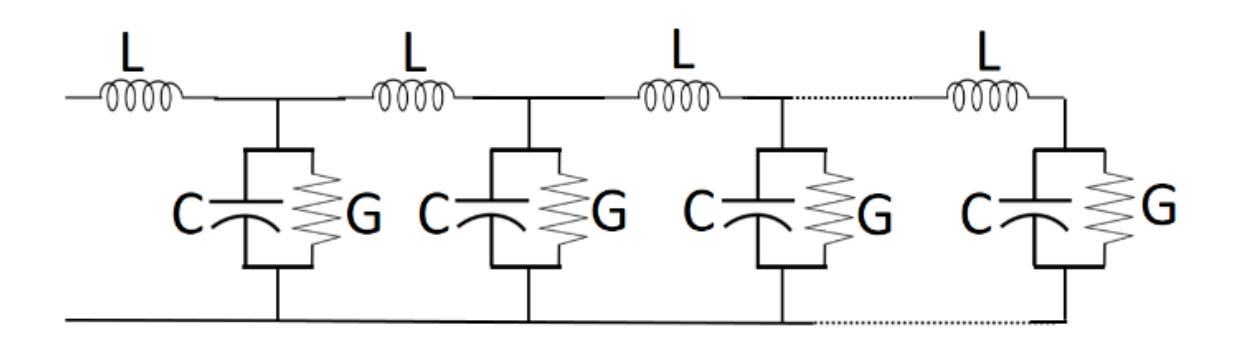


Figure 3.4 Ladder network representation of a healthy cable at high frequencies divided into *n* sections

Using (3.4), the admittance per unit length of the cable, y can be written as,

$$y = G + j\omega C = j\omega C (1 - j \tan \delta) = j\omega KC$$
(3.9)

Where,  $|(1 - j \tan \delta)| = K$ , a factor dependent on the material properties.

The driving point impedance of the ladder network of Fig. 3.4, with *n*-sections, can be obtained by using the Cauer-1 method [74], as;

$$Z(s) = sL + \frac{1}{sC + \frac{1}{sL + \frac{1}{sC + \dots \frac{1}{sL + \frac{1}{sC}}}}}$$
(3.10)

However (3.10) is not in pole-zero format, and in this form, it is not useful for frequency response analysis.

After a careful analysis of the patterns followed by the coefficients of the polynomials in the numerator and denominator, for different values of n, the following formula is proposed, as an equivalent to (3.10), which can be proved by mathematical induction.

$$Z_{\rm n}(s) = \frac{1 + \sum_{j=n}^{1} \sum_{i=1}^{n} a_{(2i),j} \times s^{2i} \times k^{i} \times L^{i} \times C^{i}}{\sum_{j=n}^{1} \sum_{i=1}^{n} a_{(2i-1),j} \times s^{2i-1} \times k^{i} \times L^{i-1} \times C^{i}}$$
(3.11)

Here,  $a_{p,q}$  represent the  $q^{th}$  polytopic number of  $p^{th}$  dimension regular simplex [77]. The coefficients of the polynomials are observed to be functions of polytopic numbers of different dimensions, except that they start with a natural number (i.e. excluding the zero terms in the beginning). The numerator and denominator of  $Z_n(s)$  are of even and odd degree polynomials, respectively.

The DPIFs are represented as a polynomial as a function of "s" to construct a rational function and to compare the analytical function with the simulated and experimental results later. This rational function must conform to a Hurwitz polynomial [74]. If a cable's frequency response signature does not exist, the frequency response signature of a healthy cable can be obtained using (3.5) or (3.11), while, the frequency response of a faulty cable can be measured experimentally. The method does not require post-recorded data.

### 3.2 Estimated Short Circuit Fault Location Using Impedance Spectroscopy

In the ladder network representation of a cable, the key difference between a healthy cable and one with a short-circuit fault lies in the network's termination. For a healthy cable, the network concludes with shunt capacitance and conductance, while for a cable with a short-circuit fault, it ends with series inductance (assuming the fault resistance is negligible).

To understand how the DPIF (Driving Point Impedance Function) of a healthy cable changes due to a short circuit, consider a fault at the far end of the cable such that the lengths of the healthy and faulty segments are equal. For the ladder network with a short circuit at the far end, as shown in Fig. 5, the DPIF can be expressed as:

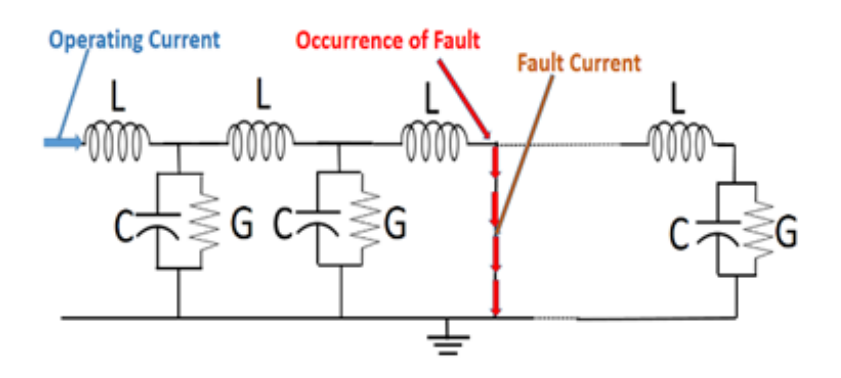


Figure 3.5 Proposed ladder network model for the cable at high frequencies with a fault.

$$Z(s) = sL + \frac{1}{sC + \frac{1}{sL + \frac{1}{sC + \dots \dots \frac{1}{sL}}}}$$
(3.12)

Using mathematical induction, the above equation can be rewritten as:,

$$Z_{n}(s) = \frac{\sum_{j=n}^{1} \sum_{i=1}^{n} a_{(2i-1),j} \times s^{(2i-1)} \times k^{i} \times L^{i} \times C^{i-1}}{1 + \sum_{j=n}^{1} \sum_{i=1}^{n} a_{(2i),j} \times s^{2i} \times k^{i} \times L^{i} \times C^{i}}$$
(3.13)

Here,  $a_{p,q}$  represent the  $q^{th}$  polytopic number of  $p^{th}$  dimension regular simplex

By comparing the DPIF for a healthy cable (3.11) with that of a faulty cable (3.13), it is evident that the numerator of the healthy cable's DPIF becomes the denominator of the faulty cable's DPIF. For a healthy cable,  $Z(s) \to \infty$  as  $s \to 0$ , indicating a pole at zero frequency. Conversely, for a faulty cable,  $Z(s) \to 0$  as  $s \to 0$ , showing a zero at zero frequency. Thus, the impedance graph for a healthy cable starts with a pole, while that of a faulty cable starts with a zero at the same frequency when the fault occurs at the far end.

The angular frequency of the zero or pole,  $\omega_{zp}$ , is proportional to:

$$\omega_{zp} \propto \frac{1}{\sqrt{L_{eqv}C_{eqv}}} \tag{3.14}$$

Where  $L_{eqv}$  and  $C_{eqv}$  are the cable's total inductance and capacitance. For a cable of length l, this becomes:

$$\omega_{zp} \propto \frac{1}{l\sqrt{LC}}$$
 (3.15)

or

$$l \times \omega_{zp} = constant$$
 (3.16)

For intermediate short-circuit faults, the effective electrical length of the cable decreases, causing a rightward shift in the impedance graph (resonance frequencies occur at higher values). This behavior aligns with (3.16), as the effective cable length reduces. The first zero or pole of the impedance graph provides a straightforward way to estimate fault location. Based on (3.16), the fault location  $L_s$  can be calculated as:,

$$L_{s} = \frac{f_{z,s}^{1}}{f_{p}^{1}} \times l \tag{3.17}$$

Here,

- $f_{z,s}^1$  is the frequency of the first zero in the signature graph,
- $f_p^1$  is the frequency of the first pole for the faulty cable,
- $L_s$  is the fault's location, and,
- *l* is the total cable length

The first pole's location remains unaffected by the magnitude of the fault resistance  $(R_{fault})$  as long as  $(R_{fault} \ll \Gamma)$ , ensuring the rest of the cable remains inactive beyond the fault. However, the pole's magnitude is inversely proportional to the effective fault resistance:

$$P_{1,mag} \propto \frac{1}{R_{effective}}$$
 (3.18)

Thus, the fault location can be determined using the first zero of the healthy cable's impedance graph (obtained experimentally or analytically via (3.5) and (3.11) and the first pole's frequency for the faulty cable (measured experimentally). The following sections validate this methodology through simulations and experiments

# 3.3 Experiments and Simulations to Estimate the Locations of Short Circuit Faults in a Cable

Two Practical Case studies are conducted to validate the proposed methodology.

Case Study 1: A 25-meter-long test cable was used, where six faults were intentionally introduced at various locations to assess the proposed method's accuracy.

The cable specifications were as follows: an 11 kV, three-core XLPE cable with a 35 mm<sup>2</sup> aluminum conductor, an outer grounded sheath diameter of 7.35 mm, a relative permittivity of 2.3 for the insulation, and a loss tangent ( $tan \delta$ ) of 0.0005. The cable parameters were  $R_{dc} = 2.4312 \times 10^{-3} \Omega$ ,  $L_{eq} = 2.7934 \times 10^{-2} H$  and  $C_{eq} = 6.8392 \times 10^{-15}$  F. Faults were introduced at six locations: 5 m, 10 m, 15 m, 20 m, 22.5 m, and at the far end (25 m). Two fault resistances (1 m $\Omega$  and 3.5  $\Omega$ ) were applied at these locations on a specific phase to validate the results. To create short-circuit faults, an iron nail was used to pierce the phase under study, and SFRA tests were conducted as illustrated in Fig. 3.8(b). While performing experiments to ensure precise measurement (mainly at the troughs and peak), a small frequency increment of 500 Hz was selected, while the simulation trace was obtained directly from the probe data. The measurement of the current at low frequencies are performed within the limit of the current probe. Averaging of the signal was performed for both current and voltage waveform to reduce the effect of noise on the signal at low current values.

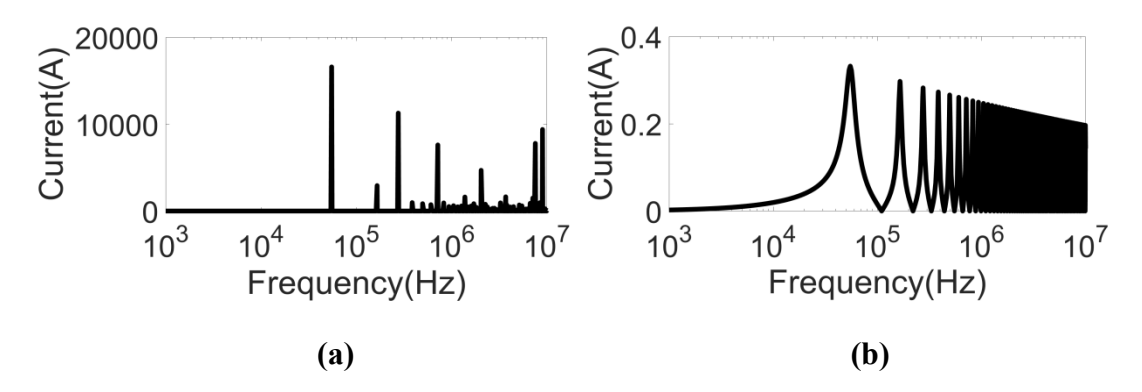


Figure 3.6 Simulation results showing: (a) Current from the function generator without a current-limiting resistor, and (b) Current from the function generator with the inclusion of the current-limiting resistor  $R_C$ .

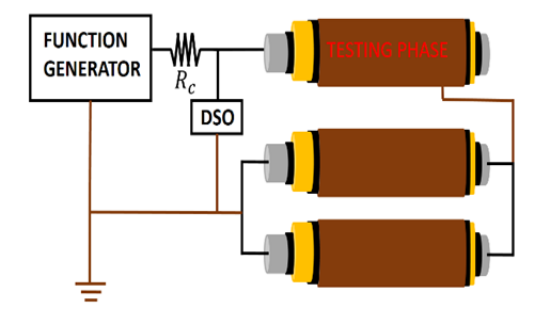


Figure 3.7 Illustration of the connection setup for a three-core cable with a DSO, function generator, and current-limiting resistor..

Case Study 2: A This case involved a real-world scenario from IIT Ropar in Punjab, India. The cable was a 440 V, 50 A, four-core XLPE cable, 146.7 meters long, with a 300 mm<sup>2</sup> aluminium conductor, an outer grounded sheath diameter of 21.36 mm, insulation relative permittivity of 2.3, and a loss tangent ( $tan \delta$ ) of 0.0005. The cable parameters were  $R_{dc} = 1.0312 \times 10^{-1} \Omega$ ,  $L_{eq} = 3.9544 \times 10^{-1} H$  and  $C_{eq} = 2.5481 \times 10^{-12} F$ . The cable

included three joints along its length, and SFRA tests were performed from both open ends, as depicted in Fig. 3.10. A short-circuit fault was observed in this cable, providing a practical example to verify the methodology.

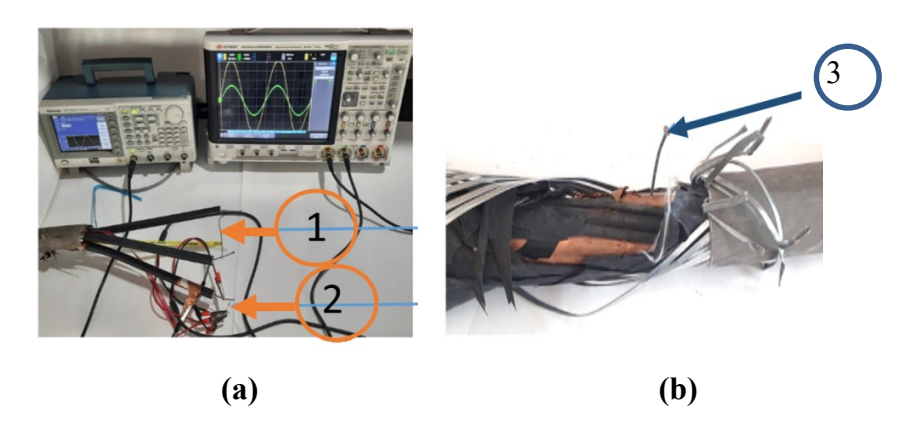
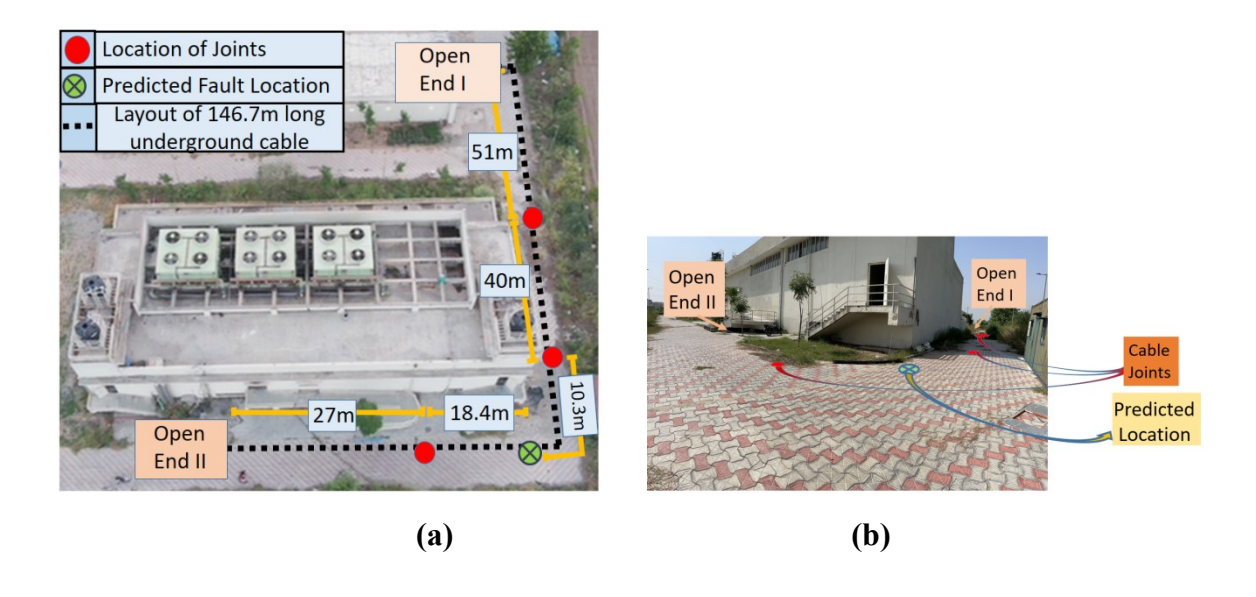


Figure 3.8 Experimental setup for measuring DPIF: (a) (1) Remaining phases short-circuited using a wire, (2) Current-limiting resistor of 20  $\Omega$ , (b) Short-circuit fault introduced using a nail..



Figure 3.9 Experimental configuration for determining the location of the short-circuited fault.





(c)

Figure 3.10 (a) Top view of a practical setup with a 146.7m cable connected at both ends, (b) 360-degree panoramic view of the setup, (c) Section of the cable with a short circuit..

For SFRA measurements, when the test cable is directly connected to the voltage source, it must deliver a current in the range of several kilo amperes, even at low voltages, as illustrated in Fig. 3.6(a). This is due to the cable's low impedance at resonant frequencies.

To limit the maximum current to the voltage source's rated capacity during SFRA testing, a current-limiting resistor  $R_c$  of 20  $\Omega$  is connected in series with the cable and function generator, as shown in Fig. 3.7. This ensures the current remains within safe limits, as depicted in Fig. 3. 6(b). For tests on a three-phase cable, the unused two phases are shorted to minimize interference from stray inductance or capacitance, as illustrated in Figs. 3.7 and 3.8. The peak-to-peak voltage is set at 10 volts, and the frequency is varied while capturing voltage and current waveforms using a DSO. Measurement accuracy near resonance peaks and troughs is enhanced by using a frequency increment as small as 1 kHz. Voltage and current probes, with a maximum frequency range of 50 MHz, are employed for the measurements. The impedance symmetry across all phases ensures identical FRA results for each phase. The complete test setup is displayed in Fig. 3.9.

In addition to experimental testing on a short cable, FEM-based frequency domain simulations were performed on a 1 km cable. The simulated cable is an XLPE-insulated model with a conductor radius of 22.5 mm and an outer sheath radius of 44.2 mm. The parameters, calculated using equations (3.1)–(3.4),  $R_{dc}=1.7508\times 10^{-1}\Omega$ ,  $L_{eq}=5.0903\times 10^{-2} H$ ,  $C_{eq}=1.7657\times 10^{-9}$  F. A corresponding model was created in ANSYS software to simulate six fault cases at various locations along the cable. Fault locations were chosen at 50 m, 250 m, 500 m, 750 m, 950 m, and 1000 m from the source, with fault resistances of 1 m $\Omega$ , 1  $\Omega$ , and 10  $\Omega$  considered for the analysis.

## 3.4 Results and Discussion of the Estimating the Location of Short-circuit Fault in a Cable

This section presents and discusses the analytical, experimental, and simulation results.

#### 3.4.1 Impedance Spectroscopy of a Healthy Cable of 25m long

Frequency Response Analysis plots for a 25m power cable, as described in Section 3.3, are displayed in Fig. 3.11. For the Driving Point Impedance Function, which comprises six Short-Circuited Network Functions six sections of a ladder network are analyzed for comparison with analytical estimations. Additionally, eleven singularities (six zeros and five poles) are considered in the Transmission Line model.

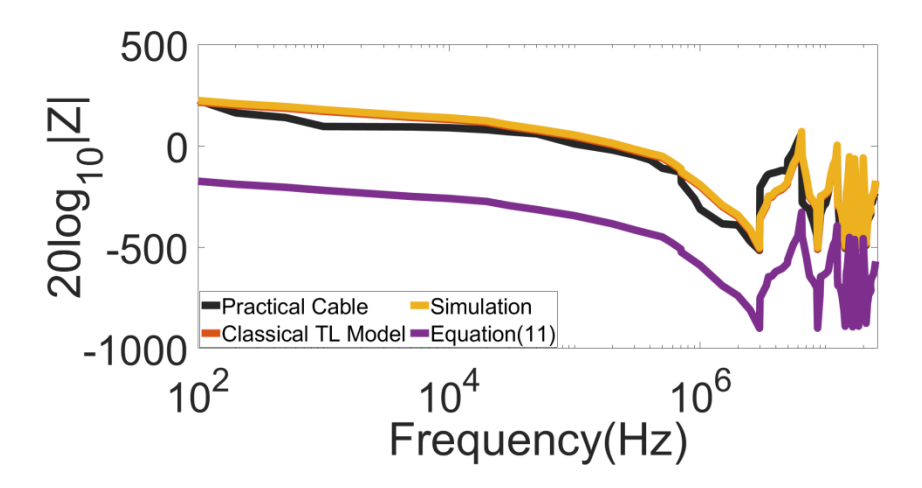


Figure 3.11 Estimating driving point impedance function analytically with practical and simulation results.

The numerator  $N_6(s)$  and denominator  $D_6(s)$ , based on the analytical Equation (3.11) and the parameters of the 11 kV cable mentioned earlier, are given as follows:

Polynomial Expression:

$$N_6(s) = L^6(KC)^6 s^{12} + 11L^5(KC)^5 s^{10} + 45L^4(KC)^4 s^8 + 84L^3(KC)^3 s^6 + 70L^2(KC)^2 s^4 + 21LKCs^2 + 1$$

$$D_6(s) = L^5(KC)^6 s^{11} + 10L^4(KC)^5 s^9 + 36L^3(KC)^4 s^7 + 56L^2(KC)^3 s^5 + 35L^1(KC)^2 s^3 + 6KCs$$
(3.19)

The Expanded from are as follows

$$N_6(s) = 4.8588 \times 10^{-95} s^{12} + 2.5638 \times 10^{-78} s^{10} + 5.1413 \times 10^{-62} s^8 + 4.8561 \times 10^{-46} s^6 + 2.1366 \times 10^{-30} s^4 + 3.5497 \times 10^{-15} s^2 + 1$$

$$D_6(s) = 1.7406 \times 10^{-93} s^{11} + 3.7499 \times 10^{-78} s^9 + 1.1535 \times 10^{-61} s^7 + 1.6405 \times 10^{-45} s^5 + 1.3491 \times 10^{-29} s^3 + 4.1035 \times 10^{-14} s$$
(3.20)

The experimental frequency response aligns closely with both the simulation results and the analytical estimations, particularly regarding the resonant frequencies. However, slight distortions are observed. Tables 3.1 and 3.2 summarize these findings. A Pearson correlation coefficient of 0.9995 was calculated when comparing the experimental graph with the analytical and simulation outputs. The primary difference between the proposed DPIF plot and the experimental results lies in the scaling factor, which is influenced by the resistance omitted in the analytical equation. This resistance significantly affects the initial magnitude of the plots, as noted in references [16,20].

Tables 3.1, and 3.2 present the percentage differences in resonant frequency locations. Difference I represents the percentage variation between the resonant frequencies of the test cable and the simulated model, while Differences II and III correspond to the percentage variations between the test cable and the TL model and analytical expression (3.11), respectively. From Tables 3.1 and 3.2, it is evident that the differences are minimal, with discrepancies less than 0.0738%, demonstrating the accuracy of the analytical approach.

Table 3.1 Position of Zeroes (w.r.t Fig. 3.11)

Zeroes	1 <sup>st</sup> Zero	2 <sup>nd</sup> Zero	3 <sup>rd</sup>	4 <sup>th</sup> Zero	5 <sup>th</sup>	6 <sup>th</sup> Zero
	(MHz)	(MHz)	Zero	(MHz)	Zero	(MHz)
			(MHz)		(MHz)	
Methods						
Test Cable	2.9762	8.6271	14.3562	16.4161	18.3457	21.0034
Simulation	2.9781	8.6313	14.3475	16.4245	18.3384	21.0165
TL model	2.9766	8.6359	14.3601	16.4158	18.3395	21.0189
Equation (11)	2.9745	8.6307	14.3651	16.4079	18.3381	20.9902
Difference I	0.0672%	0.0487%	0.0603%	0.0604%	0.0397%	0.0623%
Difference	0.0134%	0.1020%	0.0271%	0.0018%	0.0337%	0.0738%
II						
Difference III	0.0575%	0.0415%	0.0617%	0.0617%	0.0412%	0.0624%

**Table 3.2 Position of Poles (w.r.t Fig. 3.11)** 

Poles	1 <sup>st</sup> Pole	2 <sup>nd</sup> Pole	3 <sup>rd</sup> Pole	6 <sup>th</sup> Pole	5 <sup>th</sup> Pole
	(MHz)	(MHz)	(MHz)	(MHz)	(MHz)
Methods					
Test Cable	6.4318	12.3214	15.5217	16.9992	19.9879
Simulated	6.4304	12.3146	15.5285	16.9906	19.9978
TL model	6.4299	12.3158	15.5288	16.9868	19.9910
Equation (11)	6.4297	12.3274	15.5285	16.9898	19.9979
Difference I	0.0217%	0.0551%	0.0443%	0.0501%	0.0499%
Difference II	0.0295%	0.0454%	0.0457%	0.0729%	0.0155%
Difference III	0.0313%	0.0488%	0.0457%	0.0550%	0.0501%

### 3.4.2 Estimating the Location of Short-Circuit Fault in a Laboratory Cable of 25m long

In Fig. 3.12 illustrates the experimental impedance graphs for the cable in a healthy condition and for six fault locations discussed in Section 3.3, while Fig. 3.13 shows impedance graphs for varying fault resistances. A key characteristic distinguishing the DPIF graph of a healthy cable from that of a faulty cable is that the faulty cable graph consistently begins with a pole, whereas the healthy cable graph starts with a zero, as demonstrated analytically in equation (3.13).

For a healthy cable, the first zero (Table 3.I) occurs at a frequency of 2.9745 MHz, as calculated using equation (3.11), and at 2.9766 MHz using equation (3.5). Using equation (3.17), Table 3.3 provides the fault location estimates for six different cases along with their corresponding accuracy. The results indicate that short-circuit faults in the test cable can be identified with a minimum accuracy of 99.1365%, regardless of the fault's position—whether near the beginning, middle, or end of the cable. This high level of accuracy is maintained even with variations in fault resistance.

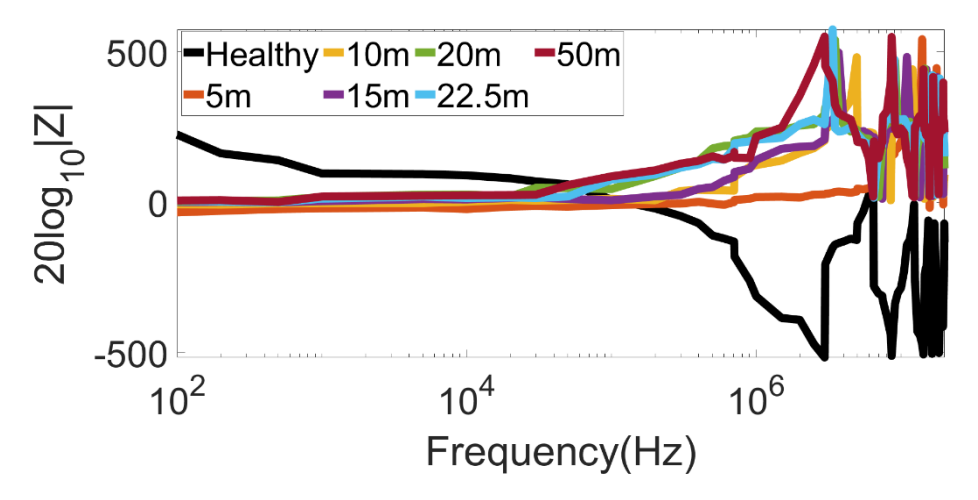


Figure 3.12 Impedance spectroscopy of healthy cable along with six different cases of fault with fault resistance of 1m  $\Omega$ .

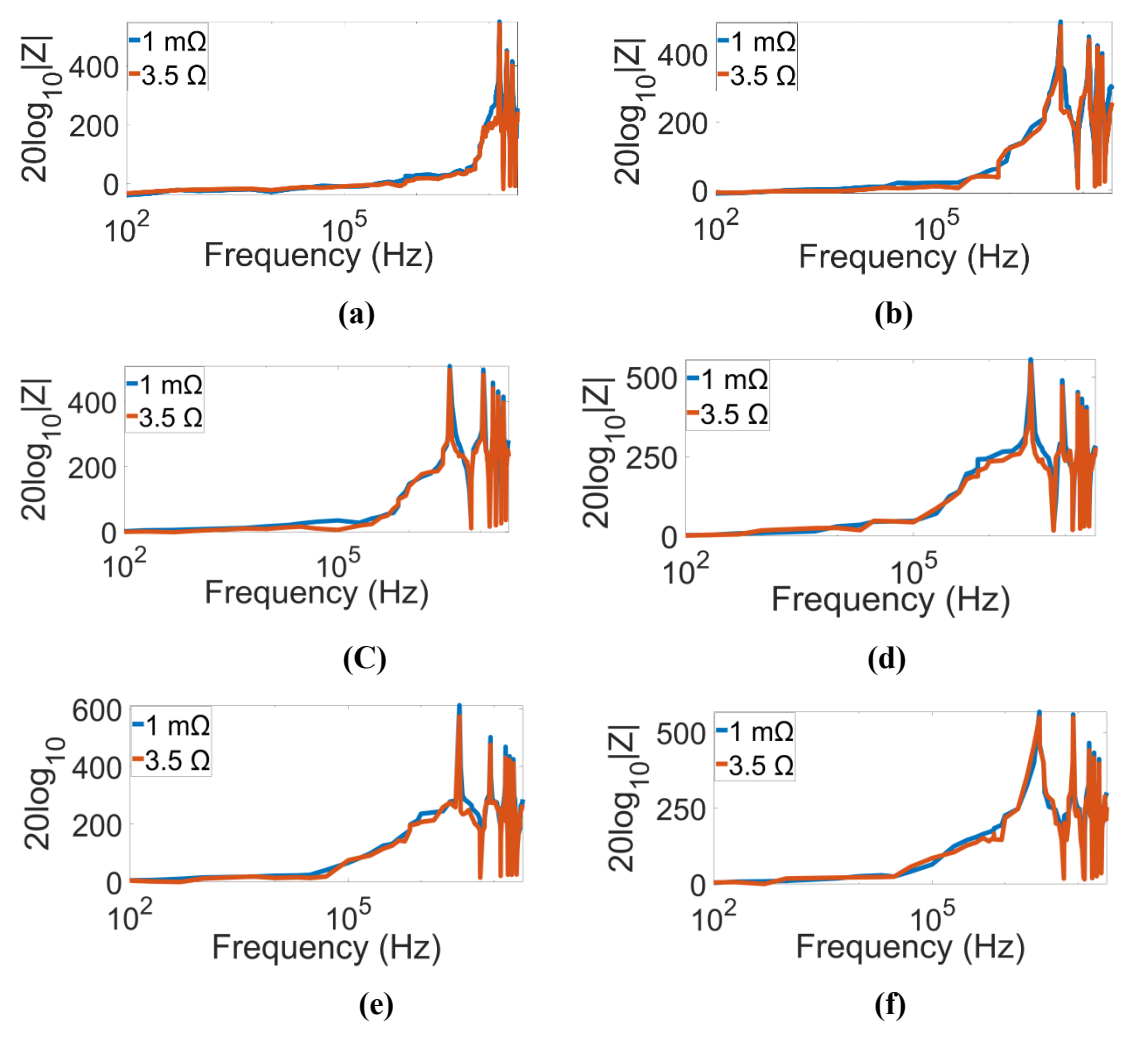


Figure 3.13 Various fault resistance scenarios in a 25-meter experimental cable located at (a) 5 meters, (b) 10 meters, (c) 15 meters, (d) 20 meters, (e) 22.5 meters, and (f) 25 meters.

Table 3.3 Accuracy to estimate the location of fault a/c to proposed formula in a experimental cable

Sl. No	First pole of a faulty cable(MHz	Actual fault location. (m)	Estimated location of fault as per (3.5)(m)	Estimated location of fault as per (3.11)(m)	Accuracy a/c to (5)(%)	Accuracy a/c to (11)(%)
1.	14.91	5	4.98	4.99	99.73	99.81
2.	7.46	10	9.96	9.97	99.68	99.75
3.	4.96	15	14.97	14.98	99.86	99.93
4.	3.75	20	19.82	19.84	99.13	99.20
5.	3.32	22.5	22.38	22.39	99.47	99.54
6.	2.97	25	24.99	25.01	99.99	99.93

#### 3.4.3 Estimating the Location of Short-Circuit Fault in an On-Field Case Study

The experimental impedance graphs for the cable in a healthy condition could not be obtained due to the shorting of all cable phases. Therefore, based on the proposed equation (3.11) and considering seven sections of the ladder network (as the maximum number of SCNFs identified is seven), the numerator  $N_7(s)$  and denominator  $D_7(s)$  are derived using the parameters of a 440V cable mentioned earlier:

The polynomial forms of the functions are as follows:

$$\begin{split} N_7(s) &= L^7C^7s^{14} + 13L^6C^6s^{12} + 66L^5C^5s^{10} + 165L^4C^4s^8 + 210L^3C^3s^6 + 126L^2C^2s^4 + \\ 28LCs^2 + 1 \\ D_7(s) &= L^6C^7s^{13} + 12L^5C^6s^{11} + 55L^4C^5s^9 + 120L^3C^4s^7 + 126L^2C^3s^5 + 56L^1C^2s^3 + 7Cs \\ &\qquad \qquad (3.21) \end{split}$$

Its Expanded from

$$\begin{split} N_7(s) &= 1.0548 \times 10^{-86} s^{14} + 3.1459 \times 10^{-73} s^{12} + 3.4923 \times 10^{-60} s^{10} + 1.8089 \times \\ 10^{-47} s^8 + 4.4876 \times 10^{-35} s^6 + 4.8973 \times 10^{-23} s^4 + 1.8274 \times 10^{-11} s^2 + 1 \\ D_7(s) &= 2.6671 \times 10^{-84} s^{13} + 2.5128 \times 10^{-73} s^{11} + 2.1727 \times 10^{-60} s^9 + 8.4394 \times \\ 10^{-48} s^7 + 1.4763 \times 10^{-35} s^5 + 1.0132 \times 10^{-23} s^3 + 1.7864 \times 10^{-11} s \end{split} \tag{3.22}$$

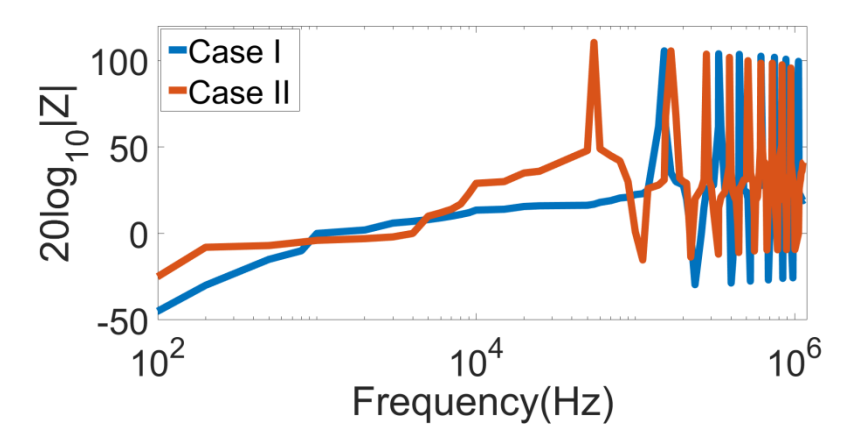


Figure 3.14 Impedance measurement graph: Case I represents the impedance graph measured from open-end I, while Case II corresponds to the impedance graph measured from open-end II.

Table 3.4 Accuracy to estimate the location of fault a/c to proposed formula in an onfield cable

Sl. No.	First pole of a faulty cable (KHz)	Actual fault location (m)	Estimated location of fault as per (5)(m)	Estimated location of fault as per (11)(m)	Accuracy a/c to (5) (%)	Accurac y a/c to (11) (%)
Case 1.	134.02	45.4	44.50	44.67	97.83	98.39
Case 2.	60.16	101.3	99.83	99.51	98.02	98.53

From these equations, the first zero of the healthy cable is calculated to be at a frequency of 40.755 kHz. In comparison, using equation (3.5), where the number of singularity points is considered to be thirteen, the first zero is located at 40.812 kHz. The impedance graph for the faulty cable, measured from both ends, is depicted in Fig. 14. Using equation (3.17), the estimated fault locations from both ends, along with their accuracies, are summarized in Table 3.14.

Despite the presence of joints, the estimated fault location accuracy remains high at 97.8302%. This is attributed to the negligible impact of the joints on the cable's inductive reactance. While joints slightly alter the capacitive reactance and shunt conductance, their

length is minimal compared to the overall length of the cable, resulting in negligible influence on fault location accuracy.

#### 3.4.4 Estimating the Location of Short-Circuit Fault in a Simulation Study

The details of the simulated cable are described in Section 3.3. Fig 3.15 presents the graphs representing the cable under healthy conditions, along with six cases of fault locations. Additionally, Fig. 3.16 illustrates the impedance characteristics for varying fault resistances. Using the cable dimensions and the short-circuited impedance graph, the fault's precise location can be determined through Equation (3.17).

Constructing an infinite series signature function for the simulated cable is complex and computationally intensive. To simplify the process, five SCNFs were utilized to develop the healthy cable's DPIF, while the transmission line model incorporated nine singularity points (five zeros and four poles). The primary goal is to demonstrate how closely the proposed analytical equations align with the healthy cable's impedance characteristics.

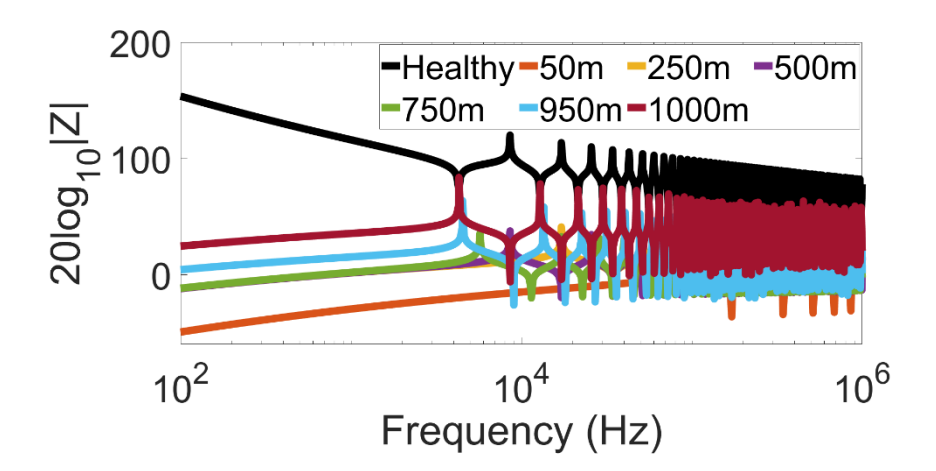
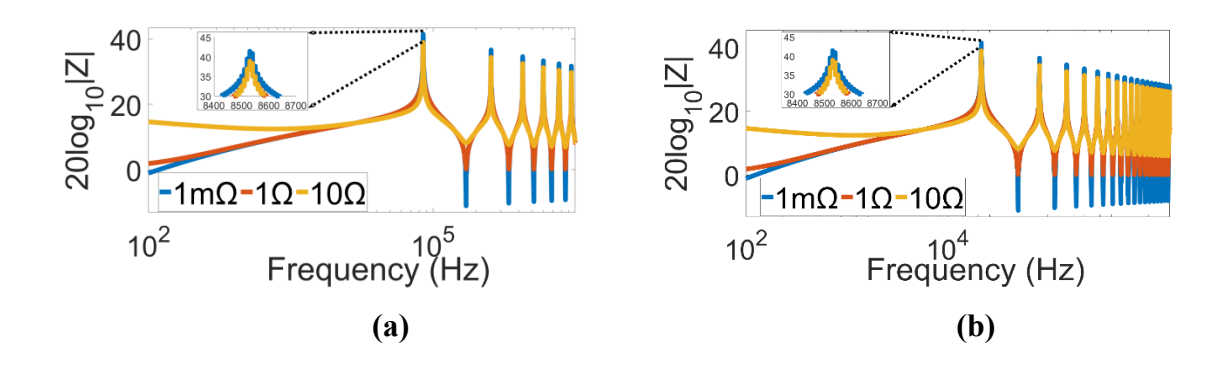


Figure 3.15 Various fault scenarios in a simulated cable with a fault resistance of 1 m $\Omega$ .



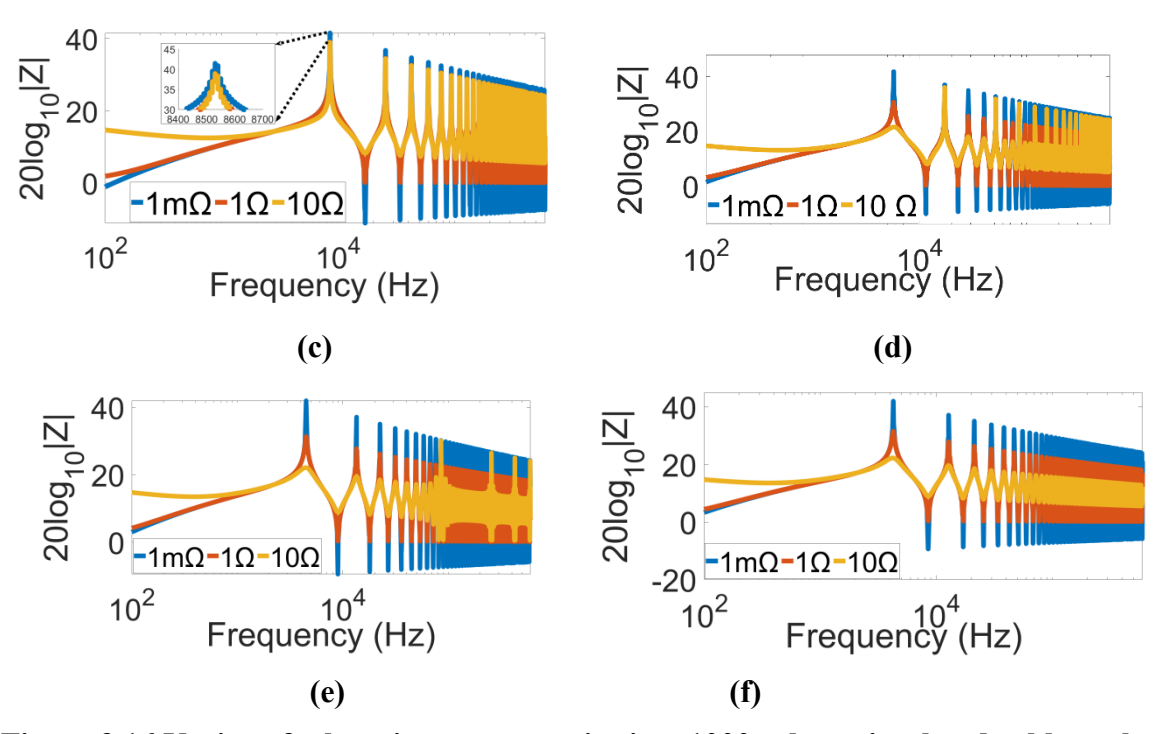


Figure 3.16 Various fault resistance scenarios in a 1000m-long simulated cable at the following locations: (a) 50m, (b) 250m, (c) 500m, (d) 750m, (e) 950m, and (f) 1000m.

Table 3.5 Accuracy to estimate the location of fault a/c to proposed formula in an simulated cable

SI. No.	First pole of a faulty cable (kHz)	Actual fault location (m)	Estimated location of fault as per (5)(m)	Estimated location of fault as per (11)(m)	Accuracy a/c to (5) (%)	Accuracy a/c to (11) (%)
1.	86.5138	50	49.5539	49.4845	99.1078	98.9618
2.	17.1585	250	249.8528	249.5032	99.9411	99.8013
3.	8.5997	500	498.5173	497.8197	99.7034	99.5639
4.	5.7276	750	748.4984	747.4509	99.7997	99.6601
5.	4.5268	950	947.0486	945.7232	99.6893	99.5498
6.	4.2871	1000	1000.000	998.6005	100.0000	99.8600

The numerator N(s) and denominator D(s) of the predicted healthy cable impedance, based on Equation (3.13), where the first zero is located at 4.2871 kHz, are expressed as follows:

#### Polynomial form:

$$N_5(s) = L^5(KC^5)s^{10} + 9L^4(KC)^4s^8 + 28L^3(KC)^3s^6 + 35L^2(KC)^2s^4 + 15LKCs^2 + 1$$

$$D_5(s) = L^4(KC)^5s^9 + 8L^3(KC)^4s^7 + 21L^2(KC)^3s^5 + 20L^1(KC)^2s^3 + 5KCs$$
(3.23)

### **Expanded form**

$$N_5(s) = 5.8647 \times 10^{-51} s^{10} + 6.9472 \times 10^{-40} s^8 + 2.6534 \times 10^{-29} s^6 + 3.7516 \times 10^{-19} s^4 + 1.6488 \times 10^{-9} s^2 + 1$$

$$D_5(s) = 1.1521 \times 10^{-49} s^9 + 8.4264 \times 10^{-40} s^7 + 4.4210 \times 10^{-29} s^5 + 1.0016 \times 10^{-18} s^3 + 8.2866 \times 10^{-11} s$$
(3.24)

In comparison, Equation (3.5) locates the first zero at 4.2811 kHz. Table 3.4 highlights the accuracy of fault location predictions achieved using Equation (3.17). From Fig. 3.15, it is evident that the impedance graph for a healthy cable has positive values, while fault conditions result in negative values. This behavior is due to the effective impedance of the cable being proportional to its total length:

$$Z_{effective} \propto length \ of \ the \ cable$$
 (3.25)

Table 3.5 confirms that the proposed method offers high accuracy in locating faults, achieving at least 98.96% precision for a 1 km cable, even when fault resistance varies.

### Chapter 4

### Identifying the Location of Semiconducting Screen Defect in a High Voltage Cable using Impedance Spectroscopy

In this chapter with the use of impedance spectroscopy, the location of single-point semiconducting screen defect in a high-voltage power cable is estimated. In high-voltage power cables, the semiconducting screen is used in both the conductor and insulation screen. Any small defect in this screen will escalate the water tree phenomenon in the cable. To estimate the location pure analytical methods are used, which is described in detail in this chapter.

### 4.1 Relationship Between Zeroes of the Impedance Graph and Electrical Parameters of the Cable

The impedance graph of a healthy cable typically begins with a zero [71]. It has been demonstrated that the zeros identified through impedance spectroscopy can accurately predict the location of small defects in the semiconducting screen. This section explores the correlation between these zeros and the cable's electrical parameters.

#### 4.1.1 Obtaining the Relationship through Classical Transmission Line Model.

Based on classical transmission line theory, the open-circuit impedance of a cable can be expressed as [76]:

$$z_{open} = \frac{\Gamma}{\tanh(\gamma.l)} \tag{4.1}$$

The frequencies corresponding to the zeros are given by:

$$\omega_{Zero} = \frac{\pi \cdot n}{\gamma \cdot l}, \sum \omega_{Zero} = \sum_{i=1}^{J} \frac{\pi \cdot n}{\gamma \cdot l}, \text{ and } \prod \omega_{Zero} = \prod_{i=1}^{n} \frac{\pi \cdot n}{\gamma \cdot l} n \in \mathbb{N}$$
 (4.2)

Equation (2) establishes a connection between the number of zeros (J) and the propagation constant ( $\gamma$ ) of the cable. However, calculating the propagation constant directly from the cable parameters becomes challenging, particularly when joints are present. To address this, a state-space model is introduced, enabling the estimation of the relationship between the sum and product of the zeros and the cable parameters

#### 4.1.2 Obtaining the Relationship through State Space Model

The general state-space representation for any linear, time-invariant system is expressed as follows [78]

$$\dot{x} = [A]x + [B]u \tag{4.3}$$

$$y = [C]x + [D]u \tag{4.4}$$

In these equations,  $\dot{x}$  represents the derivative of the state vector, x is the state vector, u is the input vector, and y is the output vector. The matrices A, B, C, and D characterize the system.

At high frequencies, the shunt parameter of the cable is  $j\omega KC$ , where  $K = \lfloor (1 - j \tan \delta) \rfloor$ , which depends on the material properties. The per-unit-length electrical parameters of the cable at high frequencies are derived as outlined in [71]. For this model, the conductor current and the voltage across the insulation are selected as state variables.

In the n -section ladder network shown in Fig. 3.4, the state variables are assigned as follows:

- Conductor current:  $x_1 = i_1, x_2 = i_2, \dots, x_n = i_n$
- Nodal voltages between the current-carrying conductor and the grounded screen:  $x_{n+1} = e_2, x_{n+2} = e_3, \dots, x_{2n} = e_{n+1}$

Since an n-section ladder network contains 2n energy storage elements, the total number of state variables for the system is 2n [79]. Among these variables, the nodal voltage  $e_1$  is designated as the input voltage  $e_1$ , and thus the input vector  $e_1$  is represented as  $e_2$ .

#### *i)* Formulation of state equation

For an n-section ladder network shown in Fig. 3.4 (where n corresponds to the total number of short-circuit natural frequencies (SCNFs) or zeros, as the SCNFs match the number of sections in the measured impedance graph), the system matrices are expressed as:

$$[A] = \begin{bmatrix} [\varepsilon_2] & [\gamma_2] \\ [\varepsilon_3] & [\varepsilon_4] \end{bmatrix} \text{ and } [B] = \begin{bmatrix} [\gamma_1] \\ 0 \end{bmatrix}$$

$$(4.5)$$

Here,

$$\varepsilon_{2} = \epsilon_{4} = \begin{bmatrix} 0 & \cdots & 0 \\ \vdots & \ddots & \vdots \\ 0 & \cdots & 0 \end{bmatrix}_{(n \times n)} , \qquad \gamma_{2} = \begin{bmatrix} \frac{-1}{L} & 0 & 0 & \cdots & 0 \\ \frac{1}{L} & \frac{-1}{L} & 0 & \cdots & 0 \\ \vdots & \cdots & \ddots & \ddots & \vdots \\ 0 & \cdots & 0 & \frac{1}{L} & \frac{-1}{L} \end{bmatrix}_{(n \times n)}$$

$$\epsilon_{3} = \begin{bmatrix} \frac{1}{kCg} & \frac{-1}{kCg} & 0 & \cdots & 0 \\ 0 & \frac{1}{kCg} & \frac{-1}{kCg} & \cdots & 0 \\ \vdots & \cdots & \ddots & \ddots & \vdots \\ 0 & \cdots & 0 & 0 & \frac{-1}{kCg} \end{bmatrix}_{(n \times n)}, \gamma_{1} = \begin{bmatrix} \frac{1}{L} \\ 0 \\ \vdots \\ 0 \end{bmatrix}_{(n \times 1)}$$

$$(4.6)$$

#### ii) Formulation of output equation

To develop the Driving Point Admittance Function (DPAF,  $\left(\frac{i_{in}}{v_{in}}\right)$ ) the input current  $(i_{in})$  is considered as the output. This can be written as:

$$Y = \begin{bmatrix} 1 & 0 & 0 & \dots & 0 \end{bmatrix}_{(1 \times 2n)} \begin{bmatrix} i_1 \\ \vdots \\ i_n \\ e_2 \\ \vdots \\ e_{n+1} \end{bmatrix}_{(2n \times 1)}$$

(4.7)

Thus, the output equation can be written in terms of the state variables:

$$[C] = [100 \dots 0]_{(1 \times 2n)} \text{ and, } [D] = [000 \dots 0]$$
 (4.8)

Using Laplace transformation, the state-space equations are converted into the *s*-domain. The DPAF is obtained as:

$$DPAF = \frac{Y(s)}{e_1(s)} = ([C][sI - A]^{-1}[B])$$
(4.9)

Similarly, the Driving Point Impedance Function (DPIF,  $\frac{e_1(s)}{Y(s)}$ ) can be written as:

$$DPIF = \frac{e_1(s)}{Y(s)} = ([C]^{-1}[sI - A][B]^{-1})$$
(4.10)

From (4.10), it is evident that the zeros of the DPIF depend solely on the system matrix [A]:.

#### iii) Resonance Frequency and Eigenvalues

In the high-frequency ladder network, consisting of L and kCg, the resonant frequency  $(\omega_{scnf}^2)$  (troughs only) is given by  $\frac{1}{LKCg}$ . A matrix must exist whose eigenvalues are  $\frac{1}{\omega_{scnf}^2}$ , expressed in terms of inductance and shunt parameters. Assuming  $j\omega$  represents the eigenvalues of matrix [A]:

$$\begin{vmatrix} j\omega_{(2n\times 2n)} & -\begin{bmatrix} [0] & [\gamma_2] \\ [\epsilon_3] & [0] \end{bmatrix} \end{vmatrix} = 0 \tag{4.11}$$

By evaluating the determinant for the block matrix, let:,

Let 
$$\gamma_2 \epsilon_3 = \theta$$
 (4.12)

$$\left| -\omega^2_{(n \times n)} - \vartheta \right| = 0 \tag{4.13}$$

Matrix A has dimensions  $(2n \times 2n)$ , while matrix  $\vartheta$  has dimensions  $(n \times n)$ . Each resonance point corresponds to two eigenvalues  $(+j\omega \text{ and } -j\omega)$  for matrix [A] or one eigenvalue  $(-\omega^2)$  for matrix  $\vartheta$ .

The trace and product of the eigenvalues of  $\theta$  are given as:

$$Trace \,\vartheta = -\sum_{i=1}^{n} \omega^{2}_{i} \tag{4.14}$$

product of the root (P.O.R) of 
$$\vartheta = \pm \prod_{i=1}^{n} \omega_{i}^{2}$$
 (4.15)

By expanding  $\vartheta$ ::

Trace 
$$\vartheta = -(1+2+\dots+n)\frac{1}{LK \, Ca} = -\left(\frac{n^2}{2} + \frac{n}{2}\right)\frac{1}{LK \, Ca}$$
 (4.16)

And

$$P.O.R\ of\ \vartheta = \pm \frac{(1 \times 2 \times ... \times n)}{(LK\ Cg)^n} = \pm \frac{n!}{(LK\ Cg)^n}$$
 (4.17)

Comparing with earlier results:

$$\sum_{i=1}^{n} \omega^{2}_{i(healthy)} = \left(\frac{n^{2}}{2} + \frac{n}{2}\right) \frac{1}{LK Cg}$$

$$\tag{4.18}$$

$$\prod_{i=1}^{n} \omega^{2}_{i(healthy)} = \frac{n!}{(LK Cg)^{n}}$$

$$(4.19)$$

This establishes a relationship between the electrical parameters and the sum and product of the zeros in the cable's impedance spectrum.

### 4.2 Relationship between Zeroes of the Impedance Graph and Electrical Parameters of the Cable

The Fig. 4.1(a) depicts the cross-sectional view of a healthy cable, where  $C_{cs}$ ,  $C_i$  and  $C_{is}$  represent the capacitance between the conductor and screen, the conductor screen and insulation screen, and the insulation screen and grounding sheath, respectively. These capacitances are calculated using the following formula [75].

$$Cap = \frac{\frac{\mu_0}{2\pi} \ln(\frac{r_2^2}{r_1^2})}{\left(\frac{1}{\mu_E}\right) \left(\left(\frac{\mu_0}{2\pi} \ln(\frac{r_2^2}{r_1^2})\right)^2 - \left(\frac{\mu_0}{2\pi} \ln(\frac{r_2}{r_1})\right)^2\right)} F/m$$
(4.20)

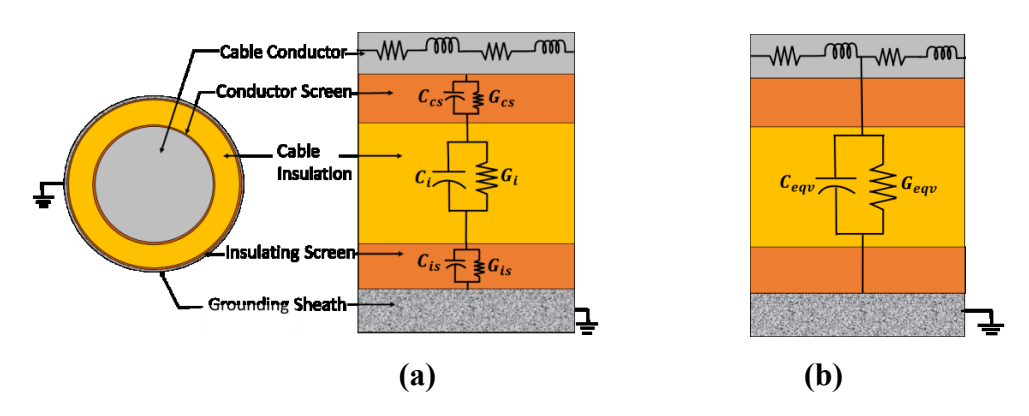


Figure 4.1 (a) Comprehensive parametric representation of a cross sectional single-core cable with a grounded outer sheath., (b) Simplified parametric model of a cross sectional single-core cable with a grounded outer sheath

Here,  $r_1$  and  $r_2$  are the inner and outer radii for each specific capacitance ( $C_{cs}$ ,  $C_i$  and  $C_{is}$ ),

while  $\varepsilon_r$  and  $\mu_r$  are the relative permittivity and permeability of the respective medium. The approximate effective capacitance of a healthy cable, with no deformities, is illustrated in Fig. 4.1(b).

For  $C_{cs}$  and  $C_{is}$ ,  $\varepsilon_r$  typically ranges from  $10^4 - 10^5 [80]$ , while for XLPE material,  $\varepsilon_r$ = 2.3. Similar to capacitance, the conductance values are denoted as  $G_{cs}$ ,  $G_i$  and  $G_{is}$ . The equivalent capacitance of a healthy cable is approximately:

$$C_{eqv(healthy)} \sim \frac{C_{cs}C_iC_{is}}{C_{cs}C_i + C_iC_{is} + C_{cs}C_{is}} \sim C_i$$
(4.21)

When a defect occurs in the semiconducting screen, a portion of it comes into contact with the conducting material, altering the equivalent capacitance, as shown in Fig. 4.2. The effective capacitance for a conductor screen-defective cable is given by:

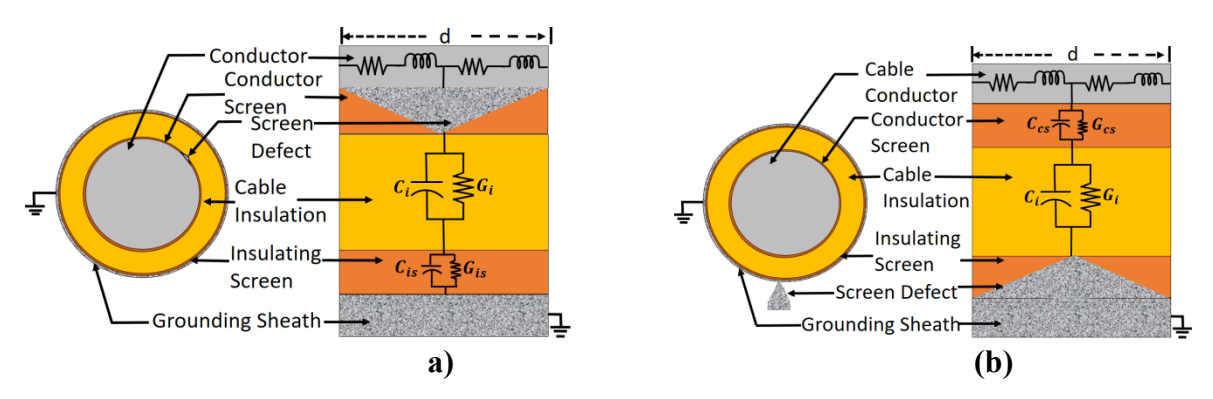


Figure 4.2 Parametric representation of a single-core cable with defects in (a) the conductor screen and (b) the insulation screen.

$$C_{eqv(defective)} \sim \frac{(C_{cs} - \psi c)C_i C_{is}}{(C_{cs} - \psi c)C_i + C_i C_{is} + (C_{cs} - \psi c)C_{is}}$$

$$(4.22)$$

In (4.22),  $\psi C$  represents the defect's capacitance. Assuming  $C_{cs}C_{is} \gg C_iC_{is} + C_{cs}C_i - \psi CC_i - \psi CC_{is}$  and given that  $\varepsilon_r$  f the semiconducting screen is significantly greater than that of the insulating or conducting material, the defective capacitance over a defective length 'd' can be approximated as:

$$C_{eqv(defectiv)} \sim C_i \cdot (1 - \psi C \cdot d \times \frac{1}{C_{cs}})$$
 (4.23)

From the comparison between Equations (21) and (23), it is evident that  $C_{eqv(healthy)} > C_{eqv(defectiv1)}$  cable. Consequently, the impedance spectrum of a defective cable starts at a

higher frequency compared to a healthy cable, as  $(\omega \propto \frac{1}{\sqrt{L_{eqv}C_{eqv}}} [71])$ .

For an *n*-section ladder network, if the defect occurs at the m-th node, resulting in a net capacitance  $C_{eqv(defects)}$  at the defect location while the remaining sections retain  $C_{eqv(healthy)}$ , the difference in the sum of the square of the zeroes between healthy and defective cables is:

$$\sum_{i=1}^{n} \omega^{2}_{i(defective)} - \sum_{i=1}^{n} \omega^{2}_{i(healthy)} = \frac{1}{mKLC_{eqv(healthy)}} \left( \frac{C_{eqv(healthy)}}{C_{eqv(defects)}} - 1 \right)$$
(4.24)

The product of roots (P.O.R.) for healthy and defective cables is:

$$\prod_{i=1}^{n} \omega^{2}_{i(defective)} = \prod_{i=1}^{n} \omega^{2}_{i(healthy)} \frac{KLC_{eqv(healthy)}}{KLC_{eqv(defects)}}$$
(4.25)

The defect location  $l_{defect}$  can be empirically derived as:

$$l_{defect} = \frac{\sum_{i=1}^{n} \omega^{2}_{i(defect/Measured)} - \sum_{i=1}^{n} \omega^{2}_{i(analytical)}}{\frac{1}{KLC_{eqv(healthy)}} (\frac{\prod_{i=1}^{n} \omega^{2}_{i(defect/measured)}}{\prod_{i=1}^{n} \omega^{2}_{i(healthy/analytical)}} - 1)} \times l$$
(4.26)

In the above formula, l represents total cable length. For cables with multiple defects r, the cumulative defect length is:

$$\sum_{i=1}^{r} l_{i(defect)} = \frac{\sum_{i=1}^{n} \omega^{2}_{i(defect/Measured)} - \sum_{i=1}^{n} \omega^{2}_{i(analytical)}}{(\frac{1}{KLC_{eqv}(healthy)})^{2-r} \frac{\prod_{i=1}^{n} \omega^{2}_{i(defect/measured)}}{\prod_{i=1}^{n} \omega^{2}_{i(healthy/analytical)}} \times l$$

$$(4.27)$$

A single defect satisfies the condition,  $\partial > 1$ , while multiple defects satisfy  $0 < \partial \le 1$ , where  $\partial$  is defined as::

$$\partial = \frac{\sum_{i=1}^{n} \omega^{2}_{i(defect/Measured)} - \sum_{i=1}^{n} \omega^{2}_{i(analytical)}}{\prod_{i=1}^{n} \omega^{2}_{i(healthy/analytical)}} - 1)$$

$$(4.28)$$

Impedance spectroscopy, influenced by the reflection coefficient, varies with defect location. Defects nearer to the source exhibit minimal frequency shifts compared to distant defects. Defect diameter minimally affects location accuracy within a permissible range (1–10 mm) due to the dominance of  $C_{eqv(healthy)}$  over  $C_{eqv(defectiv)}$ 

The formulas are validated through simulation and experimental results in subsequent sections.

# 4.3 Experiments and Simulations Performed to Estimate the Location of Semiconducting Screen Defect in a Cable.

In a 25-meter-long test cable, six insulation screen defects were intentionally introduced at different locations, one at a time, to validate the accuracy of the proposed methodology, as illustrated in Fig. 4.3. The cable specifications are as follows: 11 kV, three-core XLPE cable with an aluminum conductor cross-sectional area of  $41mm^2$ . The insulation thickness is 4.3 mm, while the insulation screen is 1.5 mm thick. The cable insulation has a relative permittivity ( $\varepsilon_r$ ) of 2.3 and a loss tangent ( $\tan \delta$ ) of 0.0005. The insulation and conductor screens exhibit a relative permittivity of  $11.2 \times 10^5$ . The calculated cable parameters are:  $R_{dc} = 1.9614 \times 10^{-3} \Omega$ ,  $L_{eq} = 9.6586 \times 10^{-2} \mathrm{H}$  and  $C_{eq(healthy)} = 7.3273 \times 10^{-7} \mathrm{F}$ .

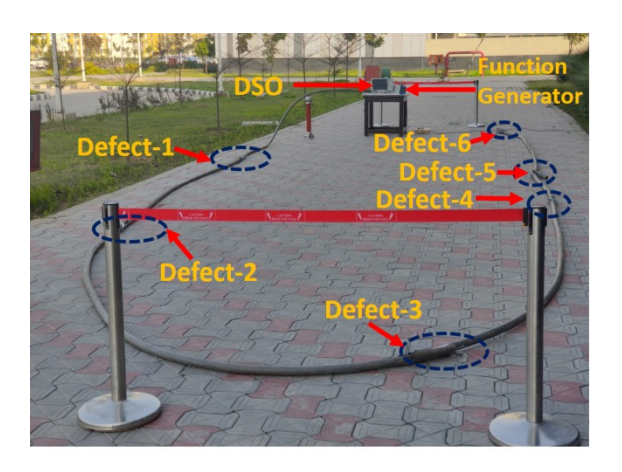


Figure 4.3 Experimental setup for locating insulation screen defects.

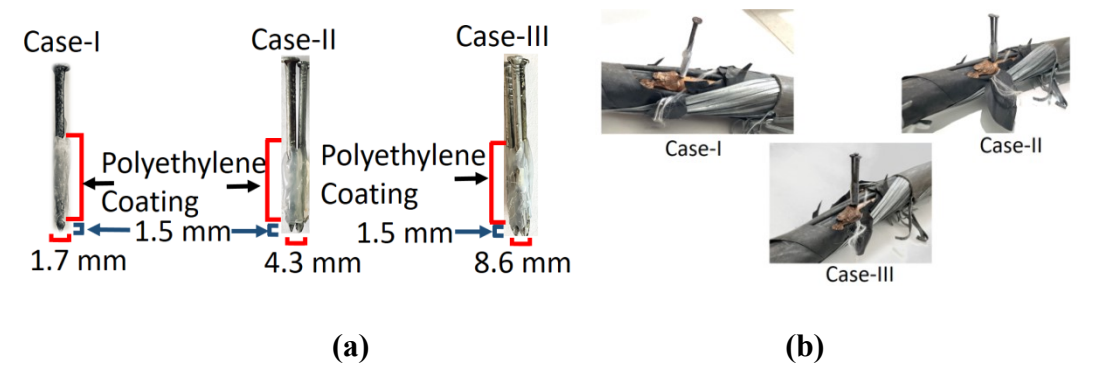


Figure 4.4 (a) Polyethylene-coated nails of varying diameters, (b) Process of creating defects in the insulation screen.

The defects were positioned at distances of 5 m, 10 m, 15 m, 20 m, 22.5 m, and 25 m from the source. Three case studies were performed with defect diameters of 1.7 mm, 4.3 mm, and

8.6 mm, representing practical scenarios I, II, and III, respectively. Defects were created using polyethylene-coated iron nails (with the pointed end removed for safety) of thickness 1.5 mm, equivalent to the insulation screen thickness, as shown in Fig. 4.4 (a) and (b). The experimental process followed the methodology established in previous studies [12].

To validate equations (4.28), an extreme-case scenario was analyzed. This involved comparing two defects located at 3 m and 5 m from the source, each with a diameter of 1.7 mm, to a single defect at 22.5 m with a diameter of 8.6 mm.

In addition to the experimental setup, finite element method (FEM)-based frequency mode simulations were conducted for a 1-km-long cable with three factory joints to mimic practical conditions, as shown in Fig. 4.5. Both conductor screen and insulation screen defects were simulated. The modeled XLPE cable had a conductor radius of 22.5 mm, an outer screen radius of 44.2 mm, an insulation thickness of 1.5 mm, and joint lengths of 1 m. Electrical properties matched those of the experimental setup, and the calculated parameters were  $R_{dc} = 1.7508 \times 10^{-1} \Omega$ ,  $L_{eq} = 8.0901 \times 10^{-1} H$ ,  $C_{eq} = 9.7876 \times 10^{-5} F$ . (including contributions from the joints and continuous sections). The model was implemented using COMSOL software.

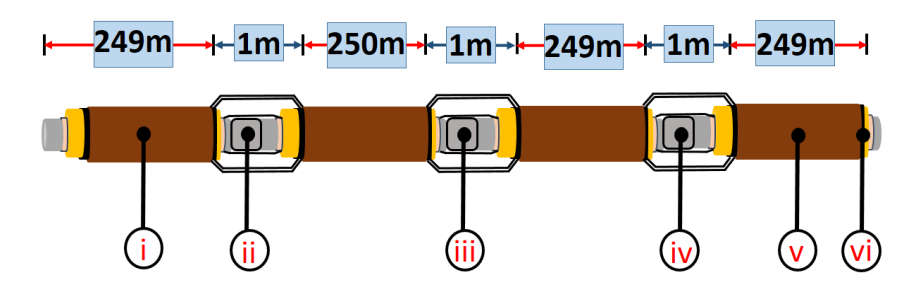


Figure 4.5 Cable model for simulation with three factory joints and defects located at :i) Conductor screen: 50 m, 250 m, and 500 m. ii) Insulation screen: 750 m, 950 m, and 1000 m.

Six cases were simulated, covering defects in both the conductor and insulation screens at different locations, including joint sections. Defect diameters of 2 mm, 4 mm, and 6 mm were considered, representing simulation scenarios I, II, and III, with defect thicknesses equal to the screen thickness of 1.2 mm, as shown in Fig. 4.6. The conductor screen defects were simulated at 50 m, 250 m, and 500 m, while insulation screen defects were positioned at 750 m, 950 m, and 1000 m.

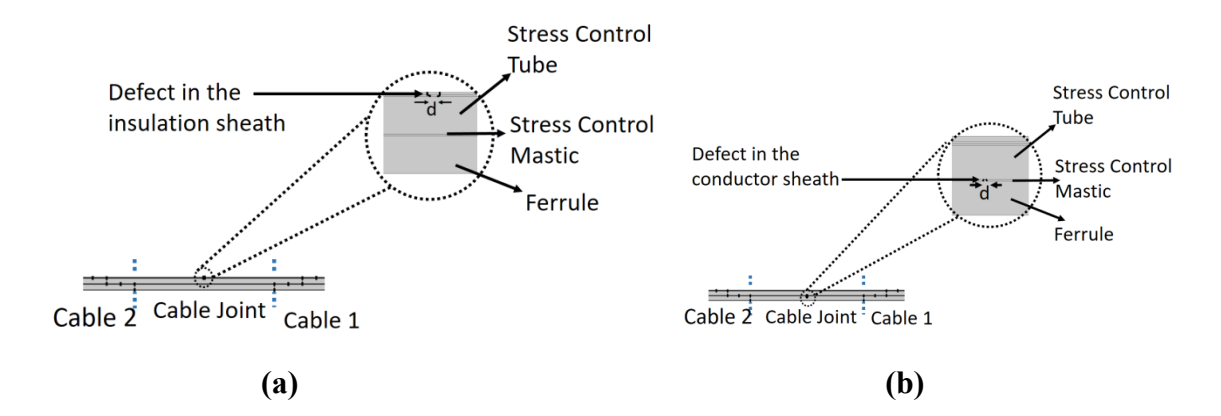


Figure 4.6 FEM-based model of a straight-through joint showing defects in (a) the insulation screen and (b) the conductor, each with defect diameter d.

To validate equations (4.28) through simulation, another extreme-case scenario was considered. This involved comparing two conductor screen defects located at 5 m and 10 m, each with a diameter of 2 mm, against a single defect located at 1000 m with a diameter of 6 mm

# 4.4 Results and Discussion of the Experiments and Simulations Performed to Estimate the Location of Semiconducting Screen Defect in a Cable

This section presents and discusses the analytical, experimental, and simulation results

#### 4.4.1 Healthy Cable Impedance Analysis (25m Test Cable)

The impedance graph of the 25-meter-long test cable described in Section 4.3 is presented in Fig. 4.7. Using the DPIF, which includes six SCNFs, the impedance analysis was performed by considering six ladder network sections for comparison with analytical estimations. Additionally, six singular points (zeroes) were analyzed in the TL model.

The identified zeroes occur at frequencies of 2.9865, 8.6389, 14.4145, 16.9547, 18.8871, and 21.4736 MHz. Table 4.1 summarizes the sum and product of these zeroes, comparing experimental measurements with analytical results obtained using equations (4.2), (4.18), and (4.19). Both analytical methods demonstrate exceptional accuracy exceeding 99.99% when compared to practical data from the test cable.

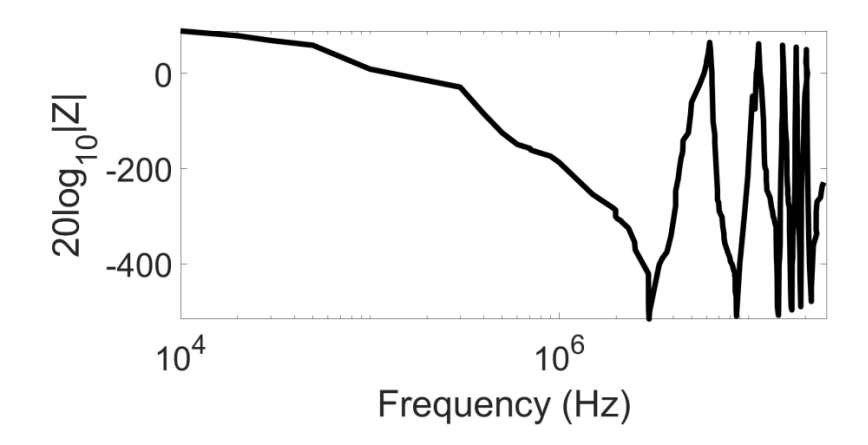


Figure 4.7 Driving point impedance plot of the 25-meter length healthy test cable.

Table 4.1 Comparison of the sum and product of zeroes for the healthy cable

Function	Practically obtained sum and product of zeros (Hz)	Analytically obtained sum and product of zeros (2) (Hz)	Analytically obtained sum and product of zeros (18) &(19) (Hz)	Accuracy Compari ng with (2) %	Accuracy Comparing with (18) & (19) %
$\sum \omega$	83.3553× 10 <sup>6</sup>	83.3538× 10 <sup>6</sup>	83.3547× 10 <sup>6</sup>	99.9982	99.9985
$\prod \omega$	2.5572× 10 <sup>42</sup>	2.5570× 10 <sup>42</sup>	2.5571× 10 <sup>42</sup>	99.9921	99.9987

The analytical results obtained using cable electrical parameters (easily measurable in practice) closely match experimental values, verifying the accuracy of the method.

#### 4.4.2 Healthy Cable Impedance Analysis (25m Test Cable)

Impedance plots for a healthy cable and for six defect locations (each with a defect diameter of 1.7 mm) are shown in Fig. 9. Defects were placed at distances of 5 m, 10 m, 15 m, 20 m, 22.5 m, and 25 m. Additionally, Fig. 10 illustrates impedance plots for defects of varying diameters (1.7 mm, 4.3 mm, and 8.6 mm). Using equation (26), the estimated defect locations and corresponding accuracies for all cases are summarized in Table II.

The analysis reveals a minimum accuracy of 98.24%, irrespective of defect location or diameter, demonstrating the robustness of the method.

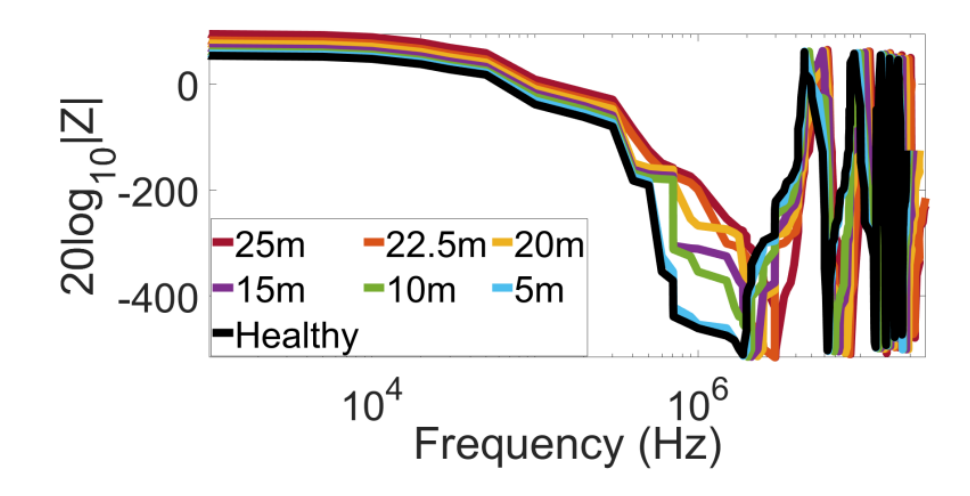


Figure 4.8 Impedance plots for the healthy cable and various defect cases with a diameter of 1.7 mm.

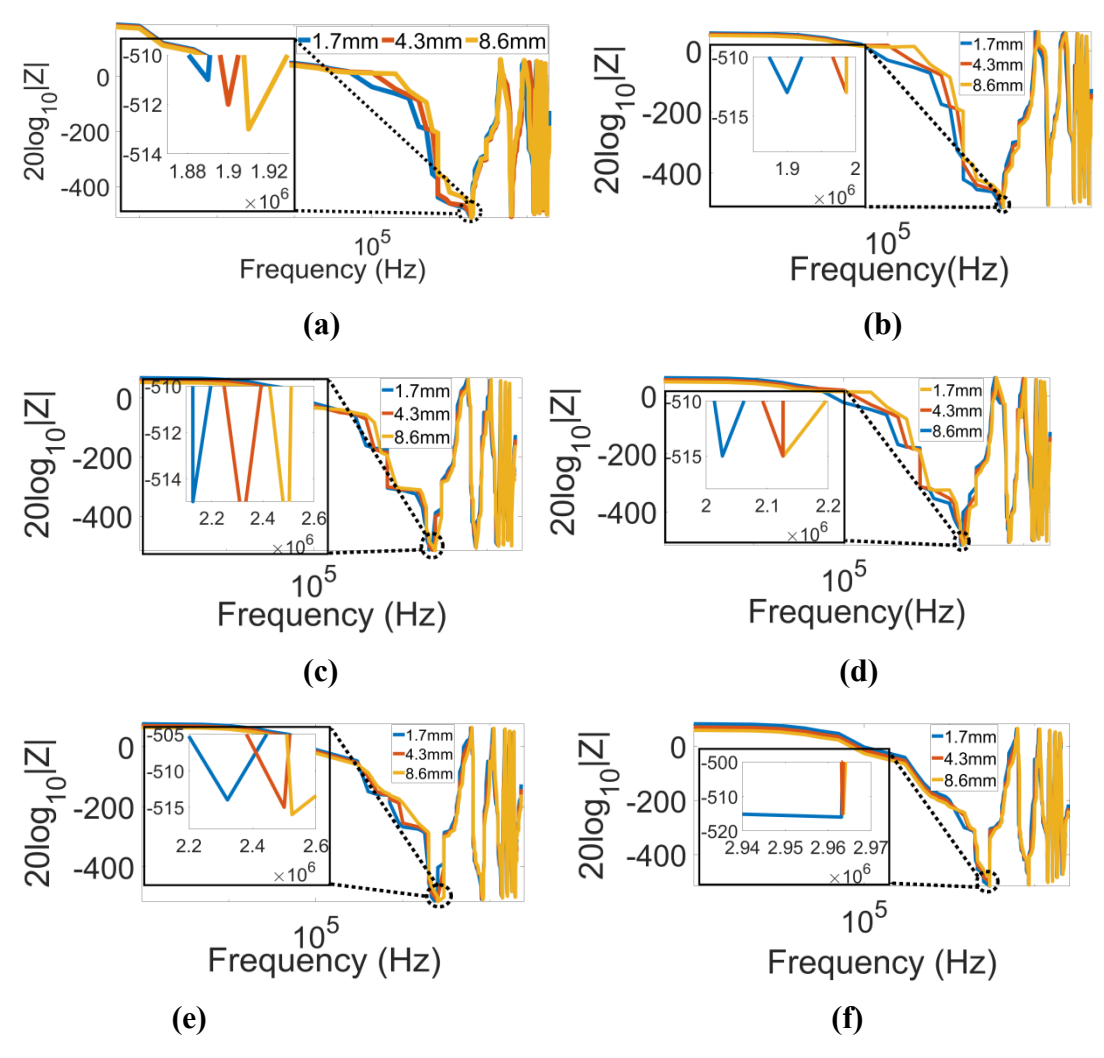


Figure 4.9 Impedance plots for defects of varying diameters in a 25-meter cable at: (a) 5 m, (b) 10 m, (c) 15 m, (d) 20 m, (e) 22.5 m, (f) 25 m.

Table 4.2 Accuracy to detect defect in a practical cable

Case	-		1 abic 1.2 / 10	euracy to a	etect defect i	n a praetical	cubic	
Case-   R6.1252   3.8280   9.8623   9.8638   98.6238   98.6380	Location	Cases	Sum of	Product	Estimated	Estimated	Accuracy	Accuracy
Defectiv c cable   C	.(m)		zeroes of	of zeroes	location	location	a/c to	a/c to
Defectiv c cable   C			a	of a	of defect	of defect	(4.2) (%)	(4.18) &
Case-   Realizer   R			Defectiv	Defectiv	as per	as per		(4.19) (%)
Case   84.4218   3.5401   4.9112   4.9116   98.2240   98.2320			e cable	e cable×	-	-		
5         Case-I Case-I I Case-I II         84.4218         3.5401         4.9112         4.9116         98.2240         98.2320           Case-III Case-III Case-IIII         84.4219         3.5402         4.9117         4.9121         98.2420         98.2421           10 Case-IIII Case-IIII Case-IIII         86.1252         3.8279         9.8623         9.8638         98.6238         98.6380           15 Case-III Case-IIII Case-IIII Case-IIII Case-IIII Case-IIII Case-IIII Case-IIII Case-IIII Sp. 6127         3.9608         14.9117         14.9132         99.4119         99.4213           20 Case-III Sp. 6127         3.9610         14.9112         14.9127         99.4085         99.4180           20 Case-III Sp. 6127         3.9728         19.8506         19.8521         99.2534         99.2605           22.5 Case-III Sp. 6127         3.9729         19.8504         19.8519         99.2524         99.2585           22.5 Case-III Sp. 6127         3.9729         19.8502         19.8517         99.2514         99.2585           22.5 Case-III Sp. 6581         4.0242         22.3638         22.3653         99.3937         99.4000           25 Case-III Sp. 6582         4.0243         22.3634         22.3649         99.3932         99.3995           25 Case-III Sp.			(MHz)	$10^{42}(Hz)$				
Tase-   84.4219   3.5402   4.9117   4.9121   98.2420   98.2421	5	Case-	` ′	· ·	4.9112	` ' ' '	98.2240	98.2320
Case-   84.4219   3.5402   4.9117   4.9121   98.2420   98.2421			011.210	0.0.01	, 112	, 110	J 012210	30.2020
II			84 4219	3 5402	4 9117	4 9121	98 2420	98 2421
Case-			01.1219	3.3 102	1.9117	1.7121	70.2420	70.2421
III			84 4220	3 5403	4 9120	4 9122	98 2400	98 244
10			04.4220	3.3403	4.7120	7.7122	70.2700	70.277
Tase-   86.1252   3.8280   9.8620   9.8635   98.6208   98.6350	10		96 1252	2 9270	0.9622	0.9629	00 (220	00 (200
II	10	Case-	80.1232	3.8219	9.8023	9.8038	90.0230	90.0300
II			96 1252	2.0200	0.9620	0.9625	00 (200	00 (250
Case-			86.1252	3.8280	9.8620	9.8633	98.6208	98.6350
III			06.1254	2.0200	0.0610	0.0624	00 (100	00.6240
15			86.1254	3.8280	9.8619	9.8634	98.6198	98.6340
Case-   87.9815   3.9609   14.9115   14.9130   99.4105   99.4200								
Case-   87.9815   3.9609   14.9115   14.9130   99.4105   99.4200     Case-   87.9817   3.9610   14.9112   14.9127   99.4085   99.4180     20	15	Case-	87.9814	3.9608	14.9117	14.9132	99.4119	99.4213
II		_						
Case-III         87.9817         3.9610         14.9112         14.9127         99.4085         99.4180           20         Case-II         3.9728         19.8506         19.8521         99.2534         99.2605           Case-III         89.6127         3.9729         19.8504         19.8519         99.2524         99.2595           Case-III         89.6129         3.9729         19.8502         19.8517         99.2514         99.2585           22.5         Case-III         90.6581         4.0242         22.3638         22.3653         99.3950         99.4013           Case-III         90.6582         4.0243         22.3635         22.3650         99.3937         99.4000           25         Case-III         90.6583         4.1261         24.8973         24.9251         99.5893         99.7003           Case-III         92.0241         4.1262         24.8781         24.9028         99.5123         99.6113           II         92.0242         4.1263         24.8531         24.8781         99.4125         99.5126		Case-	87.9815	3.9609	14.9115	14.9130	99.4105	99.4200
III		II						
Case-		Case-	87.9817	3.9610	14.9112	14.9127	99.4085	99.4180
Record   R		III						
Record   R	20	Case-		3.9728	19.8506	19.8521	99.2534	99.2605
Case-II       89.6127       3.9729       19.8504       19.8519       99.2524       99.2595         Case-III       89.6127       3.9729       19.8502       19.8517       99.2514       99.2585         22.5       Case-III       89.6129       4.0242       22.3638       22.3653       99.3950       99.4013         Case-III       90.6581       22.3635       22.3650       99.3937       99.4000         Case-III       90.6582       4.0243       22.3634       22.3649       99.3932       99.3995         25       Case-III       90.6583       4.1261       24.8973       24.9251       99.5893       99.7003         Case-III       92.0241       4.1262       24.8781       24.9028       99.5123       99.6113         Case-III       92.0242       4.1263       24.8531       24.8781       99.4125       99.5126			89.6127					
II			0,1011	3.9729	19.8504	19.8519	99.2524	99.2595
Case-III       89.6129       3.9729       19.8502       19.8517       99.2514       99.2585         22.5       Case-II       90.6581       22.3638       22.3653       99.3950       99.4013         Case-III       90.6582       4.0243       22.3635       22.3650       99.3937       99.4000         Case-III       90.6583       4.0243       22.3634       22.3649       99.3932       99.3995         25       Case-III       92.0241       4.1261       24.8973       24.9251       99.5893       99.7003         Case-III       92.0242       4.1262       24.8781       24.9028       99.5123       99.6113         Case-III       92.0242       4.1263       24.8531       24.8781       99.4125       99.5126			89.6127				>> <b>\_</b>	// = = /
III   89.6129   4.0242   22.3638   22.3653   99.3950   99.4013			0310121	3 9729	19 8502	19 8517	99 2514	99 2585
22.5       Case-I 90.6581       4.0242       22.3638       22.3653       99.3950       99.4013         Case-III 90.6582       4.0243       22.3635       22.3650       99.3937       99.4000         Case-III 90.6583       4.0243       22.3634       22.3649       99.3932       99.3995         25       Case-I 92.0241       4.1261       24.8973       24.9251       99.5893       99.7003         Case-II 92.0242       4.1262       24.8781       24.9028       99.5123       99.6113         Case-II 92.0242       4.1263       24.8531       24.8781       99.4125       99.5126			89 6129	3.5725	19.0302	19.0317	<i>)</i>	77.2303
I       90.6581       4.0243       22.3635       22.3650       99.3937       99.4000         II       90.6582       4.0243       22.3634       22.3649       99.3932       99.3995         Case-III       90.6583       4.1261       24.8973       24.9251       99.5893       99.7003         Case-II       92.0241       4.1262       24.8781       24.9028       99.5123       99.6113         Case-II       92.0242       4.1263       24.8531       24.8781       99.4125       99.5126	22.5		07.0127	4 0242	22 3638	22 3653	99 3950	99 4013
Case-II       90.6582       4.0243       22.3635       22.3650       99.3937       99.4000         Case-III       90.6583       4.0243       22.3634       22.3649       99.3932       99.3995         25       Case-II       92.0241       24.8973       24.9251       99.5893       99.7003         Case-II       92.0242       4.1262       24.8781       24.9028       99.5123       99.6113         Case-II       92.0242       4.1263       24.8531       24.8781       99.4125       99.5126	22.3		90 6581	7.04 <b>7</b> 4	22.3030	22.3033	77.3730	77.7013
II       90.6582       4.0243       22.3634       22.3649       99.3932       99.3995         III       90.6583       4.1261       24.8973       24.9251       99.5893       99.7003         Case-       4.1262       24.8781       24.9028       99.5123       99.6113         Case-       4.1263       24.8531       24.8781       99.4125       99.5126			70.0301	4.0242	22 3625	22 3650	00 3037	00 4000
Case-III       90.6583       4.0243       22.3634       22.3649       99.3932       99.3995         25       Case-I       4.1261       24.8973       24.9251       99.5893       99.7003         Case-II       92.0241       4.1262       24.8781       24.9028       99.5123       99.6113         Case-II       92.0242       4.1263       24.8531       24.8781       99.4125       99.5126			00 6592	4.0243	22.3033	22.3030	77 <b>.</b> 373/	22 <b>.4</b> 000
III     90.6583     24.8973     24.9251     995893     99.7003       I     92.0241     24.8973     24.9251     995893     99.7003       Case- II     92.0242     4.1262     24.8781     24.9028     99.5123     99.6113       Case- Case-     4.1263     24.8531     24.8781     99.4125     99.5126			90.0382	4.0242	22 2624	22 2640	00 2022	00 2005
25 Case- I 92.0241			00 6592	4.0243	22.3034	22.3049	99 <b>.</b> 39 <b>3</b> 2	77.3775
I     92.0241     92.0241       Case-II     92.0242       Case-II     92.0242       Case-II     4.1263       24.8781     24.8781       24.8781     99.4125       99.5126	2.5		90.0383	4.1071	24.0052	24.0251	00 5005	00.5000
Case-II       92.0242       4.1262       24.8781       24.9028       99.5123       99.6113         Case-II       92.0242       24.8531       24.8781       99.4125       99.5126	25		0000011	4.1261	24.8973	24.9251	995893	99.7003
II     92.0242       Case-     4.1263     24.8531     24.8781     99.4125     99.5126			92.0241					
Case- 4.1263 24.8531 24.8781 <b>99.4125 99.5126</b>				4.1262	24.8781	24.9028	99.5123	99.6113
		II	92.0242					
				4.1263	24.8531	24.8781	99.4125	99.5126
III 92.0242		III	92.0242					

### 4.4.3 Multi-point Defects in an Experimental Cable

For two insulation defects (1.7 mm diameter) located at 3 m and 5 m from the source, and

one larger defect (8.6 mm) at 25 m, the sum and product of the measured zeroes are 92.6245 MHz and  $4.5454 \times 10^{42}$  Hz, respectively, as shown in Fig. 4.10. Using equation (4.2) and the state-space model, the deviation factor ( $\partial$ ) is 0.8631 and 0.8638 for the multi-defect case, compared to 1.00002 and 1.00004 for a single defect at the cable's end. These results validate equations (4.28).

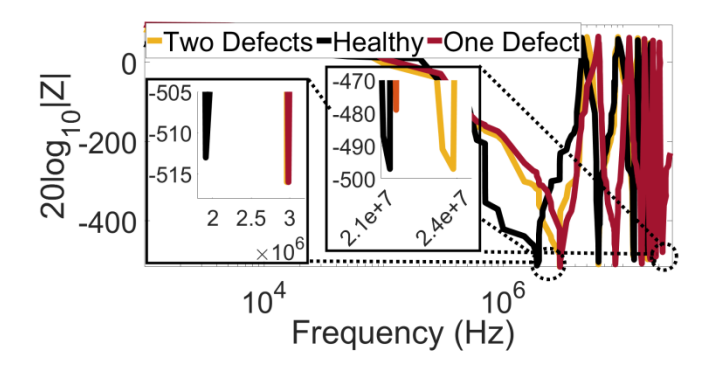


Figure 4.10 Impedance plots for two insulation defects near the source (3 m and 5 m) and one defect at 25 m.

In the lower frequency range, multi-defect impedance closely resembles the healthy condition. However, deviations increase with frequency due to reduced net capacitance.

#### 4.4.4 Simulation Results for Defects in a 1000m Cable

Simulation graphs for the healthy condition and six defect locations in the conductor and insulation screens (defect diameter: 2 mm) are shown in Fig. 4.11. Figure 4.12 evaluates the effect of the number of zeroes considered on estimation accuracy. Five zeroes were sufficient to achieve stable accuracy, as shown in Table III. Impedance plots for different defect diameters (2 mm, 4 mm, 6 mm) are illustrated in Fig. 4.13.

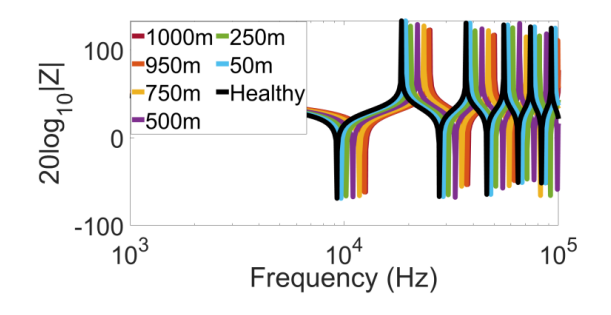


Figure 4.11 Impedance plots for the simulated cable with defects (diameter: 2 mm).

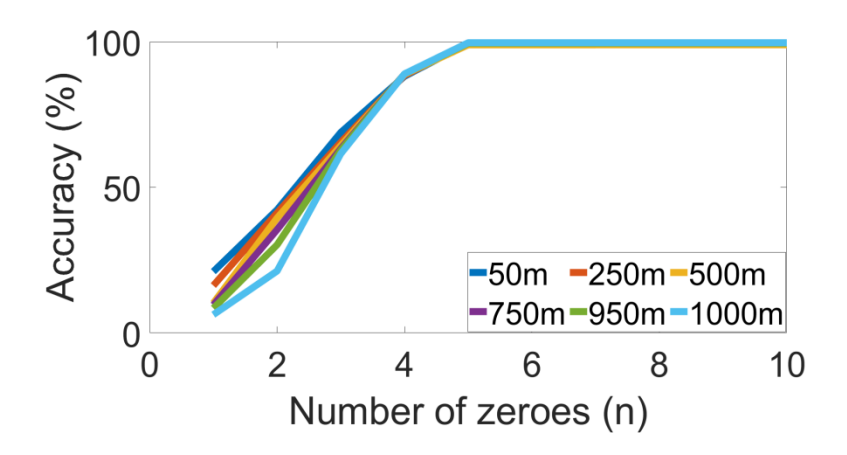


Figure 4.12 Accuracy with varying numbers of zeroes for defect location estimation.

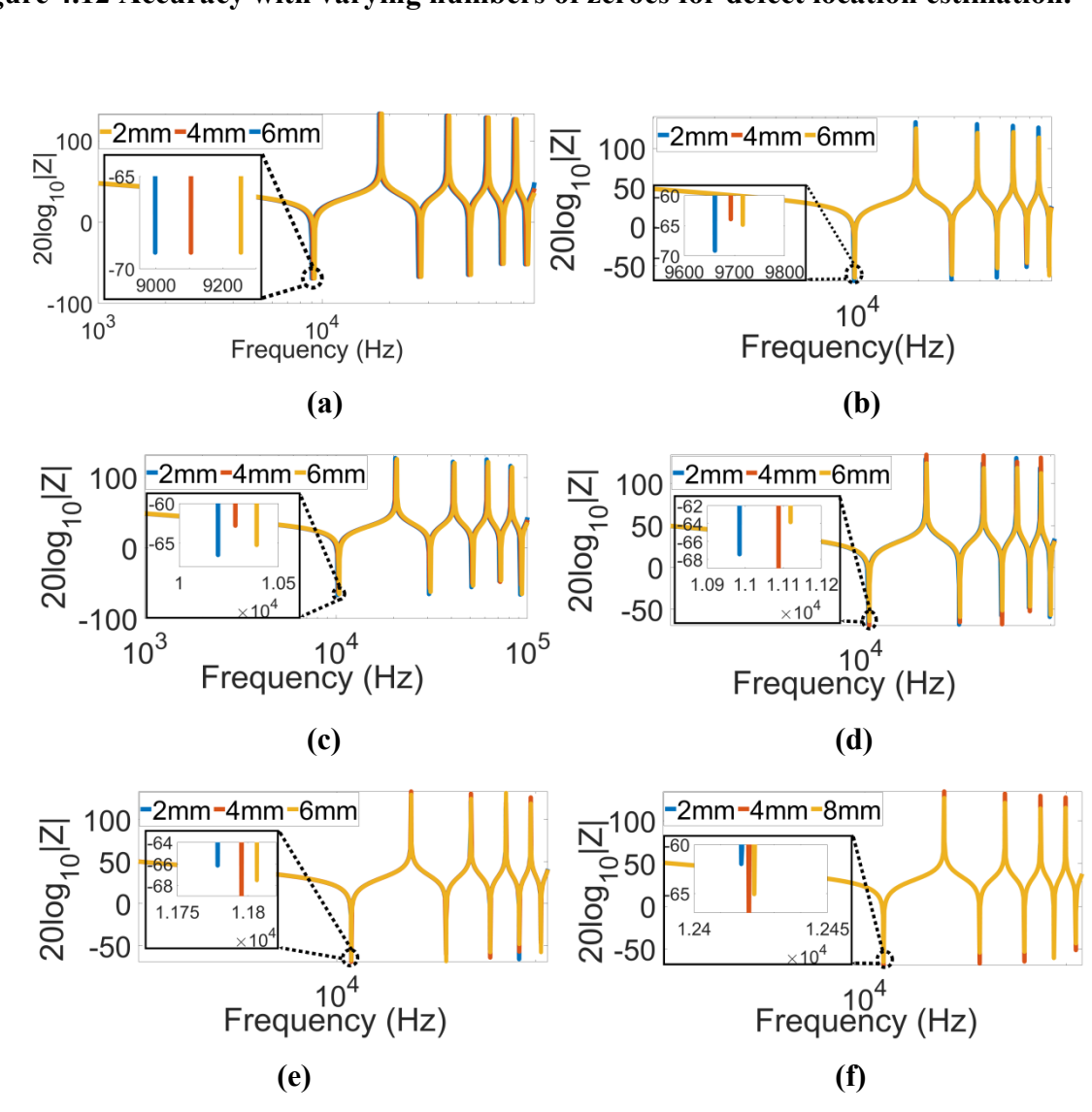


Figure 4.13 Impedance plots for different screen defect diameters at: (a) 50 m, (b) 250 m, (c) 500 m, (d) 750 m, (e) 950 m, (f) 1000 m.

Table 4.3 Accuracy to detect defect in a simulated cable

	Table 4.3 Accuracy to detect defect in a simulated cable							
Location	Cases	Sum of	Product	Estimat	Estimated	Accuracy	Accuracy	
		zeroes	of zeroes	ed	location of	a/c to	a/c to	
(m)		of a	of a	location	defect as	(4.2)	(4.18) &	
<b>(</b> )		Defectiv	Defectiv	of	per (4.18)	(%)	(4.19)(%)	
		e cable	e cable	defect	& (o)	(,0)	(1.17)(70)	
		(MHz)	X	as per	(4.19)(m)			
			$10^{23}(Hz)$	(4.2)(m)				
50	Case-	0.3109	6.1080	49.4625	49.7521	98.9251	99.5042	
	Case- II	0.3910	6.1081	49.4311	49.6183	98.8622	99.2366	
	Case- III	0.3910	6.1082	49.3124	49.4542	98.6248	98.9084	
250	Case-	0.3759	7.1376	246.064 5	248.6141	98.4258	99.4456	
	Case- II	0.3760	7.1377	245.542 0	248.0916	98.2168	99.2366	
	Case-	0.3761	7.1377	245.223	247.7735	98.0895	99.1094	
	III			9				
500	Case-	0.4738	7.6390	494.762	497.3124	98.4625	98.9525	
300	I	0.4730	7.0370	8	777.5124	70.4023	70.7323	
	Case-	0.4739	7.6391	494.269	496.8193	00 2620	00 0520	
		0.4/39	7.0391		490.8193	98.3638	98.8539	
	II	0.4720	7.6201	7	407 1022	00.5065	00.2277	
	Case-	0.4739	7.6391	493.633	496.1832	98.7267	99.2366	
	III			6				
750	Case-	0.6114	8.1714	743.790	746.3399	99.1720	99.5119	
	I			3				
	Case-	0.6114	8.1715	743.315	745.8651	99.1087	99.4486	
	II			5				
	Case-	0.6115	8.1716	742.679	745.2290	99.0239	99.3638	
	III		0.12, 20	4				
950	Case-	0.7501	8.6031	942.708	945.2577	99.2324	99.5008	
930	T Casc-	0.7301	8.0031	1	943.2377	<i>99.232</i> <del>4</del>	<i>99</i> .3000	
	<u> </u>	0.7502	0.6022	042 106	044 (5(4	00.1601	00 4275	
	Case-	0.7502	8.6032	942.106	944.6564	99.1691	99.4375	
	II	0.5500	006.00	8	044.0202	00.1051	00.050	
	Case-	0.7503	806.33	941.470	944.0203	99.1021	99.3705	
	III			7				
1000	Case-	0.7793	8.6417	994.941	996.5738	99.4941	99.6574	
	I			1				
	Case-	0.7794	8.6418	992.393	995.1124	99.2393	99.5112	
	II			2				
	Case-	0.7795	8.6418	991.119	994.00290	99.1119	99.4003	
	III	0.1193	0.0710	3	777.00230	77.1117	77.7003	
	111			3				

Sum and product of five zeroes for a single defect were 0.3142 Mhz and  $5.4365 \times 10^{23} \text{ Hz}$ 

(Eq. 4.2), closely matching state-space results 0.3144 MHz and  $5.4378 \times 10^{23} \text{ Hz}$ . Table 4.3 presents the estimated locations of screen defects for six different positions and three defect diameters (2 mm, 4 mm, and 6 mm), along with their corresponding accuracy. The proposed method achieves an accuracy of at least 98.09%, even in cables with joints.

#### 4.4.5 Multi-point Defects in Simulated Conductor Screens

For two conductor defects (2 mm diameter) at 3 m and 5 m, and one larger defect (6 mm) at 1000 m, the sum and product of five zeroes were 0.3356MHz and  $1.0214 \times 10^{24}$  Hz, respectively, as shown in Fig. 4.14. The deviation factor ( $\partial$ ) for multi-defects was 0.8116 (Eq. 4.2) and 0.8191 (state space), compared to 1.0003 and 1.0005 for a single defect at the cable's end. These results further validate equations (4.28).

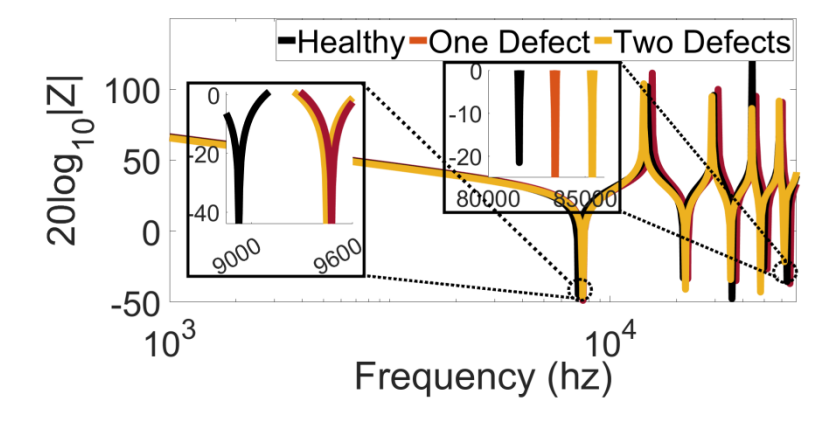


Figure 4.14 Impedance plots for two conductor defects (3 m and 5 m) and one defect at 1000 m.

The analysis confirms the effectiveness of the proposed method in identifying defect locations in both experimental and simulated cables, regardless of defect size or position.

### Chapter 5

# **Estimating the Location of Sheath to Ground Fault** in a Cross-Bonded Power Cable

In this chapter, the estimation of the location of sheath-to-ground (SG) fault in a cross-bonded (CB) HVAC power cable at any arbitrary location during online conditions is explained in detail. One experimental study along with one on-field case study is presented to validate the proposed methodology. The location of the SG fault is estimated by using the analytical formulae which are derived from the proposed circuit model of the cable. The details are explained below.

# **5.1** Analytical Formulae For Grounding Current in a CB Power Cable During Healthy Condition.

The laying of the CB cable is configured in a trefoil formation as shown in Fig. 5.1. The schematic diagram of a major section of CB cable is shown in Fig. 5.2.  $L_1$ ,  $L_2$ , and  $L_3$  are the lengths of the three minor sections named as  $R_j$ ,  $Y_j$ , and  $B_j$  (j= 1, 2, and3 representing each minor section), interconnected with SVLs in the link box to form three loops:  $R_1$ - $Y_2$ - $B_3$  (loop 1),  $Y_1$ - $B_2$ - $R_3$  (loop 2), and  $B_1$ - $R_2$ - $Y_3$  (loop 3).  $V_R$ ,  $V_Y$ , and  $V_B$  are the three-phase source voltages and  $RL_R$ ,  $RL_Y$ , and  $RL_B$  are the loads of each phase. The metallic sheath of each phase is grounded at the grounding box through grounding resistances ( $RG_1$ ,  $RG_2$ ,  $RG_1'$ ,  $RG_2'$ ,  $RG_1''$  and  $RG_2''$ )

The circuit model of a major section CB cable is shown in Fig. 5.3.  $Z_{ci}$ ,  $Z_{si}$   $C_{i}$ , and  $G_{i}$ , are the conductor impedance, sheath impedance, insulation capacitance, and conductance respectively (throughout this chapter, i=1, 2, 3 for three different phases). In this chapter, it is assumed that the condition of the insulation of the cable will remain unchanged throughout the length of the cable, during measurement. The per unit capacitance (C) and impedance of the metallic sheath ( $Z_{S}$ ) in each minor section can be obtained analytically as:

$$C_{\rm i} = \frac{55.63 \times 10^{-12} \times \varepsilon_r}{\ln\left(\frac{r_{\rm is}}{r_{\rm c}}\right)} \,\text{F/m} \tag{5.1}$$

$$Z_{\rm Si} = R_{\rm Si} + j\omega (L_{\rm Si} + M_{\rm CSi} + M_{\rm SSi}) \,\Omega/m \tag{5.2}$$

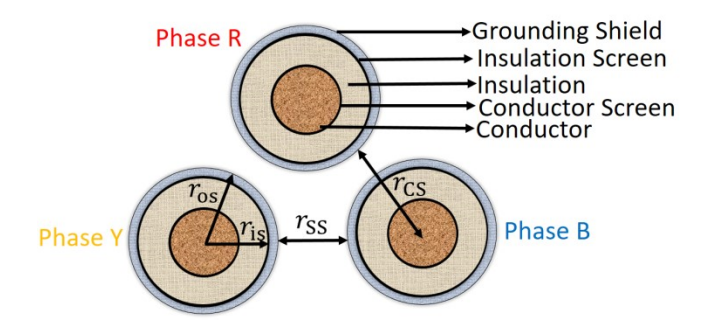


Figure 5.1 Schematic diagram of a trefoil laying cable configuration.

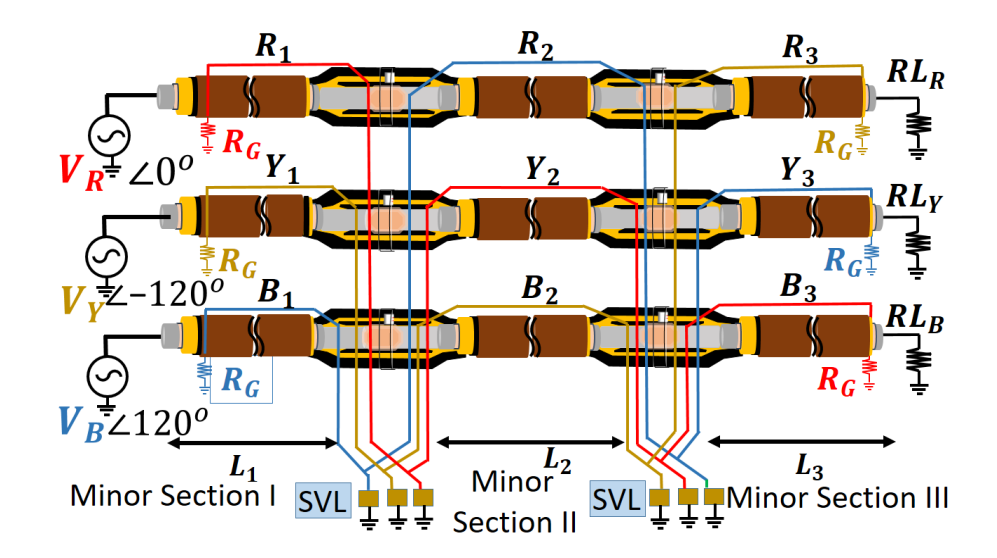


Figure 5.2 Schematic diagram of a major section in a CB cable.

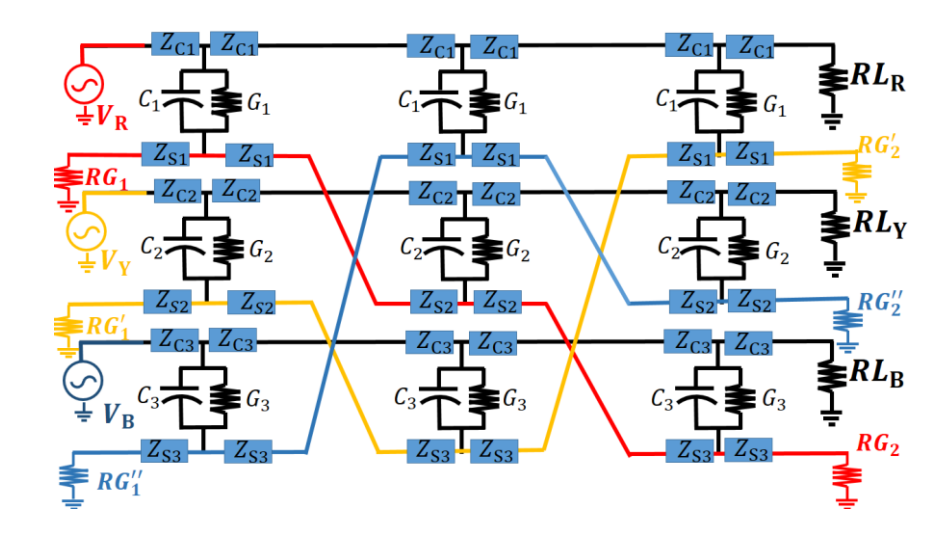


Figure 5.3 Circuit model of a major section CB cable.

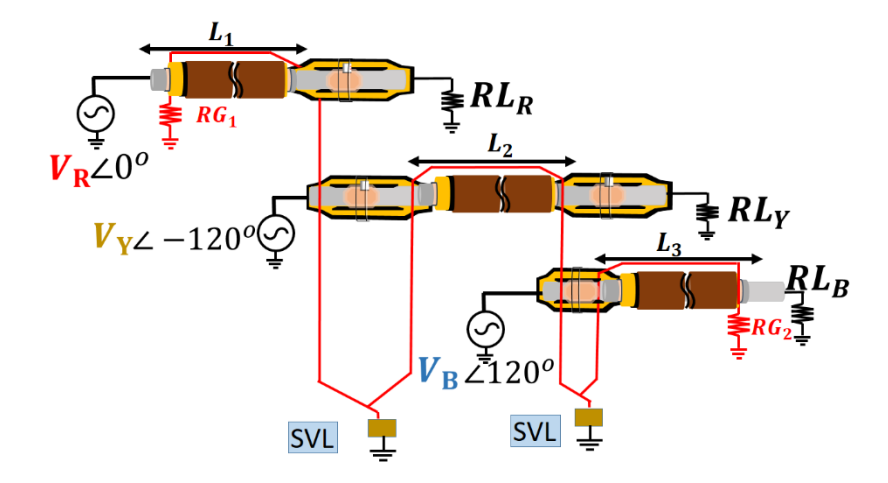


Figure 5.4 Schematic diagram of loop 1 (R<sub>1</sub>-Y<sub>2</sub>-B<sub>3</sub>) in a major section.

In (5.1) and (5.2),  $\varepsilon_r$  is the relative permittivity of the insulating material,  $r_c$  is the conductor radius,  $R_s$  is the resistance of the sheath and  $L_s$  is the self-inductance of the sheath caused by the circulating current,  $M_{CS}$  and  $M_{SS}$  are the mutual inductance between the current-carrying conductor in each phase to the measuring sheath and the mutual inductance between other phase sheaths to the measuring sheath. The analytical formula to obtain each of the above-mentioned terms for a trefoil formation of the cable is [62]:

$$R_{\rm s} = \frac{k_{\rm r} \left(1 + k_{\rm t} (T - 20)\right)}{\pi \left((r_{\rm os})^2 - (r_{\rm is})^2\right)} \ \Omega/{\rm m}, \quad L_{\rm s} = 2 \times 10^{-7} \ln\left(\frac{2}{r_{\rm os} + r_{\rm is}}\right) \, {\rm H/m}$$
 (5.3)

$$M_{\rm cs} = 2 \times 10^{-7} \ln \left( \frac{\sqrt[3]{2}}{r_{\rm cs}} \right) \text{H/m}, M_{\rm ss} = 2 \times 10^{-7} \ln \left( \frac{\sqrt[3]{2}}{r_{\rm ss}} \right) \text{H/m}$$
 (5.4)

In the above formulae  $k_r$ ,  $k_t$ , and T are the metal sheath resistivity, temperature, and ambient temperature respectively.  $r_{os}$  and  $r_{is}$  are the inner and outer radius of the metallic sheath, and  $r_{cs}$  and  $r_{ss}$  are the average distance between the conductor of one phase to the sheath of the calculating phase and the sheath of one phase to the sheath of the calculating phase respectively. From the above-mentioned analytically obtained electrical parameters, the sheath circulating current for a particular loop can be obtained analytically as below.

#### 5.1.1 Inductive current in the metallic sheath

In each phase and minor section, the current in the conductor of different phases and sheath produces magnetic flux in the measuring phase. This magnetic flux links the metallic sheath and produces a pseudo voltage due to Maxwell laws of electromagnetism, and due to the presence of a closed surface in the metallic sheath (grounded at both ends of a major section),

an inductive circulating current will flow in the sheath, and it is represented as a voltage-controlled current source as shown in Fig. 5.5.

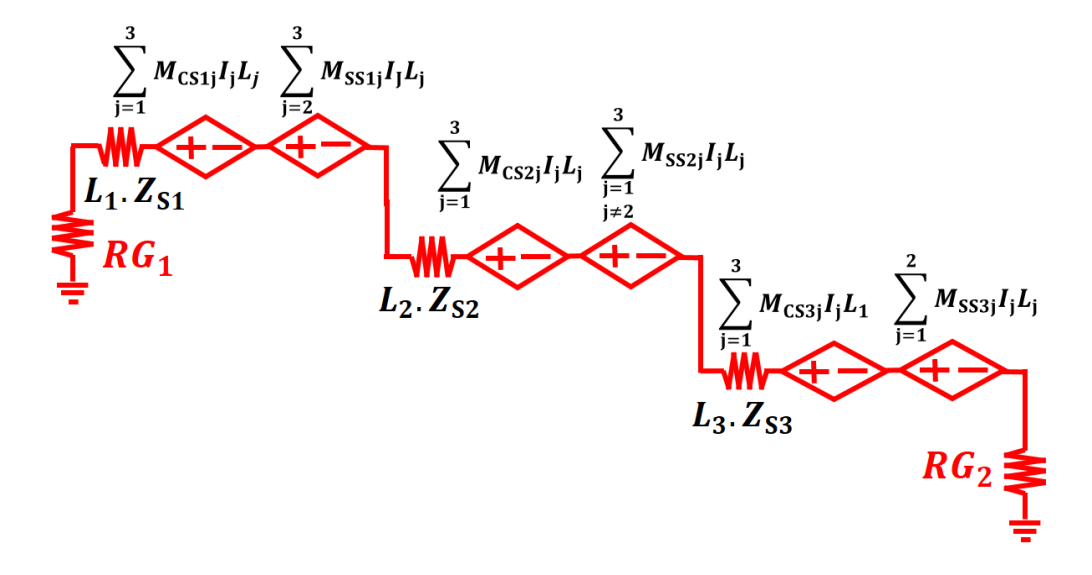


Figure 5.5 Equivalent circuit for inductive current in loop 1.

The inductive current in the grounding resistance is obtained using Krichoffs voltage law (KVL) and is represented as:

$$I_{\rm m} = \frac{(M_{\rm eq}I_{\rm eq}L_{\rm eq})}{(RG_2 + Z_{\rm S}L_{\rm eq} + RG_1)}$$
(5.5)

Where,

$$Z_{S}L_{eq} = Z_{S1}L_{1} + Z_{S2}L_{2} + Z_{S3}L_{3}, \quad \text{and} \quad M_{eq}I_{eq}L_{eq} = (\sum_{j=1}^{3} M_{CS1j}I_{j}L_{j} + M_{CS2j}I_{j}L_{j} + M_{CS3j}I_{j}L_{j}) + (\sum_{j=2}^{3} M_{SS1j}L_{j}I_{j} + \sum_{j=1}^{3} M_{SS2j}L_{j}I_{j} + \sum_{j=1}^{2} M_{SS3j}L_{j}I_{j})$$

$$(5.6)$$

#### 5.1.2 Capacitive current in the metallic sheath

The phase voltage in each minor section is responsible for the capacitive current in the metallic sheath. The analytical relation between the per-phase voltage (V) and per-unit capacitive current  $(I_C)$  in the metallic sheath is  $I_{Ci} = j\omega C_i V_i$ , Therefore for loop 1, it is represented by the voltage control current source. The capacitive current flows out from the middle of each section [47] as shown in Fig. 5.4.

The capacitive current through grounding resistance  $RG_1$  and  $RG_2$  as  $I_{CRG1}$  and  $I_{CRG2}$  is obtained using Krichoff's current law (KCL) and is represented as:

$$I_{\text{CRG1}} = \frac{\binom{I_{\text{C1}}(Z_{\text{S3}}L_3 + Z_{\text{S2}}L_2 + \frac{Z_{\text{S1}}L_1}{2} + RG_2) + I_{\text{C2}}(Z_{\text{S3}}L_3 + \frac{Z_{\text{S2}}L_2}{2} + RG_2) + }{\binom{I_{\text{C2}}(Z_{\text{S3}}L_3 + RG_2)}{2}}$$

$$\frac{I_{\text{CRG1}} = \frac{\binom{I_{\text{C1}}(Z_{\text{C3}}L_3 + Z_{\text{S2}}L_2 + RG_2) + I_{\text{C2}}(Z_{\text{C3}}L_3 + RG_2) + I_{\text{C2}}(Z_{\text{C3}}L_3 + RG_2) + I_{\text{C2}}(Z_{\text{C3}}L_3 + RG_2) + I_{\text{C3}}(Z_{\text{C3}}L_3 + RG_2) + I_{\text{C3}}(Z$$

$$I_{\text{CRG2}} = \frac{\binom{I_{\text{C1}}\left(\frac{Z_{\text{S1}}L_{1}}{2} + RG_{1}\right) + I_{\text{C2}}\left(Z_{\text{S1}}L_{1} + \frac{Z_{\text{S2}}L_{2}}{2} + RG_{1}\right) +}{I_{\text{C3}}\left(Z_{\text{S1}}L_{1} + Z_{\text{S2}}L_{2} + \frac{Z_{\text{S3}}L_{3}}{2} + RG_{1}\right)}}{\binom{RG_{2} + Z_{\text{S}}L_{eq} + RG_{1}}{2}}$$
(5.8)

In equations (5.5)-(5.8), the value of each term can be analytically obtained using (5.2)-(5.4). Therefore the total circulating current ( $I_{cc}$ ) in healthy conditions flowing through the grounding resistances  $RG_1$  and  $RG_2$  demonstrated as  $I_{ccRG1}$  and  $I_{ccRG2}$  respectively can be analytically obtained as:

$$I_{\text{ccRG1}} = I_{\text{m}} + I_{\text{CRG1}}, \qquad I_{\text{ccRG2}} = I_{\text{m}} + I_{\text{CRG2}}$$
 (5.9)

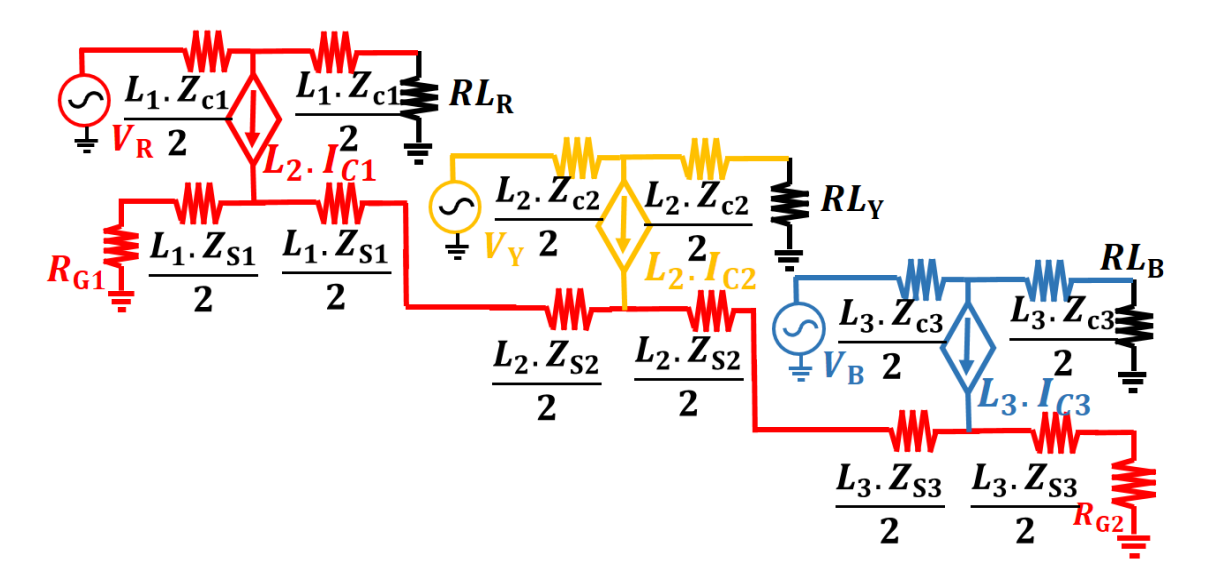


Figure 5.6 Equivalent circuit for capacitive current in loop 1.

The above-mentioned analytical formula (5.9), will only match with practical measurements when the load is connected with the source with a single CB. However, whenever there is simultaneous CB as shown in Fig 5.7, then the measuring grounding current ( $I_{\rm msrd1}$  and  $I_{\rm msrd2}$ ) for a particular loop in the major section II will be the simultaneous circulating current ( $I_{\rm ccRG1S}$  and  $I_{\rm ccRG2S}$  from the simultaneous previous and succeeding major sections respectively) subtracted from the actual circulating current in the major section II. Therefore, from Fig. 5.7, the measuring grounding current of  $RG_1$  and  $RG_2$  in the major section II would be:

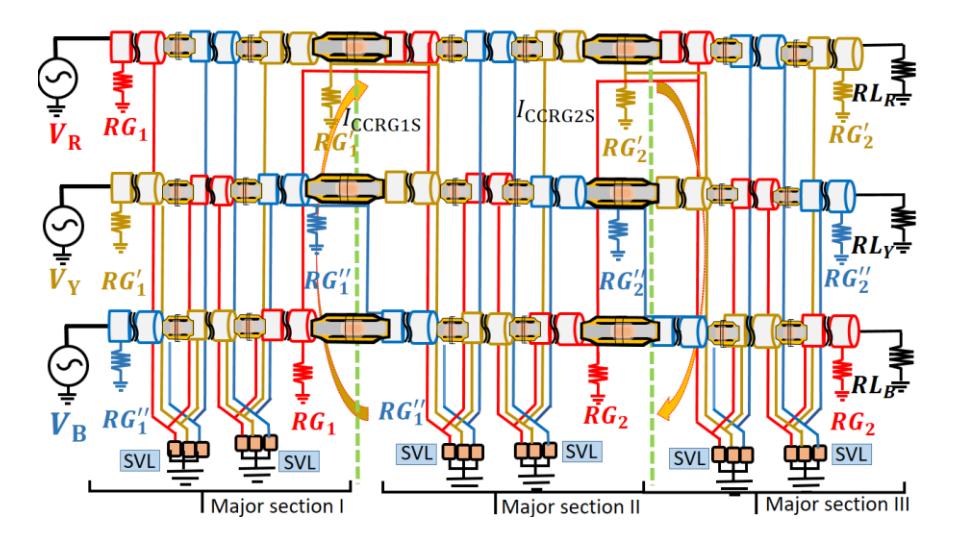


Figure 5.7 Schematic diagram of three simultaneous major sections.

$$I_{\text{msrd1}} = I_{\text{ccRG1}} - I_{\text{ccRG1S}}, \quad I_{\text{msrd2}} = I_{\text{ccRG2}} - I_{\text{ccRG2S}}$$
 (5.10)

 $I_{\text{ccRG1S}}$  and  $I_{\text{ccRG2S}}$  are the analytically obtained simultaneous circulating current flowing in the major sections I and III and can be obtained similarly to  $I_{\text{ccRG1}}$  and  $I_{\text{ccRG2}}$  using (5.9).

#### 5.2 Analytical formulae for the location of the SG fault

In this section, the analytical range of the sheath fault current for the SG fault at each minor section is obtained and its location is estimated through proposed analytical formulae. Whenever any part of this metallic sheath comes in contact with the ground it causes changes in the inductive and capacitive circuit which causes fault current ( $I_{ccRG1}$  and  $I_{ccRG2}$ ) to flow between the fault location and two grounding resistance  $RG_1$  and  $RG_2$ . as shown in Fig 5.8. This fault current will be different when compared with the healthy case.

The simulated results for faults at different locations in a major section of a CB cable are shown in Fig. 5.8 (b). The dimensions and electrical properties of the cable are the same as in Case: I of the practical case mentioned in Section IV, with three minor sections of length 500m each. As shown in Fig. 5.8 (b), the ranges for both  $I_{RG1}$  and  $I_{RG2}$  will be unique, for SG faults at different minor sections, since the grounding current depends on the per unit impedance (5.1), (5.3), and (5.4), and for a particular minor section, the grounding current is governed by the particular phase current and voltage. Range of  $I_{RG1}$  and  $I_{RG2}$  values was obtained analytically by applying a KVL and KCL between both the grounding resistance and SG fault. The measured ground current of both the resistance was compared with the analytically obtained range of values. If the measured value is not in any of the analytically obtained ranges or matches with the healthy values of current (5.9) then the particular loop

does not have an SG fault. The equations are further solved to obtain the pinpoint locations of the SG fault. To facilitate the calculation, the distance from the source to the fault is considered to be x for the particular minor section, whereas from the fault location to the load is considered to be  $L_i - x$ , here i = 1, 2, and 3 represents the length of the minor sections as shown in Fig. 5.8.

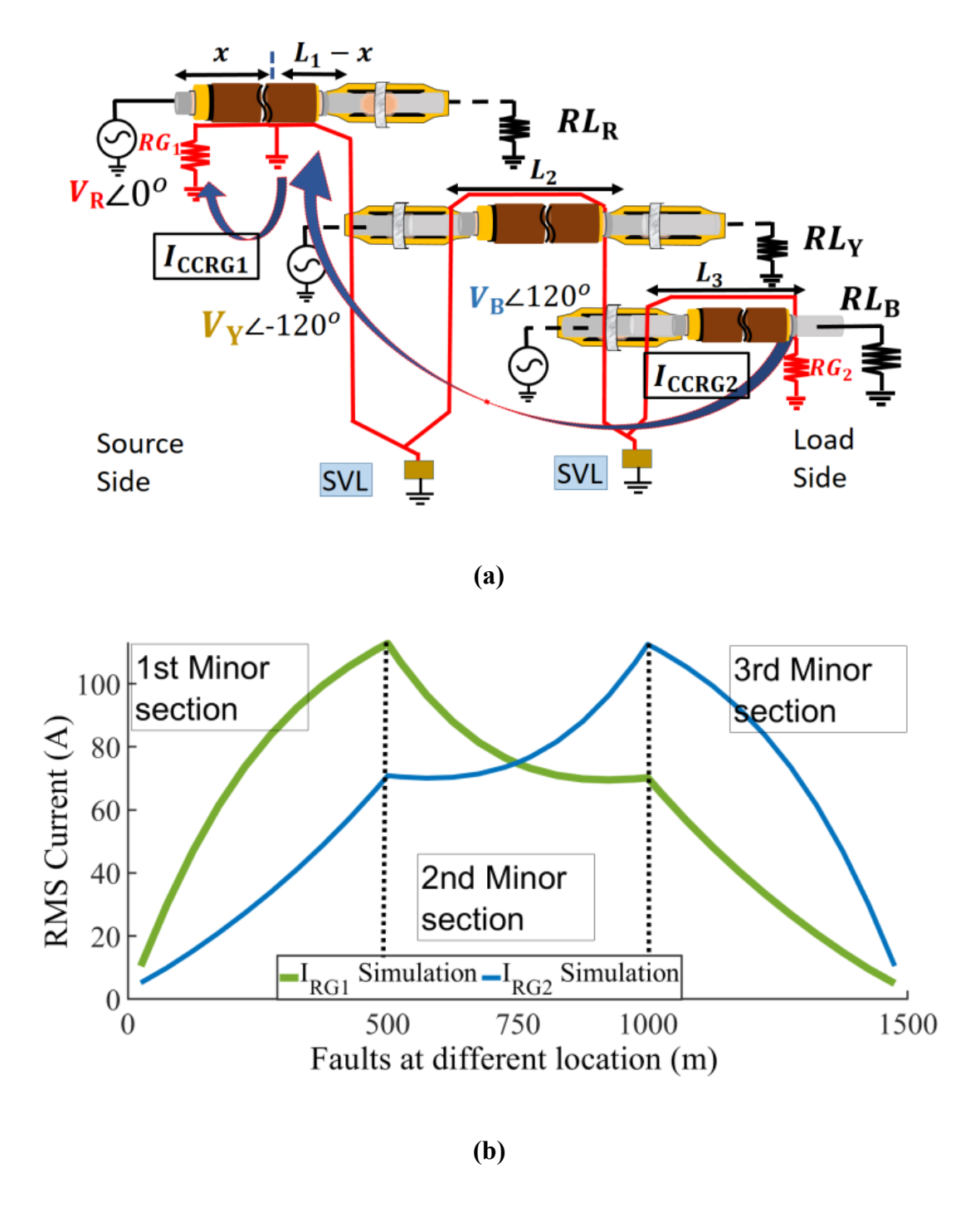


Figure 5.8 (a) Schematic diagram for SG fault in loop 1 (b) Grounding currents for fault at different locations.

#### 5.2.2 Sheath fault at first minor section

The equivalent circuit for inductive and capacitive current for an SG fault at the first minor section is shown in Fig. 5.9. To obtain the maximum and minimum value of  $I_{RG1}$  and  $I_{RG2}$  for an SG fault at the first minor section, the maximum and minimum value of x is considered ( $0 \le x < L_1$ ). The range of values of the grounding currents for the sheath fault at the first minor section is expressed as:

$$I_{\text{RG1}} = \left[0, \frac{I_{\text{C1}} Z_{\text{S1}} L_1 + 2(\sum_{j=1}^{3} M_{\text{CS1}j} I_j L_j + \sum_{j=2}^{3} M_{\text{SS1}j} L_j I_j)}{2(Z_{S1} L_1 + RG_1)}\right)$$
(5.11)

$$I_{\text{RG2}} = \left[\frac{(M_{\text{eq}}L_{\text{eq}}I_{\text{eq}}) + Z'I'}{ZL_{\text{eq}} + RG_2}, \frac{(M_{2,3}L_{2,3}I_{2,3}) + Z''I''}{ZS_2L_2 + ZS_3L_3 + RG_2}\right)$$
(5.12)

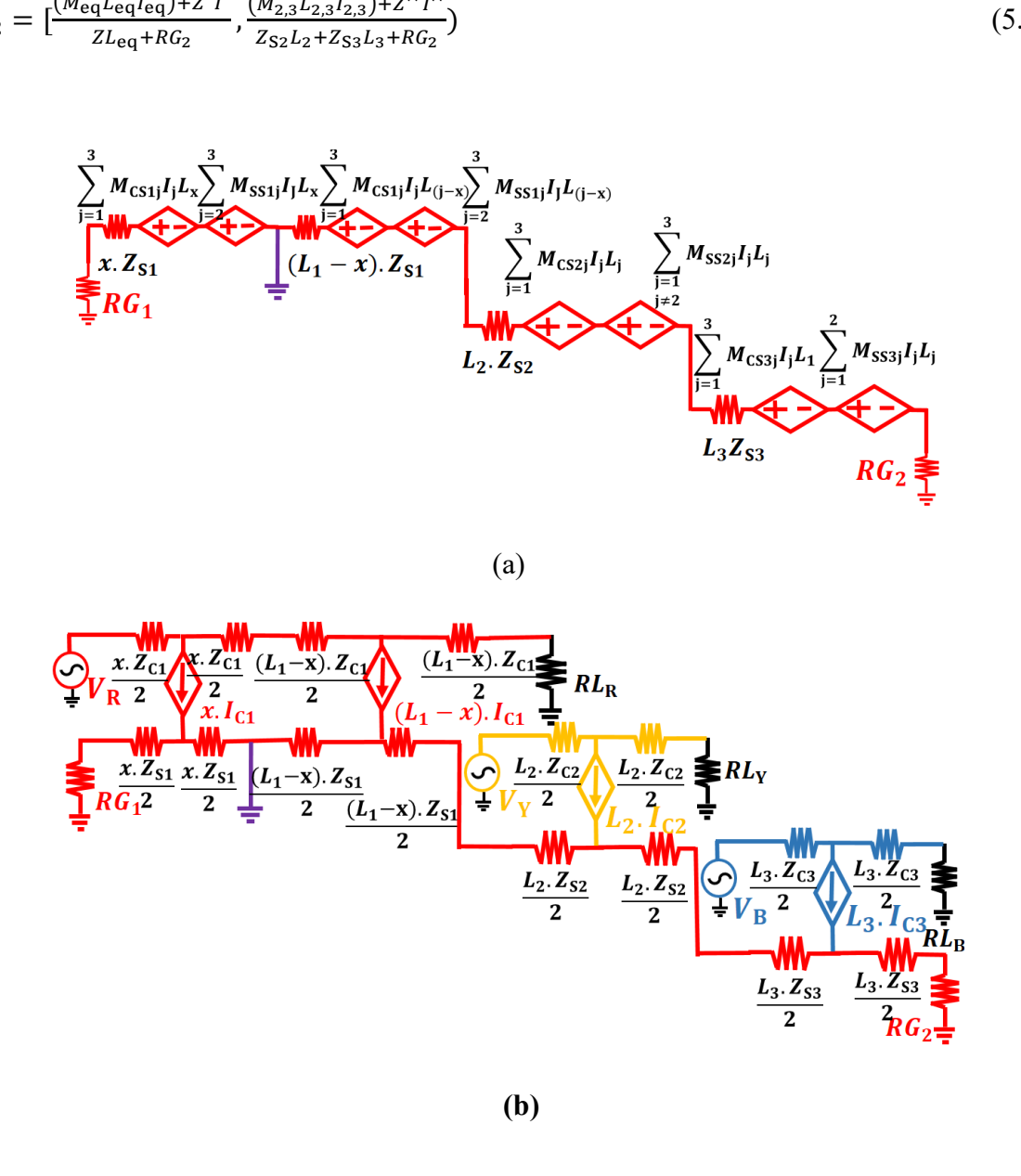


Figure 5.9 Equivalent circuit for an SG fault (a) inductive current (b) capacitive current in first minor section.

In the above formulae,

$$\begin{split} Z'I' &= \frac{I_{\text{C1}}Z_{\text{S1}}L_{1}}{2} + I_{\text{C2}}\left(Z_{\text{S1}}L_{1} + \frac{Z_{\text{S2}}L_{2}}{2}\right) + I_{\text{C3}}\left(Z_{\text{S1}}L_{1} + Z_{\text{S2}}L_{2} + \frac{Z_{\text{S3}}L_{3}}{2}\right), \\ \sum_{\text{i=2,j=1}}^{i=3,j=3} M_{\text{CSij}}I_{\text{j}}L_{\text{j}} + \sum_{\text{i=2,j=1}}^{i=3,j=3} M_{\text{SH3j}}I_{\text{j}}L_{\text{j}} \text{ , and } Z''I'' = I_{\text{C2}}\left(\frac{Z_{2}L_{2}}{2}\right) + I_{\text{C3}}\left(Z_{2}L_{2} + \frac{Z_{3}L_{3}}{2}\right) \end{split}$$

The equation corresponding to Fig. 5.9 is further solved to obtain the location of x (location of sheath fault) for both  $I_{RG1}$  and  $I_{RG2}$  values. The location of SG fault a/c to  $I_{RG1}$  is:

$$\chi = \frac{I_{RG1}RG_1}{\sum_{j=1}^{3} M_{CS1j}I_j + \sum_{j=2}^{3} M_{SS1j}I_j - I_{RG1}Z_{S1} + I_{C1}}$$
(5.13)

The location of SG fault a/c to  $I_{RG2}$  (considering the positive value of x) is:

$$x = \frac{-\alpha' + \sqrt{(\alpha')^2 - 4I_{C1}\beta'}}{I_{C1}}$$
 (5.14)

In the above formulae,

$$\alpha' = Z_{S1}I_{RG2} - (I_{C1}Z_1 + I_{C2}Z_2 + I_{C3}Z_3) - \sum_{j=1}^{3} M_{CS1j}I_j + \sum_{j=2}^{3} M_{SS1j}I_j, \text{ and } \beta' = Z'I' + M_{eq}L_{eq}I_{eq} - I_{RG2}(RG_2 + Z_SL_{eq}).$$

#### 5.2.2 Sheath fault at second minor section

The equivalent circuit for inductive and capacitive current for a SG fault at the second minor section is shown in Fig. 5.10.

Maximum and minimum values of  $I_{RG1}$  and  $I_{RG2}$  are obtained by substituting the value of x as  $0 \le x < L_2$ . The range of values of the ground currents for the sheath fault at the second minor section is expressed as:

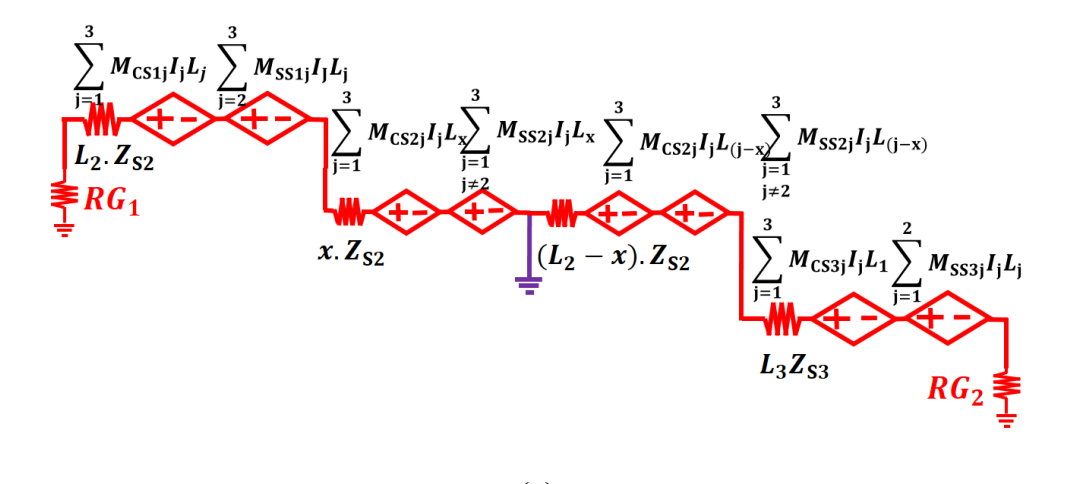
$$I_{\text{RG1}} = \left[\frac{I_{\text{C1}}Z_{\text{S1}}L_1 + 2(\sum_{j=1}^{3} M_{\text{CS1}j}I_jL_j + \sum_{j=2}^{3} M_{\text{SS1}j}L_jI_j)}{2(Z_{\text{S1}}L_1 + RG_1)}, \frac{M_{1,2}L_{1,2}I_{1,2} + Z'''I'''}{Z_{\text{S1}}L_1 + Z_{\text{S2}}L_2 + RG_1}\right)$$
(5.15)

$$I_{\text{RG2}} = \left[\frac{\left(M_{2,3}L_{2,3}I_{2,3}\right) + Z''I''}{Z_{S2}L_2 + Z_{S3}L_3 + RG_2}, \frac{2(\sum_{j=1}^{3} M_{\text{CS3}j}I_jL_j + \sum_{j=1}^{2} M_{\text{SS3}j}L_jI_j) + I_{\text{C3}}Z_{\text{S3}}L_3}{2(Z_{\text{S3}}L_3 + RG_2)}\right)$$
(5.16)

In the above formula,

$$Z'''I''' = \frac{I_{C1}Z_1L_1}{2}$$
, and  $M_{1,2}L_{1,2}I_{1,2} = \sum_{i=1,j=1}^{i=2,j=3} M_{CS1j}I_jL_j + \sum_{i=1,j=2,i\neq j}^{j=2,j=3} M_{SSij}I_jL_j$ 

The equation corresponding to Fig. 5.10. is further solved to obtain the location of x for both  $I_{RG1}$  and  $I_{RG2}$  values. The location of SG fault a/c to  $I_{RG1}$  (considering the positive value of x) is:



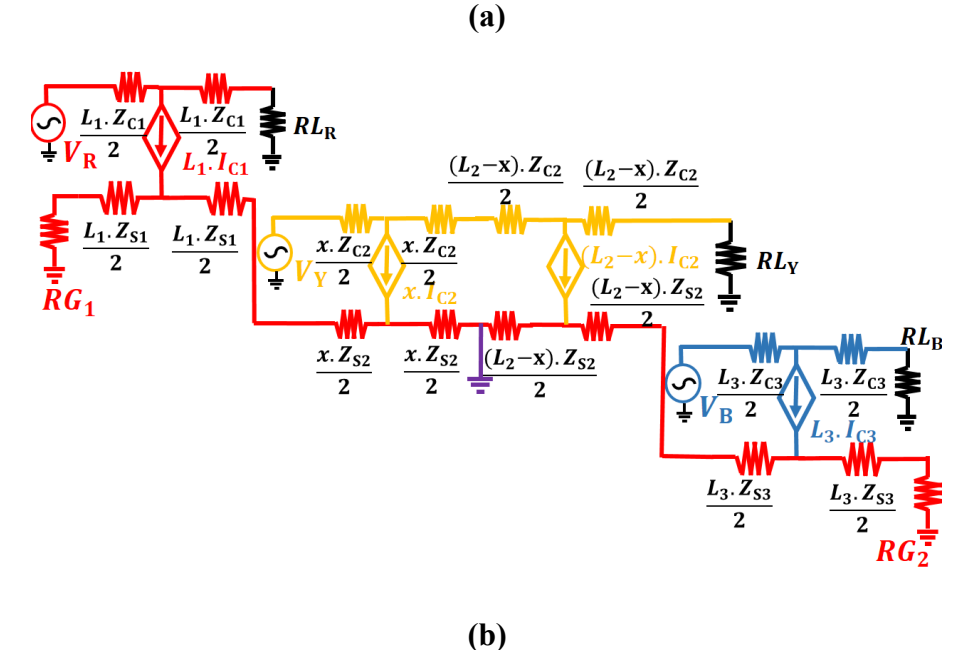


Figure 5.10 Equivalent circuit for an SG fault (a) inductive current (b) capacitive current in second minor section.

$$\chi = \frac{-\alpha'' + \sqrt{(\alpha'')^2 - 4 \cdot I_{C2} \cdot \beta''}}{2 \cdot I_{C2}}$$
 (5.17)

The location of SG fault a/c to  $I_{RG2}$  considering the positive value of x) is:

$$\chi = \frac{-\alpha''' + \sqrt{(\alpha''')^2 - 4 \cdot I_{C2} \cdot \beta'''}}{2 \cdot I_{C2}}$$
 (5.18)

In the above formula,

$$\alpha'' = I_{C1}Z_{S1} + \sum_{j=1}^{3} M_{CS2j}I_j + \sum_{\substack{j=1\\j\neq 2}}^{3} M_{SS2j}I_j - Z_{S2}I_{RG1}, \qquad \alpha''' = Z_{S2}I_{RG2} - (I_{C2}Z_2 + I_{C3}Z_{S3}) - \sum_{j=1}^{3} M_{CS2j}I_j + \sum_{\substack{j=1\\j\neq 2}}^{3} M_{SS2j}I_j, \qquad \beta'' = Z'''I''' + \sum_{j=1}^{3} M_{CS1j}I_jL_j + \sum_{j=2}^{3} M_{SS1j}L_jI_j - I_{RG1} - (RG_1 + Z_{S1}L_1), \text{ and } \beta''' = Z'''I''' + M_{2,3}L_{2,3}I_{2,3} - I_{RG2}(RG_2 + Z_{S2}L_2 + Z_{S3}L_3)$$

#### 5.2.3 Sheath fault at third minor section

The equivalent circuit for inductive and capacitive current for an SG fault at the third minor section is shown in Fig. 5.11. Maximum and minimum values of  $I_{RG1}$  and  $I_{RG2}$  are obtained by substituting the value of x as  $0 \le x < L_3$ . The range of values of the ground currents for the sheath fault at the second minor section is expressed as:

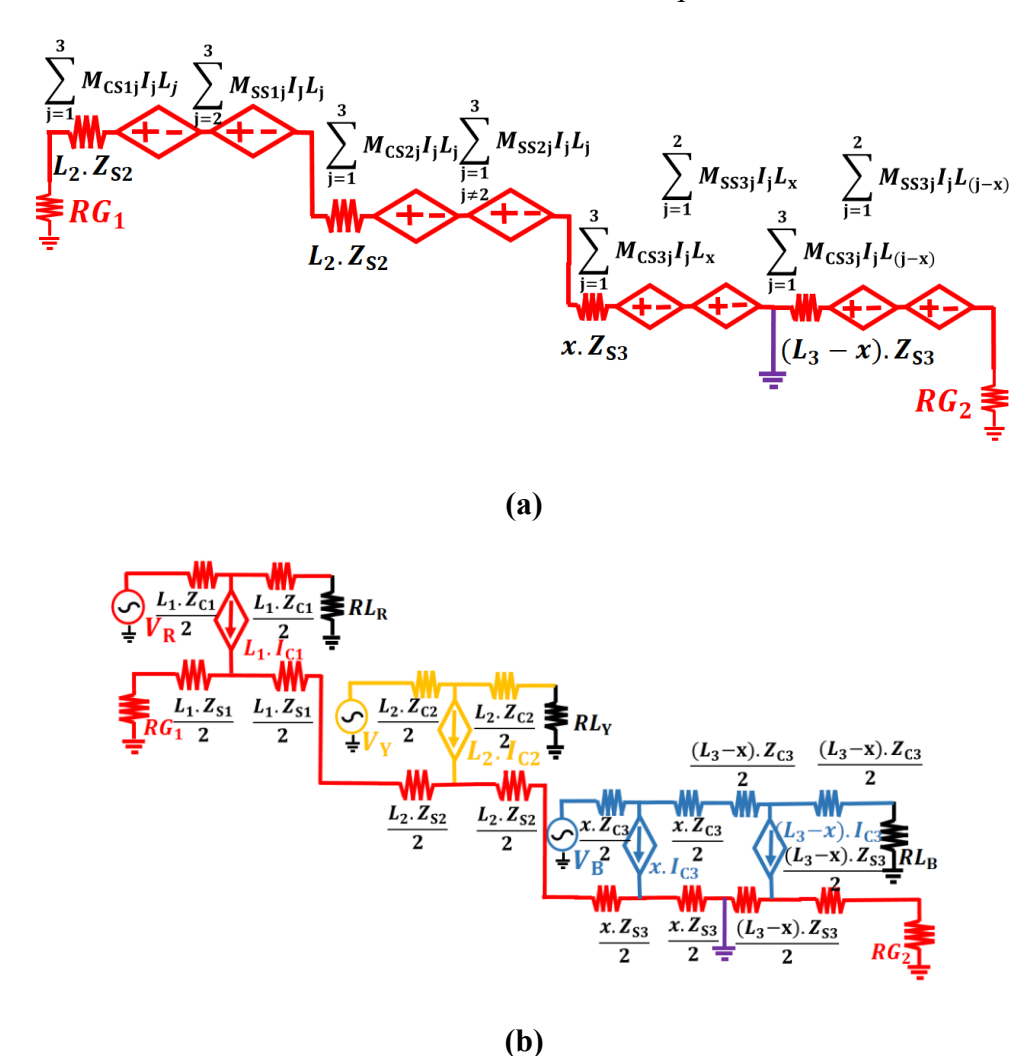


Figure 5.11 Equivalent circuit for an SG fault (a) inductive current (b) capacitive current in third minor section.

$$I_{\text{RG1}} = \left[\frac{\frac{M_{1,2}L_{1,2}I_{1,2} + Z^{iv}I^{iv}}{Z_{\text{S1}}L_{1} + Z_{\text{S2}}L_{2} + RG_{1}}}{RG_{1}}, \frac{\frac{M_{\text{eq}}I_{\text{eq}}L_{\text{eq}} + I_{\text{C1}}\left(\frac{Z_{\text{S1}}L_{1}}{2} + Z_{\text{S2}}L_{2} + Z_{\text{S3}}L_{3}\right) + I_{\text{C2}}\left(\frac{Z_{\text{S2}}L_{2}}{2} + Z_{\text{S3}}L_{3}\right) + I_{\text{C3}}\left(\frac{Z_{\text{S3}}L_{3}}{2}\right)}{RG_{1} + Z_{\text{SLeq}}}\right) (5.19)$$

$$I_{\text{RG2}} = \left[\frac{2(\sum_{j=1}^{3} M_{\text{CS3}j} I_j L_j + \sum_{j=1}^{2} M_{\text{SS3}j} L_j I_{j)} + I_{\text{C3}} Z_{\text{S3}} L_3}{2(Z_{\text{S3}} L_3 + RG_2)}, 0\right)$$
(5.20)

In the above formula,

$$Z^{iv}I^{iv} = \frac{I_{C1}Z_{S1}L_1}{2} + I_{C1}Z_{S2}L_2 + \frac{I_{C2}Z_{S2}L_2}{2}$$

The circuit shown in Fig. 5.11 is further solved to obtain the location of x for both  $I_{RG1}$  and  $I_{RG2}$  values. The location of SG fault a/c to  $I_{RG1}$  (considering the positive value of x) is

$$\chi = \frac{-\alpha^{iv} + \sqrt{(\alpha^{iv})^2 - 4 I_{C3} \cdot \beta^{iv}}}{2 I_{C3}}$$
 (5.21)

The location of SG fault a/c to  $I_{RG2}$  is:

$$x = \frac{2\left(\sum_{j=1}^{3} M_{\text{CS3}j} I_j L_j + \sum_{j=1}^{2} M_{\text{SH3}j} L_j I_j\right) + I_{\text{C3}} - 2I_{\text{RG2}}(RG_2 + Z_{\text{S3}}L_3)}{I_{\text{C3}} + 2\left(\sum_{j=1}^{3} M_{\text{CS3}j} I_j + \sum_{j=1}^{2} M_{\text{SS3}j} I_j\right) - 2I_{\text{RG2}}Z_{\text{S3}}}$$
(5.22)

In the above formula,

$$\alpha^{iv} = I_{C1}Z_{S1} + I_{C2}Z_{S2} + \sum_{j=1}^{3} M_{CS3j}I_j + \sum_{j=1}^{2} M_{SS3j}I_j - Z_{S3}I_{RG1}, \quad \text{and} \quad \beta^{iv} = Z^{iv}I^{iv} + M_{1,2}L_{1,2}I_{1,2} - I_{RG1}(RG_1 + Z_{S1}L_1 + Z_{S2}L_2)$$

The flowchart to estimate the location of SG fault in any arbitrary location is shown in Fig. 5.12.

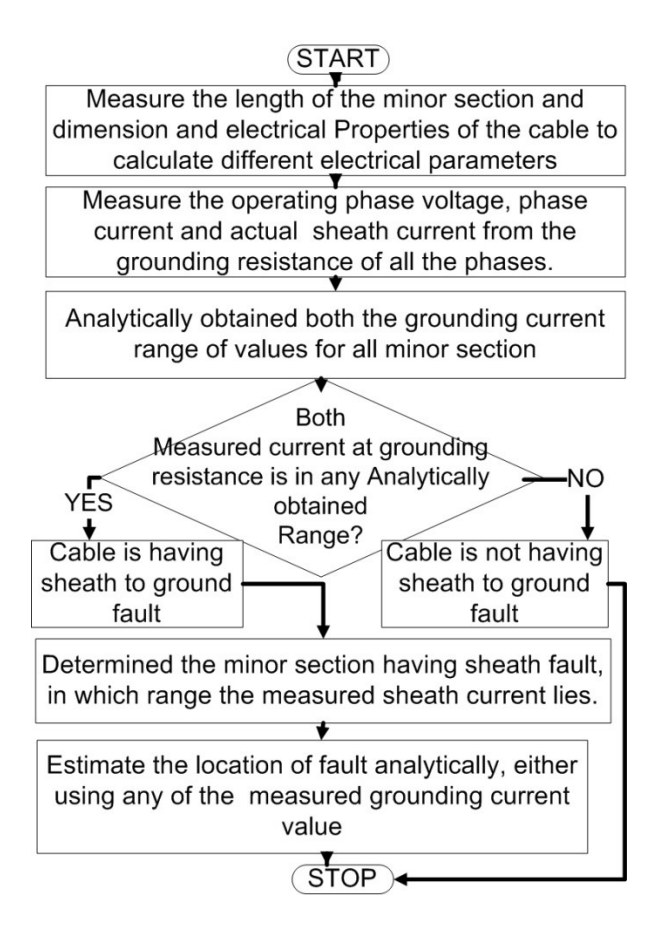


Figure 5.12 Flowchart to estimate the location of SG fault at any arbitrary location in a CB cable system during online condition.

In the following section, the above-mentioned formulae are verified by simulation as well as by experimental results for balanced as well as unbalanced conditions.

#### 5.3 Simulations and Experiments on CB Cable

Two experimental case studies were presented to verify the analytical results. In the first experimental study, commercial three-core, XLPE insulated material was selected, with an inner conductor (Aluminium) area of  $35mm^2$ , outer grounded sheath diameter of 7.35mm, the radius of the metallic sheath is 1mm, and insulation relative permittivity of 2.3. The cable is laid in a trefoil formation with  $r_{cs}$  and  $r_{ss}$  as 8cm and 10cm respectively. The value of  $RG_1$  and  $RG_2$  is kept at  $0.2\Omega$  respectively. The cable is supplied with a three-phase voltage of 440V and a load current of 15 A. The ground current is measured using a DSO and current probe whose uncertainty in measurement is 1.5%, and 1% respectively. CB of the sheath is performed using metallic wire as shown in Fig. 5.13.

To validate the analytical results seven different case studies are considered in this chapter, in which the first four case studies are for the balance condition (unity power factor and same minor section length) and the next three are the unbalanced conditions (load of different power factor or length of minor section or both) but maintaining voltage and current magnitude same. The faults are created using a grounding rod of magnitude 3 m $\Omega$ . To crossverify the analytical and experimental results, simulations are performed of the same dimension and fault location for all seven cases in MATLAB Simulink. These case studies are:

- i) Case Study 1: One major section considered between the source and the load. Three 6m long cables of the above-mentioned is CB (total sheath length of 18m), and faults are created at 0m, 3m, 6m, 9m, 12m, 15m, and 18m measuring from the source.
- ii) Case Study II:: Three major sections are considered between the source and the load. Each major section is 6m in length, and faults are created at 0m, 3m, 6m, 9m, 12m, 15m, and 18m in the middle major section.
- iii) Case Study III: Two major sections are considered between the source and the load. Each major section is 6m in length, and faults are created at 0m, 3m, 6m,

- 9m, 12m, 15m, and 18m at the first major section from the source end.
- *Case Study IV:* Similar to Case III, faults are at 0m, 3m, 6m, 9m, 12m, 15m, and 18m at the second major section from the source end.
- v) Case Study V: Similar to Case I, however, the power factor at three phases are 1, 0.9, and 0.85, while the magnitude of the current remains the same as a balanced case.
- vi) Case Study VI: One major section considered between the source and the load with unity power factor. Minor sections are 6m, 5m, and 4.5m in length, and faults are created at 0m, 3m, 6m, 8.5m, 11m, 13.5m, and 15.5m measuring from the source.
- vii) Case Study VII: Similar to CaseVI, however the power factor at three phases is 1, 0.9, and 0.85, while the magnitude of the current remains the same as a balanced case.



Figure 5.13 Experimental setup to estimate the location of the SG fault.

The second experimental case study was about a practical case that was reported by a local utility sector of the Mumbai sub-urban region of Maharashtra, India. The operating voltage and current in the CB cable are 220kV and 550A and the load is of unity power factor, having XLPE insulated material with a relative permittivity of 2.3 and thickness of 27mm. The conductor radius is 21mm and the metallic sheath is 6mm. The cable is laid in a trefoil

formation with  $r_{cs}$  and  $r_{ss}$  as 85cm and 115cm respectively. The value of  $RG_1$  and  $RG_2$  is 0.2 $\Omega$  respectively. The ground current is measured using a HIOKI 3196 power quality analyzer whose uncertainty in measurement is 0.5%. as shown in Fig. 5.14(a). The length of each minor section is 500m. The above-mentioned cable is reported to have an SG fault as shown in Fig. 5.14(b). The targeted major section is in between two major sections similar to case II, the single line diagram of the utility sector is shown in Fig. 5.14(c).

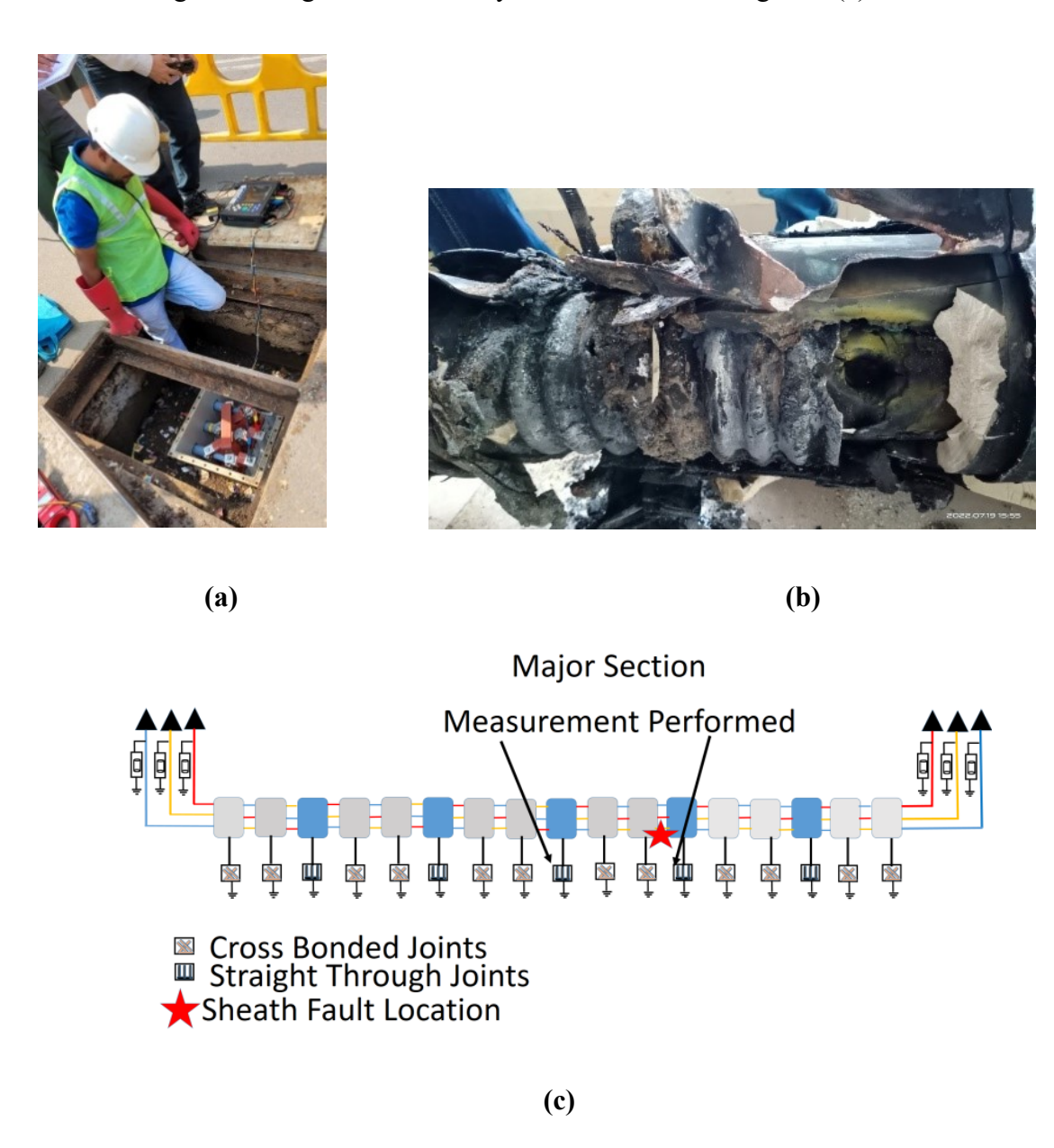


Figure 5.14 (a) Experimental setup to measure the grounding current to estimate the location of the SG fault on a filed case (b) SG fault in the cable (c) Single line diagram of the on field case study.

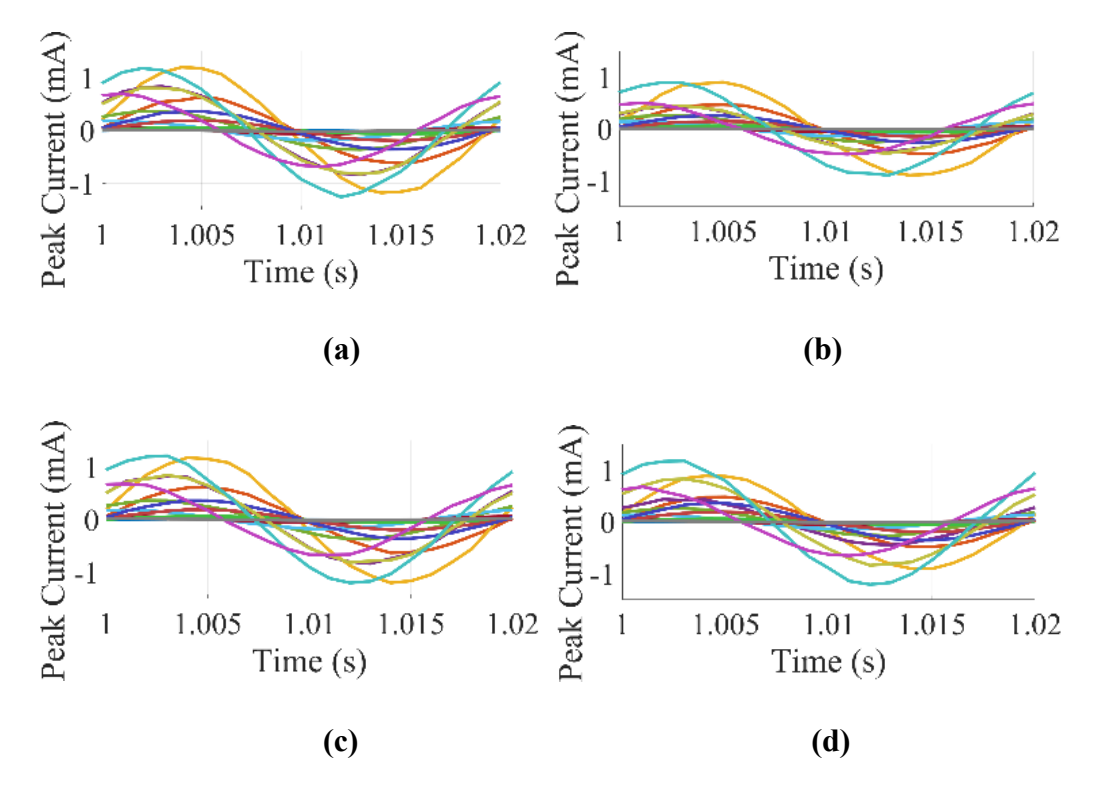
#### 5.4 Results and Discussions

In this section, the analytical, experimental, and simulation results are presented. The section is further divided into two subsections. At first, the estimation of the location of SG fault in the test cable, performed in the laboratory is presented, followed by an onfield case study as discussed in section IV is presented.

#### 5.4.1. Experimental results for SG fault location for the first experimental case study

Analytically obtained the range of grounding currents ( $I_{RG1}$  and  $I_{RG2}$ ) using (5.10)-(5.11), (5.14)-(5.15), and (5.18)-(5.19) for faults at different sections for seven different case studies is presented in Table 5.1. Measured current from DSO at  $RG_1$  and  $RG_2$  for faults at different locations is shown in Fig. 5.15, and the RMS value compared with practical results is shown in Fig. 5.16. After obtaining the measured current and comparing it with the range of values from Table I, the faults at the particular section are determined. Based on the particular section, (5.12) or (5.13), (5.16) or (5.17), (5.20) or (5.21) is applied to obtain its location. The accuracy of the proposed method for different case studies is shown in Table 5.2.

It can be seen that the SG faults for a test cable can be located with an uncertainty of  $\pm 0.08$ m, irrespective of the location of the fault, whether the fault is at the beginning, middle, or the end or balanced or unbalanced condition.



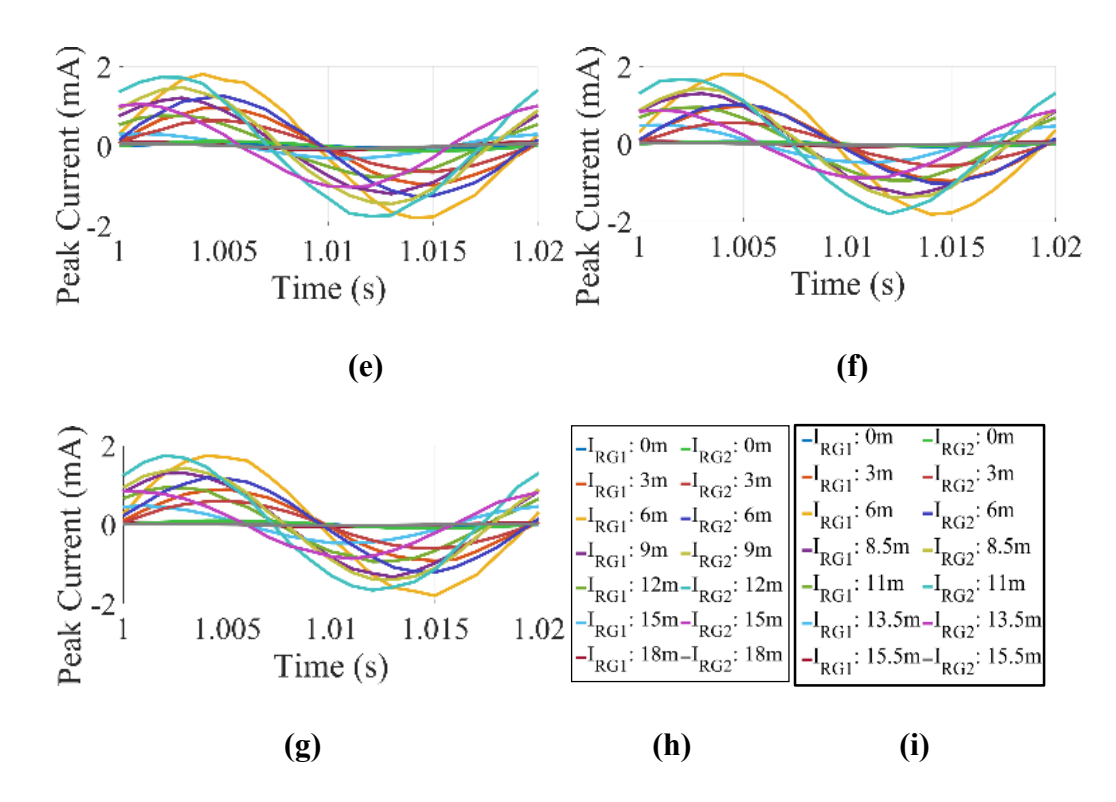
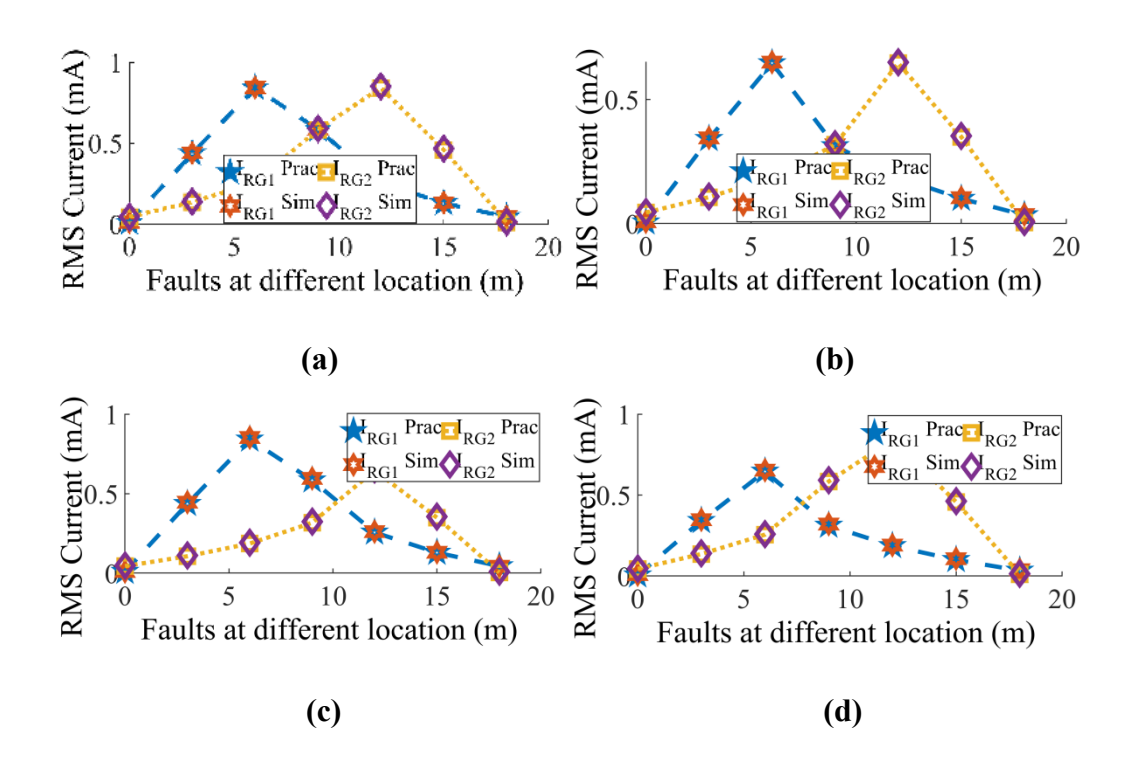


Figure 5.15 Measured faults current from DSO at RG<sub>1</sub> and RG<sub>2</sub> for different practical case studies (a) Case I, (b) Case II, (c) Case III, (d) Case IV (e) Case V (f) Case VI (g) Case VII (h) legend for case I-V (i) legend for case VI-VII



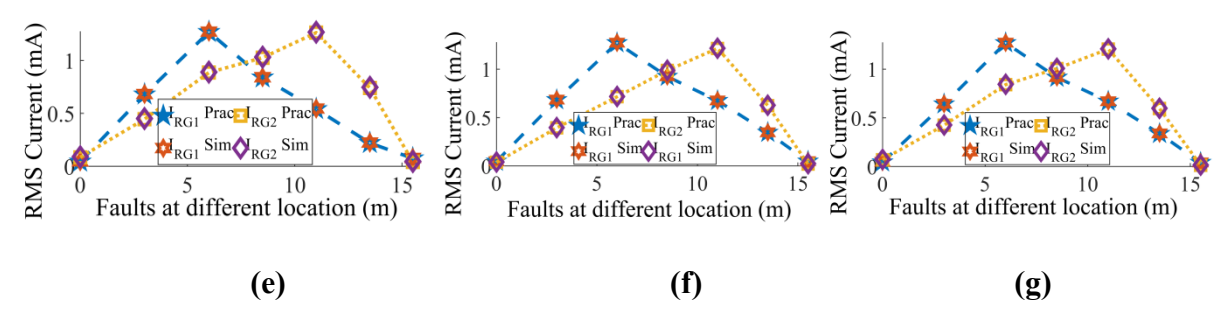


Figure 5.16 Measured rms faults current at  $RG_1$  and  $RG_2$  for different practical case studies (a) Case I, (b) Case II, (c) Case III, (d) Case IV (e) Case V (f) Case VI (g) Case VII.

**Table 5.1 Analytically Obtained Range of Fault Current** 

Case s	1 <sup>st</sup> Minor section rms current (mA)		2 <sup>nd</sup> Minor section rms current (mA)		3 <sup>rd</sup> Minor section rms current (mA)	
	$I_{RG1}$	$I_{RG2}$	$I_{RG1}$	$I_{RG2}$	$I_{RG1}$	$I_{RG2}$
1	[0, 0.841)	[0.044, 0.256)	[0.841, 0.256)	[0.256,0.8 41)	[0.256, 0.044]	[0.841,
2	[0, 0.646)	[0.034, 0.186)	[0.646,0.1	[0.186, 0.646)	[0.186, 0.034]	[0.646, 0]
3	[0, 0.841)	[0.034, 0.186)	[0.841,0.2 56)	[0.186, 0.646)	[0.256,0. 044)	[0.841, 0]
4	[0, 0.646)	[0.044, 0.256)	[0.646,0.1	[0.256,0.8 41)	[0.186, 0.034]	[0.841, 0]
5	[0.045, 1.268)	[0.086, 0.866)	[1.268, 0.541)	[0.866,1.2 62)	[0.541, 0.076]	[1.262,0. 043]
6	[0.047, 1.271)	[0.038, 0.715)	[1.271,0.6 74)	[0.715,1.2 15)	[0.674,0. 048]	[1.215,0. 021]
	[0.046, 1.269)	[0.071, 0.841)	[1.269, 0.669)	[0.841,1.2 06)	[0.669,0. 041]	[1.206, 0.014]

Table 5.2 Accuracy of the Location of an SG Fault

Table 5.2 Accuracy of the Location of an SG Fault							
	Actual	Estimated	Estimated	Accuracy	Accuracy		
Cases	Location	location A/c to			-		
	(m)	$I_{RG1}$	$I_{RG2}$	$I_{RG1}$ (%)	$I_{RG2}$ (%)		
	0	0.03	0.06	-	-		
	3	2.97	2.93	99	97.66		
	6	5.95	5.94	99.16	99.00		
1	9	8.92	8.93	99.11	99.22		
	12	11.90	11.93	99.16	99.41		
	15	14.91	14.95	99.4	99.66		
	18	17.93	17.96	99.61	99.77		
	0	0.05	0.07	-	-		
	3	2.96	2.91	98.66	97.00		
	6	5.97	5.94	99.50	99.00		
2	9	8.94	8.95	99.33	99.44		
	12	11.91	11.96	99.25	99.66		
	15	14.93	14.94	99.53	99.60		
	18	17.90	17.96	99.44	99.77		
	0	0.04	0.08	-	-		
	3	2.98	2.94	99.33	98.00		
	6	5.96	5.91	99.33	98.50		
3	9	8.95	8.97	99.44	99.66		
	12	11.91	11.94	99.25	99.50		
	15	14.91	14.93	99.40	99.53		
	18	17.93	17.96	99.61	99.77		
	0	0.05	0.07	-	-		
	3	2.95	2.90	98.33	96.66		
	6	5.96	5.93	99.33	98.83		
4	9	8.94	8.96	99.33	99.55		
	12	11.91	11.94	99.25	99.50		
	15	14.93	14.96	99.53	99.73		
	18	17.93	17.97	99.61	99.83		
	0	0.05	0.06	-	-		
	3	2.96	2.94	98.66	98.00		
-	6	5.96	5.91	99.33	98.50		
5	9	8.93	8.95	99.22	99.44		
	12	11.90	11.93	99.16	99.42		
<u> </u>	15	14.89	14.93	99.26	99.53		
	18	17.91	17.95	99.50	99.72		
6	0	0.04	0.05	-	-		
	3	2.95	2.91	98.33	97		
	6	5.96	5.93	99.33	98.83		
	8.5	8.45	8.46	99.41	99.52		
	11	10.91	10.94	99.18	99.45		
	13.5	13.41	13.46	99.33	99.70		
	15.5	15.42	15.46	99.48	99.74		
	0	0.05	0.07	-	-		
	3	2.96	2.93	98.66	97.67		
	6	5.95	5.94	99.16	99.00		
7	8.5	8.44	8.46	99.29	99.53		
	11	10.93	10.96	99.36	99.63		
	13.5	13.43	13.44	99.48	99.55		
	15.5	15.42	15.48	99.48	99.87		

# 5.4.2. Experimental results for SG fault location for the first experimental case study

The measured values of the grounding resistance current ( $I_{RG1}$  and  $I_{RG2}$ ) are 51.45A and 98.12A respectively. Using the analytical form discussed in Section 5.3, the range of values of current is calculated and is shown in Table 5.3. Comparing the measured values and the analytical obtained range, it was estimated that the  $3^{rd}$  minor section has a fault, and using (5.20) and (5.21) the location of the SG fault is determined and is shown in Table 5.4.

Table 5.3 Range of Fault Current for On-field Case

1 <sup>st</sup> Minor so current		2 <sup>nd</sup> Minor section rms current (A)		3 <sup>rd</sup> Minor section rms current (A)	
$I_{RG1}$	$I_{RG2}$	$I_{RG1}$ $I_{RG2}$		$I_{RG1}$	$I_{RG2}$
[0,	[5.17,	[113.01,	[70.85,	[69.97,	[112.51,
113.01)	70.85)	69.97)	112.51)	5.01]	0]

Table 5.4 Accuracy for an On-field Cable

Actual Location (m)	Estimated location A/c to $I_{RG1}$	Estimated location A/c to $I_{RG2}$	Accuracy $I_{RG1}$ (%)	Accuracy $I_{RG2}$ (%)
1280	1278.5	1279.1	99.88	99.92-

The measured distance presented in Table 5.4 is from the source side. The location of the defect is located with an uncertainty of less than 1.5m with an accuracy of more than 99.8%, demonstrating the efficiency of the proposed method.

# Chapter 6

# **Estimating the Location of Sheath to Ground Fault** in a Non Cross-Bonded Power Cable

In this chapter, the estimation of the location of sheath-to-ground (SG) fault in a non-cross bonded (NCB) HVAC power cable at any arbitrary location during online conditions is explained in detail. According to IEEE standard 575 [32], different types of NCB cables are considered to estimate the location of SG fault. The location of the SG fault is estimated by using the analytical formulae which are derived from the proposed circuit model of the cable. The details are explained below.

# 6.1 Analytical Formulae for Circulating Current in An NCB Power Cable - Healthy Condition.

In this section, circuit models for different types of NCB power cables were developed, as well as analytical formulae for healthy condition circulating current in the grounding resistance of an NCB cable are derived. The analytical formulae to estimate the electrical parameters of the cable sheath is shown in equations (5.1) - (5.4). Using the above formulae, the healthy condition grounding current for different types of bonding can be obtained as discussed below:

# 6.1.1 Single-point bonding (bonding at the end or beginning)

In each phase, the different phases' conductor current and current in the other metallic sheath produces magnetic flux on a particular sheath. This magnetic flux links the metallic sheath and produces a pseudo voltage, and due to the presence of a closed circuit in the metallic sheath (grounded at one end and SVL on the other), an inductive circulating current will flow inside the sheath. Since the current is produced due to the pseudo voltage source which is dependent on the current in the conductor ( $I_i$ ) and sheath of other phases, this is represented as a voltage-controlled current source, as shown in Fig. 6.1(a).

The phase voltage in each minor section is responsible for the capacitive current in the metallic sheath. The analytical relation between the per-phase voltage (V) and per-unit capacitive current ( $I_C$ ) in the metallic sheath is  $I_C = j\omega CV$ . Since the capacitive current is dependent on per-phase voltage, it is represented by the voltage control current source. The capacitive current flows out from the middle of each section [47] as shown in Fig. 6.1(b).

In Fig. 6.1, 'i' represents the particular sheath where the measurements/calculation is carried out and  $L_i$  represents the length of the cable of the particular phase. Since a closed path is formed between ground RG1 and  $Z_{ZVL}$ , the inductive current ( $I_{induct}$ ) and capacitive current ( $I_{CRG}$ ) in the metallic sheath is obtained using Krichoffs voltage law (KVL) and Krichoffs current law (KCL), and is represented as:

$$I_{\text{induct}} = \frac{\left(M_{\text{eq}}I_{\text{eq}}L_{\text{eq}}\right)}{\left(RG1 + Z_{\text{S}}L + Z_{\text{SVL}}\right)}, \qquad I_{\text{CRG}} = \frac{\left(I_{\text{C}}\left(\frac{Z_{\text{S}}L}{2} + Z_{\text{SVL}}\right)\right)}{\left(RG1 + Z_{\text{S}}L + Z_{\text{SVL}}\right)}$$
(6.1)

In the above formula,  $M_{eq}I_{eq}L_{eq} = \sum_{j=1}^{3} M_{CS1j}I_{j}L_{j} + \sum_{j=2}^{3} M_{SS1j}L_{j}I_{j}$ . The analytical form of measured current  $(I_{M1})$  can be analytically obtained as:

$$I_{\rm M1} = I_{\rm induct} + I_{\rm CRG} \tag{6.2}$$

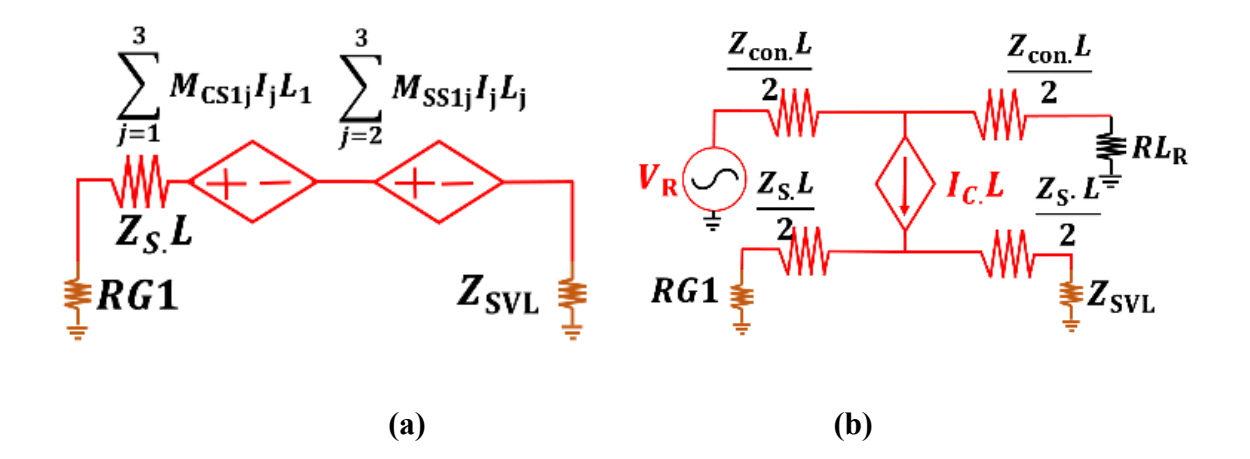


Figure 6.1 Circuit model (a) inductive, (b) capacitive for a healthy single point bonding at the beginning.

In the above formulae, the value of each term can be analytically obtained using (5.1)-(5.4).

# **6.1.2** Single-point bonding (bonding in the middle)

Similar to the Single-point bonding (bonding at the end or beginning), the inductive  $(I_{\text{induct1}} \text{ and } I_{\text{induct2}})$  and capacitive current  $(I_{CRG2})$  flowing through the grounding resistance RG1 for single point bonding at the middle as shown in Fig. 6.2 can be analytically expressed as:

$$I_{\text{induct1}} = \frac{\sum_{j=1,3,5} M_{CS1j} I_j L_j + \sum_{j=1,3,5} M_{SS1j} I_j L_j}{Z_{S.L1} + Z_{SVL1} + RG1}$$
(6.3)

$$I_{\text{induct2}} = -\frac{\sum_{j=2,4,6} M_{CS2j} I_j L_j + \sum_{j=2,4,6} M_{SS2j} I_j L_j}{Z_{S,L2} + Z_{SVL2} + RG1}$$
(6.4)

$$\sum_{j=1,3,5} M_{\text{CS1}j} I_{j} L_{j} \sum_{j=2,4,6} M_{\text{SS2}j} I_{j} L_{j} \underbrace{Z_{\text{con.}} L_{1}}_{j=2,4,6} \underbrace{Z_{\text{con.}} L_{1}}_{2} \underbrace{Z_{\text{con.}} L_{2}}_{2} \underbrace{Z_{\text{con.}} L_{2}}_{2}$$

$$\sum_{j=1,3,5} M_{\text{SS1}j} I_{j} L_{j} \sum_{j=2,4,6} M_{\text{CS2}j} I_{j} L_{j}$$

$$\sum_{j=2,4,6} M_{\text{CS2}j} I_{j} L_{j}$$

$$\sum_{j$$

Figure 6.2 Circuit model (a) inductive, (b) capacitive for a healthy single point bonding at the middle.

$$I_{\text{CRG1}} = \frac{I_{\text{C}}\left(\frac{Z_{\text{S}},L_{1}}{2} + Z_{\text{SVL1}}\right)\left(Z_{\text{S}},L_{2} + Z_{\text{SVL2}}\right) + I_{\text{C}}\left(\frac{Z_{\text{S}},L_{2}}{2} + Z_{\text{SVL2}}\right)\left(Z_{\text{S}},L_{1} + Z_{\text{SVL1}}\right)}{\left(Z_{\text{S}},L_{2} + Z_{\text{SVL2}}\right)\left(Z_{\text{S}},L_{1} + Z_{\text{SVL1}}\right) + RG1\left(Z_{\text{S}},L_{1} + Z_{\text{S}},L_{2} + Z_{\text{SVL1}} + Z_{\text{SVL2}}\right)}$$
(6.5)

In Fig. 6.2. L1, L3, and L5 are the lengths of the three phases from the source to the grounding resistance, and L2, L4, and L6 are the lengths of the three phases from the grounding resistance to the load.

The analytical form of the measured current  $(I_{M2})$ , from the grounding resistance (RGI), is expressed as:

$$I_{M2} = I_{CRG1} + I_{induct1} + I_{induct2} \tag{6.6}$$

### 6.1.3 Two-point bonding

The circuit model of a two-point grounding system is similar to Fig. 6.1, only in place of  $Z_{ZVL}$ , which would be the grounding resistance RG2. Like the above two types of bondings, the inductive ( $I_{induct3}$ ) and capacitive ( $I_{CRG2}$  and  $I_{CRG3}$ ) current can be analytically obtained as:

$$I_{\text{induct3}} = \frac{(M_{\text{eq}}I_{\text{eq}}L_{\text{eq}})}{(RG1+Z_{\text{c}}L+RG2)} \tag{6.7}$$

$$I_{\text{CRG2}} = \frac{\left(I_{\text{C}}\left(\frac{Z_{\text{S}}L}{2} + RG2\right)\right)}{\left(RG1 + Z_{\text{S}}L + RG2\right)}, \ I_{\text{CRG3}} = \frac{\left(I_{\text{C}}\left(\frac{Z_{\text{S}}L}{2} + RG1\right)\right)}{\left(R_{\text{GS1}} + Z_{\text{S}}L + R_{\text{GS2}}\right)}$$
(6.8)

In the above formula,  $M_{\rm eq}I_{\rm eq} = \sum_{j=1}^{3} M_{\rm CS1j}I_jL_j + \sum_{j=2}^{3} M_{\rm SS1j}L_jI_j$ , and  $I_{\rm CRG2}$  and  $I_{\rm CRG3}$  are the capacitive current flowing through the RGI and RG2 respectively. The analytical form of the measured current ( $I_{M3}$  and  $I_{M4}$ ), from the grounding resistances (RGI and RG2) are expressed as:

$$I_{M3} = I_{\text{induct3}} + I_{\text{CRG2}}, I_{M4} = I_{\text{induct3}} + I_{\text{CRG3}}$$
 (6.9)

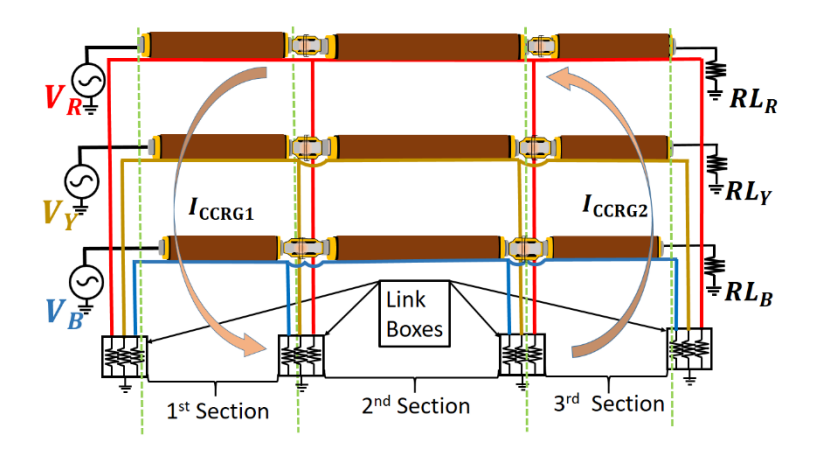


Figure 6.3 Schematic diagram of three simultaneous sections.

Whenever there is a simultaneous cable section as shown in Fig 6.3 (major sections I, II, and III), then the measuring grounding current ( $I'_{M3}$  and  $I'_{M4}$ ) for a particular loop in the major section II will be the simultaneous circulating current ( $I_{ccRG1}$  and  $I_{ccRG2}$  from the simultaneous previous and succeeding major sections respectively) subtracted from the actual circulating current in the major section II. Therefore, from Fig. 6.3, the measuring grounding current of RG1 and RG2 in the major section II would be:

$$I'_{M3} = I_{m3} - I_{ccRG1}, \quad I'_{M4} = I_{M4} - I_{ccRG2}$$
 (6.10)

 $I_{\rm ccRG1}$  and  $I_{\rm ccRG2}$  are the analytically obtained simultaneous circulating current flowing in the major sections I and III can be obtained similarly to  $I_{\rm m3}$  and  $I_{\rm m4}$  using (6.9).

# 6.2 Analytical formulae for the location of the SG fault for different types of bonding

In this section, equations for various types of NCB power cables that correspond to the location of SG faults are derived. Whenever any part of this metallic sheath comes in contact with the ground it causes changes in the inductive and capacitive circuit which in turn causes fault current to flow between the fault location and grounding resistances. As a result, the grounding current in a defective and healthy state will be different. Whenever the healthy

condition grounding current does not match with the analytically obtained values (6.2), (6.6), (6.9), and (6.10), an SG fault is confirmed. To facilitate the calculation, the distance from the source to the fault is considered to be x, whereas from the fault location to the load is considered to be L-x. The magnitude of the grounding current ( $I_{RG1}$  or  $I_{RG1}$ ) for an SG fault on different types of bonding will be different as shown in the simulation results in Fig. 6.4, 6.6, 6.7. The dimensions and electrical properties of the simulated cable are the same as the practical case mentioned in Section 6.3 for each type of bonding, while the length of the simulated cable is considered 500m.

# 6.2.1 Estimating the location of SG fault at Single-point bonding (bonding at the end or beginning)

The inductive and capacitive circuit for an SG fault in single-point bonded cable (bonding at the beginning) is shown in Fig. 6.4 and its simulated grounding current for faults at different locations is shown in Fig. 6.5.

The equation corresponding to Fig. 6.4 is solved to obtain the value of x, by only using the electrical parameters, measured sheath current and operating voltage, and capacitive current of the cable. The estimated location of the SG fault, from the source can be obtained as:

$$\chi = \frac{I_{M1}RG1}{\sum_{j=1}^{3} M_{CS1j}I_j + \sum_{j=2}^{3} M_{SS1j}I_j + I_C}$$
(6.11)

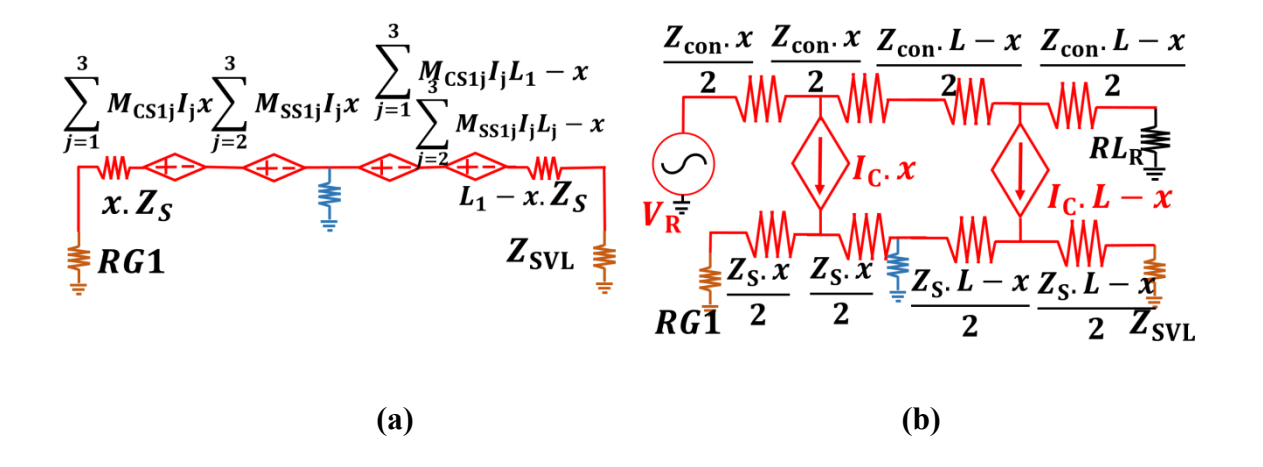


Figure 6.4 Circuit model (a) inductive, (b) capacitive for a single point bonding at the beginning having an SG fault.

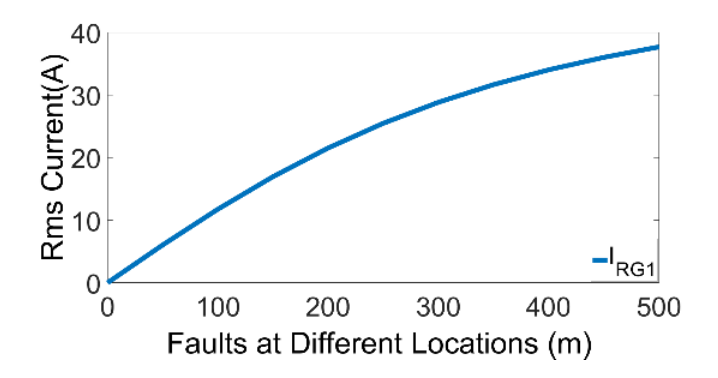
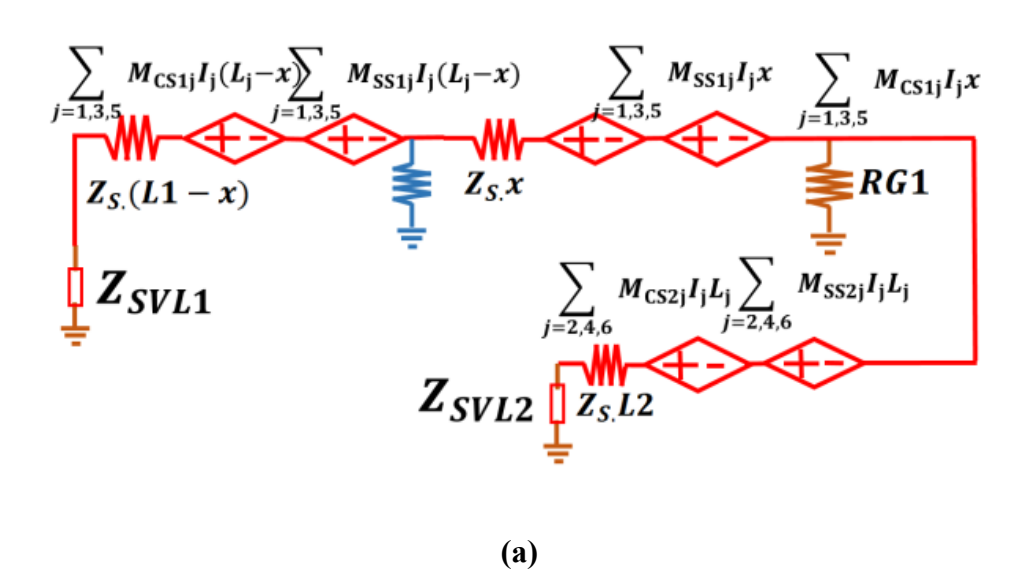


Figure 6.5 Grounding resistance currents for fault at different locations for a single point bonding at the beginning.

# 6.2.2 Estimating the location of SG fault at Single-point bonding (bonding at the middle)

From the simulation results as shown in Fig. 6.7, identical values of grounding current are observed, for an SG fault occurring on either side of the grounding resistance RGI. Therefore, in addition to the current magnitude, the phase difference (PD) between the conductor and sheath currents is necessary to estimate the location of an SG fault. Whenever an SG fault occurs between the source and ground the PD will be  $\sim 0^{\circ}$  (the presence of impedance of the sheath the PD will never be perfect 0) and whenever an SG fault occurs between ground to load, the PD will be  $\sim 180^{\circ}$ . This happens because the conductor current will not change its direction, however, the SG fault current will change its direction and flow from the load side to grounding resistance (since  $Z_{SVL} \gg RG1$ ) as shown in Fig. 6.7(b).



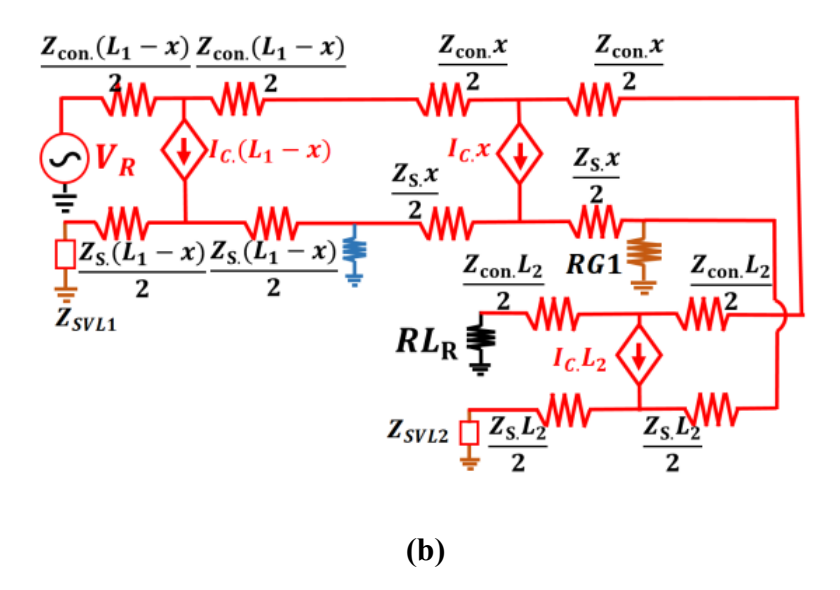


Figure 6.6 Circuit model (a) inductive, (b) capacitive for a single point bonding at the middle having an SG fault.

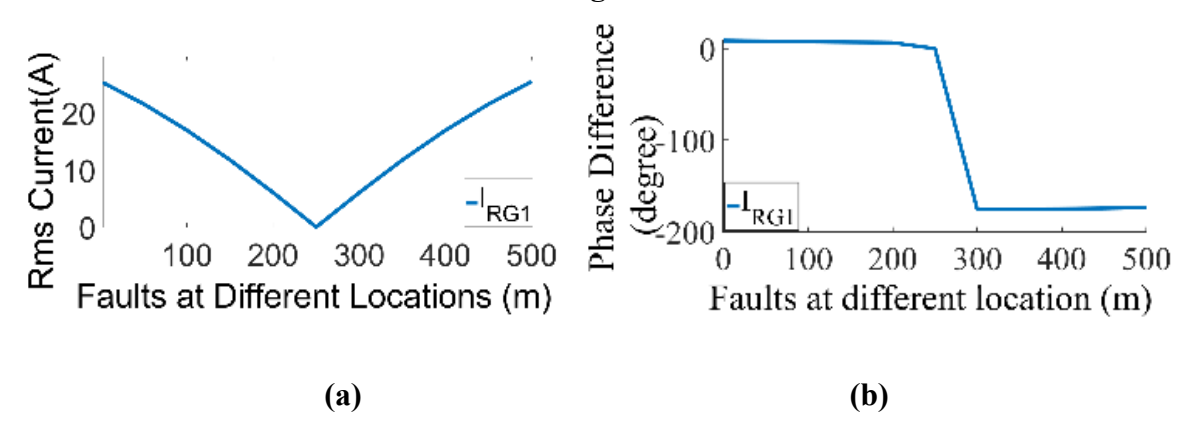


Figure 6.7 (a) Grounding resistance currents (b) Phase difference between sheath and conductor current for fault at different locations for a single point bonding at the

After obtaining the PD, the location of the SG fault between the source side and *RG1* can be estimated from Fig. 6.6 by:

$$x = \frac{-\beta + \sqrt{(\beta)^2 - 4\alpha\gamma}}{2\alpha} \tag{6.12}$$

In the above formula,

$$\alpha = \frac{I_{\text{CRG1}} Z_{S.} Z_{SVL2}}{2}, \qquad \beta = I_{\text{CRG1}} L_2 Z_{S.} Z_{SVL2} - I_{M2} Z_{S.} Z_{SVL2} + (\sum_{j=1,3,5} M_{SS1j} I_j L_j + \sum_{j=1,3,5} M_{SS1j} I_j L_j) Z_{SVL2}, \text{ and } \gamma = -I_{\text{M2}}. RG1. Z_{\text{SVL2}}$$

The location of the SG fault between RG1 and the load side can be estimated from Fig. 6.6

by:

$$\chi = \frac{-\beta' + \sqrt{(\beta')^2 - 4\alpha'\gamma'}}{2\alpha'} \tag{6.13}$$

In the above formula,

$$\alpha' = \frac{I_{\rm CRG1} Z_{\rm S.} Z_{\rm SVL1}}{2}, \qquad \beta' = I_{\rm CRG1} L_1 Z_{\rm S.} Z_{\rm SVL1} - I_{\rm M2} Z_{\rm S.} Z_{\rm SVL1} - \left(\sum_{j=2,4,6} M_{SS2j} I_j L_j + \sum_{j=2,4,6} M_{SS2j} I_j L_j\right) Z_{\rm SVL1}, \quad \alpha = -I_{\rm M2} RG1. Z_{\rm SVL1}$$

# 6.2.3 Inductive current in the metallic sheath

The simulated grounding current for faults at different locations is shown in Fig. 6.8. Similar to the circuit for single-point bonded cable (grounding at the beginning or end), the expression of x is estimated for both grounding currents.

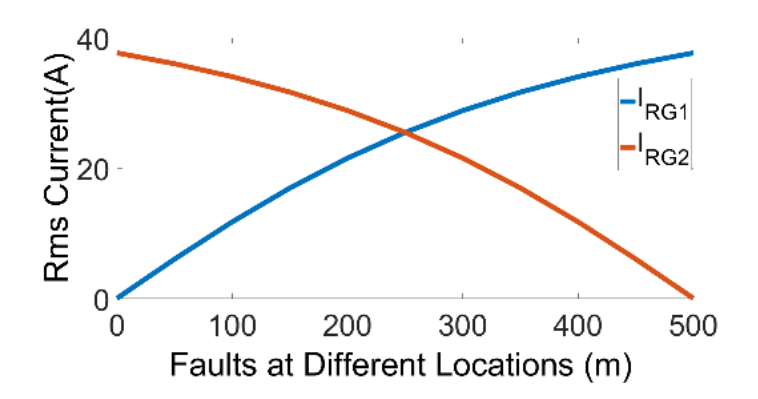


Figure 6.8 Grounding resistance currents for fault at different locations for a single point bonding at the beginning.

The estimated location of the SG fault, measuring from the source side grounding current is:

$$\chi = \frac{I_{M3}RG1}{\sum_{i=1}^{3} M_{CS1i} I_i + \sum_{i=2}^{3} M_{SS1i} I_i + I_{CRG2}}$$
(6.14)

The estimated location of the SG fault, measuring from the load side grounding current is:

$$\chi = \frac{2\left(\sum_{j=1}^{3} M_{\text{CS1j}} I_{j} L_{1} + \sum_{j=1}^{2} M_{\text{SS1j}} I_{j} L_{j}\right) + I_{\text{CRG3}} - 2I_{\text{M4}} (RG2 + Z_{S}L)}{I_{\text{CRG3}} + 2\left(\sum_{j=1}^{3} M_{\text{CS1j}} I_{j} + \sum_{j=2}^{3} M_{\text{SS1j}} I_{j}\right) - 2I_{\text{M4}} Z_{\text{S}}}$$
(6.15)

Therefore the location of an SG fault in different types of NCB cables can be obtained using (6.11)-(6.15) analytically. The flowchart to estimate the location of a SG in a NCB power cable is shown in Fig 6.9.

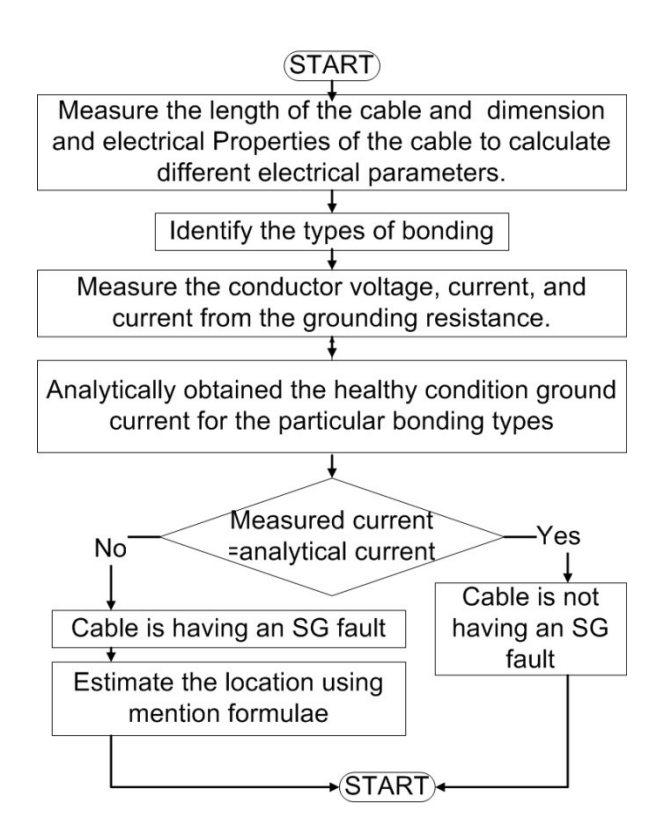


Figure 6.9 Flowchart to estimate the location of SG fault at any arbitrary location in a NCB cable system during online condition.

# 6.3 Experiments and Simulation in a NCB power cable to Estimate the Location of SG fault.

Experiments are performed on a commercial three-core, XLPE insulated material was selected, with an inner conductor (Aluminium) area of  $35mm^2$ , outer grounded sheath diameter of 7.35mm, the radius of the metallic sheath is 1mm, and insulation relative permittivity of 2.3. The cable is laid in a trefoil formation with  $r_{cs}$  and  $r_{ss}$  as 8cm and 10cm respectively. The grounding resistance for three types of bonding ( $RG_1$  or  $RG_2$ ) is kept at  $0.2\Omega$  respectively. The cable is supplied with a three-phase voltage of 440V and a load current of 15 A. The ground current is measured using a FLUKE 17B digital multimeter whose uncertainty in measurement is 1.5%. To measure PD, the HIOKI PW3198 power quality analyzer of uncertainty in measurement is 1% is used. CB of the sheath is performed using metallic wire as shown in Fig. 6.10. The faults are created using a grounding rod of magnitude 3 m $\Omega$  for each case study.

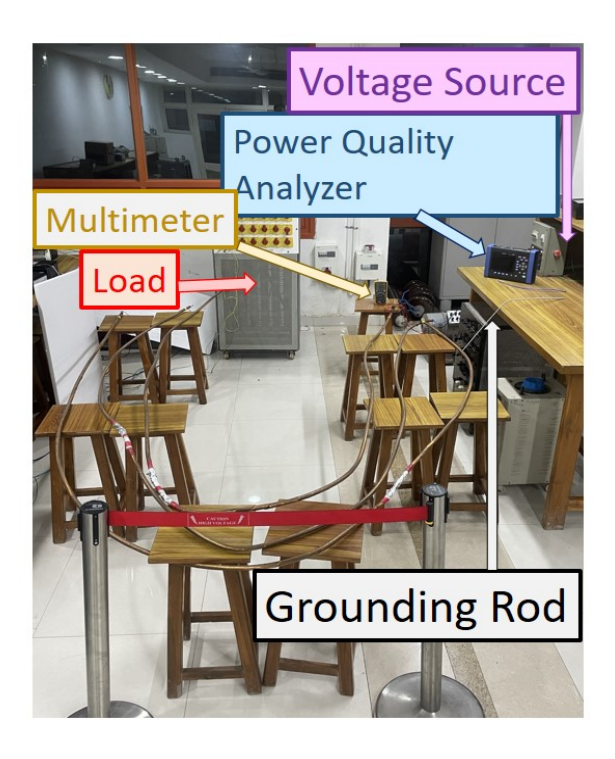


Figure 6.10 Experimental setup to estimate the location of the SG fault

To verify the analytical and experimental results, simulations are performed in MATLAB Simulink, of the same dimension and fault location for all bonding types and case studies. These different case studies are:

#### 6.3.1 Experiments on Single-point bonding (bonding at the beginning)

The experiments were performed on a three-phase 15m long cable (all phases are of the same length). The healthy condition grounding current is measured for a balanced load having power factor one and is mentioned as an ideal case study. Two different case studies (Case I and Case II) are considered and faults are created in five different locations for each of the above case studies. Case study I is of balanced load condition of each phase having power factor one, while in case study II, the power factor at three phases are 1, 0.9, and 0.85, while the magnitude of the current remains the same as a balanced case, and the faults are created in the phase having power factor one.

# 6.3.2 Experiments on Single-point bonding (bonding at the middle)

To estimate the healthy condition grounding current and phase for an ideal case study, the experiments were performed on a 15m long three-phase cable (all phases are of the same length), grounding at 7.5m (at the middle),. To validate the analytical results to estimate the location of an SG fault three case studies (Case I, II, and III) are considered. All three case

studies have balanced load and power factor one. In cases I, II, and III, the system is grounded at 7.5m, 5m, and 10m respectively. Faults are created at seven different locations for each of the three case studies.

# **6.3.3** Experiments on Two-point bonding

The experiments were performed on a 15m long three-phase cable (all phases are of the same length), to measure the healthy condition grounding current for an ideal case study. To validate the analytical results to estimate the location of an SG fault, five case studies (Case I, II, III, IV, and V) are considered. Faults are created at five different locations in each case study. Cases I–IV have have balanced load of power factor one in each phase. In case I, only one major section is considered between source and load. In case II-IV, three major sections are considered between source to load. Fault is created at the middle, adjacent to the source end, and adjacent to the load end major section for cases II, III, and IV respectively. Case V is similar to the case I, however, the power factor at three phases are 1, 0.9, and 0.85, while the magnitude of the current remains the same as a balanced case, faults are created in the phase having power factor one.

# 6.4 Experiments and Simulations on a NCB cable to estimate the location of SG fault.

In this section, the analytical, experimental, and simulation results are presented and discussed. The section is further divided into two subsections. At first, the accuracy of the proposed analytical methods to obtain the healthy conditions grounding current is compared with the practical and simulation case study, followed by the practical results for the estimation of the location of the SG fault at any arbitrary locations for different types of bonding.

#### 6.4.1 Healthy condition grounding current for different types of bonding

The healthy condition grounding current compared with analytically obtained values (6.2), (6.6), and (6.9), for different types of bonding for the practical case study as mentioned in Section IV is presented in Table 6.1. In Table I, types 1, 2, and 3 are the single-point bonding at the beginning, at the middle, and two-point bonding respectively. Accuracy I and II, are the analytical results compared with measured and simulated study. An ideal case study is considered for both the practical and simulation cases.

**Table 6.1 Healthy Condition grounding current** 

Type	Measured Current (R <sub>GS</sub> ) (mA)	Simulated Current (R <sub>GS</sub> ) (mA)	Analytical current	Accuracy 1 (%)	Accuracy 2 (%)
1	1.0296	1.0298	1.0297	99.99	99.99
2	0.2341	0.2340	0.2339	99.98	99.95
3	0.2328	0.2327	0.2326	99.98	99.96

From Table 6.1, it is observed that the healthy condition grounding current was reasonably accurate when compared with practical and simulation results for all types of bonding.

# 6.4.2 Experimental results for SG fault location for different types of bonding

The accuracy of the proposed methodology to locate SG faults at any arbitrary location for different types of NCB practical cable is discussed below:

### 6.4.2.1 Experiments on Single-point bonding (bonding at the beginning)

The measured and simulation results of two case studies of the grounding current obtained for faults at different locations are shown in Fig. 6.11. After obtaining the measured current, the faults at the particular locations are determined using (6.11). The accuracy of the proposed method for different case studies is shown in Table 6.2 and it is observed that the proposed method can able to locate an SG fault for a single-point bonded (bonding at the beginning) test cable with a minimum accuracy of 97.77%, irrespective of the location of the fault.

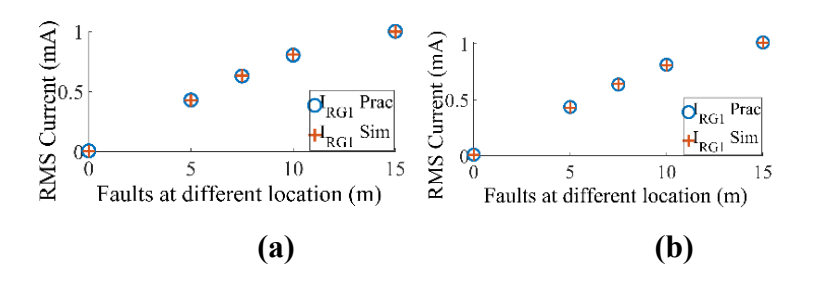


Figure 6.11 Measured faults current at RG<sub>1</sub> for single-point bonding at the beginning of practical case studies (a) Case I, (b) Case II.

Table 6.2 Accuracy of the SG fault location for a single-point bonded practical cable (bonding at the beginning)

Cases	Actual Location (m)	Estd location a/c to measured $I_{RG1}$	Accuracy $I_{RG1}$ (%)
	0	0	-
	5	4.9927	99.27
1	7.5	7.4910	99.88
	10	9.9849	98.49
	15	14.9786	97.86
	0	0	-
	5	4.9915	99.15
2	7.5	7.4886	99.84
	10	9.9874	98.74
	15	14.9777	97.77

# 6.4.2.2 Experiments on Single-point bonding (bonding at the middle)

The measured and simulation results of three case studies of grounding current (magnitude and PD) obtained for faults at different locations are shown in Fig. 6.12 - Fig. 6.14. After obtaining the measured current and PD, the faults at the particular are determined using (6.12) or (6.13) depending on the value of PD. The accuracy of the proposed method for different case studies is shown in Table 6.3.

From Table 6.3, it is observed that the proposed method can able to locate an SG fault for a single-point bonded (bonding at the middle) test cable with a minimum accuracy of 98.98%.

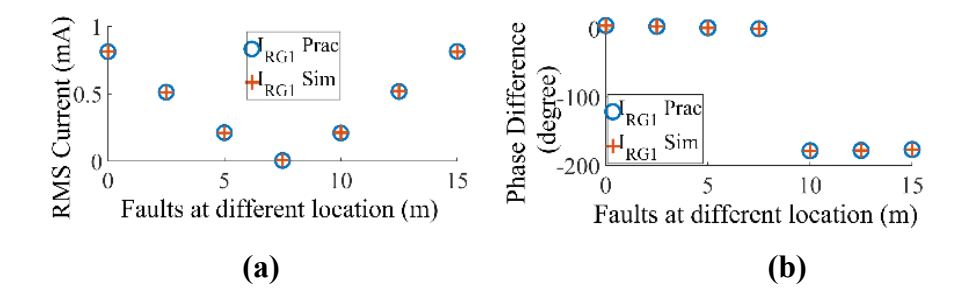


Figure 6.12 Measured (a) current (b) phase at RG<sub>1</sub> for Case I of single point bonding at the middle.

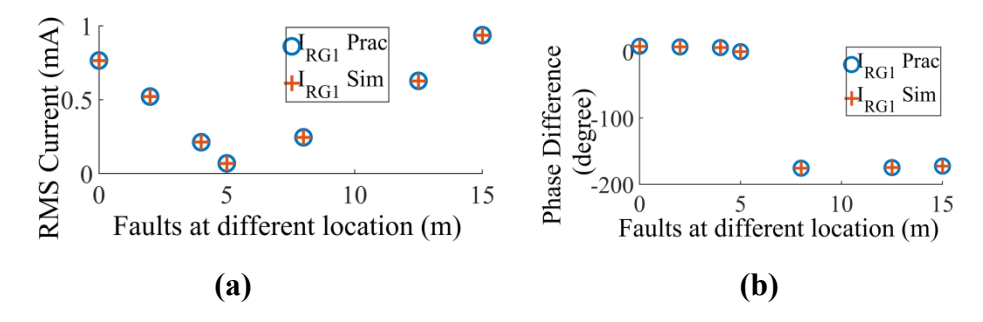


Figure 6.13 Measured (a) current (b) phase at RG<sub>1</sub> for Case II of single point bonding at the middle.

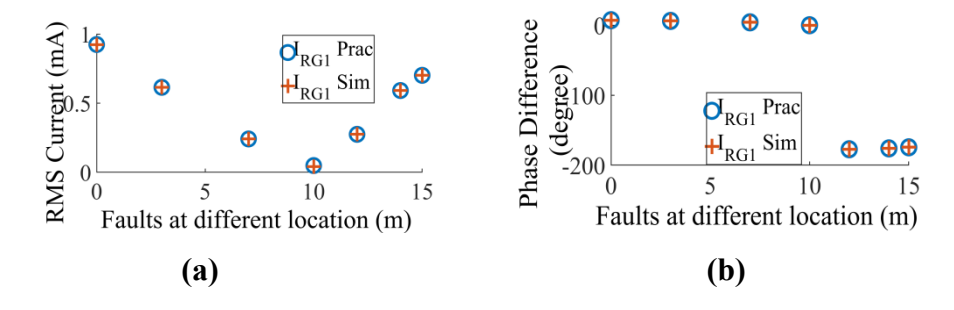


Figure 6.14 Measured (a) current (b) phase at RG<sub>1</sub> for Case III of single point bonding at the middle.

Table 6.3 Accuracy of the SG fault location for a single-point bonded practical cable (bonding at the middle)

		maing at the image;	
Cases	Actual Location (m)	Estd location A/c to measured $I_{RG1}$	Accuracy $I_{RG1}$ (%)
	` ,		
	0	0.0074	-
	2.5	2.4985	99.94
1	5	4.9716	99.43
	7.5	7.4969	99.95
	10	9.9846	99.84
	12.5	12.4875	99.90
	15	14.8969	99.31
	0	0.0076	-
	2	1.9806	99.03
	4	3.9764	99.41
2	5	4.9930	99.86
	8	7.9696	99.62
	12.5	12.4012	99.21
	15	14.8620	99.08
	0	0.0082	-
	3	2.9694	98.98
3	7	6.9482	99.26
	10	9.9840	99.84
	12	11.9556	99.63
	14	13.8964	99.26
	15	14.8530	99.02

# 6.4.2.3 Experiments on Two-point bonding

The measured and simulation results of five case studies of grounding current obtained for faults at different locations are shown in Fig 6.15. After obtaining the measured current, the faults at the particular locations are determined using (6.14) and (6.15). The accuracy of the proposed method for different case studies is shown in Table 6.4.

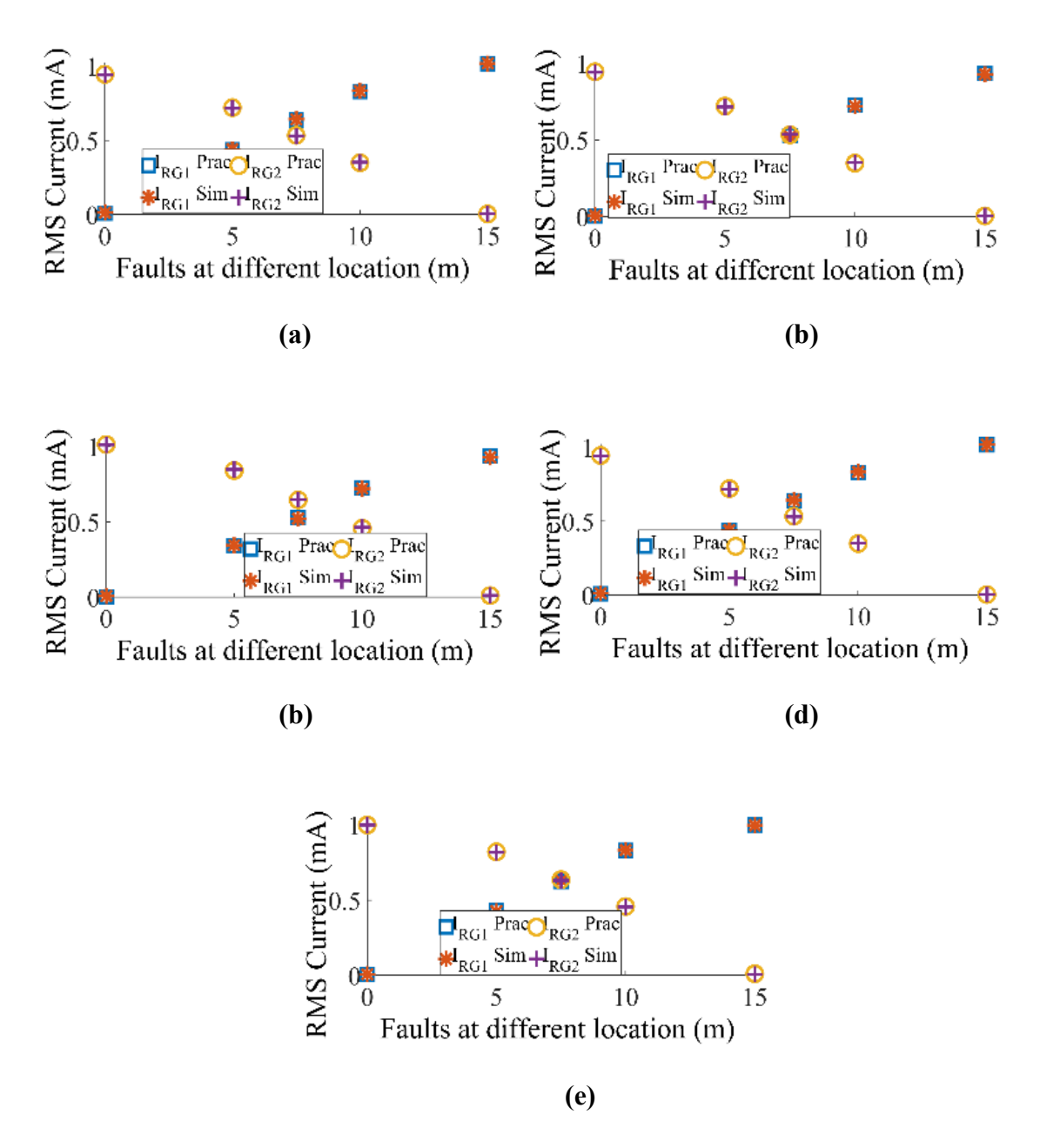


Figure 6.15 Measured faults current at  $RG_1$  and  $RG_2$  for different practical case studies (a) Case I, (b) Case II, (c) Case III, (d) Case IV (e) Case V of two-point bonded cable.

From Table 6.4, it is observed that the proposed method can able to locate an SG fault for a two-point bonded test cable with a minimum accuracy of 98.57%

# Chapter 7

# Estimating the Location of Sheath-to-Ground in an HVDC Cable Using Regression-Based Online TDR

In this chapter, the estimation of the location of sheath-to-ground (SG) fault in an HVDC power cable at any arbitrary location during online conditions is explained in detail. The location of the SG fault is estimated by using the proposed model of using online TDR combined with machine learning DTR method and FFT. The details of the proposed method are explained below.

# 7.1 Circuit Model And Feature Extraction from Cable Dimension To Perform Online TDR in the Sheath

In this section, a novel circuit model is proposed to perform online TDR within the sheath of an HVDC cable and the key features based on cable dimension that are required to train the system are described.

# 7.1.1 Circuit Model to Perform Online TDR in the Sheath

The inductive coupler is employed to transmit and receive impulse waveforms within the sheath of an HVDC cable. The auxiliary circuit contains an impulse voltage source to send the signal, a DSO to obtain the traveling waveform, and an inductive coupler that functions through magnetic induction, enabling signal transmission and reception without direct electrical connection all connected together with the sheath as shown in Fig. 7.1.

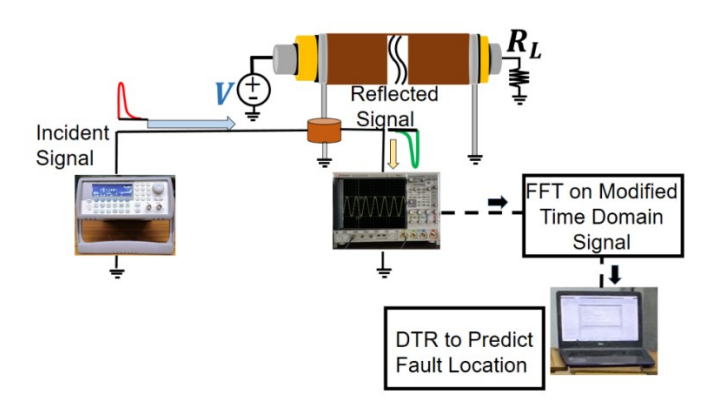


Figure 7.1 Proposed schematic model to perform online TDR in the metallic sheath to estimate SG fault location.

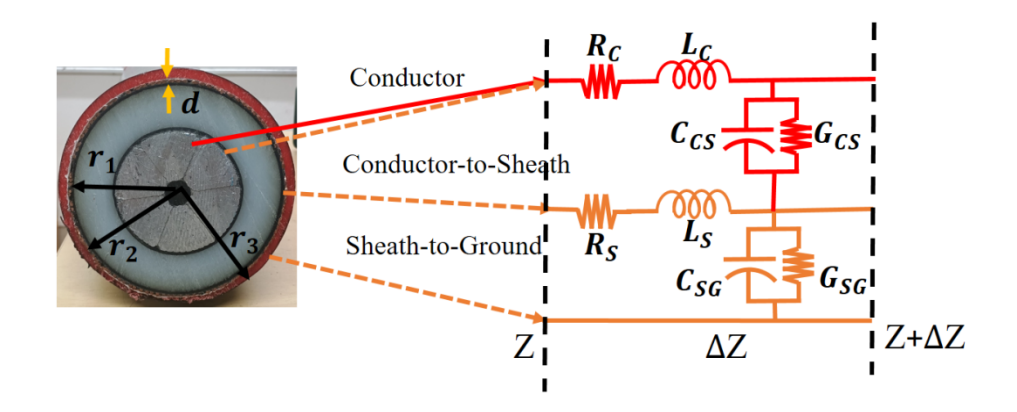


Figure 7.2 Double-circuit transmission line model to represent the sheath of a cable.

Each inductive coupler operates effectively within a specified frequency band, ensuring that signals remain linearly transmitted and received within this range. In this case, the coupler used is designed for a frequency band centered at 500 kHz, which provides a stable and distortion-minimized channel for signal transmission. To perform online TDR in the sheath, an impulse waveform with a frequency of 100 kHz and a magnitude of 50V is selected. This frequency and magnitude were chosen to maintain compatibility within the coupler's linear frequency range while ensuring accurate fault localization.

The circuit setup, as shown in Fig. 7.1, is simulated to model the signal propagation and accurately estimate the fault location within the cable. DTR is then applied, using key features extracted from the simulated results to train a model that accounts for minor noise and linear distortions that may arise in practical applications. This approach enhances the reliability of the fault location estimates, even under variable field conditions, by compensating for subtle irregularities that could otherwise affect accuracy.

# 7.1.2 Transmission Line Model of the Sheath to Extract Key Parameters from Cable Dimensions

Since the TDR impulse is transmitted through the sheath, a double-circuit transmission line (TL) model is employed to analyze the signal propagation along the sheath accurately. According to the TL model, the input sheath impedance of the cable sheath ( $Z_{inS}$ )can be obtained analytically as:

$$Z_{inS} = \Gamma \frac{R_G + \Gamma \tanh(\gamma Z)}{\Gamma + R_G \tanh(\gamma Z)}$$
(7.1)

Here,

$$\Gamma(Characteristics\ Impedance) = \sqrt{\frac{R_S + j\omega L_S}{G + jwC}}$$
(7.2)

$$\gamma = \alpha + j\beta = \sqrt{(R_S + j\omega L_S)(G + j\omega C)}$$
(7.3)

$$G = G_{CS} + G_{GS}, \qquad C = C_{SG} + C_{SG} \tag{7.4}$$

In equation (7.1), Z represents the total length of the cable, and  $R_G$  is the grounding resistance. Parameters  $R_S$  and  $L_S$  denote the resistance and inductance of the sheath, respectively. and  $G_{GS}$  are the capacitance and conductance between the conductor and sheath, while and  $G_{SG}$  represent the capacitance and conductance between the sheath and ground, as illustrated in Fig. 7.2.  $\gamma$  is the propagation constant,  $\alpha$  and  $\beta$  are the attenuation and phase constant respectively. The analytical formulas for these per-unit-length electrical parameters are provided in equations (7.5) and (7.8).

$$R_S = \frac{1}{\pi \sigma \left[ d^2 - \left( d - \frac{1}{\sqrt{\pi \mu \sigma f}} \right)^2 \right]} \Omega/m \tag{7.5}$$

$$L_{S} = \frac{\mu_{0}}{2\pi} \ln \left( \frac{r_{2}^{2}}{r_{1}^{2}} \right) H/m \tag{7.6}$$

$$C_{CS} = \frac{\frac{\mu_0}{2\pi} \ln\left(\frac{r_2^2}{r_1^2}\right)}{\left(\frac{1}{\mu\varepsilon}\right) \left(\left(\frac{\mu_0}{2\pi} \ln\left(\frac{r_2^2}{r_1^2}\right)\right)^2 - \left(\frac{\mu_0}{2\pi} \ln\left(\frac{r_2}{r_1}\right)\right)^2\right)} F/m$$
(7.7)

$$C_{GS} = \frac{\frac{\mu_0}{2\pi} ln(\frac{r_3^2}{r_2^2})}{(\frac{1}{\mu\epsilon}) ((\frac{\mu_0}{2\pi} ln(\frac{r_3^2}{r_2^2}))^2 - (\frac{\mu_0}{2\pi} ln(\frac{r_3}{r_2}))^2)} F/m$$
(7.8)

$$G_{CS} = G_{GS} = 2\pi f \times tan\delta \times (C_{CS} \text{ or } C_{GS}) \text{ S/m}$$
(7.9)

Here,  $\mu_0$  the permeability of free space,  $\mu_r$  relative permeability of the conductor material,  $\sigma$  the conductivity of the conductor material,  $\varepsilon_0$  the permittivity of free space,  $\varepsilon_r$  the relative permittivity of the insulating material and  $\tan \delta$  the dissipation factor, d is the thickness of the sheath,  $r_1$  and  $r_2$  are the outer and inner radius of the sheath and  $r_3$  is the outer radius of the jacket.

Therefore from (7.1)-(7.8), the input sheath impedance of the sheath is dependent on the dimension, electrical properties of the cable (different cable dimensions will have different input impedance), and length of each section ( $L_H$ ) (each section means, length between two solid grounding). Therefore, $Z_{inS}$  will be used to train the system, as mentioned detailed in Section 7.2.

# 7.2 Sheath Fault Location Using Fast Fourier Transform and DTR

The HVDC cable sheath grounded at both ends as shown in Fig. 7.1, forms a long section that can extend for thousands of meters. An SG fault occurs when the metallic sheath comes into direct contact with the ground, puncturing the outer insulation. When an impulse is sent along the cable sheath of an HVDC cable, it will always have a negative reflection coefficient. In a healthy cable, the impulse reflects back from the solid grounding at the ends. However, if an SG fault is present, the impulse reflects from the fault location, allowing the fault's position to be identified based on the reflection timing.

Since the magnitude and center frequency of the incident signal is fixed, reflections from a short cable section or a fault close to the source can overlap with the original signal before it fully dissipates, making the actual reflection indistinguishable, as shown in Fig. 7.3(a). To address this and accurately estimate the location of an SG fault, the modified reflected signal captured by the DSO was analyzed using FFT. This approach enhances signal analysis and reduces noise, enabling precise identification of the fault's position. In this section, a novel method to extract key features from the modified reflected signal and use of DTR to estimate the location of SG faults is described in detail.

# 7.2.1 FFT on the Captured Signal on the DSO: Problem and Solution

# 7.2.1.1 Challenges of Applying FFT to the Entire Signal

In Fig. 7.3 (a), it is observed that faults closer to the source result in impulse signal tails with more significant negative dips than faults farther away, as the frequency-dependent attenuation progressively diminishes high-frequency components over distance. Consequently, shorter cables experience less attenuation (Z is less in (7.9)) than longer ones, further influencing the impulse signal shape based on the fault location. The relation between the voltage at a given point along the sheath (V), and the initial or input voltage at the start of the transmission line at Z = 0 ( $V_0$ ) at a particular frequency is given as:

$$V(Z,t) = V_0 e^{-\alpha Z} e^{-\beta Z} \tag{7.9}$$

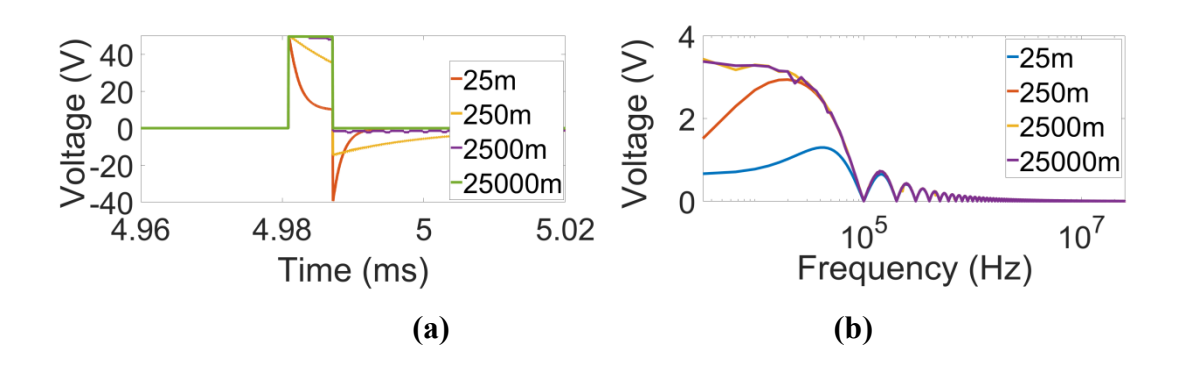


Figure 7.3 (a) Simulation results of TDR response for faults at different locations in its complete time spectrum of a 220 Kv long cable, (b) FFT of the complete time spectrum of simulated TDR response having fault at different locations.

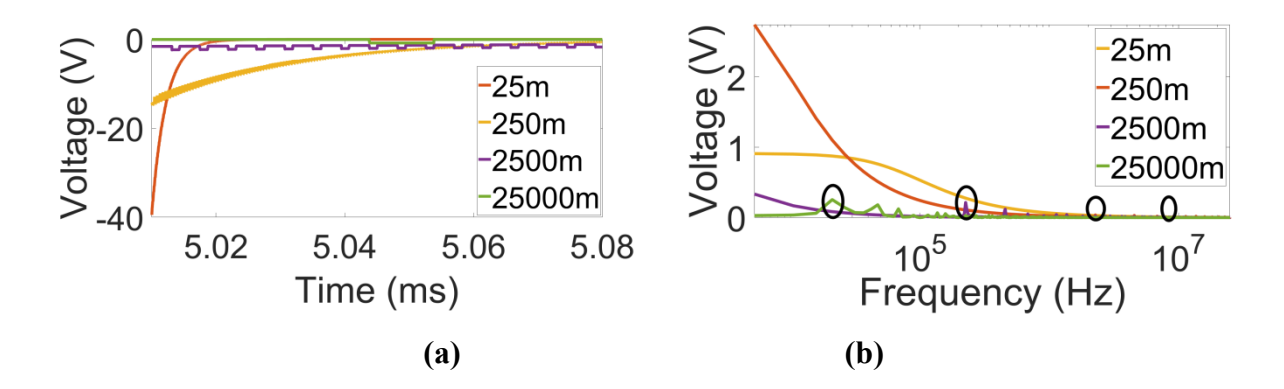


Figure 7.4 (a) Simulation results of TDR response for faults at different locations in its modified time spectrum of a 25000m long cable, (b) FFT of the modified time spectrum of simulated TDR response having fault at different locations.

The V(Z,t) is actually a linear combination of incident  $(v_{incedent})$  and reflected signal  $(v_{reflected})$  can be given as:

$$V(Z,t) = v_{incedent}(Z,t) + v_{reflected}(Z,t)$$
(7.10)

In (7.10),  $v_{incedent}$  is the high-energy initial impulse whereas  $v_{reflected}$  is a weaker, delayed, and potentially attenuated version due to the fault reflection. Since Fourier Transform is a linear operation, therefore FFT of V(Z,t), can be written as:

$$V(Z,f) = v_{incedent}(Z,f) + v_{reflected}(Z,f)$$
(7.11)

Since  $v_{incedent}(Z, f)$  has a much higher magnitude than  $v_{reflected}(Z, f)$ , the overall spectrum V(Z, f) is largely determined by  $v_{incedent}(Z, f)$ . The weaker  $v_{reflected}(Z, f)$  only

makes a minor addition to the spectrum and does not significantly alter the main frequency peaks or pattern in the FFT. Therefore the FFT spectrum of the SG fault for different lengths of the cable will be the same as shown in Fig. 7.3(b), making it nearly impossible to estimate the location of the SG fault.

# 7.2.1.2 Proposed Method to Apply FFT to Obtain Distinctive features for Faults at Different Lengths

To obtain a distinct FFT representation for faults at different locations, the time waveform V'(Z,t) is analyzed starting from the minimum point of the negative dip, as shown in Fig. 7.4(a). This approach effectively removes the influence of the incident wave  $v_{incedent}(Z,t)$ , which carries the highest energy, allowing for clearer identification of fault-specific reflections.

Table 7.1 Algorithm 1: Extracting key parameters from time domain data

**Step 1)** Perform the FFT on the modified time-domain spectrum V'(Z, t) to obtain V'[Z, f].

**Step 2)** Compute the magnitude |V'[Z, f]| for each f.

**Step 3)** Identify the index  $f_{peak}$  where |V'[Z, f]| is maximum:

$$f_{peak} = \arg_{f}^{max} |V'[Z, f]|$$

**Step 4)** The magnitude of the highest peak is |V'[Z, f]|.

The FFT waveform of the modified time spectrum is shown in Fig. 7.4(b). In an FFT graph, the highest magnitude peak typically represents the fundamental frequency component of the time-domain signal, corresponding to the frequency with the most significant power. In the time domain, reflected signals from faults near the source will overlap, making their identification difficult. Consequently, in the frequency domain, both the peak magnitude (|V'[Z, f]|) and the frequency  $(f_{peak})$  at which this peak occurs will be unique for faults at different locations. This distinctiveness of  $(f_{peak})$  and peak magnitude for each fault location makes frequency-domain analysis advantageous, as these variations are not observable in the time domain, as shown in Fig. 7.4.

The |V'[Z, f]|, and  $f_{peak}$  vary with fault location and cable dimensions, making these properties essential features for training the DTR system. The algorithm to obtain these two parameters from the modified time domain graph is in Table 7.1:

#### 7.2.2 DTR Method to Estimate the Location of SG Fault

The precise measurement of  $f_{peak}$  and |V'[Z, f]| are extremely important to ensure the exact location of the SG fault. However, in the practical environment, this measurement might be affected due to the presence of noise, engineering, and measurement negligence. Therefore, simulations of different lengths and dimensions of cables having SG fault at different locations are performed to obtain  $Z_{inS}$ ,  $f_{peak}$ , and |V'[Z, f]| (details of simulation is described in section 7.3). Then, these key parameters are used to train the system based on the DTR model. The testing data set will be obtained from the practical measurement of  $Z_{inS}$ ,  $f_{peak}$  and |V'[Z, f]|, and based on the pre-processed model, actual location of the SG fault  $(L_F)$  can be obtained. The complete flowchart to estimate the location of SG in an HVDC cable using DTR-based online TDR is shown in Fig. 7.5.

DTR was employed to predict location values, selected for its interpretability and its ability to capture nonlinear relationships in the dataset. DTR is particularly suited for this application, as it recursively partitions the feature space  $(Z_{inS}, f_{peak}, \text{ and } |V'[Z, f]|)$  to minimize variance in the target variable, making it effective when handling structured data with non-linear patterns without extensive feature engineering. Unlike neural networks, DTR provides a more straightforward model that requires less computational power, is less prone to overfitting on smaller datasets, and does not require intensive hyperparameter tuning to achieve consistent results.

A Decision Tree could be structured as follows: consider a tree as shown in Fig. 7.6 having input feature vectors A1, A2, and A3 to predict output classes Z1, Z2, Z3, and Z4 by comparing with threshold values T1, T2, and T3 values The prediction is determined by applying an if-then rule to the feature vector. This process continues, with each node representing a decision rule, until a terminal node or leaf is reached.

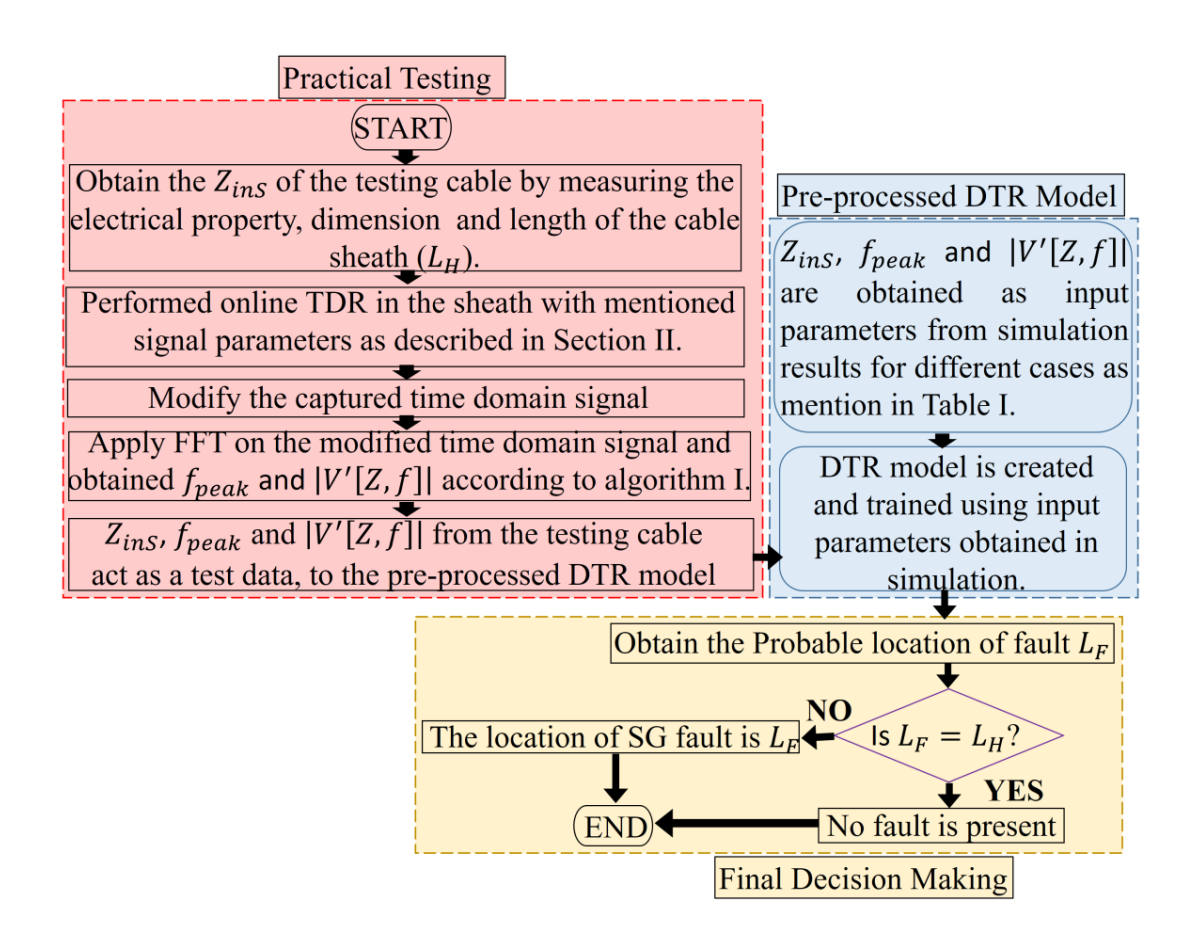


Figure 7.5 Complete flowchart of the proposed methodology to estimate the location of SG fault.

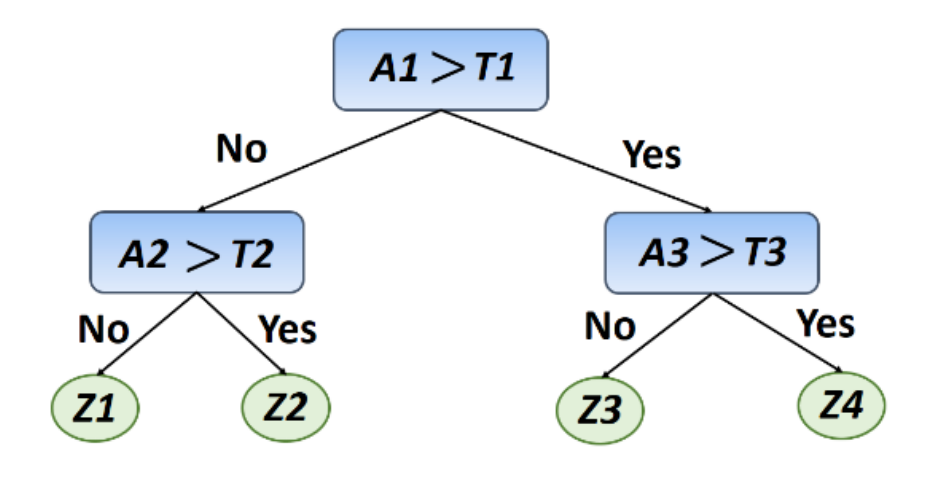


Figure 7.6 Illustration of a basic regression decision tree.

DTR-based methods employ several key steps: defining an accuracy criterion, selecting splits, establishing a stopping condition, and optimizing tree structure. Prediction accuracy can be assessed using metrics like re-substitution error, cross-validation error, or test sample

error. Splits are determined by minimizing the least-squared deviation to reduce node impurity. Splitting stops when a minimum node size is reached, preventing overfitting. Tree optimization is achieved through pruning, which reduces the tree's complexity by setting an optimal minimum leaf size to balance error minimization and model simplicity. The mathematical details of the above methods are thoroughly explained in references [81] and [82].

### 7.3 Experiments and Simulation to Estimate the Location of SG fault in a HVDC cable

In this section, a comprehensive description of the simulation process for training the system is provided. Ten distinct types of XLPE cables, each with a length of 765 km, are considered in the simulation. The radius of each cable type, along with the supplied DC voltage and current, are detailed in Table 7.2 (The cable specifications, including ratings and dimensions, are based on standard industrial cable models). The relative permeability is considered as 1.00058 while the permittivity of insulation and the outer jacket is considered as 2.3 and 2.8 respectively, with a  $tan\delta$  of 0.0005 for both insulation and jacket at a frequency of 100 kHz. The electrical parameters of the cable sheath are determined using equations (7.5)–(7.8). Utilizing these parameters, the input impedance  $Z_{inS}$  is then calculated for each cable type, with the results presented in the last column of Table 7.2. The cable sheath is solidly grounded, making the value of  $R_G$  negligible; however, for the simulation and practical study, it is set to 0.2  $\Omega$  based on values reported in the existing literature [43].

In simulations, SG faults are created at seventeen different locations for each type of cable. The locations of SG faults are 5m, 10m, 25m, 100m, 250m, 500m, 1Km, 2.5Km, 10Km, 25Km, 50Km, 100Km, 150Km, 200Km, 250Km, 500Km, and 750Km. It is to be noted that only one type of cable length is considered in simulation, because under normal conditions, both ends of the cable sheath are solidly grounded, and a sheath-to-ground (SG) fault occurs only when the sheath makes direct contact with the ground. Thus, analyzing SG faults at various locations effectively simulates different shorter cable segments under healthy conditions. TDR analysis is conducted, and  $f_{peak}$  and |V'[Z, f]| are recorded for all ten cable types, each with seventeen distinct fault locations. The TDR graphs and its FFT response for type 7 cable are shown in Fig. 7.3 and Fig. 7.4.

To validate the proposed method, two distinct practical case studies are considered. The dimensions, operating voltage, current, and  $Z_{inS}$  of both cables are presented in Table 7.3.

Both cables feature XLPE insulation with an outer jacket made of polyethylene. Type 1 cable is 30m in length, while Type 2 cable is 40m in length. The relative permittivity of the insulation and outer jacket is 2.41 and 2.7, respectively, while  $tan\delta$  for both the insulation and jacket is 0.00048, as specified at 100 kHz. The inductance of the inductive coupler is 15 mH. The incident waveform is sent through a Tektronix-based function generator (model no. AFG3052C) and the total waveform is captured by a keysight Digital Oscilloscope (DSOX4054A) as shown in Fig. 7.7. Faults are created at a location of 5m, 10m, 15m, 20m, 22.5m, and 25m for type 1 cable and at 7m, 12.5m, 18m, 28m, 35m, and 38.5m for type 2 cable using a grounding rod whose impedance is of  $2m\Omega$ . The captured TDR waveform is fed to a computer, where FFT will be performed on the modified TDR waveform to obtain practical  $f_{peak}$  and |V'[Z, f]|.  $Z_{inS}$  along with these two values will act as a testing set for the DTR model to estimate its exact location. The captured TDR waveform is transferred to a computer, where the modified TDR signal undergoes FFT analysis to determine the practical peak frequency  $f_{peak}$  and the magnitude |V'[Z,f]|. These values, together with the calculated input impedance  $Z_{inS}$ , form the testing dataset for the DTR model to accurately estimate the fault location.

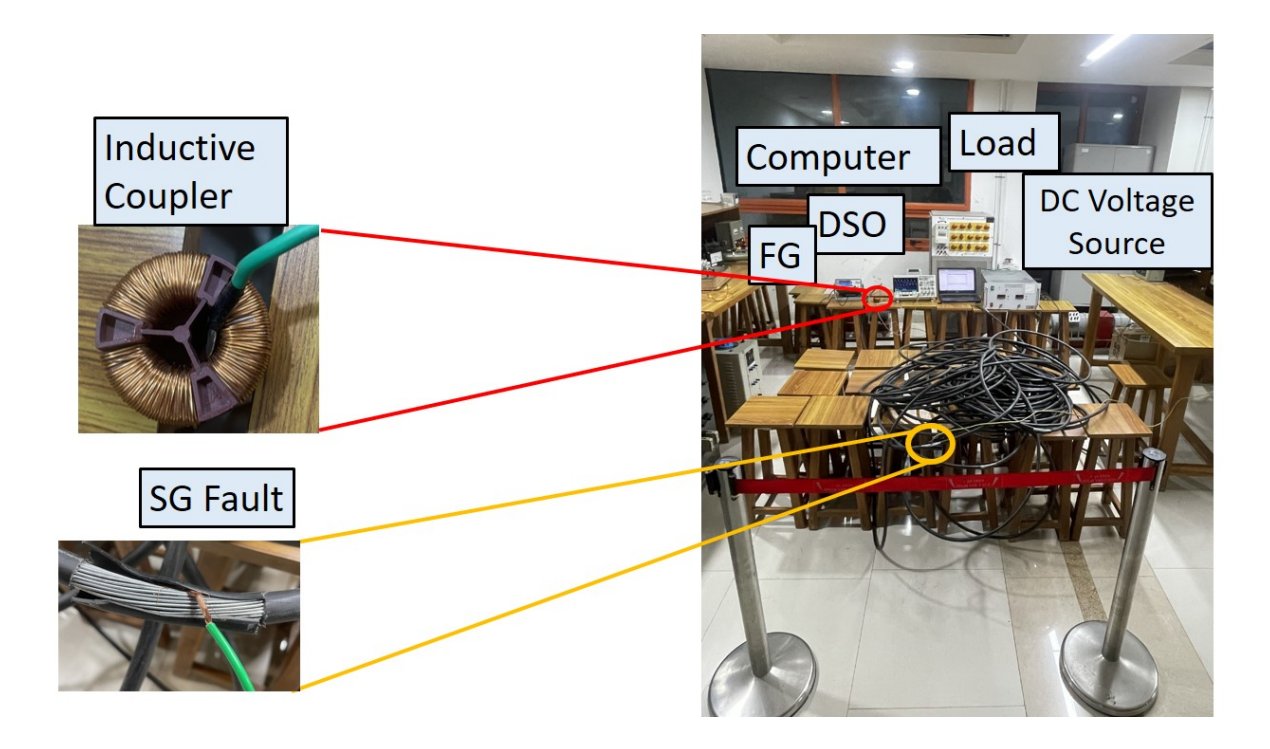


Figure 7.7 Experimental setup to perform online TDR on type 1 HVDC cable. FG stands for Function Generator.

**Table 7.2 Different Types of Cable Considered in Simulation** 

Types	Voltage	Current	$r_1$	$r_2$	$r_2$	$Z_{inS}\left(\Omega\right)$
	(KV)	(A)	(mm)	(mm)	(mm)	
1	1	50	5.33	6.28	7.35	0.20123
2	5	75	6.21	7.23	8.26	0.20392
3	22	150	7.35	9.32	14.32	1.5657
4	66	200	15.61	19.83	24.24	2.2438
5	110	350	22.37	26.61	33.66	2.6524
6	150	500	36.62	41.41	48.64	2.6789
7	220	550	48.76	53.28	61.72	2.7026
8	250	575	52.31	58.57	66.73	2.7125
9	350	600	56.48	63.33	74.56	2.8026
10	550	650	60.29	68.36	78.58	2.8654

Table 7.3 Two Types of Cable Considered for practical test

Types	Voltage (KV)	Current (mA)	<i>r</i> <sub>1</sub> (mm)	r <sub>2</sub> (mm)	r <sub>2</sub> (mm)	$Z_{inS}\left(\Omega\right)$
1	1.1	10	5.33	6.28	7.35	0.20123
2	11	10	6.58	7.88	12.25	0.20392

# 7.4 Experiments to estimate the location of SG fault in a HVDC cable.

This section presents the practical results, divided into two parts: the first discusses the results for Type I experimental cables, and the second covers the results for Type II experimental cables.

# 7.4.1 Estimating the location of SG fault in type 1 cable system

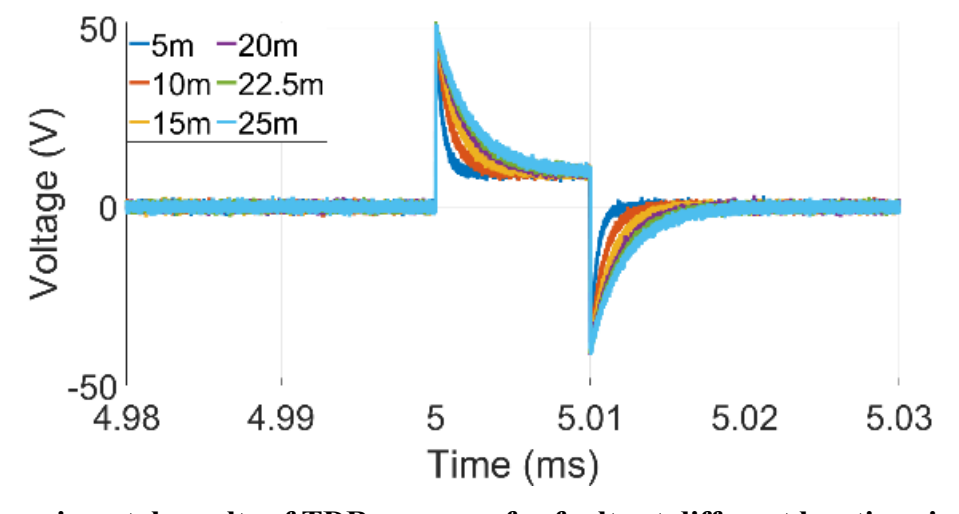


Figure 7.8 Experimental results of TDR response for faults at different locations in its complete time spectrum of a Type 1 cable.

The full time-domain response of the SG fault at various locations, as recorded by the

DSO, is presented in Fig. 7.8. Due to the overlapping of reflected signal as discussed in Sections III and IV, detecting reflections for faults located at shorter distances is challenging using conventional TDR alone. Therefore, each captured waveform was processed according to the proposed method before applying the FFT. The resulting FFT spectra of the waveforms for faults at different locations are shown in Fig. 7.9.

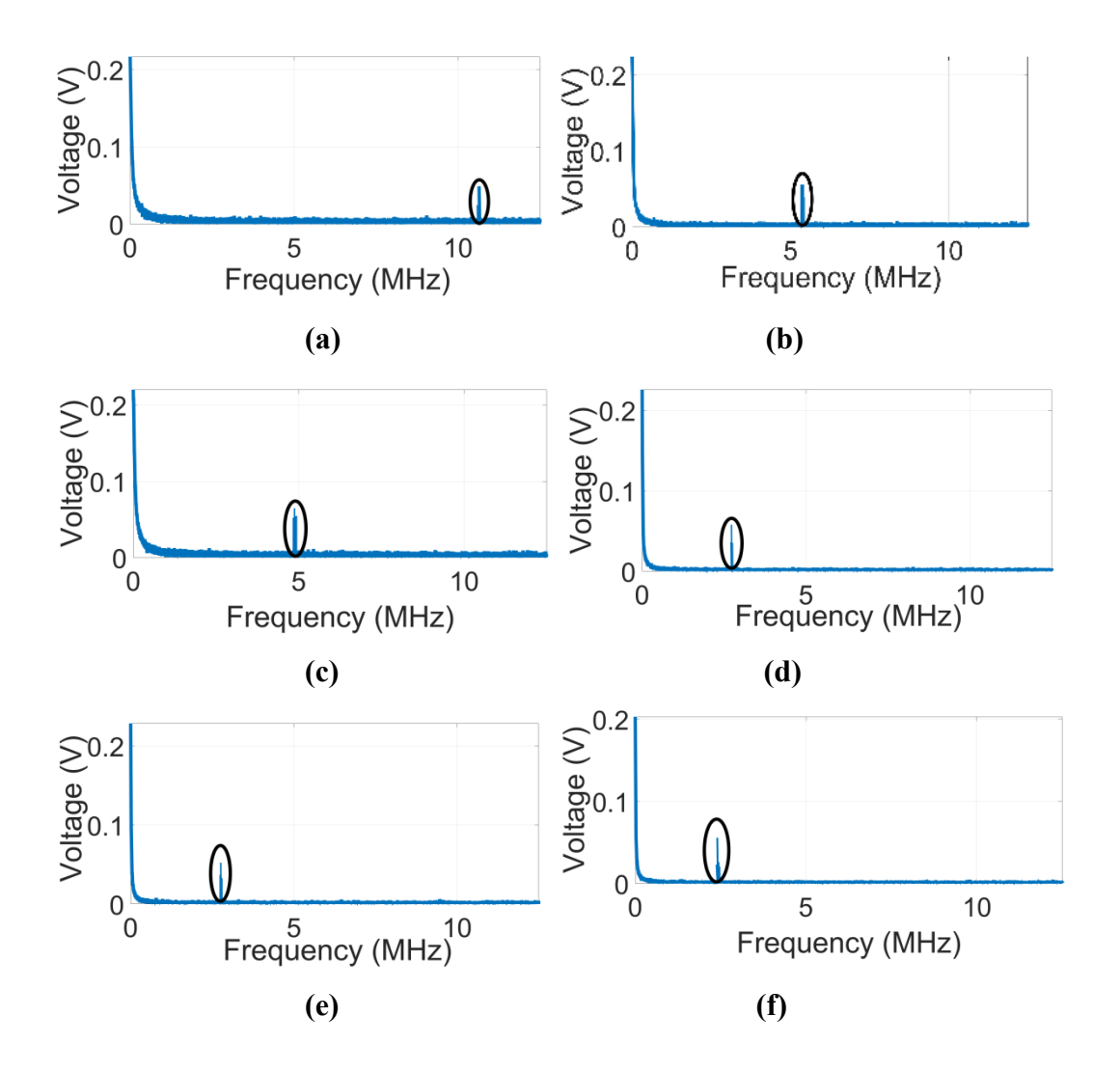


Figure 7.9 FFT of the modified time spectrum of practical cable of Type 1 having fault at (a) 5m, (b) 10m, (c) 15m, (d) 20m, (e) 22.5m (f) 25m.

From the FFT analysis of the practical cable with faults at different locations, the  $f_{peak}$  and |V'[Z,f]| were determined using Algorithm 1, as shown in Fig. 7.10. These extracted features, along with  $Z_{inS}$ , were then input into the DTR system to estimate the SG fault location, following the flowchart in Fig. 5. The accuracy of the DTR system in estimating the SG fault location is presented in Table 7.4.

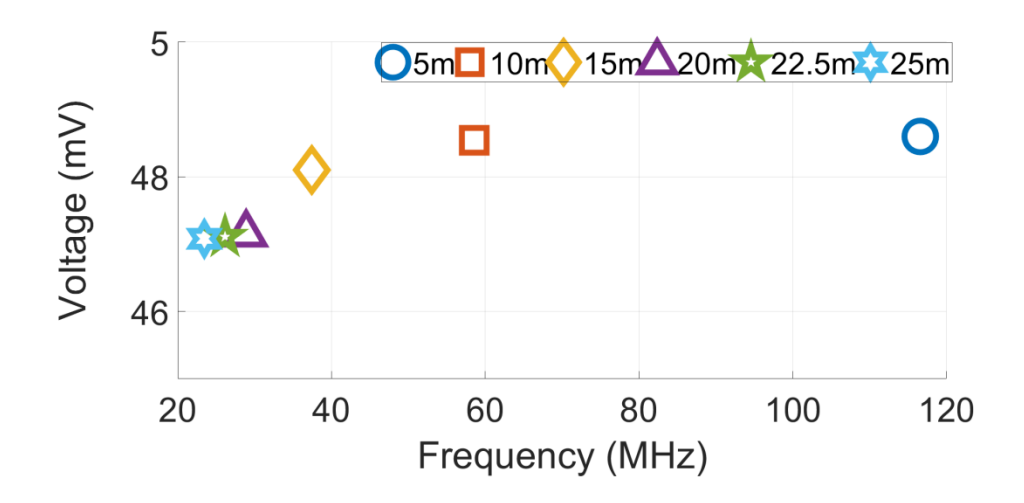


Figure 7.10 The magnitude of  $f_{peak}$  and |V'[Z, f]| of faults at different locations for Type 1 cable, obtained from the FFT graph and Algorithm 1.

Table 7.4 Accuracy of the Proposed Method For Cable Type 1

SL	Actual	Estimated	Accuracy
	Fault	Fault	%
No	Location	Location	
	(m)	(m)	
1.	5	4.9898	99.796
2.	10	10.0006	99.994
3.	15	14.7989	98.659
4.	20	19.8786	99.393
5.	22.5	22.5687	99.694
6.	25	25.0156	99.937

The proposed method achieved a minimum accuracy of 99.393% in the Type 1 cable system, demonstrating its effectiveness in practical applications for estimating SG fault locations in HVDC cables.

# 7.4.2 Estimating the location of SG fault in type 2 cable system

Similar to Type 1, the full-time domain response for faults at different locations captured in the DSO is shown in Fig.7.11. The FFT waveform of the proposed modified time domain signal for faults at different locations is shown in Fig. 7.12.

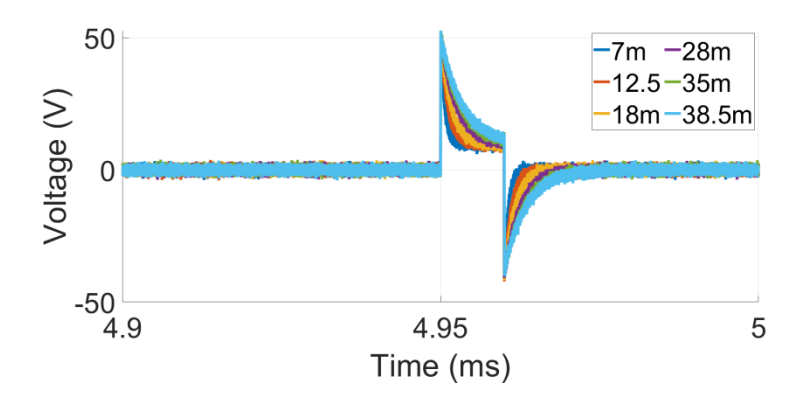


Figure 7.11 Experimental results of TDR response for faults at different locations in its complete time spectrum of a Type 2 cable.

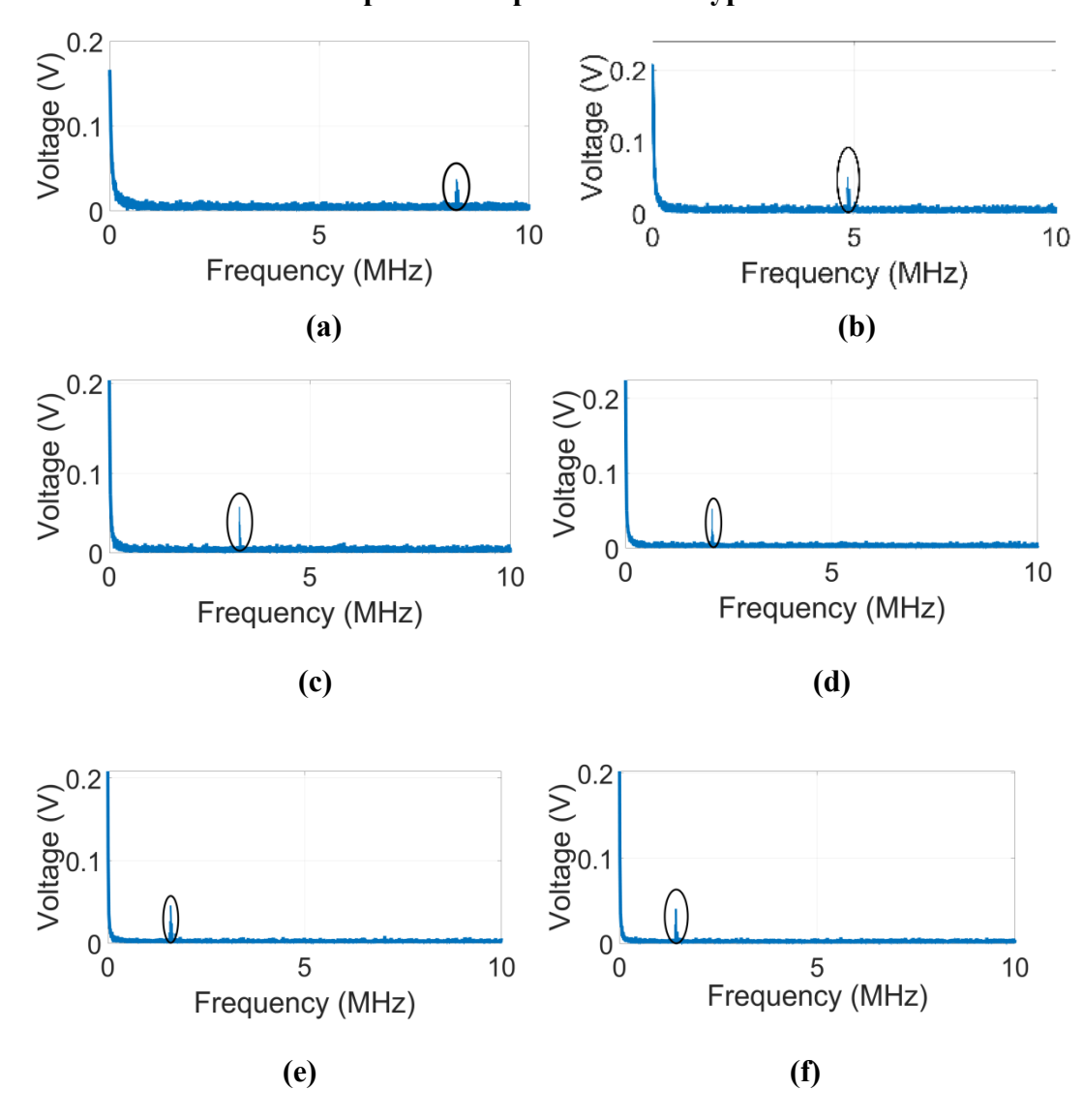


Figure 7.12 FFT of the modified time spectrum of practical cable of Type 1 having fault at (a) 7m, (b) 12.5m, (c) 18m, (d) 28m, (e) 35m (f) 38.5m.

The  $f_{peak}$  and |V'[Z, f]| were determined using Algorithm 1, as shown in Fig. 7.13, and

served as an input for the proposed DTR system, whose accuracy is shown in Table 7.5.

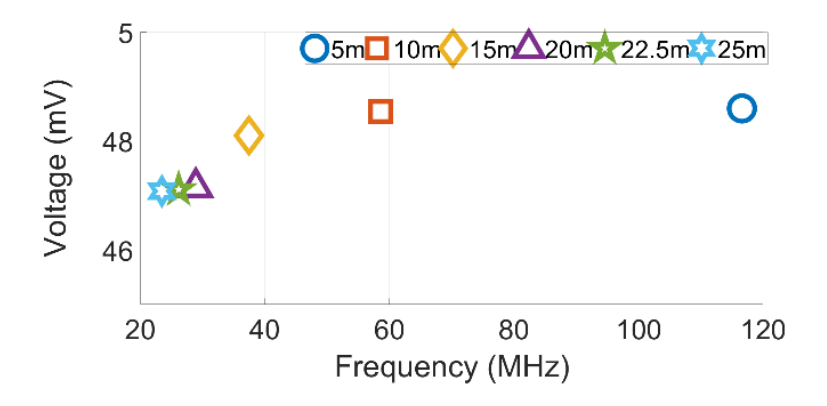


Figure 7.13 The magnitude of  $f_{peak}$  and |V'[Z, f]| of faults at different locations for Type 2 cable, obtained from FFT graph and Algorithm 1.

Table 7.5 Accuracy of the Proposed Method For Cable Type 2

SL. No	Actual Fault	Estimated Fault ocation (m)	Accuracy %
1.	7	7.0015	99.97857
2.	12.5	12.4667	99.7336
3.	18	17.9856	99.92
4.	28	28.0014	99.995
5.	35	35.0004	99.99886
6.	38.5	38.4963	99.99039

The following discussion critically evaluates the practical results and implications of the proposed method for real-world applications:

1. Two different ratings, dimension length, and power supply of cable are chosen to validate the proposed method to estimate the location of SG fault during online conditions. Even in the presence of noise during an uncontrolled practical environment, the minimum accuracy of detecting the location of SG fault is 99.39% as shown in Tables 7.4 and 7.5 over the two different types of cable.

- 2. For an SG fault near the ground, the location of  $f_{peak}$  is significantly higher compared to a fault at the far end as shown in Fig. 7.10 and 7.13. This is because the reflected signal from a near-source fault returns much sooner due to the shorter propagation distance, while |V'[Z, f]| will decrease with an increase in the fault length due to attenuation as shown in Fig. 7.10 and 7.13.
- 3. The only assumption made in this study for estimating the location of SG faults is that the cable is considered to be in a healthy condition along its entire length. In other words, the capacitance between the conductor and the sheath is assumed to remain consistent throughout the cable.

# Comparative Study of Different End Bonding Methods in a Non-Uniform Minor Section Length of a Cross-Bonded Cable

This chapter presents a comparative study of various end-bonding configurations for different minor section lengths in an existing cross-bonded (CB) cable system. In addition, a new end bonding system is also proposed for non-uniform minor section length to minimize circulating current and voltage in joints, to prevent premature breakdown. The details of the proposed ending configuration are explained below.

# 8.1 Sheath Circuit model of different types of end bonding of sheath

In this section, the circuit models for three distinct end bonding types in a CB cable with a non-uniform minor section length are proposed. To estimate the current and voltage in the joint sheath, the accurate analytical description of the per unit impedance ( $Z_S$ ) of the sheath is required for a trefoil cable laid formation and can be obtained as per equation (5.2). It is considered that the impedance of the cable for all the phases in each minor section are same i.e. impedance of the cable for the first minor section and all the phases are considered as  $Z_{Sa}$ , similarly  $Z_{Sb}$ , and  $Z_{Sn}$  for the second and third minor section which can be obtained analytically using (5.2). Therefore total sheath impedance of a particular phase or a loop of a major section ( $Z_{ST}$ ) can be represented as:

$$Z_{ST} = Z_{sa} + Z_{sh} + Z_{sn} \tag{8.1}$$

The induced voltage per unit length and capacitive effect current can be obtained as:

$$V_{i} = \sum_{i=1}^{3} M_{ij} I_{j} + \sum_{\substack{i=1,j=2\\i\neq j}}^{3} M_{SHij} I_{SHij}$$
(8.2)

$$I_{Ci} = j\omega C_i V_i \tag{8.3}$$

In equation (8.2) and (8.3), the electrical parameters described can be obtained as per equation (5.1), (5.3), and (5.4). Throughout the chapter, i, and j = 1, 2, and 3 for three different phases. To mitigate the excessive circulating current and voltage (due to inductive and capacitive effect) in the sheath caused due to non-uniformity in the length of the third minor section, three end bonding methods at the last set of straight-through joints are

described below:

# 8.1.1 The second set of Straight joints are individually solidly grounded

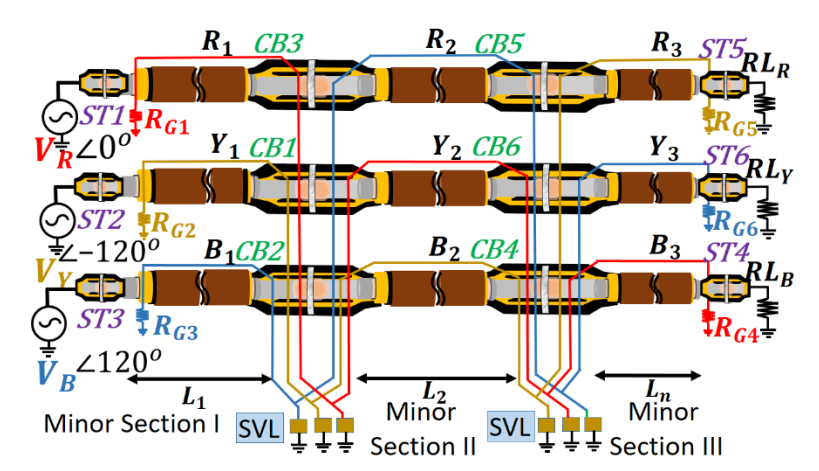


Figure 8.1 Schematic diagram of a non-uniform length minor sections in a CB cable with solid grounding at the end.

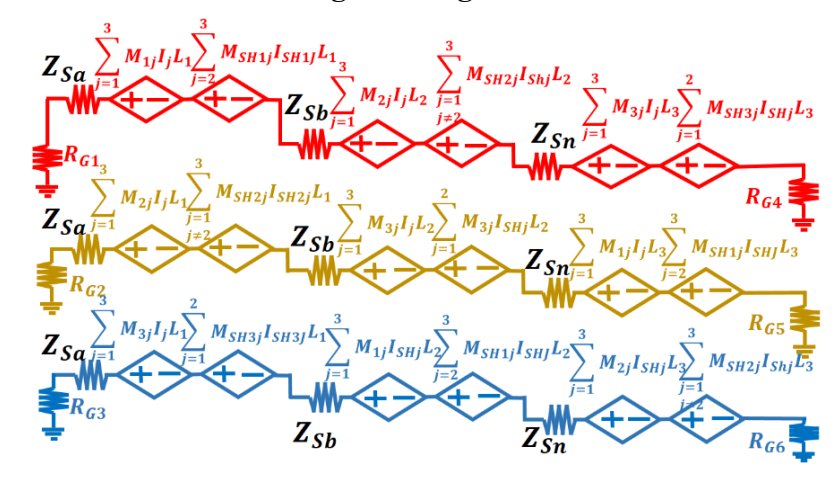


Figure 8.2 Equivalent circuit for inductive effect in a non-uniform length minor section CB cable with solid grounding at the end.

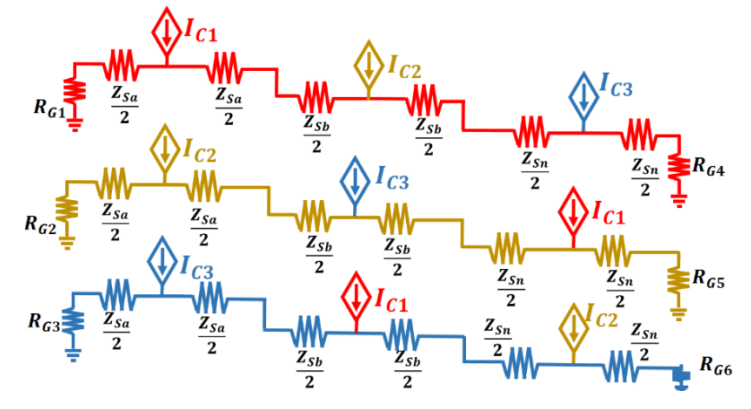


Figure 8.3 Equivalent circuit for capacitive effect in a non-uniform length minor section CB cable with solid grounding at the end.

The simplest method to mitigate the circulating current for non-uniform third minor section length CB cable is to solidly ground the terminals of the second set of ST joints with a low

value of grounding resistance. ( $R_{G4}$ ,  $R_{G5}$ , and  $R_{G6}$ ) individually as shown in Fig. 8.1. The value of the grounding resistance for the HV cable system is generally kept at  $0.2\Omega$  [43]. The circuit diagram for inductive and capacitive effects is shown in Fig. 8.2 and Fig. 8.3 respectively.

# 8.1.2 Second Straight joints are individually grounded with SVL

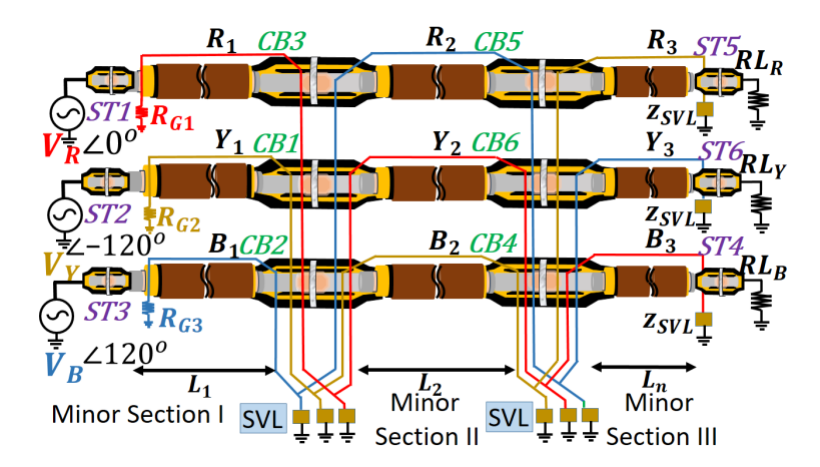


Figure 8.4 Schematic diagram of a non-uniform length minor sections CB cable grounded with SVL at the end.

The high circulating current and voltage for a non-uniform third minor section length can also be mitigated, by individually grounding the terminals of the second set of ST joints with an SVL ( $Z_{SVL}$ ) as shown in Fig. 8.4. Thus the end of the sheath will be open during steady state condition and solidly grounded during transients. The circuit diagram for inductive and capacitive effects will be the same as solidly grounded, except in the place of  $R_{G4}$ ,  $R_{G5}$ , and  $R_{G6}$  will be  $Z_{SVL}$ .

# 8.1.3 Last Straight through joints are connected and grounded together with SVL-Proposed Method

To eliminate the excessive sheath current and voltage in the joints of a CB cable for a non-uniform length third minor section, the proposed method is to merge the above two methods (connecting other phases to cancel out inductive effect from solidly grounded and introducing of SVL from grounding with SVL) by connecting the terminals of second set ST joints together in the link box and then connect the common terminal with an SVL as shown in Fig. 8.5. Under steady state condition the SVL will act as an open circuit and solidly grounded during transients. The inductive and capacitive model of the proposed method is shown in Fig. 8.6 and 8.7

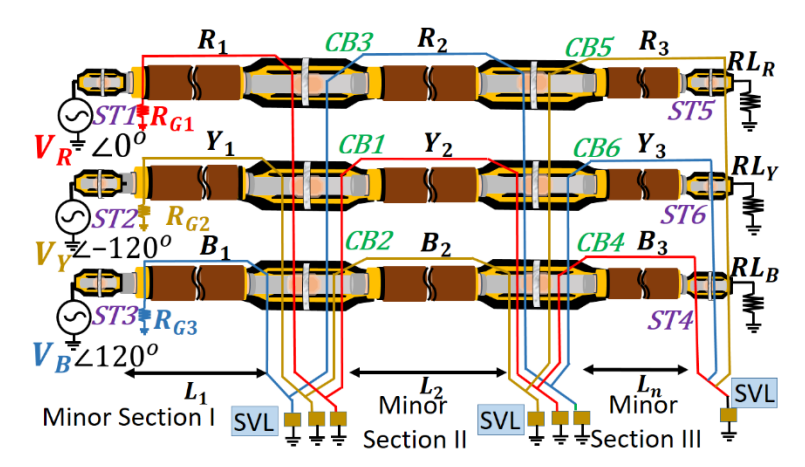


Figure 8.5 Schematic diagram of a non-uniform length minor sections CB cable with three straight-through joints terminals connected together at the end with SVL.

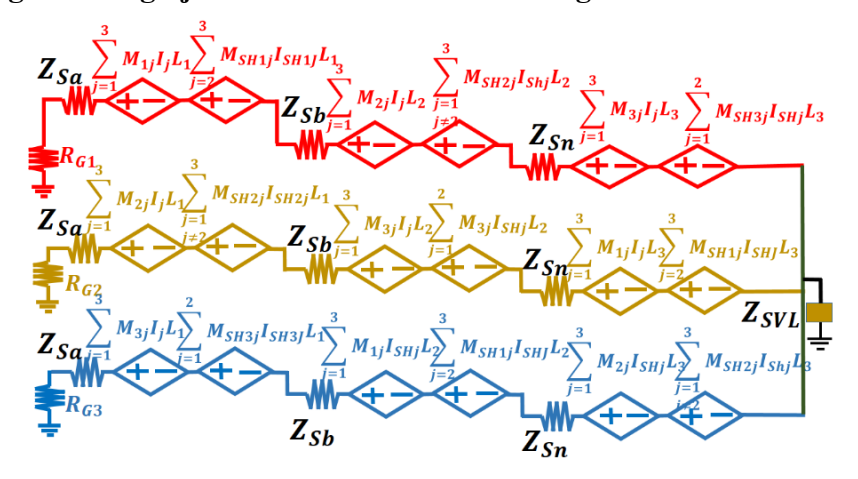


Figure 8.6 Equivalent circuit for inductive effect in a non-uniform length minor section with three straight-through joints connected together at the end with SVL.

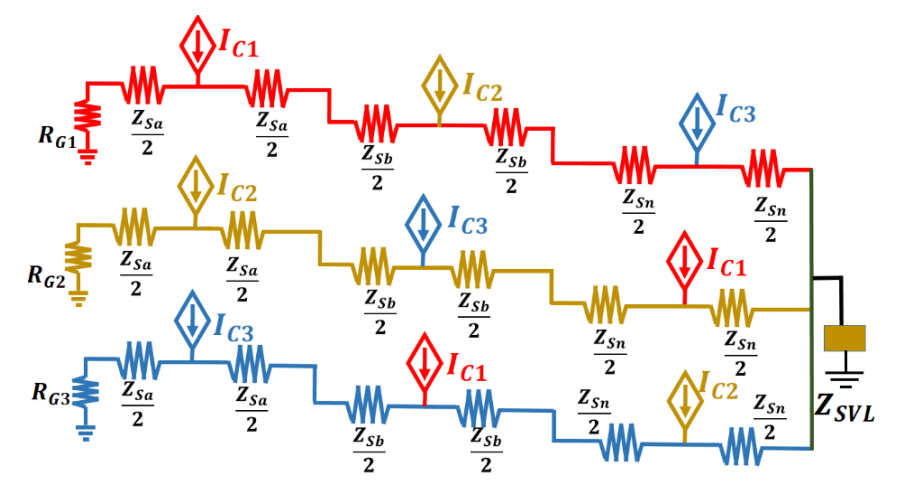


Figure 8.7 Equivalent circuit for capacitive effect in a non-uniform length minor section cable with three straight-through joints connected together at the end with SVL.

The circulating current and the voltage across the joints are derived analytically in the section below to compare the best end-terminal bonding method.

#### 8.2 Analytical Model of Total Current in the Joints for Different Types of End Bonding

While performing the analytical operations, it is considered that during steady state conditions  $Z_{svl} \gg Z_{ST}$ , and the impedance of the grounding resistance  $\ll$  total impedance of the cable sheath in a minor section and  $Z_{svl}$ . The current and voltage in the joints for solidly grounded, grounded with SVL, and the proposed method type of bonding are presented by subscript a, b, and c respectively.

#### 8.2.1 Current in the loop 1, 2, and 3 due to inductive effect

The voltage induced in loop 1, 2, and 3 can be analytically obtained as:

$$\begin{bmatrix} V_{L1} & 0 & 0 \\ 0 & V_{L2} & 0 \\ 0 & 0 & V_{L3} \end{bmatrix} = \begin{bmatrix} V_1 & 0 & 0 \\ 0 & V_2 & 0 \\ 0 & 0 & V_3 \end{bmatrix} \begin{bmatrix} L_1 & L_2 & L_n \\ L_n & L_1 & L_2 \\ L_2 & L_n & L_1 \end{bmatrix}$$
(8.4)

 $V_1$ ,  $V_2$ , and  $V_3$  can be obtained using (8.1).

By solving the equations corresponding to Fig. 8.2 and 8.6 and from (8.4), the inductive current flowing through loops 1, 2, and 3 (subscript M represent magnetic current and L1, L2, and L3, represent three loops) for solidly grounded, grounded with SVL and proposed method type of bonding can be obtained as:

$$\begin{bmatrix} I_{ML1a} \\ I_{ML2a} \\ I_{ML3a} \end{bmatrix} = \begin{bmatrix} \mathbb{Z}_0 & 0 & 0 \\ 0 & \mathbb{Z}_0 & 0 \\ 0 & 0 & \mathbb{Z}_0 \end{bmatrix} \begin{bmatrix} V_{L1} \\ V_{L2} \\ V_{L3} \end{bmatrix}, \begin{bmatrix} I_{ML1b} \\ I_{ML2b} \\ I_{ML3b} \end{bmatrix} = \begin{bmatrix} \mathbb{Z}_{svl} & 0 & 0 \\ 0 & \mathbb{Z}_{svl} & 0 \\ 0 & 0 & \mathbb{Z}_{svl} \end{bmatrix} \begin{bmatrix} V_{L1} \\ V_{L2} \\ V_{L3} \end{bmatrix}$$
(8.5)

$$\begin{bmatrix} I_{ML1c} \\ I_{ML2c} \\ I_{ML3c} \end{bmatrix} = \begin{bmatrix} \mathbb{Z}_1 & 0 & 0 \\ 0 & \mathbb{Z}_1 & 0 \\ 0 & 0 & \mathbb{Z}_1 \end{bmatrix} \cdot \begin{bmatrix} +2 & -1 & -1 \\ +1 & -2 & +1 \\ +1 & +1 & -2 \end{bmatrix} \cdot \begin{bmatrix} V_{L1} \\ V_{L2} \\ V_{L3} \end{bmatrix}$$
(8.6)

In (9) and (10), 
$$\mathbb{Z}_0 = \frac{1}{Z_{sT}}$$
,  $\mathbb{Z}_{svl} = \frac{1}{Z_{svl}}$ , and  $\mathbb{Z}_1 = \frac{1}{3Z_s}$ 

### 8.2.2 Current in the joints due to capacitive effect

By solving the equations corresponding to Fig. 8.3, the capacitive current through different ST and CB joints for a solidly grounded cable system can be obtained as (subscript C describes the capacitive current and ST and CB describe the cross-bonded and straight-through joints):

$$\begin{bmatrix} I_{CST1a} \\ I_{CST2a} \\ I_{CST3a} \end{bmatrix} = \begin{bmatrix} \mathbb{Z}_2 & 0 & 0 \\ 0 & \mathbb{Z}_2 & 0 \\ 0 & 0 & \mathbb{Z}_2 \end{bmatrix} \begin{bmatrix} \alpha_1 & \beta_1 & \gamma_1 \\ \gamma_1 & \alpha_1 & \beta_1 \\ \beta_1 & \gamma_1 & \alpha_1 \end{bmatrix} \cdot \begin{bmatrix} I_{C1} \\ I_{C2} \\ I_{C3} \end{bmatrix}$$
(8.7)

$$\begin{bmatrix} I_{CCB1a} \\ I_{CCB2a} \\ I_{CCB3a} \end{bmatrix} = \begin{bmatrix} \mathbb{Z}_2 & 0 & 0 \\ 0 & \mathbb{Z}_2 & 0 \\ 0 & 0 & \mathbb{Z}_2 \end{bmatrix} \begin{bmatrix} \alpha_2 & \beta_2 & \gamma_2 \\ \gamma_2 & \alpha_2 & \beta_2 \\ \beta_2 & \gamma_2 & \alpha_2 \end{bmatrix} . \begin{bmatrix} I_{C1} \\ I_{C2} \\ I_{C3} \end{bmatrix}$$
(8.8)

$$\begin{bmatrix} I_{CCB4a} \\ I_{CCB5a} \\ I_{CCB6a} \end{bmatrix} = \begin{bmatrix} \mathbb{Z}_2 & 0 & 0 \\ 0 & \mathbb{Z}_2 & 0 \\ 0 & 0 & \mathbb{Z}_2 \end{bmatrix} \begin{bmatrix} \alpha_3 & \beta_3 & \gamma_3 \\ \gamma_3 & \alpha_3 & \beta_3 \\ \beta_3 & \gamma_3 & \alpha_3 \end{bmatrix} \cdot \begin{bmatrix} I_{C1} \\ I_{C2} \\ I_{C3} \end{bmatrix}$$
(8.9)

$$\begin{bmatrix} I_{CST4a} \\ I_{CST5a} \\ I_{CST6a} \end{bmatrix} = \begin{bmatrix} \mathbb{Z}_{svl1} & 0 & 0 \\ 0 & \mathbb{Z}_{svl1} & 0 \\ 0 & 0 & \mathbb{Z}_{svl1} \end{bmatrix} \begin{bmatrix} \alpha_4 & \beta_4 & \gamma_4 \\ \gamma_4 & \alpha_4 & \beta_4 \\ \beta_4 & \gamma_4 & \alpha_4 \end{bmatrix} \cdot \begin{bmatrix} I_{C1} \\ I_{C2} \\ I_{C3} \end{bmatrix}$$
(8.10)

In (8.7)-(8.10), 
$$\alpha_1 = 2Z_{sa} + 3$$
  $Z_{sb} + Z_{sn}$ ,  $\beta_1 = 5Z_{sa} + 6$   $Z_{sb} + 7Z_{sn}$ ,  $\gamma_1 = 5Z_{sa} + 3$   $Z_{sb} + 4Z_{sn}$ ,  $\mathbb{Z}_2 = \frac{1}{6Z_s}$ ,  $\alpha_2 = 2Z_{sa} + 3Z_{sb} + Z_{sn}$ ,  $\beta_2 = -Z_{sa} + Z_{sn}$ ,  $\gamma_2 = 5Z_{sa} + 3$   $Z_{sb} + 4Z_{sn}$ ,  $\alpha_3 = 2Z_{sa} + 3$   $Z_{sb} + Z_{sn}$ ,  $\beta_3 = Z_{sa} - Z_{sn}$ ,  $\gamma_3 = Z_{sa} + 3$   $Z_{sb} + 2Z_{sn}$ ,  $\alpha_4 = 5Z_{sa} + 3$   $Z_{sb} + Z_{sn}$ ,  $\beta_4 = 5Z_{sa} + 3$   $Z_{sb} + Z_{sn}$ ,  $\gamma_4 = 5Z_{sa} + 3$   $Z_{sb} + Z_{sn}$ ,  $\mathbb{Z}_{svl1} = \frac{1}{6Z_{svl1}}$ 

Similarly, for grounded with SVL system, the capacitive current through different joints can be analytically obtained as:

$$\begin{bmatrix} I_{CST1b} \\ I_{CST2b} \\ I_{CST2b} \end{bmatrix} = \begin{bmatrix} 1 & 1 & 1 \\ 1 & 1 & 1 \\ 1 & 1 & 1 \end{bmatrix} \cdot \begin{bmatrix} I_{C1} \\ I_{C2} \\ I_{C2} \end{bmatrix},$$
(8.11)

$$\begin{bmatrix} I_{CCB1b} \\ I_{CCB2b} \\ I_{CCB3b} \end{bmatrix} = \begin{bmatrix} 011 \\ 101 \\ 110 \end{bmatrix} \begin{bmatrix} I_{C1} \\ I_{C2} \\ I_{C3} \end{bmatrix}, \quad \begin{bmatrix} I_{CCB4b} \\ I_{CCB5b} \\ I_{CCB6b} \end{bmatrix} = \begin{bmatrix} 001 \\ 100 \\ 010 \end{bmatrix} \begin{bmatrix} I_{C1} \\ I_{C2} \\ I_{C3} \end{bmatrix}$$
(8.12)

$$\begin{bmatrix} I_{CST4b} \\ I_{CST5b} \\ I_{CST6b} \end{bmatrix} = \begin{bmatrix} \mathbb{Z}_{svl} & 0 & 0 \\ 0 & \mathbb{Z}_{svl} & 0 \\ 0 & 0 & \mathbb{Z}_{svl} \end{bmatrix} \begin{bmatrix} \delta_2 & \theta_2 & \sigma_2 \\ \sigma_2 & \delta_2 & \theta_2 \\ \theta_2 & \sigma_2 & \delta_2 \end{bmatrix} \cdot \begin{bmatrix} I_{C1} \\ I_{C2} \\ I_{C3} \end{bmatrix}$$
(8.13)

In 
$$(8.13)$$
,  $\delta_2 = Z_{sa}$ ,  $\vartheta_2 = 2Z_{sa} + Z_{sb}$ ,  $\sigma_2 = 2Z_{sa} + 2Z_{sb} + Z_{sn}$ .

From Fig. 8.6, the capacitive effect current, flowing through different joints for the proposed method can be obtained as:

$$\begin{bmatrix} I_{CST1c} \\ I_{CST2c} \\ I_{CST3c} \end{bmatrix} = \begin{bmatrix} \mathbb{Z}_3 & 0 & 0 \\ 0 & \mathbb{Z}_3 & 0 \\ 0 & 0 & \mathbb{Z}_3 \end{bmatrix} \begin{bmatrix} \delta_1 & \theta_1 & \sigma_1 \\ \sigma_1 & \delta_1 & \theta_1 \\ \theta_1 & \sigma_1 & \delta_1 \end{bmatrix} . \begin{bmatrix} I_{C1} \\ I_{C2} \\ I_{C3} \end{bmatrix}$$
(8.14)

$$\begin{bmatrix} I_{CCB1c} \\ I_{CCB2c} \\ I_{CCB3c} \end{bmatrix} = \begin{bmatrix} \mathbb{Z}_3 & 0 & 0 \\ 0 & \mathbb{Z}_3 & 0 \\ 0 & 0 & \mathbb{Z}_3 \end{bmatrix} \begin{bmatrix} \delta_3 & \theta_3 & \sigma_3 \\ \sigma_3 & \delta_3 & \theta_3 \\ \theta_3 & \sigma_3 & \delta_3 \end{bmatrix} \cdot \begin{bmatrix} I_{C1} \\ I_{C2} \\ I_{C3} \end{bmatrix}$$
(8.15)

$$\begin{bmatrix} I_{CCB4c} \\ I_{CCB5c} \\ I_{CCB6c} \end{bmatrix} = \begin{bmatrix} \mathbb{Z}_3 & 0 & 0 \\ 0 & \mathbb{Z}_3 & 0 \\ 0 & 0 & \mathbb{Z}_3 \end{bmatrix} \begin{bmatrix} \delta_4 & \vartheta_4 & \sigma_4 \\ \sigma_4 & \delta_4 & \vartheta_4 \\ \vartheta_4 & \sigma_4 & \delta_4 \end{bmatrix} . \begin{bmatrix} I_{C1} \\ I_{C2} \\ I_{C3} \end{bmatrix}$$
(8.16)

$$\begin{bmatrix} I_{CST4C} \\ I_{CST5C} \\ I_{CST6C} \end{bmatrix} = \begin{bmatrix} \mathbb{Z}_3 & 0 & 0 \\ 0 & \mathbb{Z}_3 & 0 \\ 0 & 0 & \mathbb{Z}_3 \end{bmatrix} \begin{bmatrix} \delta_2 & \theta_2 & \sigma_2 \\ \sigma_2 & \delta_2 & \theta_2 \\ \theta_2 & \sigma_2 & \delta_2 \end{bmatrix} . \begin{bmatrix} I_{C1} \\ I_{C2} \\ I_{C3} \end{bmatrix}$$
(8.17)

In (8.14) - (8.17), 
$$\delta_1 = Z_{sa} + 2Z_{sb} + 2Z_{sn}$$
,  $\vartheta_1 = Z_{sb} + Z_{sn}$ ,  $\sigma_1 = Z_{sn}$ ,  $\mathbb{Z}_3 = \frac{1}{2Z_{sT}}$ ,  $\delta_3 = -Z_{sa}$ ,  $\vartheta_3 = Z_{sb} + 2Z_{sc}$ ,  $\sigma_3 = Z_{sn}$ ,  $\delta_4 = -Z_{sa}$ ,  $\vartheta_3 = -Z_{sa} + Z_{sb}$ ,  $\sigma_4 = Z_{sn}$ ,  $\delta_2 = Z_{sa}$ ,  $\vartheta_2 = 2Z_{sa} + Z_{sb}$ ,  $\sigma_2 = 2Z_{sa} + 2Z_{sb} + Z_{sc}$ 

Therefore, the total current flowing in the particular joints is the sum of the capacitive effect current in the particular joint and the inductive effect current flowing in the particular loop.

#### 8.3 Analytical Model of Voltage in the Joints for Different Types of End Bonding

Similar to the methods in Section 8.2, the voltage in the joints due to inductive and capacitive effects for different types of end bonding can be obtained as:

#### 8.3.1 Voltage in the joints due to inductive effect

The voltage between the ST joints 1, 2, and 3, and CB joints 1-6 to ground due to inductive effect will be the same for three different types of end bonding and can be obtained by solving the equation corresponding to Fig. 8.2 and Fig. 8.6 and represented as:

$$\begin{bmatrix} V_{MST1} \\ V_{MST2} \\ V_{MST3} \end{bmatrix} = \begin{bmatrix} \mathbb{Z}_4 & 0 & 0 \\ 0 & \mathbb{Z}_4 & 0 \\ 0 & 0 & \mathbb{Z}_4 \end{bmatrix} . \begin{bmatrix} V_1 \\ V_2 \\ V_3 \end{bmatrix}$$
(8.18)

$$\begin{bmatrix} V_{MCB1} \\ V_{MCB2} \\ V_{MCB3} \end{bmatrix} = \begin{bmatrix} \mathbb{Z}_5 & 0 & 0 \\ 0 & \mathbb{Z}_5 & 0 \\ 0 & 0 & \mathbb{Z}_5 \end{bmatrix} \begin{bmatrix} Z_{sb}.L_1 & -Z_{sa}.L_2 & 0 \\ 0 & Z_{sb}.L_1 & -Z_{sa}.L_2 \\ -Z_{sb}.L_1 & 0 & Z_{sa}.L_2 \end{bmatrix} . \begin{bmatrix} V_1 \\ V_2 \\ V_3 \end{bmatrix}$$
(8.19)

$$\begin{bmatrix} V_{MCB4} \\ V_{MCB5} \\ V_{MCB6} \end{bmatrix} = \begin{bmatrix} \mathbb{Z}_6 & 0 & 0 \\ 0 & \mathbb{Z}_6 & 0 \\ 0 & 0 & \mathbb{Z}_6 \end{bmatrix} \begin{bmatrix} Z_{sn} L_2 & -Z_{sb} L_n & 0 \\ 0 & Z_{sn} L_2 & -Z_{sa} L_n \\ -Z_{sn} L_2 & 0 & Z_{sa} L_n \end{bmatrix} . \begin{bmatrix} V_1 \\ V_2 \\ V_3 \end{bmatrix}$$
(8.20)

In (8.18)-(8.20), 
$$\mathbb{Z}_4 = \frac{L_1}{Z_{sa}}$$
,  $\mathbb{Z}_5 = \frac{1}{Z_{sa} - Z_{sb}}$ ,  $\mathbb{Z}_6 = \frac{1}{Z_{sa} - Z_{sn}}$ 

However, the voltage in the last set of ST joints will be different for different bonds ending and can be represented as:

$$\begin{bmatrix} V_{MST4a} \\ V_{MST5a} \\ V_{MST6a} \end{bmatrix} = \begin{bmatrix} \mathbb{Z}_7 & 0 & 0 \\ 0 & \mathbb{Z}_7 & 0 \\ 0 & 0 & \mathbb{Z}_7 \end{bmatrix} . \begin{bmatrix} V_1 \\ V_2 \\ V_3 \end{bmatrix}, \begin{bmatrix} V_{MST4b} \\ V_{MST5b} \\ V_{MST6b} \end{bmatrix} = \begin{bmatrix} L_n & 0 & 0 \\ 0 & L_n & 0 \\ 0 & 0 & L_n \end{bmatrix} . \begin{bmatrix} V_1 \\ V_2 \\ V_3 \end{bmatrix}$$
(8.21)

In (8.21), 
$$\mathbb{Z}_7 = \frac{L_3}{Z_{sn}}$$
.

$$V_{MST4,5,6C} = \frac{V_3 L_3 + V_1 L_3 + V_2 L_3}{3Z_{crit}} \tag{8.22}$$

#### 8.3.2 Voltage in the joints due to inductive effect

Similar to the current method, the capacitive effect of voltage in the ST and CB joints for a solidly grounded cable system can be obtained as:

$$\begin{bmatrix} V_{CST1a} \\ V_{CST2a} \\ V_{CST3a} \end{bmatrix} = \begin{bmatrix} R_{G1} \mathbb{Z}_3 & 0 & 0 \\ 0 & R_{G2} \mathbb{Z}_3 & 0 \\ 0 & 0 & R_{G3} \mathbb{Z}_3 \end{bmatrix} \begin{bmatrix} \phi_1 \phi_2 \phi_3 \\ \phi_3 \phi_1 \phi_2 \\ \phi_2 \phi_3 \phi_1 \end{bmatrix} . \begin{bmatrix} I_{C1} \\ I_{C2} \\ I_{C3} \end{bmatrix}$$
(8.23)

$$\begin{bmatrix} V_{CCB1a} \\ V_{CCB2} \\ V_{CCB3a} \end{bmatrix} = \begin{bmatrix} \mathbb{Z}_3 & 0 & 0 \\ 0 & \mathbb{Z}_3 & 0 \\ 0 & 0 & \mathbb{Z}_3 \end{bmatrix} \begin{bmatrix} \varphi_1 & \varphi_2 & \varphi_3 \\ \varphi_3 & \varphi_1 & \varphi_2 \\ \varphi_2 & \varphi_3 & \varphi_1 \end{bmatrix} . \begin{bmatrix} I_{C1} \\ I_{C2} \\ I_{C3} \end{bmatrix}$$
 (8.24)

$$\begin{bmatrix} V_{CCB4a} \\ V_{CCB5a} \\ V_{CCB6a} \end{bmatrix} = \begin{bmatrix} \mathbb{Z}_3 & 0 & 0 \\ 0 & \mathbb{Z}_3 & 0 \\ 0 & 0 & \mathbb{Z}_3 \end{bmatrix} \begin{bmatrix} \varphi_4 & \varphi_5 & \varphi_6 \\ \varphi_6 & \varphi_4 & \varphi_5 \\ \varphi_5 & \varphi_6 & \varphi_4 \end{bmatrix} . \begin{bmatrix} I_{C1} \\ I_{C2} \\ I_{C3} \end{bmatrix}$$
 (8.25)

$$\begin{bmatrix} V_{CST4} \\ V_{CST5} \\ V_{CST6} \end{bmatrix} = \begin{bmatrix} R_{G4} \mathbb{Z}_3 & 0 & 0 \\ 0 & R_{G5} \mathbb{Z}_3 & 0 \\ 0 & 0 & R_{G6} \mathbb{Z}_3 \end{bmatrix} \begin{bmatrix} \phi_4 \phi_5 \phi_6 \\ \phi_6 \phi_4 \phi_5 \\ \phi_5 \phi_6 \phi_4 \end{bmatrix} . \begin{bmatrix} I_{C1} \\ I_{C2} \\ I_{C3} \end{bmatrix}$$
 (8.26)

In (8.23)-(8.26),  $\phi_1 = Z_{sa} + 2Z_{sb} + Z_{sn}$ ,  $\phi_2 = Z_{sb} + 2Z_{sn}$ ,  $\phi_3 = Z_{sn}$ ,  $\varphi_1 = Z_{sa}Z_{sb} + Z_{sa}Z_{sn}$ ,  $\varphi_2 = Z_{sa}Z_{sb} + 2Z_{sa}Z_{sn}$ ,  $\varphi_3 = Z_{sa}Z_{sn}$ ,  $\varphi_4 = Z_{sa}Z_{sn}$ ,  $\varphi_5 = Z_{sb}Z_{sn} + 2Z_{sa}Z_{sn}$ ,  $\varphi_6 = Z_{sa}Z_{sn} + Z_{sb}Z_{sn}$ 

Similarly, for grounded with SVL system, the capacitive effect of voltage across different joints can be obtained as:

$$\begin{bmatrix} V_{CST1b} \\ V_{CST2b} \\ V_{CST3b} \end{bmatrix} = \begin{bmatrix} R_{G1} & 0 & 0 \\ 0 & R_{G2} & 0 \\ 0 & 0 & R_{G3} \end{bmatrix} \cdot \begin{bmatrix} I_{C1} \\ I_{C2} \\ I_{C3} \end{bmatrix} \begin{bmatrix} V_{CST4} \\ V_{CST5} \\ V_{CST6} \end{bmatrix} = \begin{bmatrix} \phi_7 \phi_8 \phi_9 \\ \phi_9 \phi_7 \phi_8 \\ \phi_8 \phi_9 \phi_7 \end{bmatrix} \begin{bmatrix} I_{C1} \\ I_{C2} \\ I_{C3} \end{bmatrix}$$
(8.27)

$$\begin{bmatrix} V_{CCB1} \\ V_{CCB2} \\ V_{CCB3} \end{bmatrix} = \begin{bmatrix} Z_{sa} & 0 & 0 \\ 0 & Z_{sa} & 0 \\ 0 & 0 & Z_{sa} \end{bmatrix} \begin{bmatrix} 0.5 & 1 & 1 \\ 1 & 0.5 & 1 \\ 1 & 1 & 0.5 \end{bmatrix} . \begin{bmatrix} I_{C1} \\ I_{C2} \\ I_{C3} \end{bmatrix}$$
(8.28)

$$\begin{bmatrix} V_{CCB4} \\ V_{CCB5} \\ V_{CCB6} \end{bmatrix} = \begin{bmatrix} \varphi_7 & \varphi_8 & \varphi_9 \\ \varphi_9 & \varphi_7 & \varphi_8 \\ \varphi_8 & \varphi_7 & \varphi_7 \end{bmatrix} \cdot \begin{bmatrix} I_{C1} \\ I_{C2} \\ I_{C3} \end{bmatrix}$$
(8.29)

In (8.27)-(8.29),  $\phi_7 = 0.5Z_{sa}$ ,  $\phi_8 = 0.5Z_{sb} + Z_{sa}$ ,  $\phi_9 = Z_{sa} + Z_{sb} + 0.5Z_{sn}$ ,  $\varphi_5 = Z_{sa} + 0.5Z_{sb}$ ,  $\varphi_6 = Z_{sa} + 0.5Z_{sb}$ ,  $\varphi_7 = 0.5Z_{sa}$ 

Similarly, for the proposed method, the capacitive effect of voltage across different joints can be analytically obtained as:

$$\begin{bmatrix} V_{CST1C} \\ V_{CST2C} \\ V_{CST3C} \end{bmatrix} = \begin{bmatrix} R_{G1} \mathbb{Z}_2 & 0 & 0 \\ 0 & R_{G2} \mathbb{Z}_2 & 0 \\ 0 & 0 & R_{G3} \mathbb{Z}_2 \end{bmatrix} \begin{bmatrix} \phi_{10} & \phi_{11} & \phi_{12} \\ \phi_{12} & \phi_{10} & \phi_{11} \\ \phi_{11} & \phi_{12} & \phi_{10} \end{bmatrix} . \begin{bmatrix} I_{C1} \\ I_{C2} \\ I_{C3} \end{bmatrix}$$
(8.30)

$$\begin{bmatrix} V_{CCB1} \\ V_{CCB2} \\ V_{CCB3} \end{bmatrix} = \begin{bmatrix} \mathbb{Z}_2 & 0 & 0 \\ 0 & \mathbb{Z}_2 & 0 \\ 0 & 0 & \mathbb{Z}_2 \end{bmatrix} \begin{bmatrix} \varphi_{10} & \varphi_{11} & \varphi_{12} \\ \varphi_{12} & \varphi_{10} & \varphi_{11} \\ \varphi_{11} & \varphi_{12} & \varphi_{10} \end{bmatrix} . \begin{bmatrix} I_{C1} \\ I_{C2} \\ I_{C3} \end{bmatrix}$$
(8.31)

$$\begin{bmatrix} V_{CCB4} \\ V_{CCB5} \\ V_{CCB6} \end{bmatrix} = \begin{bmatrix} \mathbb{Z}_2 & 0 & 0 \\ 0 & \mathbb{Z}_2 & 0 \\ 0 & 0 & \mathbb{Z}_2 \end{bmatrix} \begin{bmatrix} \varphi_{13} & \varphi_{14} & \varphi_{15} \\ \varphi_{15} & \varphi_{13} & \varphi_{14} \\ \varphi_{14} & \varphi_{15} & \varphi_{13} \end{bmatrix} . \begin{bmatrix} I_{C1} \\ I_{C2} \\ I_{C3} \end{bmatrix}$$
(8.32)

$$\begin{bmatrix} V_{CST4} \\ V_{CST5} \\ V_{CST6} \end{bmatrix} = \begin{bmatrix} \frac{\phi_{13}}{6} & \frac{\phi_{13}}{6} & \frac{\phi_{13}}{6} \end{bmatrix} \begin{bmatrix} I_{C1} \\ I_{C2} \\ I_{C3} \end{bmatrix}$$
(8.33)

In (8.30)-(8.33), 
$$\phi_{10} = 8Z_{sa} + 9Z_{sb} + 7Z_{sn}$$
,  $\phi_{11} = 5Z_{sa} + 6Z_{sb} + 7Z_{sn}$ ,  $\phi_{12} = 5Z_{sa} + 3Z_{sb} + 4Z_{sn}$ ,  $\varphi_{10} = 4Z_{sa}Z_{sn} + 5Z_{sa}^2 + 6Z_{sa}Z_{sb}$ ,  $\varphi_{11} = 7Z_{sa}Z_{sn} + 5Z_{sa}^2 + 6Z_{sa}Z_{sb}$ ,  $\varphi_{12} = 4Z_{sa}Z_{sn} + 5Z_{sa}^2 + 3Z_{sa}Z_{sb}$ ,  $\varphi_{13} = 4Z_{sa}Z_{sn} + 5Z_{sa}^2 + Z_{sb}Z_{sn} + 8Z_{sa}Z_{sb} + 3Z_{sb}^2$ ,  $\varphi_{14} = 7Z_{sa}Z_{sn} + 5Z_{sa}^2 + 4Z_{sb}Z_{sn} + 8Z_{sa}Z_{sb} + 3Z_{sb}^2$ ,  $\varphi_{15} = 4Z_{sa}Z_{sn} + 5Z_{sa}^2 + 4Z_{sb}Z_{sn} + 8Z_{sa}Z_{sb} + 3Z_{sb}^2$ ,  $\varphi_{15} = 4Z_{sa}Z_{sn} + 5Z_{sa}^2 + 4Z_{sb}Z_{sn} + 8Z_{sa}Z_{sb} + 3Z_{sb}^2$ ,  $\varphi_{15} = 4Z_{sa}Z_{sb} + 3Z_{sb}^2$ ,  $\varphi_{15} = 4Z_{sb}Z_{sb} + 3Z_{sb}^2$ ,  $\varphi_{15} = 4Z$ 

The total voltage in each joint for a particular type of bonding is the sum of voltage produced by both the capacitive and inductive effects for the particular joint

# 8.4 Experiments and Simulation to Estimate the Sheath Current and Voltage for Different End Bonding Methods.

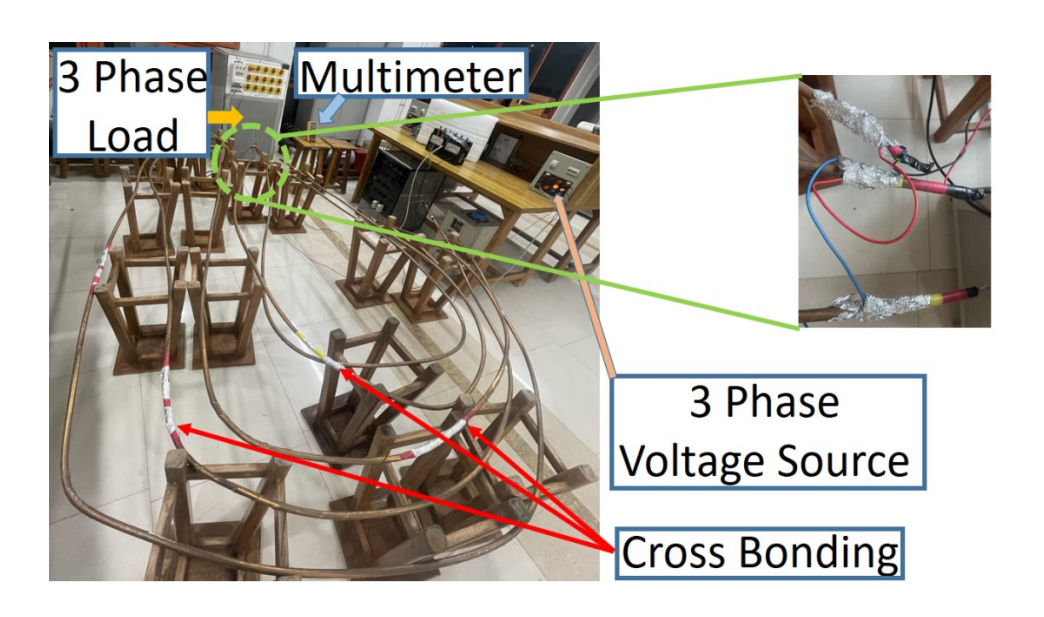


Figure 8.8 Experimental setup to measure current and voltage at different joints for the proposed end bonding method.

Steady-state experiments for three types of bonding compared with the original case study are performed on commercial three-core, XLPE insulated material, with an inner conductor (aluminum) area of  $35mm^2$ , outer grounded sheath diameter of 7.35mm, the radius of the metallic sheath is 1mm, and insulation relative permittivity of 2.3. The cable is laid in a trefoil formation with  $r_{\rm cs}$  and  $r_{\rm ss}$  as 8cm and 10cm respectively. In the original case, the first, second, and third minor sections are of length 5m, 5.5m, and 5.2m respectively. Two

different case studies are considered to verify the proposed method. In the first case, the third minor section is 3m in length and in the second case study, the third minor section is 7m. The current and voltage at different joints are compared for different types of bonding. The grounding resistance is kept at  $0.2\Omega$ , while to portray SVL, a 10 Mega-ohm resistance was used. The cable is supplied with a three-phase voltage of 440V and a load current of 15 A, while the power factors for the three phases are 1, 0.98, and 0.85. The current and voltage are measured using a FLUKE 17B digital multimeter whose uncertainty in measurement is 1.5% as shown in Fig.8.8.

Apart from the experimental cable, which was of limited length, voltage, and current supply, the simulation for three types of bonding compared with the original case study was performed on MATLAB SIMULINK. The operating voltage and current in the simulated cable are 220kV and 550A, while the power factors for the three phases are 1, 0.98, and 0.85. The cable is insulated with XLPE material with a relative permittivity of 2.3 and thickness of 27mm. The conductor radius is 21mm and the metallic sheath is 6mm. The cable is laid in a trefoil formation with  $r_{cs}$  and  $r_{ss}$  as 85cm and 115cm respectively. The value of grounding resistances is 0.2 $\Omega$ . In the original case, the first, second, and third minor sections are of length 500m, 550m, and 520m respectively. Two different case studies are considered. In the first case, the third minor section is 150m in length and in the second case study, the length of the third minor section is 800m. A transient case study was also considered in simulation for Case II, where the peak voltage and current are simulated for the conductor to sheath fault at four different places in the major section. The faults are created in the first phase, at distances of 5m, 495m, 1030m, and in 1800m. The peak voltage and current are observed just near the ST and CB joints. The fault has a duration of 0.3s.

# 8.5 Experiments to estimate to Estimate the Sheath Current and Voltage for Different End Bonding Methods.

In this section, the analytical, experimental, and simulation results are presented and discussed. The section is further divided into two subsections. At first, the experimental results performed in the laboratory are presented followed by the simulation results as discussed in section 8.4.

#### 8.5.1 Practical Case Study

Measured maximum RMS current and voltage between each set of ST and CB joints for

two different case studies and three different types of bonding as discussed in Section 8.4 are compared with the simulation and analytical results are shown in Fig. 8.9- Fig. 8.14. It is observed that the analytically obtained values of RMS current and voltage in the joints match with a minimum accuracy of 99.87% when compared with the practical results, also the RMS value of current and voltage is minimal for the proposed method when compared with the solid grounding or grounding with SVL even during the unbalanced loaded condition. Comparing the two cases, case II has the maximum current and voltage across different joints. The reduction in the maximum practical RMS value of voltage and current for case II of the proposed method in comparison to the other two bonding types is shown in Table 8.1.

Tables 8.1, (1), and (2), represent practical comparisons between the proposed method with solid grounding and grounding with SVL respectively. With one exception—for both ST and CB joints, the proposed method exhibits a better voltage and current profile when compared to alternative end bonding techniques—the current in the second set of ST joints in the proposed method only surpasses the grounded with SVL by 0.002mA margin.

The maximum RMS current and voltage at different joints for the proposed method in case II are compared with an original case study and are shown in Fig. 8.15 and Fig. 8.16. It is observed that except for the peak RMS voltage at the second set of ST joints (within the limits of 50V [5]), the voltage and current profile is even better for the proposed method when compared with the original case. This happens because due to the circulating current in the sheath is restrained by SVL and the voltage across the joints is minimal due to connecting the sheath terminals of the three phases together.

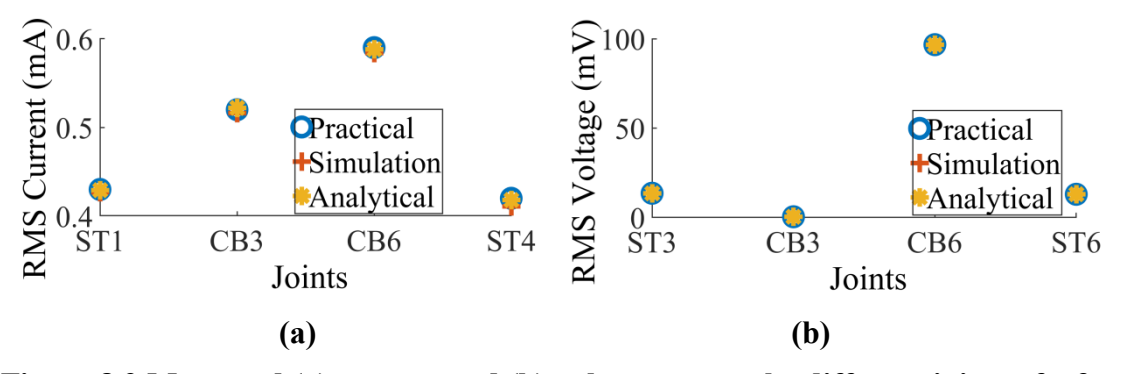


Figure 8.9 Measured (a) current and (b) voltage across the different joints of a 3m long third minor section for solid grounding.

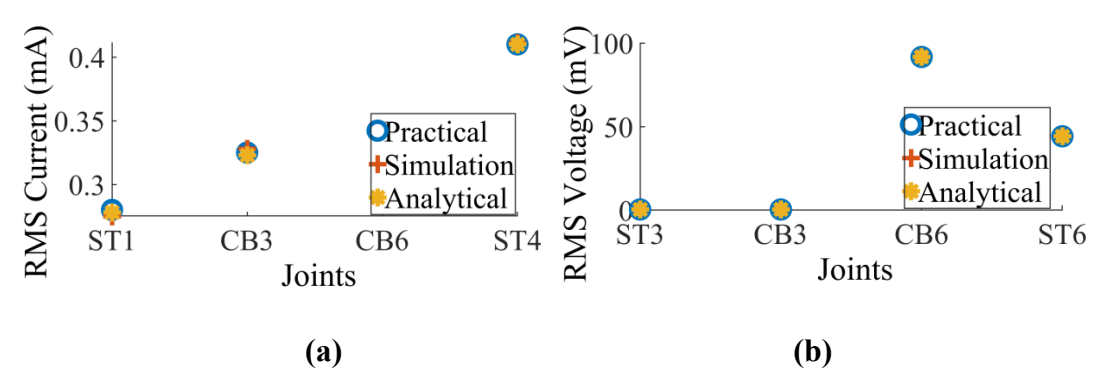


Figure 8.10 Measured (a) current and (b) voltage across different joints of a 7m long third minor section for solid grounding.

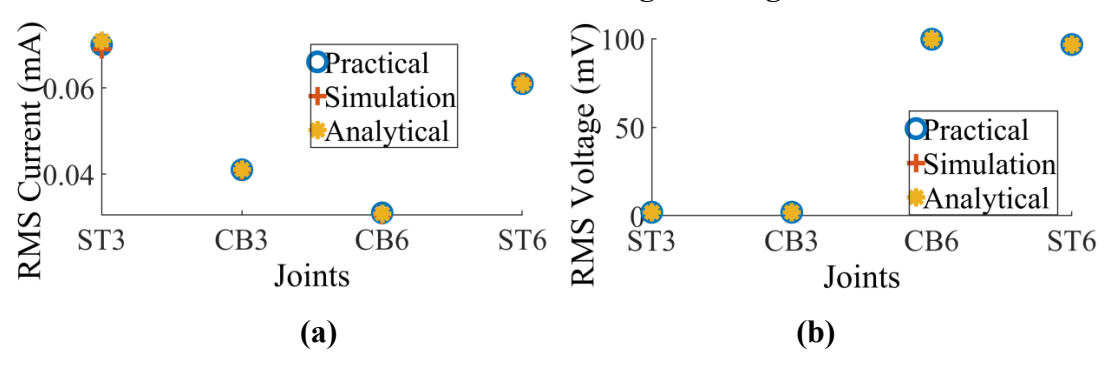


Figure 8.11 Measured (a) current and (b) voltage across different joints of a 3m long third minor section for sheath grounded with SVL.

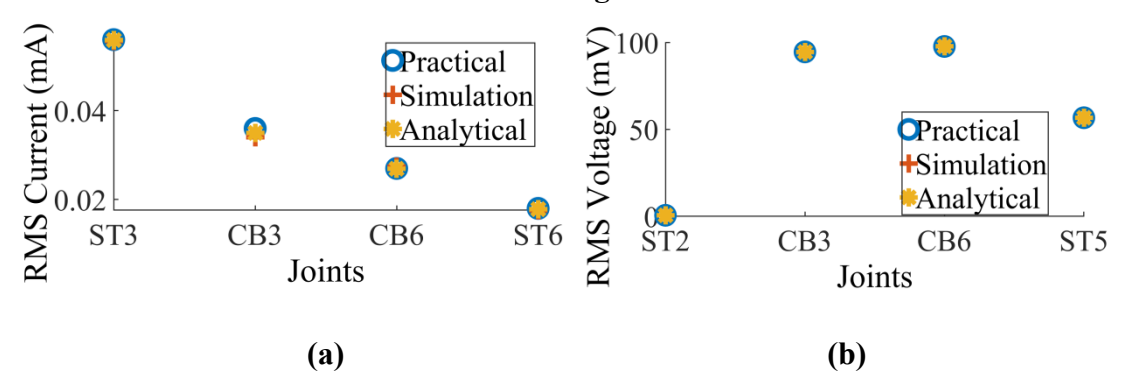


Figure 8.12 Measured (a) current and (b) voltage across different joints of a 7m long third minor section for sheath grounded with SVL.

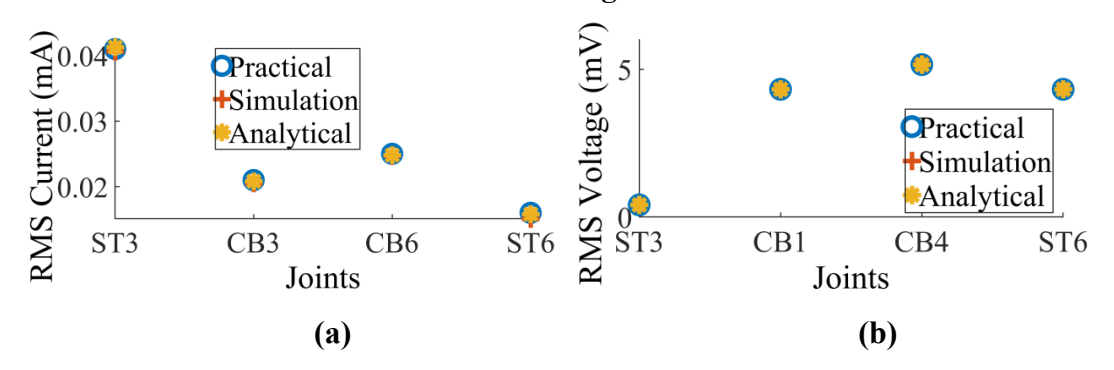


Figure 8.13 Measured (a) current and (b) voltage across different joints of a 3m long third minor section for the proposed method.

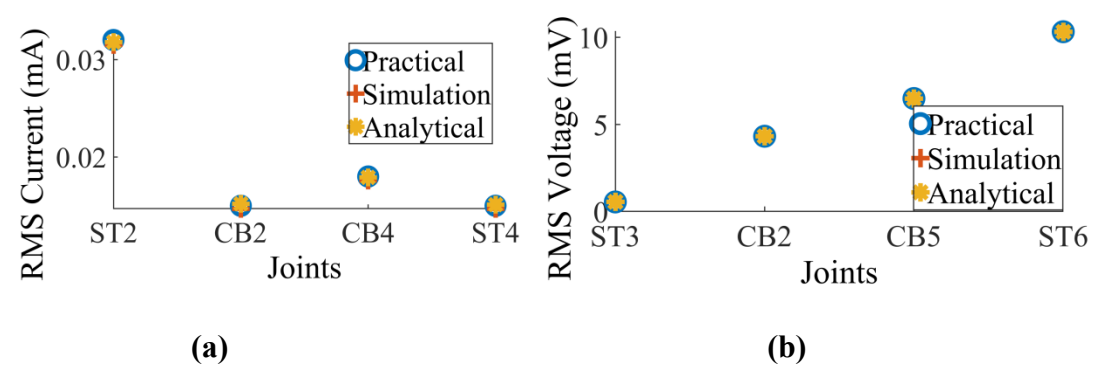


Figure 8.14 Measured (a) current and (b) voltage across the different joints of a 7m long third minor section for the proposed method.

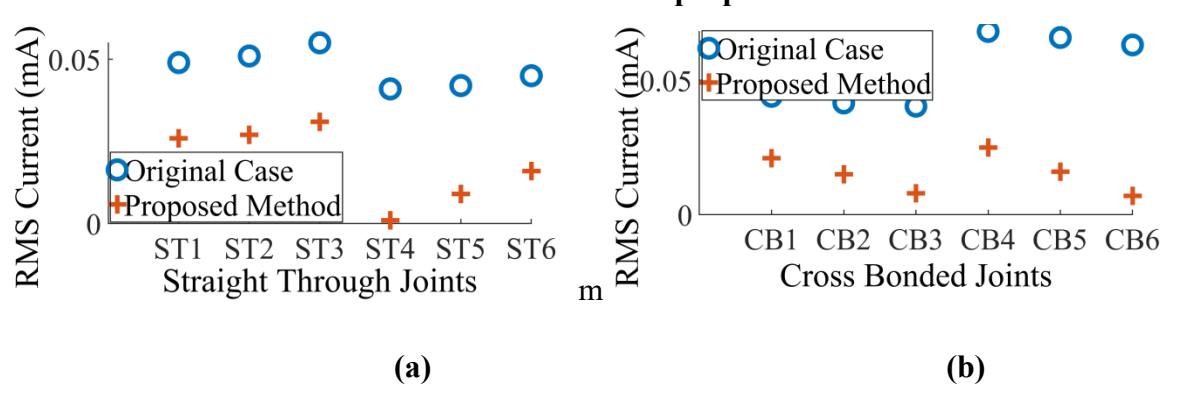


Figure 8.15 Measured (a) ST joints and (b) CB joints current for the proposed method case II and original case study.

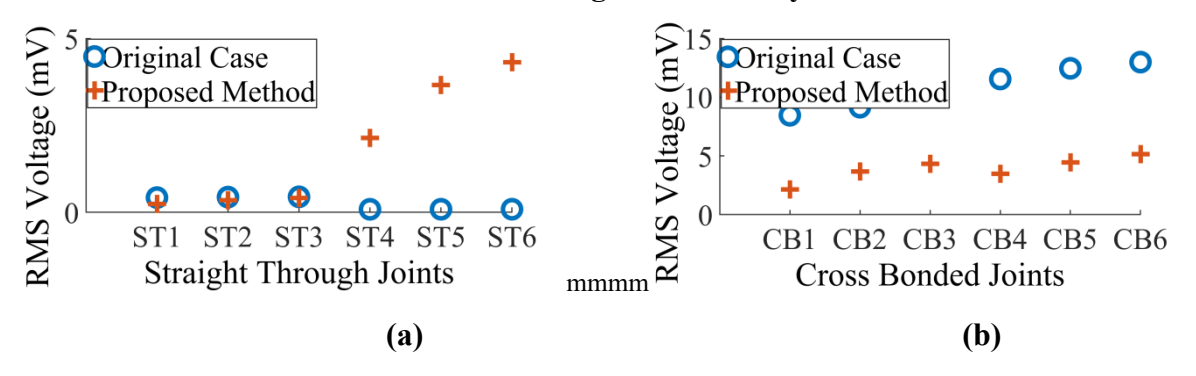


Figure 8.16 Measured (a) ST joints and (b) CB joints voltage for the proposed method case II and original case study.

#### 8.5.2 Simulation Case Study

. Simulated maximum RMS current and voltage between each set of ST and CB joints for two different case studies and three different types of bonding as discussed in Section V are compared with the simulation and analytical results are shown in Fig. 8.17- Fig. 8.22. It is observed that the simulation and analytical results match with a minimum accuracy of 99.92%. While comparing the two cases, case I has the maximum current and voltage across different joints. The reduction in the maximum simulated RMS value of voltage and current

for case I of the proposed method in comparison to the other two bonding types is shown in Table 8.2.

Table 8.1 Comparison of practical maximum current and voltage

Types of Bonding	Reduction in current compared (1)(mA)	Reduction in current compared (2) (mA)	Reduction in voltage compared (1) (mV)	Reduction in voltage compared (2) (mV)
1 <sup>st</sup> set of ST joints	0.263	0.034	0.008	0.003
1 <sup>st</sup> set of CB joints	0.295	0.015	0.007	92.451
2 <sup>nd</sup> set of CB joints	0.319	0.012	93.4513	94.2205
2 <sup>nd</sup> set of CB joints	0.401	-0.002	39.542	44.329

Tables 8.2, (1), and (2), represent simulation comparisons between the proposed method with solid grounding and grounding with SVL respectively. It is observed that the voltage across any joints does not exceed 50V [3]. The current in the second set of ST joints in the proposed method only exceeds the grounded with SVL case by a 1.08A margin. Except that, for both ST and CB joints, the proposed method shows a better voltage and current profile compared with other end bonding methods.

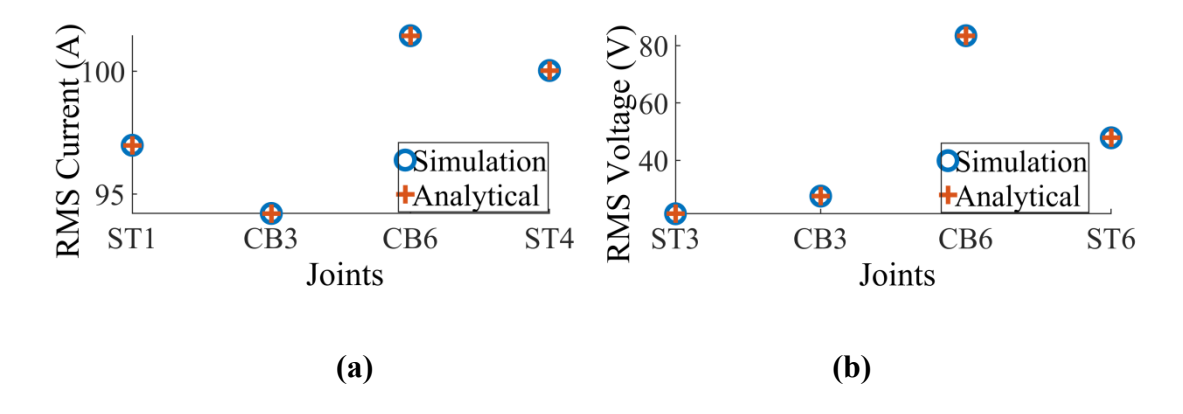


Figure 8.17 Simulated (a) current and (b) voltage across different joints of a 150m long third minor section for solid grounding

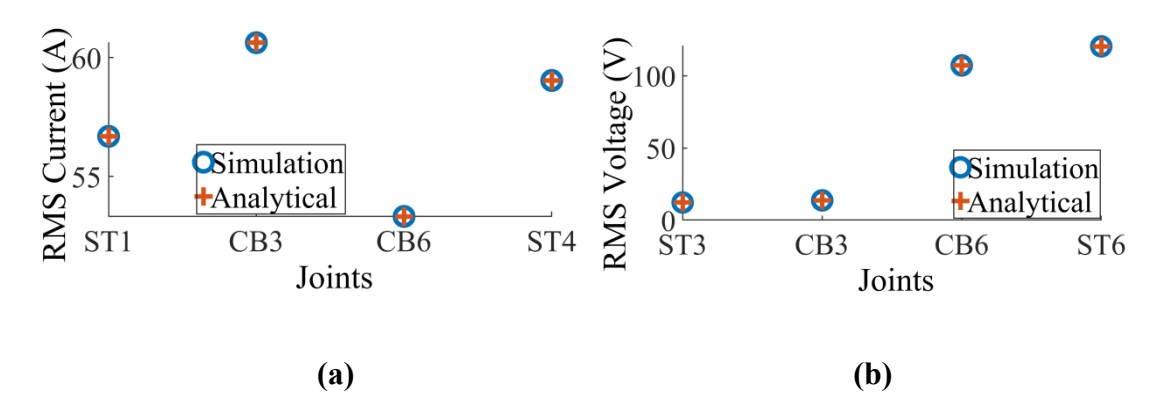


Figure 8.18 Simulated (a) current and (b) voltage across different joints of an 800m long third minor section for solid grounding.

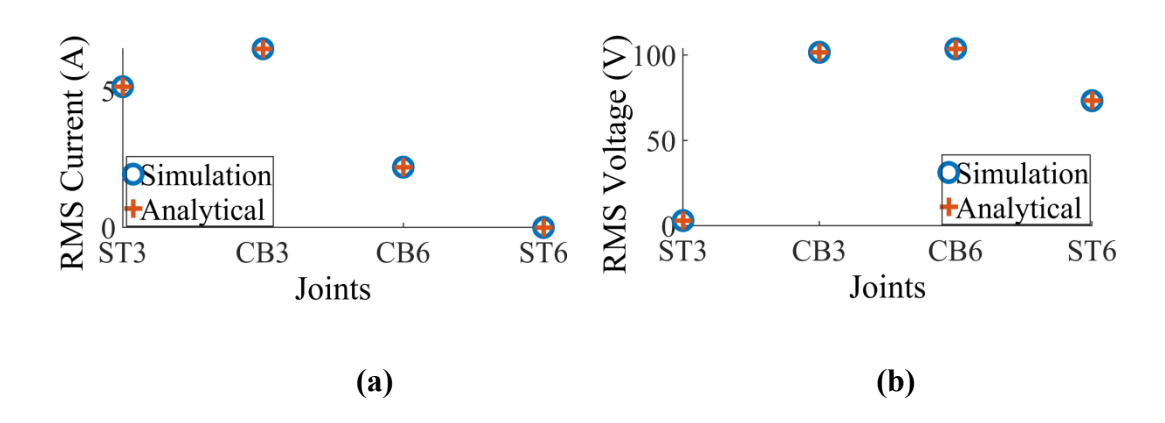


Figure 8.19 Simulated (a) current and (b) voltage across different joints of a 150m long third minor section for sheath grounded with SVL.

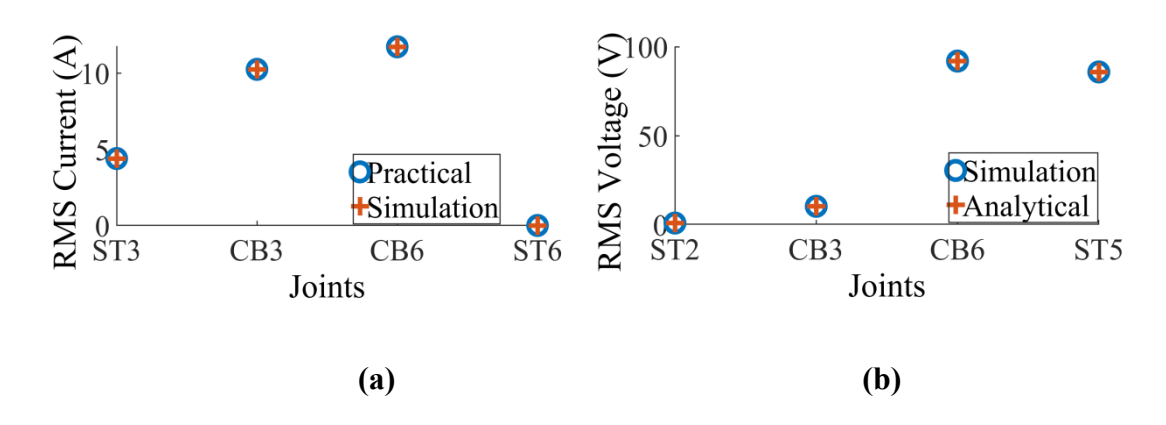


Figure 8.20 Simulated (a) current and (b) voltage across different joints of an 800m long third minor section for sheath grounded with SVL.

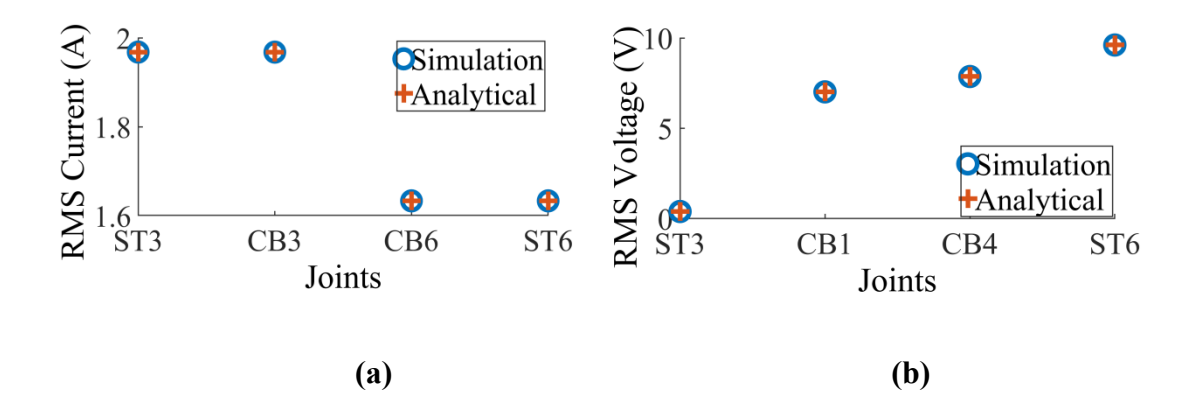


Figure 8.21 Simulated (a) current and (b) voltage across different joints of a 150m long third minor section for the proposed method.

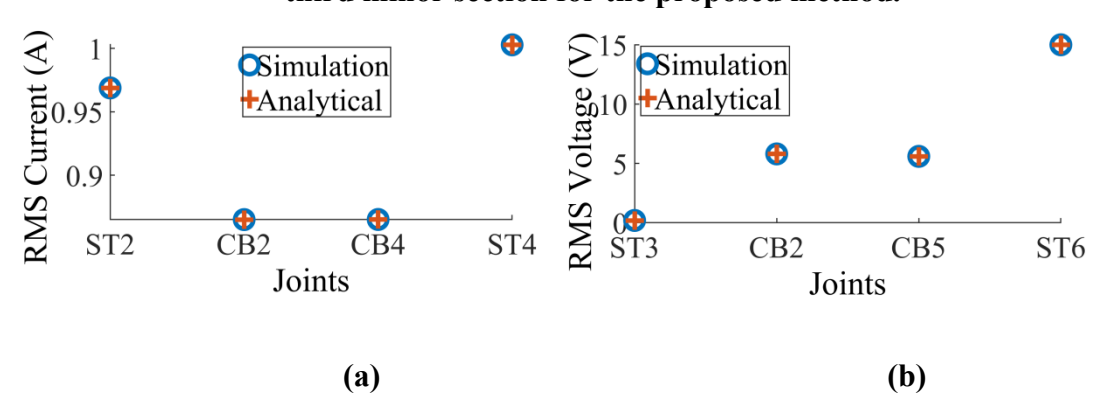


Figure 8.22 Simulated (a) current and (b) voltage across different joints of an 800m long third minor section for the proposed method.

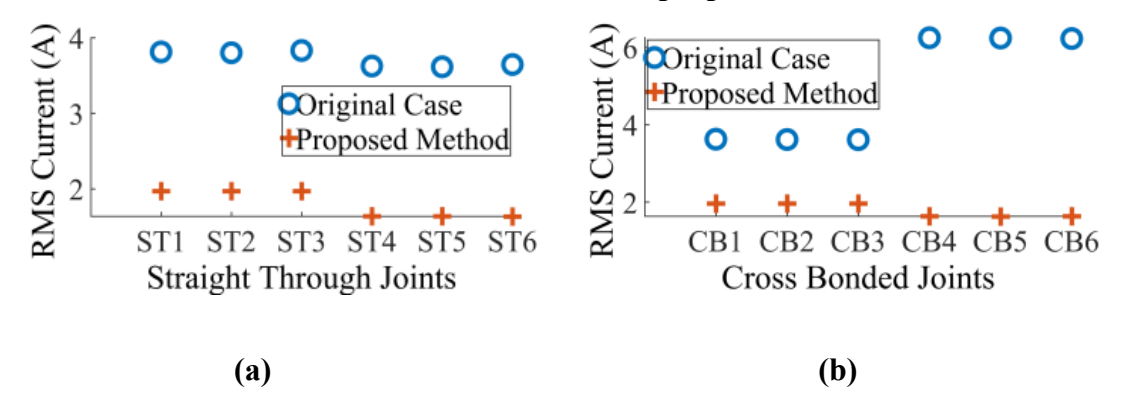


Figure 8.23 Simulated (a) ST joints and (b) CB joints current for the proposed method case I and original case study.

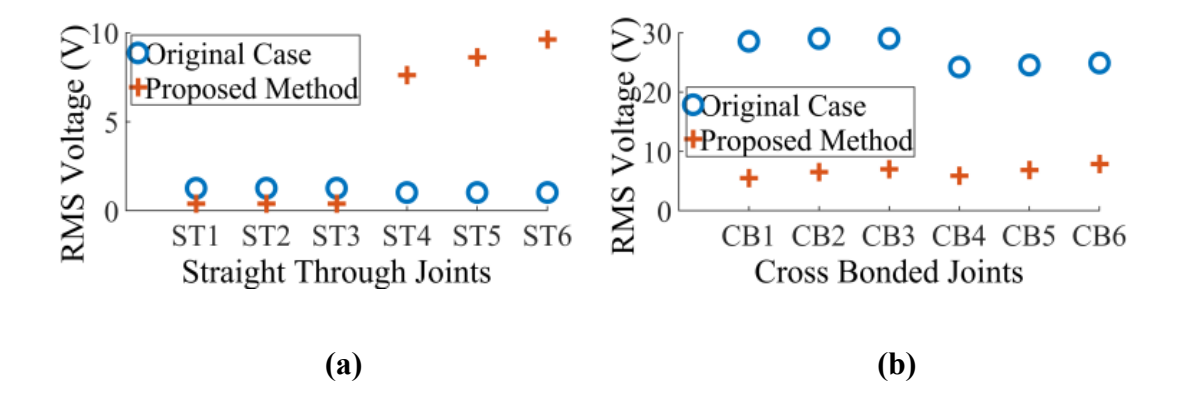


Figure 8.24 Simulated (a) ST joints and (b) CB joints voltage for the proposed method case I and original case study.

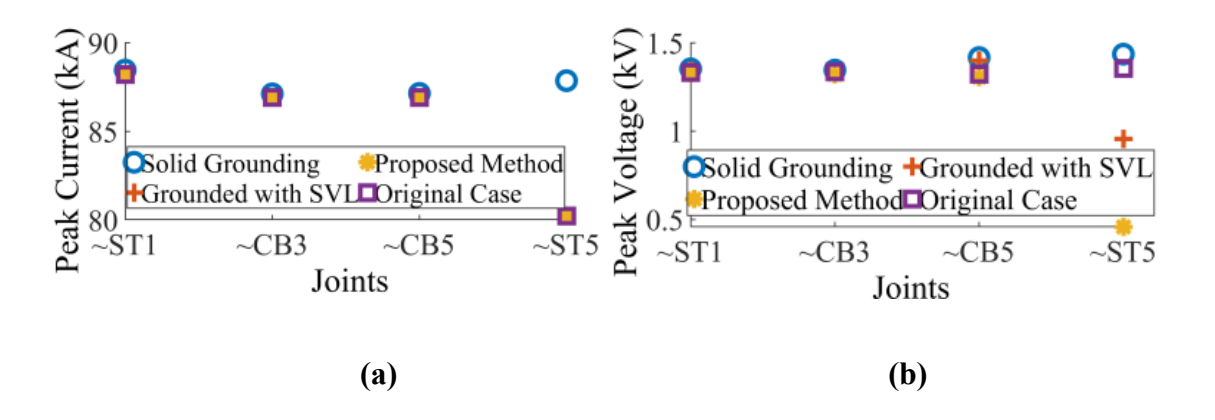


Figure 8.25 (a) Simulated peak current (b) Simulated peak voltage during transient conditions across all joints in the first phase (~ represents 2m from the particular joints).

Table 8.2 Comparison of simulated maximum current and voltage

Types of	Reduction in	Reduction	Reduction	Reduction in
Bonding	current	in voltage	in current	voltage
	compared	compared	compared	compared (2)
	(1)(A)	(1)(V)	(2)(A)	(V)
1 <sup>st</sup> set of ST				
joints	93.84	1.88	23.62	1.248
1st set of CB				
joints	94.51	6.34	19.94	98.64
2 <sup>nd</sup> set of CB				
joints	100.88	1.26	81.94	102.45
2 <sup>nd</sup> set of CB				
joints	95.87	-0.58	31.415	43.78

The maximum RMS current and voltage at different joints for the proposed method in case I are compared with the original case study and are shown in Fig. 8.23 and Fig. 8.24. It is observed that, except for the peak RMS voltage at the second set of ST joints (which remains within limits of 50V, according to standard [5]), the voltage and current profile is even better for the proposed method when compared with the original case.

The peak RMS transient current and voltage for the case I, in different joints and end bonding methods, and the original case study are shown in Fig. 8.25. When compared to the other bonding techniques and the original case study, the proposed method will always have a lower peak voltage and current, as shown in Fig. 8.25.

## 9.1 Estimating the Location of Short-circuit Fault in a Cable Using Impedance Spectroscopy

A method to detect and locate short-circuited faults in power cables using Sweep Frequency Response Analysis (SFRA) and impedance spectroscopy is proposed. The classical transmission line (TL) model is applied to derive the impedance characteristics of the cable. Additionally, a generalized analytical formula for the Differential Phase Impedance Function (DPIF) is introduced, which depends on polytopic numbers that can be easily obtained from basic cable parameters, either through direct measurement or calculation. The predicted DPIF closely matches the test cable's impedance graph, suggesting its potential as a signature function for fault detection.

A formula is also proposed to estimate the fault location based on the positions of poles and zeros in the impedance graph of both faulted and healthy cables. The effectiveness of SFRA is validated through experiments on a 25-meter long power cable and simulations of a 1-km cable. The proposed method demonstrated an accuracy of approximately 99.11% for continuous cable sections and 97.83% for cables with joints, regardless of the fault location. These findings have practical applications for utility companies and the cable industry, enabling more accurate identification of fault locations in power cables.

# 9.2 Estimating the Location of Semiconducting Screen Defect in a Cable Using Impedance Spectroscopy

An innovative analytical approach to detect and locate single-point screen defects in power cables utilizing Sweep Frequency Response Analysis (SFRA) and impedance spectroscopy. This method employs a transmission line (TL) model and state-space analysis is introduced. By applying TL theory, a correlation was established between the impedance graph's zeroes and the cable's propagation constant. Furthermore, the state-space analysis validated the relationship between the sum and product of the zeroes and the cable's electrical parameters, marking a first in cable defect analysis.

The calculated sum and product of zeroes for a test cable demonstrated excellent

agreement with both analytical techniques. A formula was developed to estimate single-point screen defects based on the sum and product of zeroes derived from the impedance graph of a defective cable. The feasibility of employing SFRA to determine the locations of both conductor and insulation screen defects was validated through experiments on a test cable and simulations on a 1 km cable featuring three joints.

The proposed methodology achieved a minimum accuracy of approximately 98.24% for continuous cable sections and 98.09% for cables with joints, irrespective of the defect's size or location. Additionally, the approach successfully identified multiple screen defects. These findings have significant implications for the cable manufacturing industry, enabling the detection and localization of conductor and insulation screen defects before installation, thereby reducing the risk of premature failures.

# 9.3 Estimating the Location of Sheath-to-Ground Fault in a Cross Bonded Power Cable During Online Condition.

A novel method to identify and locate a sheath-to-ground fault at any arbitrary location in a cross-bonded cable by only measuring the earthing currents at the grounding box during online conditions is proposed. Along with this a circuit model for the cross-bonded cable to estimate the grounding current during healthy conditions is proposed and the same circuit model is used to estimate the location of the fault. In practical case studies, faults are created at different locations in the cable and the fault current at the grounding resistance is measured using a digital multimeter and power quality analyser. To confirm the particular section having a sheath-to-ground fault, the measured fault current is compared with the analytically obtained range of values, and its location is estimated using the proposed analytical formulae. The suitability of the proposed method is tested on an actual power cable of length 18 m in the laboratory and also an onfield case study on a 1500m long cable. Irrespective of the location of the fault, balanced or unbalanced condition, the proposed method is shown to have an uncertainty of less than 0.07m for laboratory cable and 1.5m for onfield case. It is believed that the outcome is useful for the utility industries to find SG fault locations in power cables during online conditions

## 9.4 Estimating the Location of Sheath-to-Ground Fault in a Non Cross Bonded Power Cable During Online Condition.

A novel method to identify and locate a sheath-to-ground fault at any arbitrary location in a non-cross-bonded cable by only measuring the earthing currents at the grounding box in online conditions is proposed. Three types of bonding, which are commonly used in practice to estimate the sheath-to-ground faults is investigated. A circuit model to estimate the healthy condition grounding current analytically is proposed. The analytically obtained healthy condition grounding current has an accuracy of more than 99.94% when compared with practically measured values. While performing experiments, faults are created at different locations in the cable, and the fault current at the grounding resistance is measured using a digital multimeter, and the phase difference between sheath and conductor current is measured using a power quality analyzer. The SG fault in the cable for a particular type of bonding is confirmed when the measured grounding current does not match the analytically obtained healthy current values. Analytical formulae are proposed for different types of bonding to estimate the location of the SG fault. The suitability of the proposed method is tested on an actual power cable of length 15m in the laboratory. Irrespective of the location of the fault, balanced or unbalanced condition, the proposed methods are shown to have an uncertainty of less than 0.15m for the laboratory. It is believed that the outcome is useful for the utility industries to find SG fault locations in power cables during online conditions.

### 9.5 Estimating the Location of Sheath-to-Ground Fault in a HVDC Power Cable During Online Condition.

The location of sheath-to-ground fault at any arbitrary location in an HVDC cable is estimated for the first time. In order to estimate the location, novel online and contactless time domain reflectometry combined with decision tree regression method is used. By employing impulse signals into the sheath through inductive coupler and performing Fourier analysis on the modified time domain signal, fault locations were identified without deenergizing the cable, leveraging the distinct frequency signatures obtained from analyzing reflected waveforms. This approach demonstrated superior fault detection capabilities, particularly in shorter cable sections where conventional techniques often face challenges due to overlapping reflections. The proposed method was verified practically to estimate the location of sheath to ground fault for two different ratings of cable in laboratory having a minimum accuracy of 99.39%. It is believed that the proposed online TDR and DTR approach will be useful to the cable industry for real-time condition monitoring and maintenance of HVDC cable systems. this proposed online TDR and DTR approach offers a promising solution for efficient SG fault detection, paving the way for improved real-time condition monitoring and maintenance of HVDC cable systems.

## 9.6 Introduction of a new End bonding Type to Reduce the Circulating Current and Voltage for a Non-uniform Minor Section Length Cross Bonded Power Cable.

A novel end-bonding method is proposed in an existing non-uniform length cross-bonded cable, and its current and voltage profile is compared with the two existing end-bonding techniques. Analytical findings for each type of end bonding are presented to validate the proposed method. The suitability of the proposed end bonding method is tested on an actual power cable of lengths 13.5m and 17.5 in the laboratory and compared with an original cross-bonded cable length of 15.7m. Simulation studies are also performed for different minor section lengths and then compared with the original case. Irrespective of the length of the third minor section, balanced or unbalanced condition, the proposed method has a superior current and voltage profile compared with the other methods. For both steady and transient state, even the current in the joints for the simulated and practical case study of the proposed end bonding method shows a better profile when compared with the original case, and also joint voltage remains under 50V. It is believed that the outcome is useful for the utility industries to introduce this end bonding technique to reduce circulating current and voltage in the sheath for a non-uniform length cross-bonded cable.

### 9.7 Future Scope of the Work

The future scope of this research on estimating fault locations and semiconducting defects using impedance spectroscopy and other analytical methods is promising, particularly in enhancing reliability and efficiency in the power transmission industry. Building on the demonstrated capability of impedance spectroscopy to accurately locate single and multiple defects in cable insulation and semiconducting layers, further advancements can focus on real-time condition monitoring systems. By integrating the proposed methods with Internet of Things (IoT) technologies and advanced machine learning algorithms, fully automated systems can be developed for continuous monitoring of cables. These systems would be capable of detecting SG faults, thereby enabling preventive maintenance and minimizing

Finally, the commercialization of these methods presents a significant opportunity. Developing portable diagnostic equipment or software solutions for field engineers and utility companies could revolutionize the way faults and defects are managed in power transmission systems. These tools, underpinned by patented methodologies, would ensure rapid fault identification and efficient maintenance planning, contributing to the overall resilience of the power grid. Collaboration with the cable manufacturing industry to embed

such diagnostic features during cable production is another potential future direction that could prevent premature failures and enhance the service life of cables.

### References

- [1] Marc Jeroense (2023 September) LinkedIn ,"This is a post in a series that intends addressing questions of future cable development "Where are we?" (this post)".https://www.linkedin.com/posts/marc-jeroense-94410817\_hvdc-cable-project-activity-7100558420298145793Un0?utm\_source=share&utm\_medium=member\_desktop
- [2] Y. Murata, M. Sakamaki, K. Abe, Y. Inoue, S. Mashio, S. Kashiyama, O.Matsunaga, T. Igi, M. Watanabe, S. Asai, and S. Katakai, "Development of high voltage DC-XLPE cable system," SEI (Sumitomo Electric) Tech. Rev., no. 76, pp. 55–62, Apr. 2013.
- [3] CIGRE Session Paper B4-10, J P KJÆRGAARD, K SØGAARD, S D MIKKELSEN .et.al, "Bipolar operation of an HVDC VSC converter with an LCC converter"; CIGRE:2012 San Francisco Colloquium.
- [4] T. Hasegawa, M. Hatano, K. Yamaji, T. Kouan and N. Hosokawa, "Dielectric strength of transformer insulation at DC polarity reversal," in IEEE Transactions on Power Delivery, vol. 12, no. 4, pp. 1526-1531, Oct. 1997.
- [5] E. P. Dick and C. C. Erven, "Transformer Diagnostic Testing by Frequuency Response Analysis," in IEEE Transactions on Power Apparatus and Systems, vol. PAS-97, no. 6, pp. 2144-2153, Nov. 1978.
- [6] F. Ciancetta, A. del Pizzo, C. Olivieri, N. Rotondale, L. Castellini and M. d'Andrea, "SFRA technique applied to fault diagnosis on stators of electric motors," 2014 International Symposium on Power Electronics, Electrical Drives, Automation and Motion, Ischia, 2014, pp. 515-520.
- [7] C. A. Platero, F. Blázquez, P. Frías and D. Ramírez, "Influence of Rotor Position in FRA Response for Detection of Insulation Failures in Salient-Pole Synchronous Machines," in IEEE Transactions on Energy Conversion, vol. 26, no. 2, pp. 671-676, June 2011.
- [8] K. Ragavan and L. Satish, "Construction of Physically Realizable Driving-Point Function From Measured Frequency Response Data on a Model Winding," in IEEE Transactions on Power Delivery, vol. 23, no. 2, pp. 760-767, April 2008.
- [9] J. Vlach, Computerized Approximation and Synthesis of Linear Networks, New York: Wiley, 1969.
- [10] M. Kezunovic and B. Perunicic, "Fault location," in Wiley Encyclopedia of Electrical and Electronics Terminology. New York: Wiley, 1999, vol. 7, pp. 276–285.
- [11] G. Kwon, C. Lee and Y. Shin, "Diagnosis of Shielded Cable Faults via Regression-Based Reflectometry," in IEEE Transactions on Industrial Electronics, vol. 66, no. 3, pp. 2122-2131, March 2019, doi: 10.1109/TIE.2018.2840529.
- [12] W. E. Anderson, J. D. Ramboz and A. R. Ondrejka, "The Detection of Incipient Faults in Transmission Cables Using Time Domain Reflectometry Techniques: Technical Challenges," in IEEE Transactions on Power Apparatus and Systems, vol. PAS-101, no. 7, pp. 1928-1934, July 1982, doi: 10.1109/TPAS.1982.317481.
- [13] H. Ghafoori-Shiraz and T. Okoshi, "Fault location in optical fibers using optical frequency domain reflectometry," in Journal of Lightwave Technology, vol. 4, no. 3, pp. 316-322, March 1986, doi: 10.1109/JLT.1986.1074720.
- [14] Y. -. Shin et al., "Application of time-frequency domain reflectometry for detection and localization of a fault on a coaxial cable," in IEEE Transactions on Instrumentation

- and Measurement, vol. 54, no. 6, pp. 2493-2500, Dec. 2005, doi: 10.1109/TIM.2005.858115.
- [15] X. Zhang, W. Zhu, L. Zhu and K. Wang, "The design and implementation of LCX fault detection system based on linear sweep frequency," 2016 International Conference on Progress in Informatics and Computing (PIC), 2016, pp. 411-414, doi: 10.1109/PIC.2016.7949536.Q. Shi and O. Kanoun, "Wire Fault Diagnosis in the Frequency Domain by Impedance Spectroscopy," in IEEE Transactions on Instrumentation and Measurement, vol. 64, no. 8, pp. 2179-2187, Aug. 2015, doi: 10.1109/TIM.2014.2386918.
- [16] A. Das, C. Sehgal and C. C. Reddy, "Investigations on Feasibility of Fault Detection in Underground Power Cables Using SFRA," 2019 IEEE 4th International Conference on Condition Assessment Techniques in Electrical Systems (CATCON), 2019, pp. 1-4, doi: 10.1109/CATCON47128.2019.CN0015.
- [17] Q. Shi and O. Kanoun, "Wire Fault Location in Coaxial Cables by Impedance Spectroscopy," in IEEE Sensors Journal, vol. 13, no. 11, pp. 4465-4473, Nov. 2013, doi: 10.1109/JSEN.2013.2269218.
- [18] Q. Shi and O. Kanoun, "Automated wire fault location using impedance spectroscopy and Differential Evolution," 2013 IEEE International Instrumentation and Measurement Technology Conference (I2MTC), 2013, pp. 359-364, doi: 10.1109/I2MTC.2013.6555440.
- [19] Q. Shi and O. Kanoun, "Wire Fault Diagnosis in the Frequency Domain by Impedance Spectroscopy," in IEEE Transactions on Instrumentation and Measurement, vol. 64, no. 8, pp. 2179-2187, Aug. 2015, doi: 10.1109/TIM.2014.2386918.
- [20] Q. Shi and O. Kanoun, "A new method of locating the single wire fault," 2014 12th International Conference on Signal Processing (ICSP), 2014, pp. 2262-2267, doi: 10.1109/ICOSP.2014.7015397.
- [21] Power Cables with Extruded Insulation and their Accessories for Rated Voltages Above 150 kV (Um = 170 kV) up to 500 kV (Um = 550 kV) Test Methods and Requirements, IEC 62067, 2011.
- [22] A. Bulinski and R. J. Densley, "The Voltage Breakdown Characteristics of Miniature XLPE Cables Containing Water Trees," in IEEE Transactions on Electrical Insulation, vol. EI-16, no. 4, pp. 319-326, Aug. 1981, doi: 10.1109/TEI.1981.298365.
- [23] S. Rasikawan, H. Ishihara and N. Shimizu, "Comparison between water-treed and deteriorated regions. Electrical tree precursor," in IEEE Transactions on Dielectrics and Electrical Insulation, vol. 1, no. 4, pp. 597-603, Aug. 1994, doi: 10.1109/94.311702.
- [24] E. Stennis and F. H. Kreuger, "Water treeing in polyethylene cables," IEEE Trans. Electr. Insul., vol. 25, no. 5, pp. 989–1028, Oct. 1990.
- [25] D. Haddad, A. Y. Kallel, N. E. B. Amara and O. Kanoun, "Multiple Faults Detection and Location in Bus-Shaped Cable Networks by Distributed Time-Domain Reflectometry," in IEEE Sensors Letters, vol. 6, no. 5, pp. 1-4, May 2022, Art no. 6001604, doi: 10.1109/LSENS.2022.3170645.
- [26] H. M. Lee, G. S. Lee, G. -Y. Kwon, S. S. Bang and Y. -J. Shin, "Industrial Applications of Cable Diagnostics and Monitoring Cables via Time–Frequency Domain Reflectometry," in IEEE Sensors Journal, vol. 21, no. 2, pp. 1082-1091, 15 Jan.15, 2021, doi: 10.1109/JSEN.2020.2997696.

- [27] G. Robles, M. Shafiq and J. M. Martínez-Tarifa, "Multiple Partial Discharge Source Localization in Power Cables Through Power Spectral Separation and Time-Domain Reflectometry," in IEEE Transactions on Instrumentation and Measurement, vol. 68, no. 12, pp. 4703-4711, Dec. 2019, doi: 10.1109/TIM.2019.2896553.
- [28] K. W. Burkes, E. B. Makram and R. Hadidi, "Water Tree Detection in Underground Cables Using Time Domain Reflectometry," in IEEE Power and Energy Technology Systems Journal, vol. 2, no. 2, pp. 53-62, June 2015, doi: 10.1109/JPETS.2015.2420791.
- [29] W. A. Thue, Ed., "Treeing," in Electric Power Cable Engineering, 3rd ed. Boca Raton, FL, USA: Taylor & Francis, 2012, pp. 367–384
- [30] H. M. Li, R. A. Fouracre and B. H. Crichton, "Transient current measurement for the detection of water tree growth in polymeric power cables," in IEEE Transactions on Dielectrics and Electrical Insulation, vol. 2, no. 5, pp. 866-874, Oct. 1995, doi: 10.1109/94.469980.
- [31] R. R. Beer and R. A. Nelson, "Practice and Accepted Rules of Shielding Power Cables," in IEEE Transactions on Industry Applications, vol. IA-14, no. 4, pp. 352-356, July 1978, doi: 10.1109/TIA.1978.4503550.
- [32] "IEEE Guide for Bonding Shields and Sheaths of Single-Conductor Power Cables Rated 5 kV through 500 kV," in IEEE Std 575-2014 (Revision of IEEE Std 575-1988), vol., no., pp.1-83, 18 Sept. 2014, doi: 10.1109/IEEESTD.2014.6905681.
- [33] A. M. D' Amore, M. Sarto, and A. Scarlatti, "Modeling of magnetic-field coupling with cable bundle harnesses," IEEE Trans. Electromagn. Compat., vol. 45, no. 3, pp. 520–530, Aug. 2003.
- [34] M. Li, C. Zhou, and W. Zhou, "A Revised Model for Calculating HV Cable Sheath Current Under Short-Circuit Fault Condition and Its Application for Fault Location—Part 1: The Revised Model," in IEEE Transactions on Power Delivery, vol. 34, no. 4, pp. 1674-1683, Aug. 2019, doi: 10.1109/TPWRD.2019.2918159.
- [35] Z. Tang et al., "Analysis of significant factors on cable failure using the cox proportional hazard model," IEEE Trans. Power Del., vol. 29, no. 2, pp. 951–957, Apr. 2014.
- [36] IEEE Standard for the Testing, Design, Installation, and Maintenance of Electrical Resistance Trace Heating for Industrial Applications-Redline, IEEE P515/D4, 2011.
- [37] F. Xu et al., "Online Cable Insulation Condition Evaluation Using Harmonic Measurement Data," in IEEE Transactions on Instrumentation and Measurement, vol. 73, pp. 1-13, 2024, Art no. 9004213, doi: 10.1109/TIM.2024.3415780.
- [38] S. Babaev, S. Cobben, V. Cuk and H. van den Brom, "Online Estimation of Cable Harmonic Impedance in Low-Voltage Distribution Systems," in IEEE Transactions on Instrumentation and Measurement, vol. 69, no. 6, pp. 2779-2789, June 2020, doi: 10.1109/TIM.2019.2926690.
- [39] H. Lim, G. -Y. Kwon and Y. -J. Shin, "Fault Detection and Localization of Shielded Cable via Optimal Detection of Time-Frequency-Domain Reflectometry," in IEEE Transactions on Instrumentation and Measurement, vol. 70, pp. 1-10, 2021, Art no. 3521510, doi: 10.1109/TIM.2021.3092514.
- [40] C. -K. Lee et al., "Real-Time Condition Monitoring of LOCA via Time-Frequency Domain Reflectometry," in IEEE Transactions on Instrumentation and Measurement, vol. 66, no. 7, pp. 1864-1873, July 2017, doi: 10.1109/TIM.2017.2664578.
- [41] Z. Tang, K. Zhou, P. Meng and Y. Li, "A Frequency-Domain Location Method for Defects in Cables Based on Power Spectral Density," in IEEE Transactions on

- Instrumentation and Measurement, vol. 71, pp. 1-10, 2022, Art no. 9005110, doi: 10.1109/TIM.2022.3189636.
- [42] S. Mo, D. Zhang, Z. Li and Z. Wan, "Extraction of High-Frequency Power Cable Transmission Characteristics From Impedance Spectroscopy," in IEEE Transactions on Instrumentation and Measurement, vol. 70, pp. 1-10, 2021, Art no. 1503810, doi: 10.1109/TIM.2021.3087816.
- [43] M. Marzinotto and G. Mazzanti, "The Feasibility of Cable Sheath Fault Detection by Monitoring SGCurrents at the Ends of Cross-Bonding Sections," in IEEE Transactions on Industry Applications, vol. 51, no. 6, pp. 5376-5384, Nov.-Dec. 2015, doi: 10.1109/TIA.2015.2409802...
- [44] C. Jung, J. Lee, J. Kang, X. Wang, and Y. Song, "Metal sheath current characteristic and its reduction on underground power cable systems," Proc. IEEE Power Eng. Soc. Gen. Meeting, 2005, pp. 2562–2569.
- [45] W. Pan, Y. Li, K. Sun, Z. Zhu and X. Li, "Incipient Fault Location Method of Cable Based on Both-End Electric Quantities," in IEEE Access, vol. 8, pp. 219503-219512, 2020, doi: 10.1109/ACCESS.2020.3042557.
- [46] B. Zhu, X. Yu, L. Tian, and X. Wei, "Insulation Monitoring and Diagnosis of Faults in Cross-Bonded Cables Based on the Resistive Current and Sheath Current," in IEEE Access, vol. 10, pp. 46057-46066, 2022, doi: 10.1109/ACCESS.2022.3170145.
- [47] Y. Yang, D. M. Hepburn, C. Zhou, W. Zhou, and Y. Bao, "On-line monitoring of relative dielectric losses in cross-bonded cables using sheath currents," in IEEE Transactions on Dielectrics and Electrical Insulation, vol. 24, no. 5, pp. 2677-2685, Oct. 2017, doi: 10.1109/TDEI.2017.005438.
- [48] X. Dong, Y. Yang, C. Zhou, and D. M. Hepburn, "Online Monitoring and Diagnosis of HV Cable Faults by Sheath System Currents," in IEEE Transactions on Power Delivery, vol. 32, no. 5, pp. 2281-2290, Oct. 2017, doi: 10.1109/TPWRD.2017.2665818.
- [49] A. Das and C. C. Reddy, "Sheath Voltage and Sheath Current Phenomenon for Different Types of Bonding for HV Power Cable Under Steady State," 2022 IEEE 6th International Conference on Condition Assessment Techniques in Electrical Systems (CATCON), Durgapur, India, 2022, pp. 202-206, doi: 10.1109/CATCON56237.2022.10077653.
- [50] Y. Wu, P. Zhang and G. Lu, "Detection and Location of Aged Cable Segment in Underground Power Distribution System Using Deep Learning Approach," in IEEE Transactions on Industrial Informatics, vol. 17, no. 11, pp. 7379-7389, Nov. 2021, doi: 10.1109/TII.2021.3056993.
- [51] M. A. Shokry, A. Khamlichi, F. Garnacho, J. M. Malo and F. Álvarez, "Detection and Localization of Defects in Cable Sheath of Cross-Bonding Configuration by Sheath Currents," in IEEE Transactions on Power Delivery, vol. 34, no. 4, pp. 1401-1411, Aug. 2019, doi: 10.1109/TPWRD.2019.2903329.
- [52] P. Zhang, L. Kong, R. Liang, B. Xu and N. Peng, "Fault Location Method for Three-Core Cable Using Amplitude Ratio of Shield-Grounding Wire Currents," in IEEE Transactions on Industrial Informatics, vol. 19, no. 6, pp. 7456-7467, June 2023, doi: 10.1109/TII.2022.3194626.
- [53] C. S. Subudhi and S. K. Sen, "Non-Intrusive Online Time Domain Reflectometry Technique for Power Cables," in IEEE Transactions on Power Delivery, vol. 39, no. 1, pp. 101-110, Feb. 2024, doi: 10.1109/TPWRD.2023.3324655.
- [54] Y. H. Lee and Y. -J. Shin, "Time-Frequency Domain Reflectometry for Live HTS Cable System via Inductive Couplers and Neural Network," in IEEE Transactions on

- Applied Superconductivity, vol. 31, no. 5, pp. 1-5, Aug. 2021, Art no. 5400305, doi: 10.1109/TASC.2021.3067671.
- [55] C. Gao, L. Wang, J. Mao, S. Hu, B. Zhang and S. Yang, "Non-Intrusive Cable Fault Diagnosis Based on Inductive Directional Coupling," in IEEE Transactions on Power Delivery, vol. 34, no. 4, pp. 1684-1694, Aug. 2019, doi: 10.1109/TPWRD.2019.2918173.
- [56] Y. H. Lee, G. -Y. Kwon and Y. -J. Shin, "Contactless Monitoring Technique for Live Shielded Cable via Stepped-Frequency Waveform Reflectometry and Inductive Coupler," in IEEE Transactions on Industrial Electronics, vol. 69, no. 9, pp. 9494-9503, Sept. 2022, doi: 10.1109/TIE.2021.3116587.
- [57] X. Kong, Y. Xu, Z. Jiao, D. Dong, X. Yuan and S. Li, "Fault Location Technology for Power System Based on Information About the Power Internet of Things," in IEEE Transactions on Industrial Informatics, vol. 16, no. 10, pp. 6682-6692, Oct. 2020, doi: 10.1109/TII.2019.2960440.
- [58] R. Bhargav, B. R. Bhalja and C. P. Gupta, "Novel Fault Detection and Localization Algorithm for Low-Voltage DC Microgrid," in IEEE Transactions on Industrial Informatics, vol. 16, no. 7, pp. 4498-4511, July 2020, doi: 10.1109/TII.2019.2942426.
- [59] J. Xu, Z. Wu, X. Yu and C. Zhu, "Robust Faulted Line Identification in Power Distribution Networks via Hybrid State Estimator," in IEEE Transactions on Industrial Informatics, vol. 15, no. 9, pp. 5365-5377, Sept. 2019, doi: 10.1109/TII.2019.2899130.
- [60] X. Wang, J. Gao, M. Chen, X. Wei, Y. Wei and Z. Zeng, "Faulty Line Detection Method Based on Optimized Bistable System for Distribution Network," in IEEE Transactions on Industrial Informatics, vol. 14, no. 4, pp. 1370-1381, April 2018, doi: 10.1109/TII.2017.2753227.
- [61] G. Li, J. Chen, H. Li, L. Hu, W. Zhou, and C. Zhou, "Detection of Irregular Sheath Current Distribution for Diagnosis of Faults in Grounding Systems of Cross-Bonded Cables," in IEEE Access, vol. 11, pp. 68453-68461, 2023, doi: 10.1109/ACCESS.2023.3292542.
- [62] S. Noufal and G. Anders, "Sheath loss factor for cross-bonded cable systems with unknown minor section lengths field verification of the IEC standard," IEEE Trans. Power Del., vol. 35, no. 6, pp. 2722–2730, Dec. 2020.
- [63] G. J. Anders and H. Brakelmann, "Rating of underground power cables with boundary temperature restrictions," IEEE Trans. Power Del., vol. 33, no. 4, pp. 1895– 1902, Aug. 2018.
- [64] Requirements for Electrical Installations IET Wiring Regulations, Eighteenth Edition, British Standard 7671, 2018.
- [65] R. Candela, A. Gattuso, M. Mitolo, E. R. Sanseverino and G. Zizzo, "A Comparison of Special Bonding Techniques for Transmission and Distribution Cables Under Normal and Fault Conditions," in IEEE Transactions on Industry Applications, vol. 57, no. 1, pp. 101-109, Jan.-Feb. 2021, doi: 10.1109/TIA.2020.3032947.
- [66] L. Li, J. Yong, and W. Xu, "Single-Sheath Bonding—A New Method to Bond/Ground Cable Sheaths," in IEEE Transactions on Power Delivery, vol. 35, no. 2, pp. 1065-1068, April 2020, doi: 10.1109/TPWRD.2019.2929691.
- [67] "Montage Special des Lignes en Cables Souterrains," French Patent No. 517,446-X11-6, 1920.
- [68] "Electrical cable installation," U. S. Patent No. 1,512,443, R. W. Atkinson, 1924.
- [69] "Bonding circuit for reducing sheath current of power cable line," U. S. Patent No. 3857071A, 1974.

- [70] K. Usha and S. Usa, "Inter disc fault location in transformer windings using SFRA," IEEE Trans. Dielectr. Electr. Insul., vol. 22, no. 6, pp. 3567–3573, Dec. 2015.
- [71] A. Das and C. C. Reddy, "An Analytical Approach to Locate Short Circuit Fault in a Cable Using Sweep Frequency Response Analysis," in IEEE Transactions on Industrial Electronics, 2022, doi: 10.1109/TIE.2022.3189080.
- [72] "IEEE Guide for Measuring Resistivity of Cable-Insulation Materials at High Direct Voltages," in IEEE Std 402-1974 (Reaffirmed 1982), vol., no., pp.1-16, 8 Aug. 1974, doi: 10.1109/IEEESTD.1974.7409861.
- [73] X. Chen, K. Wu, Y. Cheng, and L. Yan, "Sheath circulating current calculation and measurements of underground power cables," in International Conference on Power Insulated Cables, JICABLE07, June 2007.
- [74] E. A. Guillemin, Synthesis of Passive Networks, New York: Wiley, 1962.
- [75] C.R. Paul, "Analysis of Multiconductor Transmission Lines, Wiley- Interscience Publication, Edition John Wiley and Sons, 1994, Ch.4.
- [76] Brian C. Wadell; "Transmission Lines Design Handbook," Artech House Inc, 1991, 500, pp.200-300.
- [77] Ligia Loretta Cristea, IvicaMartinjak, and Igor Urbiha, Hyperfibonacci Sequences and Polytopic Numbers, arXiv e-prints (2016), arXiv:1606.06228.
- [78] T. R. Bashkow, "The A matrix, new network description," IRE Trans. Circuit Theory, pp. 117–119, Sep. 1957.
- [79] E. A. Guillemin, Theory of Linear Physical Systems. New York: Wiley, 1963.
- [80] G. Mugala, R. Eriksson, U. Gafvert and P. Petterson, "Measurement technique for high frequency characterization of semiconducting materials in extruded cables," in IEEE Transactions on Dielectrics and Electrical Insulation, vol. 11, no. 3, pp. 471-480, June 2004, doi: 10.1109/TDEI.2004.1306725.
- [81] A. Swetapadma and A. Yadav, "A Novel Decision Tree Regression-Based Fault Distance Estimation Scheme for Transmission Lines," in IEEE Transactions on Power Delivery, vol. 32, no. 1, pp. 234-245, Feb. 2017, doi: 10.1109/TPWRD.2016.2598553.
- [82] M. Shaik, S. K. Yadav and A. G. Shaik, "An EMD and Decision Tree-Based Protection Algorithm for the Solar PV Integrated Radial Distribution System," in IEEE Transactions on Industry Applications, vol. 57, no. 3, pp. 2168-2177, May-June 2021, doi: 10.1109/TIA.2021.3058618.